

**MONASH UNIVERSITY**  
**THESIS ACCEPTED IN SATISFACTION OF THE**  
**REQUIREMENTS FOR THE DEGREE OF**  
**DOCTOR OF PHILOSOPHY**

ON..... 2 November 2001 .....

.....  
*for* Sec. Research Graduate School Committee

Under the copyright Act 1968, this thesis must be used only under the normal conditions of scholarly fair dealing for the purposes of research, criticism or review. In particular no results or conclusions should be extracted from it, nor should it be copied or closely paraphrased in whole or in part without the written consent of the author. Proper written acknowledgement should be made for any assistance obtained from this thesis.

**ADDENDUM**

p 24 para 2 line 1: Replace "PDAs are" with "PDAs and intensified PDAs are".

p 35 para 1 line 1: Replace "that this not vital" with "that this was not vital".

p 60 para 3 line 3: Replace "sewerage" with "sewage".

p 65 para 2: Comment: The spectrograph was computer controlled.

p 66: Comment: The term "spectrometer" refers to combined spectrograph and detector systems.

Sections 3.3 and 3.4: Comment: All elemental analyses were carried out using sample CRC/8-4-26/64. This sample was chosen for analysis because it contained elemental concentrations typical of many Latrobe Valley brown coals. The results obtained from the analysis of this sample were typical of those obtained from the analyses of the great majority of the Latrobe Valley coals studied.

p 90 para 2: Comment: The term "resonance line" refers to an atomic transition that terminates in the ground state and which may re-absorb energy emitted from other atoms of the same element.

p 121 para 3: Comment: The electret microphone has an internal resistance which means that the voltage output is offset from the ground. The 4  $\mu\text{F}$  capacitor acts as a blocking capacitor to perform AC coupling. Hence it would have no effect on the high frequency signal obtained and shown in Figure 5.2.

p 140 para 1 line 12: Delete "The standard error of prediction is also dramatically." and add "The standard error of prediction is also dramatically improved."

p 167 para 3 line 6: Comment: The H-to-C ratio was found to increase with irradiance below  $20 \text{ GWcm}^{-2}$  in the samples identical in all respects except moisture content. A laser irradiance of  $20 \text{ GWcm}^{-2}$  was also used because it was found to be the average optimum laser irradiance for elemental analyses in Section 3.3.

p 188 para 4 line 8: Replace Cl and Na with  $\text{Cl}^+$  and  $\text{Na}^+$  respectively.

p. 215 para 1 line 4 and para 4 line 6: Replace [stats book] with [149].

*Analysis of Latrobe Valley Brown Coal  
Using Laser-Induced Breakdown  
Spectroscopy*

*Fiona Wallis*

*B.Sc. (Hons.)*

*A thesis submitted to the  
School of Chemistry, Monash University  
for the degree of  
Doctor of Philosophy*

*May 2001*

# Table of Contents

|  | <i>Page</i> |
|--|-------------|
| <b>LIST OF TABLES</b> .....  | i           |
| <b>LIST OF FIGURES</b> .....   | iii         |
| <b>LIST OF SYMBOLS</b> .....   | xi          |
| <b>ABSTRACT</b> .....  | xv          |
| <b>DECLARATION</b> .....   | xviii       |
| <b>ACKNOWLEDGMENTS</b> .....   | xix         |
| <b>CHAPTER 1 – INTRODUCTION</b> .....  | 1           |
| <b>1.1 Background</b> .....  | 1           |
| 1.1.1 <i>Composition of Victorian Brown Coal</i> .....   | 2           |
| 1.1.2 <i>Effects of the Chemical Composition of the Coal</i> .....                                   | 5           |
| <b>1.2 Contents of Thesis</b> .....  | 8           |
| <b>CHAPTER 2 – THEORY AND LITERATURE REVIEW</b> .....  | 11          |
| <b>2.1 Introduction</b> .....  | 11          |
| <b>2.2 Methods Used to Chemically Analyse Latrobe Valley<br/>        Brown Coal</b> .....            | 11          |
| 2.2.1 <i>Standard Wet Laboratory Analysis</i> .....  | 11          |
| 2.2.2 <i>On-Line Methods for Coal Analyses</i> .....   | 15          |
| <b>2.3 Laser-Induced Breakdown Spectroscopy</b> .....  | 18          |
| 2.3.1 <i>Overview</i> .....  | 18          |
| 2.3.2 <i>Instrumentation</i> .....   | 20          |
| 2.3.2.1 <i>Choice of Laser</i> .....   | 20          |
| 2.3.2.2 <i>Choice of Detection System</i> .....  | 23          |
| 2.3.2.3 <i>Field Instruments</i> .....   | 25          |
| 2.3.3 <i>Fundamental Studies of LIBS</i> .....   | 27          |
| 2.3.3.1 <i>Spatial and Temporal Resolution of the<br/>                Laser-Induced Plasma</i> ..... | 27          |
| 2.3.3.2 <i>Effects of the Sample Matrix</i> .....  | 34          |
| 2.3.3.3 <i>Sample Surface Effects</i> .....  | 35          |
| 2.3.3.4 <i>Mass Removal</i> .....  | 37          |

|  | <i>Page</i>    |
|--|----------------|
| 2.3.3.5 <i>Temperature and Electron Density<br/>Measurements of the Laser-Induced<br/>Plasma</i> .....                                   | 41             |
| 2.3.3.6 <i>Line Broadening</i> .....   | 45             |
| 2.3.3.7 <i>Atmospheric Environment</i> .....   | 46             |
| 2.3.4 <i>Applications of LIBS</i> .....  | 49             |
| 2.3.4.1 <i>Remote Sensing Applications</i> .....   | 49             |
| 2.3.4.2 <i>Portable Instruments</i> .....  | 51             |
| 2.3.5 <i>Signal Normalisation</i> .....  | 53             |
| 2.3.6 <i>Sample Water Content</i> .....  | 58             |
| 2.3.7 <i>Calibration Methods</i> .....   | 60             |
| <br><b>CHAPTER 3 – EXPERIMENTAL DESIGN AND OPTIMISATION ..</b>   | <br>62         |
| 3.1 <i>Introduction</i> .....  | 62             |
| 3.2 <i>Experimental Apparatus</i> .....  | 62             |
| 3.2.1 <i>Laboratory-based System</i> .....   | 62             |
| 3.2.2 <i>Portable System</i> .....   | 68             |
| 3.3 <i>The Effects of Laser Irradiance on Laser-Induced<br/>Emission Spectra</i> .....   | 68             |
| 3.4 <i>The Effects of Time-Gating on Laser-Induced Spectra ...</i>   | 80             |
| 3.5 <i>Summary</i> .....   | 93             |
| <br><b>CHAPTER 4 – ANALYSIS OF THE INORGANIC CONTENT OF<br/>LATROBE VALLEY COAL USING LASER-INDUCED<br/>BREAKDOWN SPECTROSCOPY</b> ..... | <br><br><br>96 |
| 4.1 <i>Introduction</i> .....  | 96             |
| 4.2 <i>Experimental Apparatus and Methodology</i> .....  | 97             |
| 4.3 <i>Spectra of Latrobe Valley Brown Coals</i> .....   | 97             |
| 4.4 <i>Reproducibility of LIBS Analyses of the Inorganic<br/>Content of Latrobe Valley Brown Coals</i> .....                             | 99             |
| 4.5 <i>Calibration of LIBS Analyses of the Inorganic<br/>Elements in Latrobe Valley Brown Coal</i> .....                                 | 107            |

|  | <i>Page</i> |
|--|-------------|
| 4.6 <i>Comparison of LIBS and Standard Analyses of Latrobe Valley Brown Coal</i> .....                 | 117         |
| 4.7 <i>Conclusions</i> .....   | 118         |
| <br>   |             |
| <b>CHAPTER 5 – ACOUSTIC WAVE NORMALISATION OF LASER-INDUCED BREAKDOWN SPECTROSCOPIC ANALYSES</b> ..... | 120         |
| 5.1 <i>Introduction</i> .....  | 120         |
| 5.2 <i>Experimental Apparatus and Methodology</i> .....  | 121         |
| 5.3 <i>Validity of Acoustic Wave Normalisation</i> .....   | 121         |
| 5.4 <i>The Effect of Sample Matrix on Acoustic Signal Levels</i> .....                                 | 128         |
| 5.5 <i>Comparison of Normalisation Methods</i> .....   | 130         |
| 5.5.1 <i>Normalisation of Ca Emission</i> .....  | 132         |
| 5.5.2 <i>Normalisation of Fe Emission</i> .....  | 135         |
| 5.5.3 <i>Normalisation of Si Emission</i> .....  | 139         |
| 5.5.4 <i>Normalisation of Mg Emission</i> .....  | 140         |
| 5.6 <i>Conclusions</i> .....   | 143         |
| <br>   |             |
| <b>CHAPTER 6 – DETERMINATION OF COAL MOISTURE AND ITS EFFECTS ON LIBS SYSTEM RESPONSE</b> .....        | 145         |
| 6.1 <i>Introduction</i> .....  | 145         |
| 6.2 <i>Experimental Apparatus and Methodology</i> .....  | 146         |
| 6.3 <i>Effects of Coal Moisture Content on Inorganic Analyses Using LIBS</i> .....                     | 147         |
| 6.4 <i>Effects of Coal Moisture on Carbon and Hydrogen Emission</i> .....                              | 154         |
| 6.5 <i>Conclusions</i> .....   | 165         |
| <br>   |             |
| <b>CHAPTER 7 – THE MODELLING OF COAL CONSTITUENTS BY PRINCIPAL COMPONENT REGRESSION</b> .....          | 168         |
| 7.1 <i>Introduction</i> .....  | 168         |

|  | <i>Page</i> |
|--|-------------|
| 7.2 <i>Principal Component Regression</i> .....                      | 168         |
| 7.3 <i>Model Optimisation</i> .....                                  | 169         |
| 7.4 <i>Model Simplification</i> .....                                | 173         |
| 7.5 <i>Linear PCR Models</i> .....                                   | 175         |
| 7.5.1 <i>Model for Magnesium</i> .....                               | 176         |
| 7.5.2 <i>Model for Sodium</i> .....                                  | 178         |
| 7.5.3 <i>Model for Calcium</i> .....                                 | 181         |
| 7.5.4 <i>Model for Iron</i> .....                                    | 185         |
| 7.5.5 <i>Model for Aluminium</i> .....                               | 185         |
| 7.5.6 <i>Model for Silicon</i> .....                                 | 185         |
| 7.5.7 <i>Model for Chlorine</i> .....                                | 188         |
| 7.5.8 <i>Model for Sulphur</i> .....                                 | 190         |
| 7.5.9 <i>Model for Total Ash Yield</i> .....                         | 193         |
| 7.5.10 <i>Model for Coal Moisture Content</i> .....                  | 193         |
| 7.6 <i>Non-linear models</i> .....                                   | 195         |
| 7.7 <i>Conclusions</i> .....   | 195         |
| <br><b>CHAPTER 8 – GENERAL CONCLUSIONS</b> .....                     | <br>198     |
| <br><b>APPENDICES</b> .....  | <br>207     |
| <b>Appendix A Standard Analysis Results</b> .....                    | 207         |
| A.1 <i>Brown Coal Analyses</i> .....                                 | 207         |
| A.2 <i>Analyses of Other Samples</i> .....                           | 212         |
| <br><b>Appendix B Error Analysis</b> .....                           | <br>213     |
| B.1 <i>Errors in the Results in Chapter 3</i> .....                  | 213         |
| B.2 <i>Errors in the Results in Chapter 4</i> .....                  | 214         |
| B.3 <i>Errors in the Results in Chapters</i><br><i>5 and 6</i> ..... | 215         |
| B.4 <i>Errors in the Results in Chapter 7</i> .....                  | 215         |
| <br><b>LIST OF REFERENCES</b> .....                                  | <br>217     |

## *List of Tables*

---

|   | <i>Page</i> |
|---|-------------|
| Table 3.1. Experimental apparatus and characteristics of the laboratory based setup. ....   | 64          |
| Table 3.2. Experimental apparatus and characteristics of the portable Laser Plasma Spectrometer. ....   | 67          |
| Table 3.3. Calculated Plasma Properties. ....   | 93          |
| Table 3.4. Optimum delay times and laser irradiances for the elemental emission lines. ....   | 94          |
| Table 4.1. Properties of emission lines observed in laser-induced spectra of Latrobe Valley brown coals. ....   | 100         |
| Table 4.2. Emission lines used in analysis and F values obtained in reproducibility studies for (a) neutral emission lines and (b) ionic emission lines. ....           | 105         |
| Table 4.3. Detection limits of the inorganic elements in Latrobe Valley coal calculated from calibration curves constructed from LIBS analyses of 30 coal samples. .... | 117         |
| Table 4.4. Comparison of LIBS and ICP analyses of an unknown coal sample. ....  | 118         |
| Table 5.1. Chemical composition of samples that produced similar acoustic signals. ....   | 130         |
| Table 5.2. Elemental emission lines used in acoustic normalisation studies and their properties. ....   | 132         |

|  | <i>Page</i> |
|--|-------------|
| Table 7.1. Comparison of correlation coefficients and RMSEPs in PCR models, before and after outliers were removed. ....                   | 171         |
| Table 7.2. The root mean square errors of prediction for the simplified PCR models of ten constituents of Latrobe Valley brown coals. .... | 175         |
| Table A.1. Standard Chemical Analyses (obtained using AAS and ICP) of Latrobe Valley Brown Coal Samples. ....                              | 207         |
| Table A.2. Standard Chemical Analyses (obtained using AAS and ICP) of Samples used in Chapter 5. ....                                      | 212         |

## List of Figures

---

|  | <i>Page</i> |
|--|-------------|
| Figure 1.1. Typical composition of Latrobe Valley brown coal. ....   | 3           |
| Figure 1.2. Possible Mechanisms Involved in Ash Formation [17]. ....   | 6           |
| Figure 2.1. Schematic diagrams of prototype microwave transmission gauges used by Cutmore and coworkers for measurement of moisture in Latrobe Valley brown coal (a) on a conveyor belt and (b) in a shaker tube [4]. .... | 16          |
| Figure 2.2. Instrumental setup for LIBS experiments. ....  | 21          |
| Figure 3.1. Schematic diagram of the laboratory based experimental setup for LIBS analysis of Latrobe Valley brown coal. ....  | 63          |
| Figure 3.2. Schematic diagram of the Laser Plasma Spectrometer. ....   | 66          |
| Figure 3.3. Variation of (a) peak area, (b) the ratio of Mg (I) at 285 nm to Mg (II) at 279 nm, and (c) signal-to-background ratio with laser irradiance for Mg in Latrobe Valley brown coal. ....                         | 69          |
| Figure 3.4. Variation of (a) peak area and (b) signal-to-background ratio with laser irradiance for Na emission in LIBS analyses of Latrobe Valley brown coal. ....  | 72          |
| Figure 3.5. Variation of (a) peak area, (b) the ratio of Ca (I) at 423 nm to Ca (II) at 393 nm, and (c) signal-to-background ratio with laser irradiance for Ca in Latrobe Valley brown coal. ....                         | 73          |
| Figure 3.6. Variation of (a) peak area, (b) the ratio of Fe (I) at 373.5 & 373.7 nm to Fe (II) at 238.2 nm, and (c) signal-to-background ratio with laser irradiance for Fe in Latrobe Valley brown coal. ....             | 75          |

|  | <i>Page</i> |
|--|-------------|
| Figure 3.7. Variation of (a) peak area and (b) signal-to-background ratio with laser irradiance for Al emission in LIBS analyses of Latrobe Valley brown coal. ....  | 76          |
| Figure 3.8. Variation of (a) the peak area and (b) the signal-to-background ratio of Si (I) at 288.16 nm with laser irradiance during LIBS analyses of Latrobe Valley brown coal. ....                                       | 78          |
| Figure 3.9. LIBS spectra obtained after time delays between the start of the laser spark and optical detection of (a) 0.5 $\mu$ s, (b) 1.0 $\mu$ s, and (c) 1.5 $\mu$ s with a 5 $\mu$ s detection window in each case. .... | 79          |
| Figure 3.10. Variation of (a) peak area, (b) the ratio of Mg (I) at 285 nm to Mg (II) at 279 nm and (c) the signal-to-background ratio for LIBS analysis of Mg in Latrobe Valley brown coals. ....                           | 81          |
| Figure 3.11. Variation of (a) peak area and (b) signal-to-background ratio with time delay for Na in Latrobe Valley brown coals. ....  | 83          |
| Figure 3.12. Variation of (a) peak area, (b) the ratio of Ca (I) at 423 nm to Ca (II) at 393 nm and (c) the signal-to-background ratio for LIBS analysis of Ca in Latrobe Valley brown coals. ....                           | 84          |
| Figure 3.13. Variation of (a) peak area, (b) the ratio of Fe (I) at 373.5 & 373.7 nm to Fe (II) at 238 nm and (c) the signal-to-background ratio for LIBS analysis of Fe in Latrobe Valley brown coals. ....                 | 86          |

|   | <i>Page</i> |
|---|-------------|
| Figure 3.14. Variation of (a) peak area and (b) signal-to-background ratio with time delay for Al in Latrobe Valley brown coals. ....   | 87          |
| Figure 3.15. Variation of (a) peak area and (b) signal-to-background ratio with time delay for the Si emission line at 288.16 nm. ....  | 88          |
| Figure 3.16. The H $\beta$ emission lines obtained at delay times of (a) 0.5 $\mu$ s, (b) 1.0 $\mu$ s, and (c) 1.5 $\mu$ s after the start of the laser spark. The thin lines represent the experimental data and the thick lines the Lorentzian fits. .... | 91          |
| Figure 4.1. Spectrum of brown coal from the Yallourn open cut between 200 and 840 nm. ....  | 98          |
| Figure 4.2. Spectrum of brown coal from the Loy Yang open cut between 200 and 840 nm. ....  | 102         |
| Figure 4.3. Spectrum of brown coal from the Morwell open cut between 200 and 840 nm. ....   | 103         |
| Figure 4.4. Calibration curve for Na in low-ash Latrobe Valley brown coal constructed from LIBS analyses of 30 coal samples. ....   | 108         |
| Figure 4.5. Calibration curves for LIBS analyses of Mg in low-ash Latrobe Valley brown coal using linear regression (---) and Equation 4.1 (—). ....  | 110         |
| Figure 4.6. Calibration curves for LIBS analyses of Ca in low-ash Latrobe Valley brown coal using linear regression (---) and Equation 4.1 (—). ....  | 111         |

|   | <i>Page</i> |
|---|-------------|
| Figure 4.7. Calibration curve for Fe in low-ash Latrobe Valley brown coal constructed from LIBS analyses of 30 coal samples. ....                                 | 112         |
| Figure 4.8. Calibration curve for Al in Latrobe Valley brown coal constructed from LIBS analyses of 30 samples. ....  | 114         |
| Figure 4.9. Calibration curve for Si in low-ash Latrobe Valley brown coal constructed from LIBS analyses of 30 coal samples. ....                                 | 115         |
| Figure 5.1. Circuit diagram of the microphone system used to measure the acoustic signal during LIBS experiments. ....  | 122         |
| Figure 5.2. A typical trace of a laser-induced acoustic signal of Latrobe Valley brown coal, obtained using a laser irradiance of $20 \text{ GW cm}^{-2}$ . ....  | 123         |
| Figure 5.3. Laser-induced acoustic signal from a sample of Latrobe Valley brown coal as a function of laser irradiance. ....                                      | 125         |
| Figure 5.4. Laser-induced mass loss from Latrobe Valley brown coal as a function of laser irradiance. ....  | 126         |
| Figure 5.5. Elemental emission intensity as a function of acoustic signal for (a) Ca at 422.7 nm, (b) Na D lines, (c) Mg at 285.2 nm, and (d) C at 247.9 nm. .... | 127         |
| Figure 5.6. Variation of the acoustic signal with sample matrix. ....   | 129         |
| Figure 5.7. Variation of the intensity ratio of the 430.25 nm emission line of Ca to the 422.67 nm emission line with Ca concentration. ....                      | 133         |

|  | <i>Page</i> |
|--|-------------|
| Figure 5.8. Results of the normalisation of Ca at 422.67 nm. ....  | 134         |
| Figure 5.9. Results of the normalisation of Fe at 438.3 nm. ....   | 136         |
| Figure 5.10. Variation of the intensity ratio of the 288.16 nm emission<br>line of Si to the 263.13 nm emission line with Si<br>concentration in cement and cement ingredients. .... | 137         |
| Figure 5.11. Variation of the emission intensities of the Si lines at<br>263.13 nm and 288.16 nm with Si concentration in<br>cement and cement ingredients. ....                     | 138         |
| Figure 5.12. Results of the normalisation of Si at 288.16 nm. ....   | 141         |
| Figure 5.13. Results of the normalisation of Mg at 285.21 nm. ....   | 142         |
| Figure 6.1. Variation of elemental peak area with moisture<br>content in Yallourn coal sample CRC/8-4-26/68 for<br>(a) the Na D lines and (b) Mg at 285.21 nm. ....                  | 148         |
| Figure 6.2. Variation of elemental peak area with moisture<br>content in blended coal sample CRC/8-4-30/55 for<br>(a) the Na D lines and (b) Mg at 285.21 nm. ....                   | 149         |
| Figure 6.3. Variation of peak area with elemental concentration<br>for Yallourn coal sample CRC/8-4-26/68 for (a) the Na D<br>lines and (b) Mg at 285.21 nm. ....                    | 150         |
| Figure 6.4. Variation of peak area with elemental concentration<br>for blended coal sample CRC/8-4-30/55 for (a) the Na D<br>lines and (b) Mg at 285.21 nm. ....                     | 151         |

|  | <i>Page</i> |
|--|-------------|
| Figure 6.5. Variation of emission intensity with elemental concentration for 8 Latrobe Valley coal samples for (a) the Na D lines and (b) Mg at 285.21 nm. ....  | 153         |
| Figure 6.6. Variation of the H $\alpha$ emission line at 656.3 nm with coal moisture content for (a) a Yallourn coal and (b) a blended coal. ....  | 155         |
| Figure 6.7. Variation of the C emission line at 247.86 nm with coal moisture content for (a) a Yallourn coal and (b) a Loy Yang coal. ....   | 156         |
| Figure 6.8. Variation of the peak area of H $\beta$ at 486.13 nm at (●) 8 GWcm $^{-2}$ , (●) 13 GWcm $^{-2}$ , (●) 20 GWcm $^{-2}$ , and (●) 24 GWcm $^{-2}$ for (a) a Yallourn coal and (b) a Loy Yang coal. .... | 158         |
| Figure 6.9. Variation of the electron number density (N $_e$ ) of the laser induced plasma with moisture content in (a) a Yallourn coal and (b) a Loy Yang coal. ....  | 159         |
| Figure 6.10. Variation of the FWHM of the H $\alpha$ line at 656.3 nm with moisture content in (a) a Yallourn coal and (b) a blended coal. ....  | 161         |
| Figure 6.11. Variation of the ratio of H $\beta$ at 486.13 nm to C at 247.86 nm with coal moisture content at four laser irradiances for (a) a Yallourn coal and (b) a Loy Yang coal. ....                         | 162         |
| Figure 6.12. Variation of the ratio of H $\beta$ at 486.13 nm to C at 247.86 nm with moisture content in 8 Latrobe Valley coal samples at four laser irradiances. ....   | 163         |

|  | <i>Page</i> |
|--|-------------|
| Figure 7.1 Influence plot from the initial PCR model for moisture content in Latrobe Valley brown coals, illustrating outliers, influential samples and dangerous outliers. ....                                 | 170         |
| Figure 7.2. Regression plot obtained from analysis of coal moisture content. ....  | 172         |
| Figure 7.3. Variation of the RMSEP with the number of principal components used in PCR model for coal moisture content. ....   | 174         |
| Figure 7.4. PCR model for Mg concentrations in Latrobe Valley brown coals. ....  | 177         |
| Figure 7.5. PCR model for Na concentration in Latrobe Valley brown coals. ....   | 179         |
| Figure 7.6. Variation of Mg emission intensity with Na concentration in Latrobe Valley coals; (a) for the Mg (I) line at 285.21 nm and the Mg (II) line at 279.55 nm, and (b) for the Mg (II)/Mg (I) ratio. .... | 180         |
| Figure 7.7. PCR model for Ca concentration in Latrobe Valley brown coals. ....   | 182         |
| Figure 7.8. Variation of Ca concentration with Na concentration in the Latrobe Valley brown coals used to produce regression models. Ca and Na concentrations were determined by standard chemical methods. .... | 183         |
| Figure 7.9. PCR model for Fe concentration in Latrobe Valley brown coals. ....   | 184         |

|   | <i>Page</i> |
|---|-------------|
| Figure 7.10. PCR model for Al concentration in Latrobe Valley brown coals. .... | 186         |
| Figure 7.11. PCR model for Si concentration in Latrobe Valley brown coals. .... | 187         |
| Figure 7.12. PCR model for Cl concentration in Latrobe Valley brown coals. .... | 189         |
| Figure 7.13. PCR model for S concentration in Latrobe Valley brown coals. ....  | 191         |
| Figure 7.14. PCR model for total ash yield in Latrobe Valley brown coals. ....  | 192         |
| Figure 7.15. PCR model for moisture content in Latrobe Valley brown coals. .... | 194         |

### Acronyms and Abbreviations

| <i>Symbol</i> | <i>Description.</i>                                     | <i>Units</i>        |
|---------------|---|---------------------|
| AAR           | average ablation rate                                   | $\mu\text{m/pulse}$ |
| AAS           | atomic absorption spectrometry                          | -                   |
| ArF           | argon fluoride  | -                   |
| a.u.          | arbitrary units   | -                   |
| CCD           | charge-coupled device                                   | -                   |
| CID           | charge-injection device                                 | -                   |
| Corr. Coeff.  | Correlation coefficient                                 | -                   |
| CRC           | cooperative research centre                             | -                   |
| EPA           | environmental protection agency                         | -                   |
| FWHM          | full-width, half-maximum                                | -                   |
| GLM           | generalised linear model                                | -                   |
| ICCD          | intensified charge-coupled device                       | -                   |
| ICP           | inductively coupled plasma                              | -                   |
| ICP-AES       | inductively coupled plasma atomic emission spectrometry | -                   |
| ICP-MS        | inductively coupled plasma mass spectrometry            | -                   |
| KrF           | krypton fluoride  | -                   |
| LIBS          | laser-induced breakdown spectroscopy                    | -                   |
| LPS           | laser plasma spectrometer                               | -                   |
| LTE           | local thermodynamic equilibrium                         | -                   |
| LTSD          | lens-to-sample distance                                 | $\mu\text{m}$       |
| Nd:glass      | neodymium:glass   | -                   |
| Nd:YAG        | neodymium:yttrium aluminium garnet                      | -                   |
| NIST          | National Institute of Standards and Technology          | -                   |
| PACE          | predicted ash collection efficiency                     | -                   |
| PC            | personal computer                                       | -                   |
| PCA           | principal component analysis                            | -                   |
| PCI           | process control inc.                                    | -                   |
| PCR           | principal component regression                          | -                   |
| PDA           | photodiode array  | -                   |

|         |  |     |
|---------|--|-----|
| PGNAA   | prompt gamma neutron activation analysis           | -   |
| PLS     | partial least squares                              | -   |
| PMT     | photomultiplier tube                               | -   |
| RMSEP   | root mean square error of prediction               | ppm |
| RSD     | relative standard deviation                        | %   |
| TRELIBS | time resolved laser-induced breakdown spectroscopy | -   |
| US      | united states                                      | -   |
| UV      | ultraviolet  | -   |
| VBA     | visual basic for applications                      | -   |
| XeCl    | xenon chloride                                     | -   |
| XRF     | x-ray fluorescence                                 | -   |
| wb      | wet-basis  | -   |

*English Symbols*

| <i>Symbol</i>     | <i>Description</i>  | <i>Units</i>                |
|-------------------|---|-----------------------------|
| $a$               | thermal diffusivity   | $m^2s$                      |
| $A_{ki}, A_{1,2}$ | spontaneous emission rate coefficient                         | $s^{-1}$                    |
| $A_s$             | laser-induced acoustic signal                                 | V.s                         |
| $c$               | elemental concentration                                       | ppm                         |
| $C$               | capacitance   | $\mu F$                     |
| $C(N_e, T)$       | coefficient that is weakly dependent on $N_e$                 | $\text{\AA}^{-3/2} cm^{-3}$ |
| $C_L$             | detection limit   | ppm                         |
| $E_1, E_i$        | lower energy level  | $cm^{-1}$                   |
| $E_2, E_k, E_u$   | upper energy level  | $cm^{-1}$                   |
| $F_{min}$         | minimum breakdown irradiance                                  | $Wm^{-2}$                   |
| $g_1, g_i$        | degeneracy of the lower electronic level                      | -                           |
| $g_2, g_k$        | degeneracy of the upper electronic level                      | -                           |
| $g_m^z$           | degeneracy of electronic level of the higher ionisation state | -                           |
| $g_n^{z-1}$       | degeneracy of electronic level of the lower ionisation state  | -                           |

|             |   |                   |
|-------------|---|-------------------|
| $\hbar$     | Planck's constant divided by $2\pi$   | J.s               |
| $I_1$       | intensity of the first emission line  | -                 |
| $I_2$       | intensity of the second emission line   | -                 |
| $k$         | Boltzmann constant  | JK <sup>-1</sup>  |
| $L_v$       | heat of vaporisation  | Jkg <sup>-1</sup> |
| $m$         | electron rest mass  | kg                |
| $m$         | gradient of the calibration curve   | ppm <sup>-1</sup> |
| $N_m^z$     | number density of the upper energy level of the ionised element                         | cm <sup>-3</sup>  |
| $N_n^{z-1}$ | number density of the upper energy level of the neutral element                         | cm <sup>-3</sup>  |
| $N_e$       | electron number density   | cm <sup>-3</sup>  |
| $Q$         | quality   | -                 |
| $r$         | temperature normalisation coefficient   | cm <sup>-1</sup>  |
| $R$         | resistance  | k $\Omega$        |
| $R^2$       | Pearson coefficient   | -                 |
| $s$         | standard error of prediction  | wt %              |
| $S_{ave}$   | average standard deviation of the five samples with the lowest elemental concentrations | ppm               |
| $T$         | temperature   | K                 |
| $t_e$       | duration of the laser pulse   | s                 |

**Greek Symbols**

| <b>Symbol</b>     | <b>Description</b>  | <b>Units</b>     |
|-------------------|---|------------------|
| $A(^3\Pi)$        | electronic state of C <sub>2</sub>                                  | -                |
| $B(^2\Sigma)$     | electronic state of CN  | -                |
| $\Delta E$        | difference between the energy levels of the two upper energy levels | cm <sup>-1</sup> |
| $\Delta\lambda_s$ | FWHM of a Stark broadened emission line                             | Å                |
| $\Delta v$        | difference in the vibrational quantum numbers                       | -                |

|               |                                  |                   |
|---------------|----------------------------------|-------------------|
| $\lambda$     | wavelength                       | nm                |
| $\rho$        | density                          | $\text{kgm}^{-3}$ |
| $X(^2\Sigma)$ | electronic state of CN           | -                 |
| $X(^3\Pi)$    | electronic state of $\text{C}_2$ | -                 |

Laser-induced breakdown spectroscopy (LIBS) has been applied to the chemical analysis of the inorganic, mineral and moisture content of Latrobe Valley brown coal. Two different experimental systems were used for these analyses. The first of these was a sensitive bench-top system that incorporated an intensified charge-coupled device (ICCD), while the other system was a low-cost portable LIBS instrument. The optimum conditions for the analysis of Latrobe Valley brown coal were determined experimentally using the ICCD system. The optimum laser irradiance used for sample vaporisation was found to vary with the element being analysed as well as its ionisation state. The average optimum irradiance was found to be  $20 \text{ GWcm}^{-2}$ . Time-gated optical detection was implemented to improve the results in this work. The optimum time delay between the start of the laser pulse and detection window varied with element, ionisation state, and emission line. The average optimum delay was found to be  $1 \mu\text{s}$ . The electron density and plasma temperature were also measured at different delays after the laser pulse and were found to decrease with increasing time delay.

Laser-induced emission spectra recorded between 200 and 840 nm using samples from the Yallourn, Loy Yang, and Morwell mines showed that differences in the inorganic and mineral content of the coal were reflected in the spectra. Consequently, the reproducibility of LIBS analyses of the six major inorganic and mineral elements present in Latrobe Valley brown coal, Mg, Na, Ca, Fe, Al and Si, was investigated for elemental concentrations between 30 and 15700 ppm. The results of these experiments showed, with a 95 % confidence level, that most of the analyses of neutral emission during LIBS were reproducible. Calibration curves were then constructed for the six elements by correlating the areas of neutral emission peaks with results from standard chemical analyses. Linear calibration curves with standard errors of prediction of 200, 200, 300 and 500 ppm were obtained for Na, Fe, Al and Si. Non-linear calibration curves with standard errors of prediction of 100 and 200 ppm were found to better fit the data for Ca and Mg because these elements experienced atomic self-absorption at the upper ends of their concentration ranges. The detection limits of the elements ranged between 40 and 200 ppm when using the ICCD system. The analyses of a Latrobe Valley brown coal using LIBS and

inductively coupled plasma emission spectroscopy were compared and found to be in good agreement.

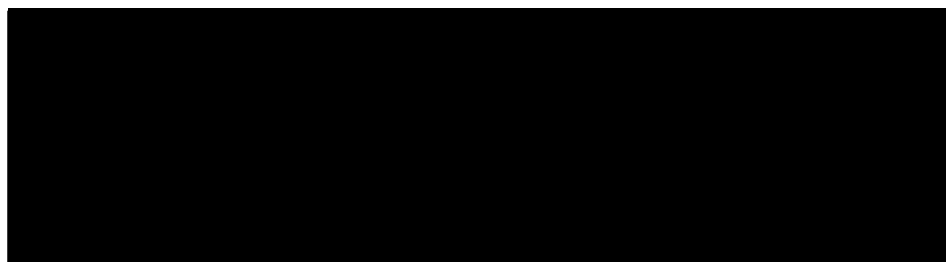
The use of signal normalisation to improve the results of LIBS elemental analyses was also investigated. Three different normalisation methods were tested, the first of which incorporated a measurement of the laser-induced acoustic shock wave. The second method incorporated a temperature normalisation coefficient, while the third method, which was proposed by Chaléard *et al.* [1], used both the acoustic signal and the temperature normalisation coefficient. The acoustic signal was found to be linearly related to the laser irradiance, elemental emission intensity and laser-induced mass loss. The acoustic signal was also found to vary with sample matrix. Hence, the validity of using the laser-induced acoustic shock wave for signal normalisation in LIBS experiments was proven. The method proposed by Chaléard *et al.* [1] was found to be the most effective signal normalisation method for LIBS analyses of Ca, Fe, Mg and Si in cement and cement ingredient samples. The standard errors of prediction obtained from the calibration curves through this data improved from 3 to 2 wt % for Ca and Fe, 3 to 0.2 wt % for Si, and 0.2 to 0.08 wt % for Mg, when this normalisation method was implemented.

The effects of moisture content on LIBS analyses of the inorganic and mineral elements in the coal were also studied. A series of experiments showed that increasing the water in the samples diluted the concentrations of the inorganic and mineral elements and changed the chemistry of the laser-induced plasma. The emission intensities of these elements were found to decrease with increasing water content. Studies of atomic hydrogen emission from the laser-induced plasma showed that the electron density remained constant as coal moisture content varied. Conversely, the plasma temperature was found to vary with coal moisture content. The ratio of the area of the H $\beta$  line at 486 nm to the area of the C emission line at 248 nm was found to increase linearly with moisture content. Hence, it was concluded that this ratio could be used to measure the moisture content of the coal from laser-induced emission spectra. The standard error of prediction obtained using this method was found to be less than or equal to 1 % at each of the laser irradiances used.

Finally, principal component regression (PCR) was applied to LIBS spectral data obtained from fifty Latrobe Valley coal samples using the portable instrument. Predictive models

for ten variables, the Na, Mg, Ca, Fe, Al, Si, Cl, and S levels, the total ash yield and the moisture content, were produced in this way. PCR models were able to be used to measure S, Cl and total ash yield in Latrobe Valley brown coal, properties that were unable to be measured from peak ratios or single peaks in the emission spectra. PCR modelling was also able to improve the prediction error in Al measurements from 300 to 100 ppm. The prediction errors of the PCR models for Na, Mg, Ca, Fe and Si were comparable to those obtained from the single peak calibration curves. Hence, it was concluded that single peak calibration was preferable because of its simplicity. The prediction error of the PCR model for coal moisture content, which was 3 %, was worse than that obtained using the H-to-C ratio method.

To the best of my knowledge, this thesis contains no material which has been accepted for the award of any other degree or diploma in any university or other institution, nor any material which has been published previously or written by another person, except where due reference has been made in the text.



Fiona Wallis

## *Acknowledgments*

---

I would like to acknowledge the financial and other support received during this research from the Cooperative Research Centre for Clean Power from Lignite, which is supported by the Australian Government's Cooperative Research Centres program. I would also like to thank the Australian Government for financial support in the form of an Australian Postgraduate Award. In particular I would like to acknowledge the management of the CRC, Peter Jackson, Howard Mitchell and David Brockway. Special thanks go to Lyn and Dawn for their help over the years.

I would like to acknowledge the assistance and support of Dr. Richard Morrison, my principal supervisor. Thank you for your efforts in proofreading and helping me prepare this thesis. I also acknowledge the contributions from my associate supervisor, Dr. Bruce Chadwick.

Special thanks must go to Dr. Doug Body who spent many tireless hours reading the drafts of this work and helping me tame unruly lab. equipment. Thanks Dr. Body for the friendship, support and Tim Tams on Sunday afternoons.

Thanks must go to Danny Hibbert and the analytical team at HRL for providing the standard analysis results for my many samples. I also gratefully acknowledge the assistance of Associate Professor Frank Burden in getting me started in the world of principal component regression.

A big thank you must go to all my colleagues at the CRC over the years, in particular Peter Griffin, Denise Charlston-Goch, James Hart, Doug Body and Trevor Thomson. I would not have made it this far without your friendship and support. Pete, thanks for the sympathetic ear, technical know-how and funny accents. Dee, thanks just for being proud of me.

I would also like to thank the others who have indirectly helped me along this journey; Helen Webb, Fi and T, Melissa Romeo, Mel Grant, Clodagh McIntyre, Gina Griffin and Tania Jortikka. Guys, thanks for keeping me sane over the years.

Finally I would like to thank my family, Mum, Edward, Philip and Genevieve, for their love and support over the years. A special big thank you goes to my mum, Jeanette, for proofreading my list of references, providing the hot meals every night and taking care of all the little things in order to let me focus on my work.

## *Introduction*

### *1.1 Background*

The large brown coal deposits in the state of Victoria, Australia have been this state's main source of energy since the 1920s. Currently, brown coal provides over 85 % of Victoria's electricity [2]. The majority of this coal is found in the Gippsland basin. The major deposits within this basin occur in the Latrobe Valley depression. It is here that Victoria's electricity is generated from brown coal using pulverised fuel boilers.

The major advantage of Latrobe Valley brown coal is that it is readily and cheaply mined from shallow open-cuts. However, this coal is characterised by its low ash yields and high moisture content. The high moisture content of this coal means that its thermal efficiency is quite low because much of the energy produced during combustion is needed to evaporate the water in the coal. Variation in the concentrations of the inorganic and mineral ash-forming components of coal may also result in reduced thermal efficiency and operational time of power station boilers. There is significant variation in the levels of these inorganics and minerals, even within individual coal seams. Thus, even though the amount of ash-forming material in Latrobe Valley coals is relatively low, variation in the chemical composition of this material can be detrimental to power generation.

The current aim of the research undertaken by the Cooperative Research Centre (CRC) for Clean Power from Lignite is to reduce the quantity of greenhouse gases produced during brown coal-fired power generation by improving efficiency, while maintaining the low cost of electricity produced in this manner [3]. This research includes the development of processes for the efficient dewatering of the coal, advanced processes for brown coal-fired power generation, and instruments that can be used to improve the operational effectiveness of the power stations and mines.

Determining the inorganic, mineral, and moisture content of Latrobe Valley brown coal, prior to its utilisation, allows the implementation of strategies to minimise moisture and ash-related problems. These strategies can include coal blending, dumping or avoiding the mining of poor quality coal. Several methods have been developed for the analysis of the inorganic, mineral, and moisture content of this coal. The techniques used most regularly

for these analyses are the standard, wet laboratory techniques, which include oven-drying and atomic absorption spectrometry (AAS). The samples analysed using these techniques can be subsections from the cores of drilled holes in the coal deposits, surface samples from an open-cut mine, from the coal dredger or the conveyor belt. Such analyses can be time and labour intensive because samples need to be transported to the laboratory and then the analyses themselves can take several hours or even days.

On-line instruments for the rapid chemical analysis of coal have been developed in order to overcome the problems associated with the standard analytical methods. Such instruments involve techniques such as neutron activation analysis, microwave transmission, and x-ray fluorescence [4-8]. However, there are drawbacks associated with applying any of these methods to the analysis of Latrobe Valley brown coal.

Laser-induced breakdown spectroscopy (LIBS) is an analytical technique that has been successfully used for on-line and *in situ* analyses of samples such as soils and paints [9-13]. Test analyses of the organic, inorganic, and mineral content of Alabama coal have also been undertaken in the laboratory using this technique [14]. These tests showed that LIBS was able to successfully identify molecular and elemental emission from many of the organic and inorganic elements found in the coal.

This thesis investigates the application of laser-induced breakdown spectroscopy to the chemical analysis of Latrobe Valley brown coal. Specifically, analyses of the inorganic, mineral, and moisture content of this coal are undertaken using this technique. This technique is then refined through the implementation of signal normalisation and data analysis methods.

### ***1.1.1 Composition of Victorian Brown Coal***

As mentioned earlier in the chapter, Latrobe Valley brown coal is characterised by its high moisture content and low levels of ash-forming elements. The typical composition of this coal is shown in Figure 1.1. Water is the main constituent of this coal, on average comprising between 60 % of the coal on a wet basis [2]. The remainder of the coal consists mainly of organic matter, with carbon comprising approximately 27 %,

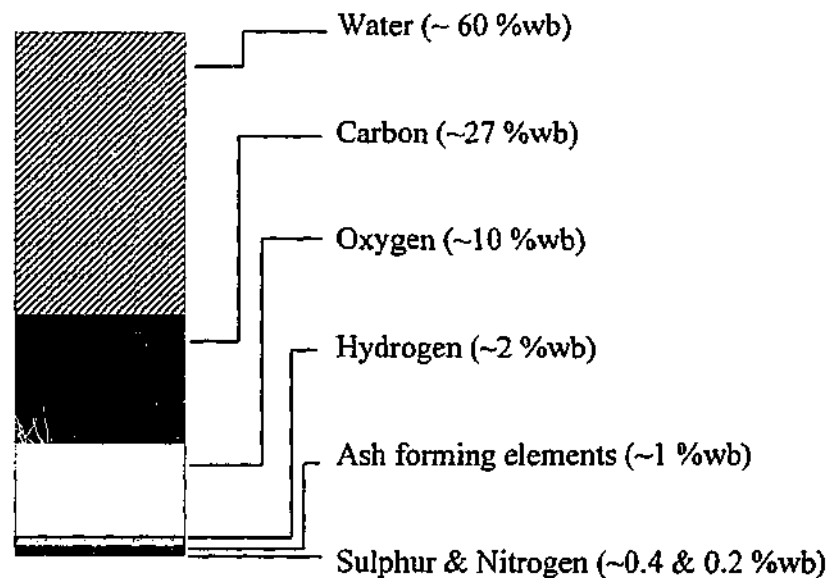


Figure 1.1. Typical composition of Latrobe Valley brown coal.

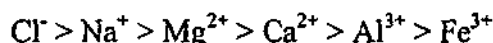
oxygen approximately 10 %, and organic hydrogen 2% of the coal, on a wet basis [2]. Small amounts of sulphur, nitrogen, inorganic and mineral ash forming elements are also present. Despite having low levels of ash-forming components, the composition of the ash forming content of the coal is such that it can impact greatly on coal utilisation.

The inorganic ash forming substances in Latrobe Valley brown coals are generally classified into two groups; discrete mineral species (minerals) and non-mineral elements (inorganics). Latrobe Valley brown coals are dissimilar to bituminous coals in that the ash produced by these coals is primarily formed from inorganics rather than minerals. These inorganics are present within the coal as soluble salts or exchangeable cations associated with the carboxyl groups that form part of the organic matter within the coal [2]. The inorganic content of the coal consists of sodium, magnesium, calcium, aluminium and iron. All of the magnesium and calcium, and much of the sodium are present as exchangeable cations in the coal. Sodium is also present as dissolved sodium chloride within the in-seam moisture. Some of the aluminium and iron in the coal are also present as inorganics. However, these elements exist as complex univalent carboxylate cations.

The main mineral constituents of Victorian low-rank coals are quartz ( $\text{SiO}_2$ ), kaolinite ( $\text{Al}_2\text{Si}_2\text{O}_5(\text{OH})_4$ ), and pyrite ( $\text{FeS}_2$ ). Muscovite ( $\text{KA}_2(\text{AlSi}_3)\text{O}_{10}(\text{OH})_2$ ) and rutile ( $\text{TiO}_2$ )

have also been found in these coals in small amounts. Overall, mineral levels in Latrobe Valley brown coal seams are very low. However, levels will vary, rising significantly near overburden and interseam sediment layers. Occasionally, pyrite and silica will also replace woody cells in the coal.

The inorganic content of Latrobe Valley brown coal has been found to vary with depth in the coal seams. The concentration of Mg, Na and Cl ions in the coal will generally decrease as depth increases. Conversely, the Al and Fe concentrations usually increase with depth. Maximum Ca concentrations are generally found somewhere in the middle of the seam. These different behaviours are a result of the different mobilities of the ions through the coal. As water is evaporated from the coal surface, more water flows up through the coal carrying ions with it. The rate of movement of the ions up through the coal will depend on their mobilities. Brockway and Borsaru [15] found the relative rates of the movement of the ions in bed-moist brown coal under the influence of water movement resulting from surface evaporation to be:



These relative rates were also found to be independent of the source of coal and lithotype. Variation in the texture of the coal and the presence of coalified wood in the coal seam can also affect the concentrations of the inorganic elements. In general, inorganic concentrations will be lower in wood samples than in the adjacent groundmass.

The high moisture content of Latrobe Valley brown coal is a feature of its young age. There are four types of water found in Latrobe Valley brown coal; bulk, capillary, multilayer, and monolayer [2]. Bulk water, which comprises most of the water found in the coal, is normal liquid water and is found in the macropores of the coal. Capillary water is contained in the small capillaries of the coal and has slightly abnormal thermodynamic properties. Multilayer water is the water that is weakly hydrogen bonded to the monolayer and is only present in Latrobe Valley brown coal in small amounts. Monolayer water, which makes the smallest contribution to the total water content, comprises the water hydrogen bonded to oxygen-containing functional groups on the coal surface. The great majority of the water found in Latrobe Valley coals is either bulk or capillary water.

The moisture content of Latrobe Valley brown coal varies between and within coalfields. In 1945, Edwards identified the major factors affecting the moisture content of these coals as being the depth of burial, lithotype, compression by folding, weathering, and thermal (or rank) effects [16]. More specifically, the moisture content of this coal has been found to decrease with depth, weathering, with increasing rank, and with increased compression by folding. Large variation in moisture content over small depth changes can be attributed to variation of the lithotype.

### *1.1.2 Effects of the Chemical Composition of the Coal*

The inorganic and mineral constituents of Latrobe Valley react during coal combustion to form ash particles. The chemistry of ash formation in this coal is generally dominated by the reactions of the inorganics, since they are usually present in larger quantities than the minerals. These elements undergo several chemical and physical changes during coal combustion, including thermal decomposition, melting, coalescence, fragmentation, vaporisation, condensation, and nucleation. These processes were summarised by Holden and coworkers and are shown in Figure 1.2 [17].

The processes illustrated in Figure 1.2 can lead to reactions of minerals and inorganic elements that produce a variety of complex mixed-phase ash species. These reactions can include:

- sulphation of Na, Ca, and Mg to form low melting point sulphate phases,
- reaction of volatile Na species, such as NaCl, Na<sub>2</sub>O, NaOH, and Na, with quartz and clays to form low melting point silicates and aluminosilicates,
- dissolution of quartz particles in molten Fe rich phases to form iron silicates,
- the formation of mixed silicate phases as a result of the dissolution of Ca, Mg, and Fe rich ash and quartz in molten Na-rich ash,
- dissolution of quartz particles into aluminosilicate melts, and
- the production of mixed aluminosilicate phases from the reaction of Ca, Mg, and Fe rich ash with clay minerals.

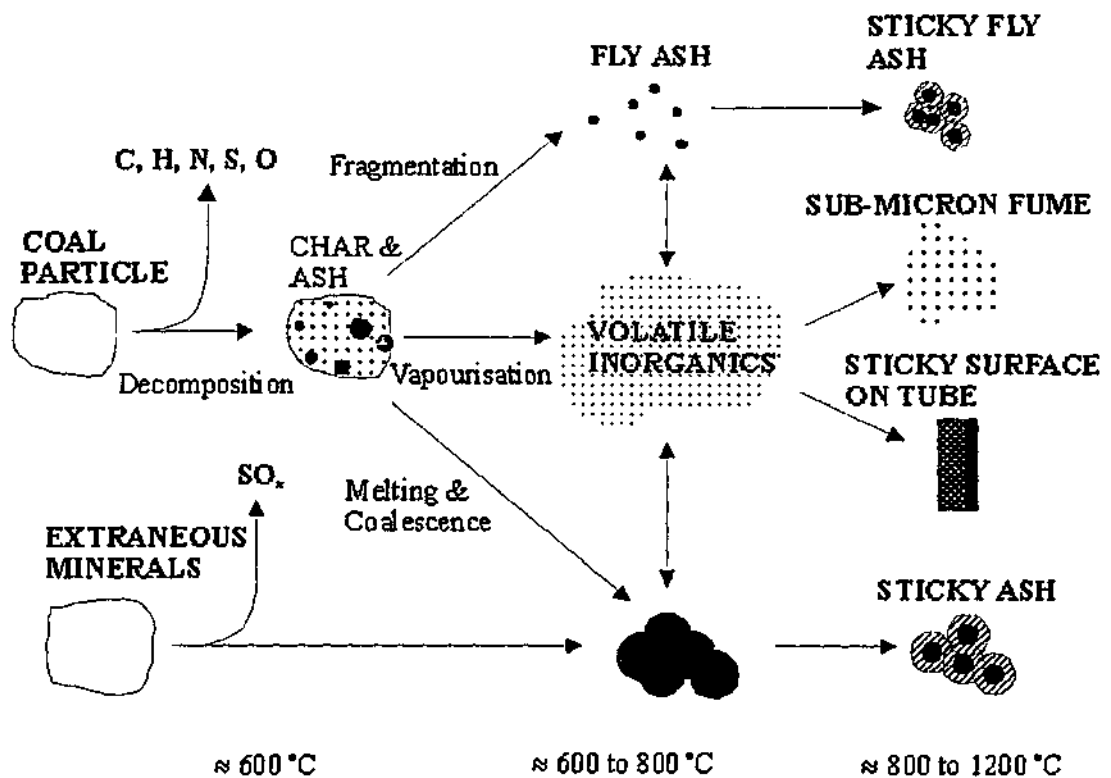


Figure 1.2. Possible Mechanisms Involved in Ash Formation [17].

The ash particles that form via several chemical reactions, including those listed above, reduce the thermal efficiency and increase the cost of brown coal-fired power generation by adhering to and corroding surfaces within the boiler. Couch [18] identified the adverse effects of ash deposition more specifically as being:

- a reduction of heat transfer as a result of solid or liquid deposits. This leads to an increase in gas temperature which, in turn, leads to an increase in the rate of ash deposition,
- the formation of sticky surfaces which can trap other ash particles,
- fouling of surfaces in the convective section of the boiler by condensation of volatile species,
- the formation of clinkers on heat transfer tubes, which can physically distort the tubes. These clinkers can also be a hazard when their removal is attempted,

- increased rates of corrosion and erosion, and
- large slag falls during operation.

The deposition of ash in coal fired boilers can be reduced by changing the operating conditions or coal feed. Soot-blowing, which involves directing jets of water onto furnace walls or steam onto other affected surfaces, is a common operational technique that is implemented to remove ash deposits.

The fouling behaviour of Latrobe Valley brown coal can be predicted using a number of empirical indices, if the inorganic, mineral and ash content of the coal is known. These indices include the Fouling Index and the Predicted Ash Collection Efficiency (PACE) Index, which estimate the weight of ash deposits on heat transfer tube banks when using Latrobe Valley brown coal [2]. Both of these indices were developed from 8 hour studies of ash deposition. In 1987, Anderson and coworkers undertook 1000 hour studies of ash deposition [19]. They found that high fouling coals could be identified by two properties of the coal, the amount of  $\text{Na}_2\text{O}$  in the ash and the ratio of  $\text{Na}_2\text{O}$  in the ash to the soluble Al in the ash. A model based on these two properties was developed to predict boiler performance. The predictions of this model were found to correlate well with the boiler performance observed from 500 MW Loy Yang power station boilers. Thus, if the inorganic, mineral and ash content of the coal is known prior to its utilisation, this model can be used to predict the performance of power station boilers. Such predictions enable the implementation of strategies to minimise fouling, when required.

The moisture content of coal has a significant impact on the thermal efficiency of coal-fired power station boilers. High moisture Latrobe Valley brown coal results in low thermal efficiencies because a large proportion of the energy produced is required to evaporate the coal moisture. Thermal efficiency is also decreased as a result of the comparatively high final temperature of the flue gas leaving the boiler and the loss of sensible heat with the evaporated water [17]. For these high moisture coals, small variations in moisture content can greatly affect the amount of coal required to produce the required energy. Hence, it is preferable not to utilise coals with very high moisture contents. In the case of Latrobe Valley brown coal, it is preferable to utilise coals with less than 65 % moisture. Analysis prior to coal utilisation allows this requirement to be met.

## 1.2 Contents of Thesis

This work forms part of the efforts by the CRC for Clean Power from Lignite to improve the operational effectiveness of the brown coal fired power stations and mines in the Latrobe Valley. This project aims to meet this objective by developing methods for applying LIBS to the analyses of the inorganic, mineral, and moisture content of Latrobe Valley brown coal in the laboratory. The findings of this work will then be able to be used in the development of instruments for the on-line and *in situ* analyses of the coal.

A review of the literature detailing the results of prior research that is relevant to this work is provided in Chapter 2 of this thesis. In particular, other methods that have been developed for the analysis of this coal as well as more general studies involving the application of LIBS in analytical chemistry have been reviewed. The review of the methods used for the analysis of Latrobe Valley brown coals includes both the Australian Standard wet laboratory methods as well as on-line methods that have been developed more recently. The review of the application of LIBS to the analysis of solid samples covers both the instrumentation used and the effects of several experimental parameters. In particular, the effects of sample water content are reviewed. The effects of implementing a number of signal normalisation and data analysis methods are also reviewed.

The experimental apparatus used for LIBS analyses of Latrobe Valley brown coal and the methods used to optimise the experimental parameters are described in Chapter 3 of this thesis. This optimisation includes determining the laser irradiance best suited to this application of LIBS. The effects of time-gating the optical detection on the observed LIBS signals are also investigated. The electron density and temperature of the laser-induced plasma are calculated at three of these time-delays.

Chapter 4 details the application of LIBS to the analysis of the inorganic and mineral content of Latrobe Valley brown coal. The results presented in this chapter include those from a series of experiments undertaken to determine the reproducibility of an analysis of the six main inorganic elements in the coal. The calibration curves produced from the analysis of thirty Latrobe Valley brown coal samples are also presented. Following this,

the detection limits of the inorganics in the coal obtained using LIBS are calculated from the calibration curves. Finally, the experiments performed in order to compare LIBS analyses of the six main inorganics in the coal with the standard analysis methods are described.

The results of the application of three signal normalisation methods to LIBS data are provided in Chapter 5. These normalisation procedures, two of which incorporate a measurement of the laser-produced acoustic signal, were first validated experimentally. The relationships between the acoustic signal and the laser irradiance, elemental emission intensity, and laser-induced mass loss are investigated for the purposes of this validation. The variation of the acoustic signal with sample matrix is also examined. A wide range of coals and powdered minerals were analysed using LIBS for this purpose. The main aim of the work in this chapter is to identify an appropriate normalisation process for laser-induced emission signals that is independent of sample type.

The effects of the moisture content of Latrobe Valley brown coal on its analysis by LIBS are presented in Chapter 6. A set of experiments was first carried out to determine the effects of coal moisture on the intensity of inorganic elemental emission lines from the laser-induced plasma. The results of these experiments are presented and discussed in this chapter. The effects of coal moisture on the intensity of emission from carbon and hydrogen were also investigated and are discussed in Chapter 6. The aim of this investigation was to develop a method for measuring the moisture content of Latrobe Valley brown coal from laser-induced emission spectra.

Principal component regression (PCR) is applied to LIBS analyses of Latrobe Valley brown coal in Chapter 7 of this thesis. PCR models were developed from laser-induced emission spectra of 50 coal samples for ten constituents of the coal; Na, Mg, Ca, Fe, Al, Si, Cl, S, moisture content, and total ash yield. Seven of these constituents could be measured directly from the laser-induced emission spectra in Chapters 4 and 6. Therefore, the purpose of producing PCR models for these constituents was to improve the precision and accuracy of their analyses. The chlorine, sulphur, and total ash yield of the coal were unable to be directly measured from the laser-induced emission spectra. Thus, the aim of producing PCR models for these components of the coal was to provide a means for their analyses.

General conclusions pertaining to the entire thesis are presented in Chapter 8. Directions for future research are also offered in this chapter.

## *Theory and Literature Review*

### *2.1 Introduction*

In this work it was important to consider the results of prior research into methods for analysing Latrobe Valley brown coals as well as studies involving the application of LIBS in analytical chemistry. A review of the literature in these two fields of study is presented in this chapter.

A review of the existing methods used to analyse the chemical composition of Latrobe Valley brown coals is first presented. This review includes both traditional laboratory-based and on-line analytical techniques. Following this, a review of the use of LIBS in analytical chemistry is presented. This review includes the instrumentation used in LIBS as well as the effects of various experimental parameters. The effects of a variety of signal normalisation and statistical methods on the analytical ability of LIBS are also detailed here.

### *2.2 Methods Used to Chemically Analyse Latrobe Valley Brown Coal*

Several analytical methods have been used to analyse the chemical composition of Latrobe Valley brown coal. These include standard wet laboratory methods for measuring the inorganic and mineral content of the coal and determining the moisture content [2]. On-line and portable instruments have also been used to measure these constituents of the coal [4].

#### *2.2.1 Standard Wet Laboratory Analysis*

Most analyses of Latrobe Valley brown coal take place in the laboratory. Generally, proximate and ultimate analyses, and analyses of the ash-forming elements in the coal provide the main measures of the chemical composition of these samples. Proximate analyses include measurements of the moisture, ash, and volatile matter in the samples. Ultimate analyses involve measurement of the C, H, N, S, and O in the coal. The samples

for such analyses can be subsections from drill cores taken from coal deposits, surface samples from an open cut, from the coal dredger or the conveyor belt. Upon collection, these samples are placed in sealed, tubular plastic bags to minimise moisture loss and prevent contamination prior to analysis. Samples can be stored in this manner for several months without any net moisture loss [2]. For all the standard wet laboratory analyses, samples are crushed prior to analysis. The type of analysis being undertaken generally dictates the particle sizes required.

The main ash-forming constituents in Latrobe Valley brown coal are non-mineral inorganic elements, commonly referred to by the generic term inorganics in the coal industry. These elements are sodium, calcium, magnesium, iron, and aluminium. The inorganics can be extracted from the coal using dilute hydrochloric acid. The Australian Standard for the chemical analysis of these inorganics in lower rank coal, such as that found in the Latrobe Valley, requires that hot hydrochloric acid be used to extract these elements from the oven-dried coal sample, after it has been wet with alcohol [20]. This extract is then filtered to remove any residual coal particles and an ionisation suppressant added. Elemental concentrations in this filtrate are subsequently determined using atomic absorption spectrometry (AAS). Inductively coupled plasma spectroscopy (ICP) is sometimes used instead of AAS.

In general, the mineral content of Latrobe Valley and other brown coals is low compared to bituminous coals. The main minerals in this coal are quartz ( $\text{SiO}_2$ ), kaolinite ( $\text{Al}_2\text{Si}_2\text{O}_5(\text{OH})_4$ ), muscovite ( $\text{KAl}_2(\text{AlSi}_3)\text{O}_{10}(\text{OH})_2$ ), and pyrite ( $\text{FeS}_2$ ). The mineral matter in this brown coal is measured by analysing the fused coal ash. This method provides measurements of  $\text{SiO}_2$ , total Al and Fe,  $\text{TiO}_2$ , and  $\text{K}_2\text{O}$  in the coal. The Na, Mg, and Ca in the coal can also be measured using this method. However, more accurate analyses for these elements are generally obtained when using the acid extraction technique described above.

In order to decompose the coal ash, samples are placed in a platinum or gold crucible and fused with lithium tetraborate or lithium metaborate by heating to  $1000^\circ\text{C}$ . This fused sample is then dissolved in dilute nitric acid. An ionisation suppressant is added to the sample, which can then be analysed using AAS, in accordance with Australian Standard 1038.14.1 [21].

There are three different standard methods that may be used to measure the moisture content of Latrobe Valley brown coals. The results from these methods do not always agree. Hence, the method used for moisture determination needs to be noted along with the results. The first of these methods, the two-stage method, is used for analyses of coal moisture content in large (> 500 g) samples and is performed in duplicate. The coal sample is first passed through an 11.2 mm sieve. It is then spread evenly on a sample tray and weighed. Samples are placed in a drying cabinet at  $38 \pm 2^\circ\text{C}$  for 5 hours. At this stage, samples are removed from the drying cabinet and allowed to stand at ambient temperature for a minimum of 2 days and until a constant mass is obtained. This sample is then crushed to produce particle sizes less than 4 mm. A 10 g portion of the crushed sample is placed in a weighing vessel, weighed, and then put into a minimum-free-space oven at 100 to  $105^\circ\text{C}$  for 3 hours, with nitrogen flowing at 1 l/min. After 3 hours, the samples are removed and placed in a desiccator until cool. The sample is then weighed and the moisture content calculated.

The second method used for moisture determination, the single-stage method, is used for samples of approximately 10 g. In this method, the coal sample should be crushed to produce particle sizes less than 4 mm in diameter. The sample is placed in a weighing vessel and weighed to the nearest milligram. It is then placed in a drying oven for 3 hours at 100 to  $105^\circ\text{C}$ , with nitrogen flowing through at 1 l/min. At this time, the sample is removed from the oven and placed in a desiccator until cooled to room temperature. It is then weighed and the moisture content calculated.

The third standard method of coal moisture determination involves azeotropic distillation. In this method, which is used for coal samples between 200 and 500 g, the sample is crushed to produce particles which are less than 11.2 mm in diameter. This sample is placed in a flask and toluene added. The flask is then connected to the distillation apparatus and heated. This continues for 20 minutes after the supernatant layer of toluene has become clear, to ensure that all water is removed from the sample and system. The water is then placed in a conical flask, weighed and the moisture content calculated. The three methods for moisture determination listed here are described in Australian Standard 2434.1 [22].

The S and Cl levels in Latrobe Valley coals are measured using the methods described in Australian Standard 2434.6.1 [23]. Total sulphur content can be measured using either of two methods – the Eschka method or the high temperature combustion method. In the Eschka method, a known mass of the coal sample is mixed intimately with Eschka mixture, which is a mixture containing calcined magnesium oxide and anhydrous sodium carbonate in a 2:1 ratio by mass, in an oxidising atmosphere at 800°C. This removes the organic material from the sample and converts sulphur to sulphate. Dilute hydrochloric acid is then used to dissolve the sulphate formed. The amount of sulphate is subsequently determined by gravimetric analysis of the precipitate formed on reaction with barium chloride. In the high temperature combustion method, a known mass of the coal sample is burnt in oxygen in a furnace at 1350°C. This causes sulphur to form oxide compounds and Cl to form HCl. These substances are then absorbed in neutral hydrogen peroxide. The S and Cl content of the sample can be determined by titrating the washings from the absorption vessel. In this way, sulphur and chlorine are measured from a single sample.

The total ash yield of Latrobe Valley coal samples is determined using the procedure detailed in Australian Standard 1038.3 [24]. This process involves combustion of a sample that has been dried in a Brabender moisture determinator or air oven. A small amount of the dried sample (ca. 3 to 5 g) is transferred to a silica dish and placed in a muffle furnace, which is then heated over 2 hours to 815°C. The sample stays in the furnace at 815°C for another hour. The sample is then removed from the furnace, cooled to room temperature and weighed. The percentage ash in the original coal can then be determined from the weight of the remaining sample. This process, which requires that the moisture be removed from the sample, allows the moisture content of the sample as well as the ash yield to be measured when using modern instruments such as the LECO MAC 400 [2].

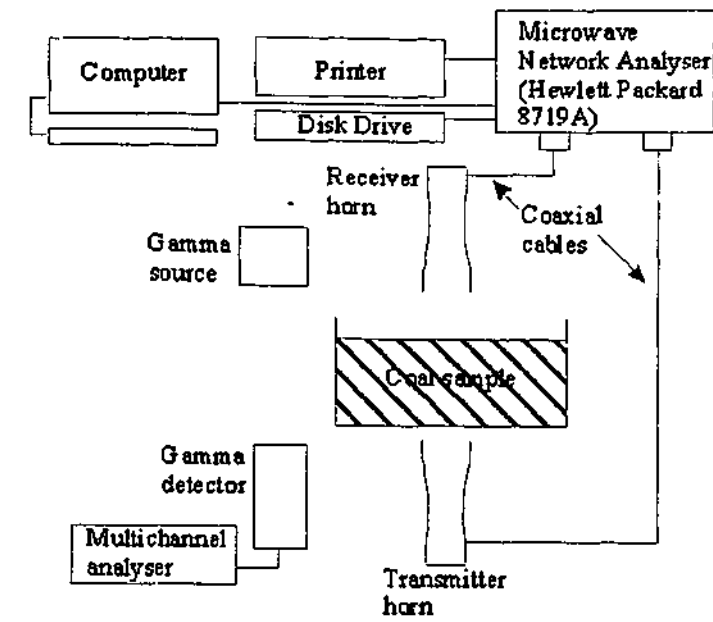
The standard methods for determining the amount of volatile matter, C, H, N, and O in Latrobe Valley brown coals are not described here because these properties were not investigated in this study. However, descriptions of these procedures can be found in Australian Standards 2434.2 and 2434.6.1 [23, 25].

### 2.2.2 On-Line Methods for Coal Analyses

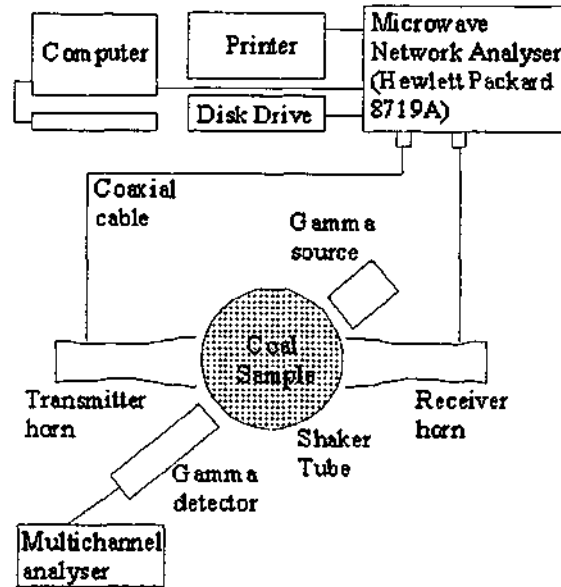
More recently, on-line methods have been applied to the analysis of coal [8]. The instruments most commonly used for on-line analyses of coal in Australia are CSIRO's COALSCAN units. While these units, which utilise neutron activation analysis, were initially developed for the analysis of Australian black coal, they have also been adapted for the analysis of Latrobe Valley brown coal. The application of neutron activation analysis to the characterisation of Latrobe Valley brown coal was first tested in the laboratory in the early 1980s [26]. This early work demonstrated the feasibility of using this technique for brown coal analyses. Cutmore and coworkers presented the results of their study of the ability of the techniques used in COALSCAN instruments to analyse Latrobe Valley brown coal in 1993 [4]. Two gauges were tested in the course of this study, one of which was a prompt gamma neutron activation analysis (PGNAA) gauge, which was used for the determination of coal moisture, ash, gross wet specific energy (GWSE), and sodium/ash ratio. Cutmore and coworkers also tested a microwave gauge for measurement of the moisture in coal in this study. These gauges were tested using two different sampling geometries; a shaker tube and an on-belt geometry.

The PGNAA gauge tested in the work by Cutmore and coworkers incorporated a high-energy neutron source and a high efficiency bismuth germanate (BGO) detector. The high-energy neutron source allowed for more precise measurements of C in the coal than when using the  $^{252}\text{Cf}$  sources that are generally employed in the analogous black coal instruments. The BGO detector provided improved spectral quality and lower background compared to the NaI(Tl) detectors used for black coal analyses. Measurements of the moisture, ash, GWSE, and Na content were determined to within 0.9 wt%, 0.2 wt%, 0.3 MJ/kg, and 0.02 wt% respectively, using the shaker-tube geometry. Measurements of the moisture content were determined to within 0.7 wt% when using the on-belt geometry. There were no differences in the ability of the gauge to monitor the other properties of the coal when using the two sampling geometries.

The microwave transmission gauge tested in the study by Cutmore and coworkers was designed specifically for Latrobe Valley brown coal. Analyses of the moisture in this coal required much lower relative errors than for analyses of the moisture content of black coals, as a result of its high moisture content. Schematic diagrams of the two sampling



(a)



(b)

Figure 2.1. Schematic diagrams of prototype microwave transmission gauges used by Cutmore and coworkers for measurement of moisture in Latrobe Valley brown coal (a) on a conveyor belt and (b) in a shaker tube [4].

geometries of the microwave gauge are shown in Figure 2.1. The moisture levels in samples were determined using the microwave phase shift, attenuation, and the sample mass per unit area. The shaker-tube geometry was found to be preferable for these analyses, determining moisture content to within 0.4 wt%, compared to the 0.6 wt% obtained using the on-belt geometry. This improvement in accuracy was due to the superior control of the microwave transmission path and constancy of the coal depth and profile provided in the shaker-tube geometry.

However, there are several drawbacks associated with using PGNAA and microwave techniques for the analysis of Latrobe Valley brown coal. While PGNAA measurements are completed relatively quickly (analysis time typically takes several minutes), this method does not provide real-time analysis. The configuration of the instrument means that it does not have the potential to be used for *in situ* analysis at the coalmine. Another drawback of the PGNAA gauge is that it cannot be used to measure Na content directly because the gamma rays from Na are very weak. Thus, Na is determined indirectly from a measurement of Cl in the coal. However, when iron is used in the construction of the gauge, Fe peaks interfere with Cl peaks. Therefore Cl, and hence Na, is determined from a combined oxygen and chlorine peak that does not experience interference from Fe peaks, which is less than ideal. While microwave instruments provide good quality moisture analyses, they are not used to analyse the other chemical constituents of the coal. Ideally, a single instrument would be used to provide complete chemical analyses of the coal samples.

X-ray fluorescence (XRF) instruments have also been used to analyse many of the inorganic, mineral and trace elements in coal. They have been used in the laboratory to analyse coal, including Latrobe Valley brown coal, for many years [2,27,28]. More recently, XRF instruments have been used for on-line and *in situ* analyses [29]. In 1996, Arikan and coworkers applied XRF to the analyses of ash and sulphur in coal, with the aim of developing an on-line instrument [7,29,30]. They obtained good correlation between XRF intensities and total ash and sulphur measurements obtained by standard methods for the Turkish coals analysed. The root mean square deviation between the results was found to be 1.5 % for the ash measurements.

Process Control Inc. (PCI) has recently developed a commercially available combined XRF and microwave instrument, which has been used for on-line analyses of both brown and black coals [7,30]. This instrument uses the fine grained particle cloud, which surrounds the bulk material as it is moved, for analysis. The PCI instrument has been able to measure the total ash contents of these samples as well as individual elemental concentrations. Up to eight individual elements can be analysed simultaneously. However, only the heavier elements between Al and U can be analysed by this system. This means that some of the key inorganic and organic elements found in Latrobe Valley brown coal cannot be measured directly using this system. The system also requires a microwave gauge as well as XRF instrumentation in order to measure coal moisture content.

XRF instruments lend themselves to on-line and *in situ* analyses because analysis time is short (typically several seconds), the simple spectra mean that the chances of spectral interference are low, analysis is non-destructive, good precision and accuracy are obtained, and instruments can be portable. However, there are also disadvantages associated with the use of XRF instruments for coal analyses. The major disadvantage of XRF instruments is that they have difficulty detecting elements with low atomic numbers. These difficulties become more serious as the atomic number falls below 23 because Auger emission reduces the fluorescence intensity. Thus, the detection limits of these light elements using XRF will be poor.

### **2.3 Laser-Induced Breakdown Spectroscopy**

#### **2.3.1 Overview**

Laser-induced breakdown spectroscopy (LIBS), which is also known as laser-induced plasma spectroscopy, involves the focussing of a high-power laser beam onto a sample. At sufficiently high irradiances, the interaction of the laser with the sample produces a plasma containing electronically excited and ionised elements. These elements emit radiation at characteristic wavelengths that can subsequently be used for identification purposes, once the plasma emission is resolved into its component wavelengths.

The laser-induced plasma will be formed if the laser irradiance is higher than the threshold for the sample being analysed. The threshold irradiance is dependent upon the bulk properties of the sample but typically ranges between  $10^6$  and  $10^9$   $\text{Wcm}^{-2}$  for most samples irradiated by a Q-switched laser [31].

Laser-induced sample breakdown was first observed by Brech and Cross [32] in the early 1960s. Subsequently this phenomenon has been utilised for the qualitative and quantitative analysis of many elements in solid, liquid, gas and aerosol samples. Many of these studies have been summarised in a series of review articles [9-13]. LIBS has also been used to analyse coal particles in combustion environments [33-36]. In these studies, LIBS was used to measure the inorganic and mineral elements in the coal particles. Coal samples from the Warrior coalfields in Alabama were analysed using LIBS in the 1989 study by Venkateswarlu and coworkers [14]. This preliminary study showed that molecular and elemental emission from the organic, mineral and inorganic material in the coal could be detected as a result of laser-sample interaction.

The main advantages associated with LIBS stem from its time and cost efficacy and the ease with which analyses may be completed. Analyses incorporating the results from several laser pulses typically take less than a minute to complete. The recent advances in laser and detector technology have resulted in LIBS becoming a potential alternative to other analytical techniques, such as COALSCAN. In particular, the advent of portable, high-power Nd:YAG lasers has led to the construction of portable LIBS instruments [37-41]. LIBS is also a reasonably sensitive technique, capable of detecting ppm levels for some elements [9-13]. Many of the advantages of using LIBS for elemental analysis are due to the minimal sample preparation required. This means that the technique is relatively simple and rapid as both vaporisation and excitation of the sample occur in a single step. Another advantage of LIBS is that very small amounts of sample are required (typically in the  $\mu\text{g}$  to  $\text{ng}$  range). Most current LIBS instruments incorporate a gated, intensified charge coupled device (CCD) detector, which allows for multi-component analysis. Background interferences may also be minimised, when using a CCD, because there is often a choice of several spectral lines for each element. LIBS instrumentation may also be located at some distance from the sample site by using optical fibres to carry laser light to the sample and sample emission back to the detector.

Conversely, there are also disadvantages associated with using the LIBS technique. The small sample size means that the accuracy of the technique is dependent on the homogeneity of the sample and that surface contaminants will decrease reproducibility. LIBS analyses are also subject to matrix effects. Thus, signal calibration must be performed for each sample type analysed or some kind of signal normalisation implemented. As discussed later, several techniques have been implemented to correct for sample heterogeneity and matrix effects [1,42-50].

The detection limits obtained using LIBS are generally higher than those of standard analytical methods, such as ICP-AES and AAS. However, the advantages provided by LIBS often outweigh this disadvantage. In particular, the mining industry has been identified as an area where the speed and portability of LIBS systems would be more of an advantage than the sensitivity of other techniques for on-line or *in situ* analyses.

### 2.3.2 Instrumentation

The basic instrumental configuration for many LIBS experiments is shown in Figure 2.2.

#### 2.3.2.1 Choice of Laser

The influence of laser parameters on the ablation of sample material has been well documented [51-57]. In particular, the wavelength, irradiance, pulse mode, and beam diameter of the output of a laser will determine the amount of material ablated and the shape of the craters produced in a solid sample.

There are several types of lasers available for use in LIBS; solid state lasers such as Nd:YAG, Nd:glass and ruby lasers, gas lasers such as CO<sub>2</sub> and N<sub>2</sub> lasers, and excimer lasers such as ArF, XeCl, and KrF lasers. The choice of laser for a particular study will depend on the nature of the experiment and the parameters of the sample to be characterised.

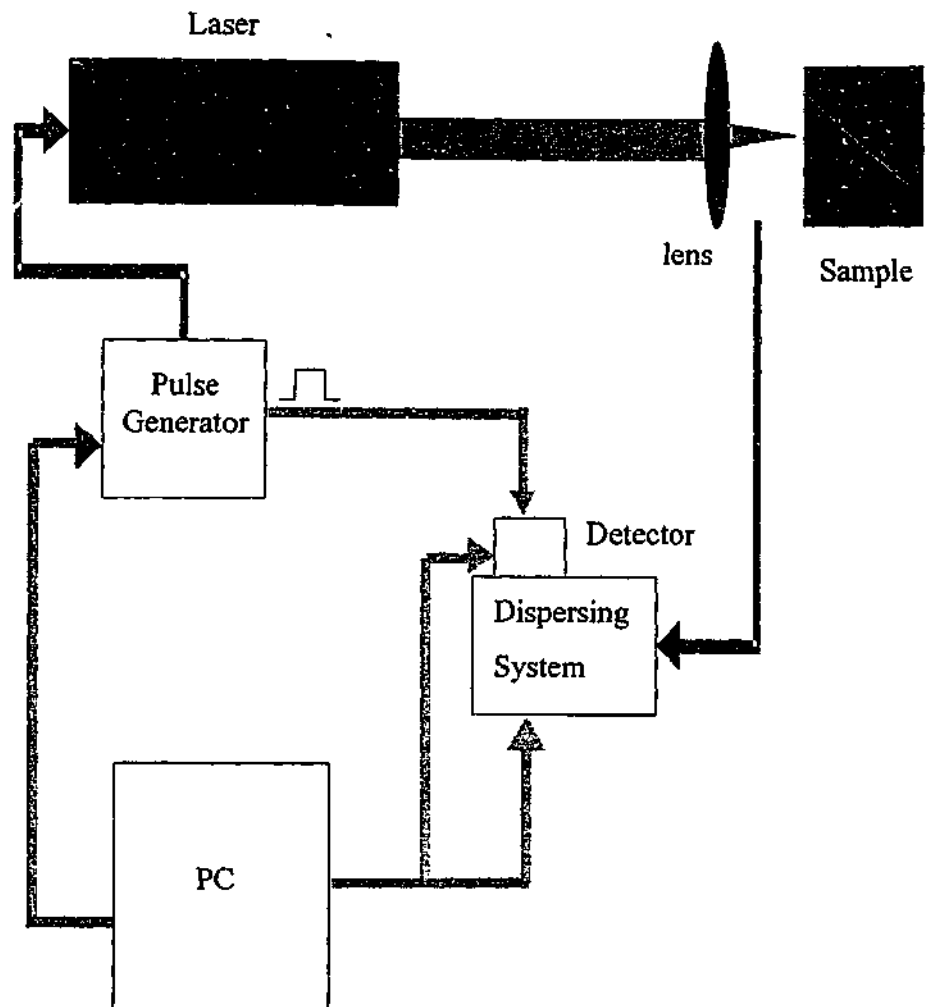


Figure 2.2. Instrumental setup for LIBS experiments.

The wavelength of the light produced by a laser is one of the major considerations when choosing the type of laser to be used for a particular application. The laser wavelength will affect the amount of material removed from a sample during the ablation process. It has also been shown that the laser wavelength affects the properties of the plasma produced by ablation [44,58-59]. Specifically, lasers with a shorter wavelength will remove more material from a sample and cause a greater degree of ionisation than their longer wavelength counterparts. This means that utilising an ultraviolet laser to analyse heterogeneous samples can often generate more reproducible results than when using a longer wavelength laser. However, the unwanted spectral interferences associated with UV laser light during emission spectroscopy can negate any advantages associated with using such a laser. The production of UV laser light also requires the addition of harmonic generating optics to Nd:YAG lasers or the presence of bulky gas cylinders in the case of gas and excimer lasers, both of which add to the cost of the measurement.

The pulse mode of solid state lasers is another factor that must be considered when designing an experiment. A laser pulse may be either Q-switched or free-running. Q-switching, which occurs when the Q (quality) of the laser resonant cavity is changed from low to high, results in very high peak powers. Q-switched pulses are shorter, typically of a few nanoseconds duration, and the average output power is less than a free-running pulse. However, the power density of a Q-switched pulse is greater than that of a free-running pulse because its duration can be up to  $10^6$  times less [60]. More recently the effects of pulse duration have also been investigated [59, 61-64]. Semerok and coworkers found that the optimum laser ablation efficiency for several metal samples was obtained using femtosecond laser pulses [62]. They proposed that this was a result of a lack of plasma shielding when using femtosecond pulses that, in turn, was a result of the short duration of these pulses. Margetic *et al.* also found that elemental concentrations were obtained most precisely by LIBS when femtosecond pulses were used [64].

The laser beam diameter, and hence the size of the affected spot on the sample, has been studied and shown to impact on the ablation event [60]. The size of the spot on the sample is determined by the laser beam profile, the focal length of the focussing lens and the lens-to-sample distance.

A Q-switched Nd:YAG laser, operating at either its fundamental wavelength (1064 nm) or the second harmonic (532 nm), is used in many LIBS experiments. Pulse energies up to 300 mJ may be used and, in general, pulse widths range between 4 ns and 20 ns [9-13]. The Nd:YAG laser is well suited to this application because of its high power, good beam quality and relatively low cost. When using the fundamental wavelength of the Nd:YAG laser, scattered light in the UV and visible regions of the spectrum can be avoided. As mentioned earlier, the advent of compact Nd:YAG lasers has led to their incorporation in portable LIBS instruments [37-39]. Some of these compact, low-cost Nd:YAG lasers are able to be operated from 12 V batteries. The pulse energies produced by these lasers are typically lower than those produced by lasers used in laboratory-based LIBS systems. However, the size of these lasers and their ability to be battery powered often outweigh this disadvantage.

### 2.3.2.2 Choice of Detection System

There are several types of photon detectors that have been used in emission spectroscopy, including photomultiplier tubes (PMT), photodiode arrays (PDA), charge-coupled devices (CCD) and charge-injection devices (CID) [9-13,51,53]. The choice of a detector for a spectroscopic application will depend on what spectral region is to be analysed and the sensitivity required.

As with most optical systems, a device that provides high signal-to-noise ratios and high gain is desirable for detection. PMTs are useful when measuring weak emission because they are extremely sensitive in the near-UV and visible regions of the spectrum. PMTs can also provide down to sub-nanosecond resolution of the laser plasma, when coupled with high-speed digitisers [65]. PMTs have been used to both scan a spectrum, when used with a monochromator, and to monitor emission from a small region of the spectrum, when used with a narrow bandpass filter. However, PMTs are limited to measuring low intensity radiation because the photocathode can be damaged by intense light. Individual PMTs are also unable to be used for simultaneous multielement detection.

PDAs, CCDs and CIDs are solid state multichannel detectors that eliminate the need to scan a spectrum. PDAs, CCDs and CIDs are coupled to spectrographs when monitoring emission spectra. The choice of a spectrograph and, in particular its focal length, will

depend on the required resolution, since the resolution of a spectrograph is inversely proportional to its focal length. Czerny-Turner grating spectrographs are generally used for light dispersion in LIBS. However, échelle spectrographs, which provide better resolution and greater spectral coverage than Czerny-Turner instruments, have also been used in LIBS experiments [45,66]. Échelle spectrographs are not widely used in LIBS because they require large two-dimensional detectors with large numbers of pixels. This also limits the speed of analyses.

PDA's are popular choices of detectors in LIBS experiments. As mentioned earlier, PDA's enable simultaneous multielement analyses. However, PDA's do not possess the sensitivity, dynamic range and noise performance associated with a PMT. The PDA is best suited to applications in which light levels are high.

The pixels in a CCD array have several conductive electrodes that overlay an insulating layer to form a metal oxide semiconductor capacitor. Underneath the insulating layer is a doped silicon region, which is used for charge storage. The amount of photogenerated charge is measured by shifting the charge from each element to an on-chip amplifier situated at the end of the array. This charge movement occurs by shifting the charge from one element to the next, until it has all been transferred to the amplifier. The greatest advantage associated with this technique is that readout noise is very low and, hence, the signal-to-noise ratio of the output is high. Thus, the sensitivity of a CCD is better than that of a PDA and, consequently, provides a means of facilitating rapid, sensitive multichannel analyses. CIDs are similar to CCDs and possess many of the same advantages. However, in general, CCDs produce higher signal-to-noise ratios than CIDs [67]. Hence, CCDs are used in preference to CIDs in LIBS experiments.

The coupling of an image intensifier to a CCD detector allows much lower light levels to be recorded, without increasing acquisition time, compared to a conventional unintensified detector. Typically, the latest commercially available intensified CCDs are operated with a system gain between 0.5 and 10 ADC counts/photoelectron [68]. The intensifier device also allows fine (ns) shuttering of the detector, which is useful when studying transient phenomena, such as the formation of a laser-induced plasma. In this instance, the intensifier can further improve signal-to-noise by selecting the appropriate time-gated window.

### 2.3.2.3 Field Instruments

The development of field instruments has been the focus of many recent studies involving laser-induced breakdown spectroscopy [37-41]. The on-line and *in situ* chemical analyses for which these instruments are used benefit most from the advantages of LIBS. There are two main types of LIBS field instruments; compact, low-cost instruments and truck-mounted systems.

The two main differences between laboratory-based and portable LIBS instruments are the size of the instrumental components and the method of delivery of the laser light to the sample. As mentioned earlier, the compact, low-cost portable LIBS systems incorporate compact Nd:YAG lasers, some of which are battery operated. The type of detector used in these compact systems also differs from those generally used in a laboratory instrument. Unintensified and non-gated CCD detectors are used in the smaller, portable instruments because they are more compact and less expensive than the intensified, gated variety. A study comparing the analytical capability of laboratory-based versus small portable LIBS instruments found that they yielded identical results and detection limits for the analysis of lead in paint [37]. It was found that non-gated detection was adequate for this application of LIBS because background interferences are much less substantial in the ultraviolet region, where lead analysis takes place, than in the visible and near-infrared regions of the electromagnetic spectrum [37]. The magnitude of the continuum emission produced was also significantly lower than that produced when laser-sample interaction occurs in air because the sample probe was placed directly onto the sample surface, which minimised the amount of air present at the sample surface. As a result time-gating was not required to obtain adequate peak resolution. However, this study also found that most of the detection limits obtained for elemental analyses of soils were five to six times greater for the briefcase than the laboratory-based LIBS instrument [37]. This result was attributed mainly to the lower pulse energies provided by the portable laser compared to the laboratory laser and partially to the use of non-gated detection.

Compact spectrometers incorporating unintensified CCDs and multiple fixed wavelength spectrographs were used in portable LIBS systems developed by Body and Chadwick to analyse gypsum, black coal, and Latrobe Valley brown coal samples [38,39]. They found that, when appropriate data analysis techniques were implemented, the sensitivity of these

spectrometers was sufficient to enable qualitative and quantitative analyses of the major elements in each of these sample types. One of the main advantages of this system was that several of the small Ocean Optics spectrometers were able to be used simultaneously to cover a wide spectral region (220 to 830 nm).

A portable LIBS instrument was developed by Yamamoto and coworkers [37] for the detection of metal contaminants on surfaces. This system incorporated a sample probe for both the delivery and collection of light to and from the sample surfaces. This probe contained the laser, focussing lens, fibre-optic cable, and safety switches to prevent operation when the probe was not lying against a flat surface. The purpose of the probe was to ensure consistent focussing of the laser beam on the sample by providing a constant lens-to-sample distance. This sampling probe was quite small; its dimensions were 23 x 6.5 x 4.5 cm [37]. An aperture in the plastic plate at the bottom of the probe allowed transmission of the focussed laser beam to the sample, while the probe housing adjacent to the surface contained openings so that the laser light could be observed. A bifurcated fibre-optic cable was used to collect emitted light and laser light reflected from the sample surface and to transmit the data back to the detection system. A replaceable quartz window covered the end of this cable in order to protect it from sample particles.

The components of truck-mounted LIBS instruments are not constrained by the size of their housing and, thus, are very similar to the components of laboratory-based instruments. However, the method of laser-light delivery to and emission collection from the sample differs from most laboratory instruments. In the truck-mounted system developed by the US Navy for detection of contaminants in soil, the light from a Nd:YAG laser, which was housed in the truck, was delivered to a probe via fused silica fibre [69,70]. The light delivered by the fibre was collimated and steered by a prism to be focussed, by a lens, through a sapphire window in this probe. The probe was hydraulically pressed into the ground by the cone penetrometer truck and, thus, soil was pressed against the sapphire window. This means that lens-to-sample distance remained fixed for all experiments. The single fibre used for laser light delivery was also used for emission collection. This type of positioning avoided alignment difficulties associated with multi-fibre design.

### 2.3.3 Fundamental Studies of LIBS

As mentioned earlier, LIBS has been used to analyse solid, liquid, gas and aerosol samples [9-13]. This review will focus on the development of LIBS for the analyses of solid samples, with an emphasis on the more recent work. Fundamental studies of the processes involved in laser-induced breakdown comprise a significant area of research in the field of solids analysis by LIBS. These studies will be reviewed in this section.

#### 2.3.3.1 Spatial and Temporal Resolution of the Laser-Induced Plasma

Fundamental studies of the plasma induced by laser interaction with solid samples have been undertaken to understand the processes occurring during breakdown and improve analytical results. Many of these studies have involved studying the spatial and temporal evolution of the laser-induced plasma. Time-resolved LIBS, often known as TRELIBS, has been implemented in many LIBS studies in order to improve the signal-to-background ratios of emission lines [9-13]. Early in the lifetime of the plasma there is a high degree of background emission as a result of bremsstrahlung processes, recombination, and Stark broadening [71]. However, these effects generally decline after a few hundred nanoseconds. Elemental emission lines decay at a slower rate than the background emission [72]. Therefore, if detection is delayed until after the background emission has decayed significantly, the signal-to-background of elemental emission lines can be improved. Spatial resolution has also been implemented more recently to improve the analytical capabilities of LIBS [73].

In 1989, Leis *et al.* studied the effects of the time delay between the start of the laser spark and optical detection on emission from the plasma induced from steel in an argon atmosphere [74]. When using a delay of 500 ns, the emission spectrum between 284.9 and 291.3 nm consisted mainly of ionic lines riding on a high background. As the time delay was increased, the signal-to-background ratio of atomic emission lines increased as a result of the plasma cooling. The different behaviour of atomic and ionic iron lines over time was also investigated in this work. The ionic Fe line was observed to be fifty times more intense than the atomic line at short delays. However, 10  $\mu$ s after the start of the laser

spark the atomic Fe line was 8 times more intense than the ionic emission line. Again this was attributed to the cooling of the plasma.

Ko *et al.* [42] also studied the temporal evolution of atomic Zn and Cu emission in the laser-induced plasma produced from brass samples in an argon atmosphere in 1989. They found that the intensity of the Zn emission line at 468.014 nm was at a maximum approximately 2  $\mu$ s after the start of the laser spark. The Cu emission line reached a maximum significantly later, at approximately 5  $\mu$ s. The ratio of the intensity of the Zn line to the Cu line decreased exponentially with time until approximately 16  $\mu$ s, after which it became constant. Ko *et al.* attributed this behaviour to the large differences in the vapour pressures of the two elements.

Shah and coworkers modelled the time-dependent spatial distribution of the number densities of the atoms and ions produced during laser interaction with a graphite sample in 1989 [75]. They used the cylindrical blast wave theory with the Saha [76] and charge conservation equations for this purpose. They obtained good agreement between the temporal and spatial evolution of atomic and ionic C emission predicted by the model and experimental data obtained using a Nd:YAG laser.

In 1991 Stoffels and coworkers studied the temporal behaviour of the emission from the plasma produced during laser interaction with uranium samples [77]. They found that there were three maxima in the total unresolved emission from the plasma, when the analysis was carried out in argon at pressures between 0.1 and 1 mbar. The first of the peaks was attributed to continuum radiation or line emission, depending on the observation height. They proposed that the other maxima were due to line emission from uranium.

Wisbrun *et al.* examined the effects of gated detection in LIBS analyses of metal, sand and soil samples in 1994 [78]. They found that the plasma induced from the metal sample lasted longer than those produced from the sand and soil samples. They proposed that this occurred because the metal released free electrons more readily than the other samples, producing a plasma earlier. This resulted in higher plasma temperatures and, hence, a longer plasma lifetime. They also determined that the optimum signal-to-background for

Zn at 481.1 nm in sand samples was achieved with a delay time of 0.28  $\mu\text{s}$  and a detection window of 1.7  $\mu\text{s}$  were used.

In 1995, Sabsabi and Cielo studied the temporal characteristics of the plasma formed during laser interaction with aluminium alloys in air and at atmospheric pressure [79]. The effects of time delay on the spectrum between 180 and 650 nm were observed. Again, at short delay times, the spectrum was dominated by ionic emission lines on a high background. As delay time was increased, neutral emission lines became the dominant spectral features. They also determined that the optimum timing for their analyses of Al alloys was achieved when using a 10  $\mu\text{s}$  delay and a detector integration time of 10  $\mu\text{s}$ .

In 1995, Jensen and coworkers studied the temporal characteristics of atomic and ionic Eu, Cr and K emission lines produced during laser-induced breakdown in air and at atmospheric pressure for samples comprised of a mixture of  $\text{Eu}_2\text{O}_3$  or  $\text{K}_2\text{Cr}_2\text{O}_7$  with granular  $\text{SiO}_2$  [80]. They found that, from 300 ns until 10  $\mu\text{s}$  after the laser spark, the atomic Eu lines at 459, 463 and 466 nm followed a power law ( $\propto t^{-1.5}$ ). They determined that this was roughly consistent with the electron densities expected in a spherically expanding plasma at atmospheric pressure. On the other hand, the decay kinetics of the ionic Eu emission lines were found to be highly dependent on elemental concentration. This indicated that the total number of ions, as well as their density, was changing with time. The rate of decay of the atomic Cr emission lines between 425 and 428 nm from the  $\text{K}_2\text{Cr}_2\text{O}_7$  samples was also shown to be dependent on concentration. They determined that this was because increasing the  $\text{K}_2\text{Cr}_2\text{O}_7$  in the sample increased the ability of the plasma to excite the atomic Cr as well as the amount of Cr in the plasma. Conversely, the decay of the atomic K line at 766 nm, like the atomic Eu lines, was well described by power law ( $t^{-1}$ ) decay. The K emission at 766 nm was also more persistent than Cr emission at 521 nm. Jensen and coworkers found that this was a result of the difference in the amount of energy required to excite each transition; the Cr transition required twice as much energy as the K transition. Therefore, as the plasma cooled, the Cr transition became less probable.

Vadillo *et al.* [81] looked at the temporal and spatial evolution of the laser-induced plasma from photovoltaic solar cells in air and at atmospheric pressure in 1996. The second harmonic of a Nd:YAG laser was used in these experiments. Vadillo and coworkers

observed narrowing of emission peaks in the spectrum between 323.8 and 339.3 nm with increasing time delay between the laser spark and optical detection. The FWHM of the ionic Ti line at 334.9 nm decreased from 0.28 nm when there was no delay after the laser spark to 0.14 nm at a 2.5  $\mu$ s delay. This was a result of decreases in Stark and Doppler broadening with time. Spectra were also measured at thirteen 36  $\mu$ m intervals above the sample surface. The most intense spectra were obtained between approximately 100 and 300  $\mu$ m above the sample surface.

In 1996, Multari and coworkers studied the evolution of the plasma produced from soil and stream sediment samples during LIBS over time [82]. They looked at the effects of the focussing lens-to-sample distance (LTSD) of a 150 mm focal length spherical lens and the angle of incidence of the Nd:YAG (1064 nm) laser pulse onto the sample on plasma evolution using an acousto-optic tunable filter. As in the studies detailed earlier, the spectra were dominated by a high continuum at short delay times after the start of the laser spark. At longer delays, atomic emission lines became more dominant. The LTSD was varied between 140 and 155 mm. The time-resolved images of ionic Ti showed that the plasma width increased with decreasing LTSD, while the plasma height decreased. The effects of the angle of incidence on LIBS analyses of atomic Cr in Cr-coated aluminium were studied at delay times between 0 and 49.81  $\mu$ s. At short delay times, the background continuum emission was found to occur along the path of the laser pulse. However at longer delays, as the background emission decayed, the Cr emission was found to occur perpendicular to the sample surface, regardless of the angle of incidence. It was also determined in this study that spatial resolution of the laser-induced plasma could be used to improve the signal-to-background ratio of elemental emission lines in a similar fashion to time-resolution.

In 1997, Castle *et al.* studied the spatial and temporal evolution of lead emission in the plasma induced by the fundamental wavelength of a Nd:YAG laser from pressed pellets of lead flakes and NIST soil standards by studying it from two orthogonal directions [83]. They obtained time-resolved images of the plasma using interference filters to isolate the ionic or atomic Pb transitions of interest. The behaviour of each of the Pb lines over time was found to be different. The time delay that produced optimum signal-to-background for

the Pb emission was also found to depend on the volume of the plasma analysed and the position of the detection optics relative to the plasma.

Also in 1997, Aragón and Aguilera studied the two-dimensional spatial distribution of time-integrated emission from the Nd:YAG laser-induced plasma from copper, stainless steel, and alumina samples [84]. This work was undertaken in air at atmospheric pressure and high irradiances (between 80 and 900  $\text{GWcm}^{-2}$ ) were used to induce the plasma. They found that the spatial distributions of atomic emission in both the horizontal and vertical axes were similar for each of the samples studied. They also found that ionic Fe emission was confined to a narrower region along the horizontal axis of the plasma formed from stainless steel than was the neutral Fe emission. The spatial profiles of atomic Fe emission produced from the stainless steel sample were also studied at different irradiances. A decrease in the maximum intensity of the emission was observed as irradiance increased from 100 to 700  $\text{GWcm}^{-2}$ . It was proposed that this effect was due to shielding by the air plasma. Shielding by the air plasma was reduced at irradiances both lower and higher than this.

In 1998, Panne and coworkers undertook TRELIBS studies of Si, Al, and Ca in glasses that were used for immobilisation of heavy metals in the ash produced during waste incineration [49]. They found that the optimum signal-to-noise ratio for atomic Si emission from the laser-induced plasma was obtained when a delay of 0.5  $\mu\text{s}$  and a gate width of 1  $\mu\text{s}$  were used.

Bulatov *et al.* studied the spatial and temporal evolution of the Nd:YAG laser-induced plasma produced from soil samples in 1998 [85]. As the time delay after the laser spark was increased, the region of the plasma producing the most intense spectra between 300 and 650 nm moved away from the sample surface. They concluded that the signal-to-background ratios of emission from Sr and Pb in soils could be optimised by spatially and temporally resolving the laser-induced plasma. The effects of sample matrix on the spatial and temporal evolution of the laser-produced plasma were also investigated. The optimum point in the plasma for analysis was found to depend on analyte concentration. Measurements of high concentrations were optimised closer to the sample surface. Matrix composition was shown to affect the signal-to-background ratios of Si, Al and Pb in soil

samples but not those for Ca, Fe, Sr. However, the optimum locations in the plasma for analyses of these elements were not affected by sample matrix.

Nelson and Myrick studied the spatial and temporal evolution of the laser-induced plasma from a solid lead sample using a fibre-optic array in 1999 [86]. A 17 x 32 array of square, close-packed optical fibres that were drawn into a 544 x 1 distal array with serpentine ordering was used to capture light from the laser-induced plasma. The 544 x 1 side of the array was imaged with a spectrograph and an ICCD used for spectral analysis. Broadband continuum emission was found to dominate in the first few hundred nanoseconds after the laser pulse, reaching a maximum between 400 and 600 ns after the pulse. Lead emission was found to reach a maximum between 1.2 and 1.4  $\mu\text{s}$  after the laser pulse.

In 1999, Liu *et al.* looked at the laser-induced plasma from crystalline silicon in the first 30 to 300 ns after the start of the laser spark [87]. The electron density and temperature were calculated at several time intervals from Stark broadened emission lines and the line-to-continuum ratio. Both electron temperature and density in this plasma were shown to be very high early in its lifetime, with the temperature decreasing from approximately 70,000 K at 30 ns to 20,000 K at 300 ns and the electron density decreasing from  $4 \times 10^{19}$  to  $5 \times 10^{18} \text{ cm}^{-3}$ . The decreases in temperature and electron density, which followed power law decay up to 300 ns, were much less rapid after this time.

Also in 1999, Setia Budi and coworkers studied the temporal and spatial evolution of the secondary plasma induced from a sample of copper in air and under reduced pressure [88]. They compared the temporal evolution of atomic Cu lines from both a free plasma and a plasma confined vertically by two parallel glass plates at air pressures of 2 and 8 Torr. The intensity of the Cu emission from both the free and combined plasma increased initially at each pressure studied. After reaching a maximum, the intensity of Cu slowly decreased in each case. The maximum intensity was reached slightly earlier at 8 Torr and for the confined plasma at both air pressures. Higher plasma temperatures were also obtained at 8 Torr than at 2 Torr. Maximum temperatures were obtained earlier for the confined plasma at each pressure. The time-resolved spatial distributions of the plasmas were also monitored during this study. The point of maximum emission intensity of the Cu line at 521.8 nm moved further away from the sample with increasing time until 3  $\mu\text{s}$ , when this

trend was reversed. As time increased, emission intensity also became more uniform over the area observed. The spatial evolution of the plasmas was also found to be more rapid at lower air pressures. The spatial distribution of the plasma temperature was investigated in this study as well. At a delay of 0.5  $\mu\text{s}$  after the formation of the secondary plasma, a maximum temperature of 9800 K was observed 6 mm from the sample surface when the plasma was confined and air pressure was 2 Torr. At longer delays, the temperature distribution was relatively uniform over the area observed.

Later in 1999, Setia Budi and coworkers reported on the time evolution of the atomic Zn emission line at 481 nm in a LIBS plasma from zinc plate at 2 Torr air pressure [89]. This evolution was monitored at 3 different laser energies ranging from 8 to 86 mJ. As laser energy increased, the length time of time after plasma formation at which the maximum intensity of the Zn emission occurred also increased. They attributed this to a longer shock excitation process at higher energies.

Bulatov *et al.* [73], in continuation of their work reported in 1998 and similar to the work by Multari and coworkers [82], looked at the advantages provided by spatial resolution of the laser-induced plasma. They did this by studying both the spatial and temporal evolution of the laser-induced plasma from brass. They showed again that, the longer the time delay, the further away from the sample the most intense spectra were obtained as a result of plasma evolution. Therefore, when they observed the plasma at some distance from the sample, they achieved similar results as when time gating was employed. They concluded that, while time resolution produced better analytical performance, spatial resolution provided a useful low-cost alternative.

In summary, the great majority of LIBS studies have found that implementing time gating of the optical detection provides improved signal-to-noise ratios for elemental emission lines. More recently, spatially resolving the laser-induced plasma has provided similar improvements in signal-to-noise ratios. The optimum time delays for the detection of elemental emission varied between studies but typically ranged between 0.5 and 10  $\mu\text{s}$ . This is because the behaviour of the laser-induced plasma is highly dependent on experimental parameters such as the sample and laser type, atmospheric environment, and

laser irradiance. Hence, the optimum time delay needs to be determined experimentally in each LIBS study.

### 2.3.3.2 Effects of the Sample Matrix

Studies of the sample matrix in LIBS experiments have been undertaken in order to elucidate their effect on the properties of the plasma. As mentioned earlier, the bulk properties of a sample affect its breakdown threshold during LIBS [31]. Thus, the content of the sample matrix can affect the production of the plasma and, hence, the intensity of emission from the plasma.

In their 1989 study, Leis et al. looked at the plasma temperature produced during LIBS analyses of several binary Fe-Cr samples with different Fe-to-Cr ratios [74]. They found that, as the proportion of Cr in the sample increased, the amount of sample ablated increased. This led to a reduction in the plasma temperature. The implication from this finding was that samples with very similar composition must be used for calibration of LIBS experiments.

González *et al.* used LIBS to analyse the sulfur content in steel samples in 1995 [90]. The fundamental wavelength of a Nd:YAG laser was used to induce a plasma in a 1000 mbar N<sub>2</sub> filled chamber. The monochromator used in this work was also filled with N<sub>2</sub> at 1000 mbar in order to avoid light absorption due to the Schumann O<sub>2</sub> band in the spectrum below 190 nm, where the optimum S emission lines for use in this work were found. González *et al.* found that variation in the other components of the sample matrix did not affect the S/Fe intensity ratio.

In 1996, Eppler and coworkers studied the effects of the sample matrix on LIBS analyses of Pb and Ba in soil samples [91]. The fundamental wavelength of a Nd:YAG laser was used to induce the sample plasma with 190 mJ pulses, in air at atmospheric pressure. Both the chemical speciation of the Pb and Ba in the sample and the bulk sample matrix were found to affect signal response. Elemental emission intensity was found to increase with sand content in soil samples. The effects of chemical speciation were not able to be attributed to a particular property of the compounds. The results from this study again demonstrated the need for matrix-matched calibration samples in LIBS analyses.

However, Eppler and coworkers also pointed out that this not vital when LIBS is used in applications such as the screening of soils for heavy metal contamination. In these instances, only sufficient accuracy to differentiate contaminated from uncontaminated areas is required.

As mentioned in the previous section, Bulatov *et al.* looked at the matrix effects on the spatial and temporal evolution of the laser-induced plasma from soil samples in 1998 [85]. They, too, found that the bulk sample matrix affected elemental emission intensity. The intensity of Pb emission was found to increase with sand content in the samples. The concentration of Pb in the soil was found, as mentioned earlier, to affect the optimum observation point in the plasma.

In general, this literature indicates that the sample matrix will affect the behaviour of the laser-induced plasma and, hence, the magnitude of elemental emission lines. The implication of this finding is that calibration curves need to be produced for each sample type or some form of signal normalisation implemented in LIBS analyses.

#### 2.3.3.3 Sample Surface Effects

Like the chemical matrix, the physical properties of samples analysed using LIBS can have an impact on signal response. In particular, the size of particles in samples such as soils and coals and the surface topography of samples such as metals can affect the intensity of plasma emission.

Wisbrun and coworkers investigated the effects of particle size in LIBS analyses of lead in sand in 1993 [44]. The sand particles were separated into size fractions using sieves with different mesh sizes. A XeCl excimer laser was used to induce plasmas from the samples, which had been spiked with a solution containing Pb, Cr and Zn. The emission intensity from Pb in the samples was shown to increase with particle sizes from 20 to 1000  $\mu\text{m}$ . After this point, the emission intensity levelled off. They proposed that this behaviour was a result of the thickness of the contaminant layer of solution on each particle, which was proportional to the radius of the particle.

In their 1995 study, Jensen and coworkers looked at the effects on plasma emission of the method by which  $K_2Cr_2O_7$  was dispersed onto quartz [80]. One method of sample preparation involved adding a  $K_2Cr_2O_7$  solution to the quartz particles and then evaporating the mixture to dryness. In the other method,  $K_2Cr_2O_7$  was mechanically dispersed throughout the quartz. Emission spectra from the mechanically dispersed sample in the 300 to 800 nm range were found to be an order of magnitude stronger than spectra from the solution dispersed sample. They found that the mechanically dispersed  $K_2Cr_2O_7$  was unevenly distributed throughout the quartz, whereas the solution dispersed sample was homogeneously distributed. Thus, the intensity of averaged emission spectra from the mechanically dispersed sample was attributed to laser-induced breakdown of  $K_2Cr_2O_7$ -rich quartz particles. It was proposed that the total emission from a small number of these rich particles was stronger than the total emission from many particles through which the  $K_2Cr_2O_7$  was homogeneously distributed.

Castle *et al.* studied the effects of surface roughness on LIBS analyses of copper samples in 1998 [72]. The roughness of the surfaces of the pure copper disks analysed was varied using a variety of sandpapers. A Nd:YAG laser, operating at its fundamental wavelength, was used to produce 220 mJ of energy in order to induce sample plasmas. Measurements of the relative standard deviations of the intensities of copper emission lines found that sample roughness had very little effect on the analytical precision.

Cabalín and coworkers looked at the effects of surface topography on LIBS analyses of stainless steel in 1999 [92]. The second harmonic of a Nd:YAG laser was used to induce plasmas from the samples in air and at atmospheric pressure. The surfaces of the stainless steel samples were polished using different grades of abrasive paper, to produce eight samples with different surface characteristics. At low irradiances, the roughness of the sample surface was found to affect the emission intensity of Cr, Mo, Fe, and Ni. At these irradiances, the sample with the smoothest surface produced the most intense emission. At higher irradiances, the emission intensity of the four elements studied was not significantly affected by surface roughness. It was proposed that this was a result of the high-energy beams destroying the surface topography. The reproducibility of the analyses of the samples with smooth surfaces was found to be better than those of the samples with rough surfaces, especially at lower irradiances. The detection limits of the samples with smooth surfaces were also better than those of the samples with the rough surfaces.

Thus, variation in the particle size or surface topography of solid samples has been found to have an impact on plasma emission produced during LIBS. As in the case of the chemical matrix effects, the implication of these findings is that calibration curves need to be produced for each sample type or a signal normalisation method implemented in LIBS analyses.

#### 2.3.3.4 Mass Removal

Laser-sample interaction during LIBS of solids results in the production of a crater at the sample surface. As mentioned briefly in the previous sections, the amount of material removed from the sample to produce this laser-induced crater and the rate at which it is removed are affected by experimental parameters. Hence, measuring the crater dimensions and the amount and rate of material removed during LIBS can lead to further understanding of the breakdown process.

Eyett and Bäuerle looked at how the laser beam spot size affected ablation rate from single crystal  $\text{LiNbO}_3$  plates when laser irradiance remained constant [93]. A XeCl excimer laser was used for this purpose and experiments were conducted in air. Scanning electron micrographs of holes produced by 1000 laser pulses with a fluence of  $3.1 \text{ Jcm}^{-2}$  and spot diameters of 175 and 42  $\mu\text{m}$  were obtained. The bottoms of these craters were found to be relatively smooth and little damage to the sample was observed. Eyett and Bäuerle also found that the ablation rate was independent of laser beam spot size, when the spot had a diameter greater than or equal to 80  $\mu\text{m}$ . When spot sizes with diameters smaller than 80  $\mu\text{m}$  were used, ablation rate was found to increase as the spot size decreased. They proposed that this behaviour was a result of an increase in the attenuation of the laser beam by plasma shielding when larger spot sizes were used.

In their study of LIBS analyses of steel samples, Leis *et al.* found that the size and shape of laser-induced craters depended upon focussing conditions, laser irradiance, and the pressure and nature of the gas environment [74]. Crater depth was found to decrease slightly with increasing laser energy. When a laser energy of 5 mJ was used, a cone-shaped crater with a rounded bottom and a raised rim at its surface was formed. The inner diameter of this crater was 100  $\mu\text{m}$ , while the rim diameter was 160  $\mu\text{m}$ . The depth of a

crater formed from 30 overlapping laser pulses was found to be 36  $\mu\text{m}$  and approximately 30 ng of the sample was removed with each pulse. These craters were obtained when the atmospheric environment consisted of argon at 1.40 kPa. Slightly smaller craters were obtained at atmospheric pressure.

Hwang *et al.* modelled laser-induced mass removal from Cu and Zn metals and, Fe and Ni alloys and compared the results of the model with experimental data [94]. The model developed was based on the one-dimensional heat equation. Good correlation between the experimental and theoretical data was obtained for all four samples. Both experimental and theoretical results showed that the mass of material removed from the samples increased with laser energy.

Wisbrun *et al.* looked at the formation of craters during LIBS analyses of soil samples [78]. They compared the results obtained when the soils were sampled at the same point on their surface with results obtained when fresh sites were sampled with each laser pulse. Emission intensity was found to decrease with pulse number when repeated sampling occurred at the same point on the soils. This was a result of the changes in the focussing and detection conditions caused by the formation of the crater. Relative standard deviations (RSD) of the analyses were also compared. The RSDs obtained when each laser pulse sampled fresh soil were relatively constant. However, when repeated sampling occurred at a single point, the RSD was shown to increase with the pulse number. The RSDs of these analyses were also higher than those obtained when fresh sample was analysed by each laser pulse. Thus, they concluded that it was preferable to probe fresh points on the sample with each laser pulse.

Ihlemann *et al.* studied the effects of laser pulse duration on the ablation rate from ceramic samples in 1995 [63]. Ablation rate was measured at laser fluences from 0.3 to 20  $\text{Jcm}^{-2}$  and using three different laser wavelengths and pulse durations. The ablation rate was found to be greatest when using a 500 fs, 248 nm pulse over the entire fluence range. Ablation rate was lowest when using the 30ns, 308 nm pulses at low fluences. However, at higher fluences, the 30ns, 248 nm pulses produced the lowest ablation rates.

In 1997, Kononenko and coworkers reported on the effects of gas environment, laser energy, wavelength and duration on the ablation efficiency from ceramic, steel and aluminium samples [59]. At low energies, ablation rate increased rapidly with the energy density of the laser pulses. At higher energies, the ablation rate was less sensitive to the energy density of the laser pulses. Ablation rates were measured in air and argon atmospheres at atmospheric pressure as well as in a vacuum. Maximum ablation rates were obtained in a vacuum. The ablation rates in the argon and air atmospheres were found to be similar.

Vadillo and coworkers reported on their study of depth-resolved analyses of Zn-coated steel using LIBS [95]. They generated a beam with a flat energy-profile from a XeCl laser that, unlike most laser beams, produced rectangular, flat-bottomed craters. Focussing of this beam resulted in more irregular craters with uneven bottoms, which are less suited to depth-resolved analyses. Depth resolution of 8 nm/pulse and good agreement with glow-discharge optical emission spectroscopic measurements were obtained.

In 1999, Vadillo and coworkers studied the effects of plasma shielding on the ablation rate from pure metal samples induced by an excimer-pumped dye laser with an output wavelength of 581 nm [96]. The effects of the laser fluence on the average ablation rate (AAR) from several pure metal samples were investigated. The AAR was found to increase non-linearly with fluence up to  $5.3 \text{ Jcm}^{-2}$  for Ti, W, Cu and Mo, and up to  $8 \text{ Jcm}^{-2}$  for Al and Zn. Above these fluences, the AARs remained relatively constant. This behaviour was caused by plasma shielding of the laser beam.

Pakhomov *et al.* reported on the mass removal rates obtained from pure plates of several elements using a Ti:Sapphire femtosecond laser in 1999 [61]. Mass removal ranged from 1 to 10 ng/pulse, which is significantly less than the amounts typically removed by nanosecond laser pulses. The mass of material removed from each sample was found to be proportional to the resistivity of the samples.

Also in 1999, Semerok and coworkers compared the efficiency of ablation from pure metal samples by femto-, pico- and nanosecond lasers [62]. They defined ablation efficiency as the ratio of the volume of ablated material to the laser energy and measured craters using a phase-stepping profilometer. The highest ablation efficiencies were obtained using a

femtosecond laser while the worst efficiencies were found with picosecond lasers. It was proposed that femtosecond lasers were the most efficient because laser beam attenuation by plasma shielding did not occur when using these short pulses. It was proposed that plasma shielding occurred when using both nano- and picosecond lasers and, hence, nanosecond lasers were more efficient because they had more time to remove sample material. The crater diameters produced by pico- and nanosecond pulses were observed to be larger than the laser beam diameters. They proposed that this could be a result of the beam being scattered by the plasma and plasma particle recondensation.

Liu *et al.* studied the frequency quadrupled, Nd:YAG laser-induced, mass removal from silicon samples in 1999 [87]. A white-light interferometric microscope was used to measure simultaneously crater volumes, depths, and diameters. The volumes of the craters as well as the volumes of the material redeposited as rims around the craters on the sample surface were measured in this work to determine the amount of material actually vaporised during ablation. Crater volume and depth were found to increase with laser irradiance. At a threshold irradiance of approximately 18 to 20 GWcm<sup>-2</sup>, both crater depth and volume showed a sharp increase. This corresponded to a sharp increase in the electron density and a decrease in the rate at which temperature increased with irradiance. Below the threshold irradiance, the volume of material redeposited on the sample surface was almost equivalent to the amount removed from the laser-induced crater. However, above the threshold irradiance, only approximately 20 % of the material was redeposited. Like the plasma temperature, the rate of increase in the diameter of the rim of redeposited material with irradiance decreases above the threshold irradiance. This suggested that the formation of the crater rims was related to the plasma temperatures. Liu *et al.* proposed that the sharp increase in mass removal from the laser-induced crater at the threshold irradiance could be a result of self-focussing of the laser by the plasma or the sample surface reaching the critical temperature.

In summary, the literature indicates that the mass removed and the craters formed during laser-sample interaction are strongly dependent on experimental parameters. In particular the laser irradiance and atmospheric environment have been found to affect mass removal. Since mass removal generally correlates with emission intensity, the optimum laser irradiance should be determined experimentally in each LIBS study.

### 2.3.3.5 Temperature and Electron Density Measurements of the Laser-Induced Plasma

In order to understand many of the processes taking place within a laser-induced plasma, the plasma temperature and electron number density need to be measured as functions of time after the laser spark. In particular, temperature and electron density data can provide information about the excitation and ionisation processes occurring within the plasma. The temperature and electron density can be determined by examining particular features of the emission spectra.

As mentioned in earlier sections of this chapter, Leis *et al.* looked at the plasma temperatures produced during LIBS analyses of several binary Fe-Cr samples in 1989 [74]. Plasma temperatures were calculated using the intensities of two Fe lines in the Boltzmann equation. The plasma temperatures (which were up to 10000 K) were shown to be dependent on the amount of material ablated. The amount of material ablated, as mentioned earlier, was dependent on the sample matrix.

Chen and Mazumder looked at the plasma temperatures produced during KrF laser-induced breakdown of graphite in an Ar/H<sub>2</sub> atmosphere in 1990 [97]. Emission intensities of the C<sub>2</sub> Swan and CN violet bands were used to calculate molecular vibrational temperatures. The temperatures calculated ranged between 11500 and 15300 K. Absorption of the laser beam by the plasma was proposed as the reason for temperatures being significantly greater than the melting point of graphite.

Ottesen and coworkers calculated plasma temperatures during their LIBS analyses of coal particles in combustion environments in 1990 [36]. They used the Saha equation to calculate ionisation temperatures using the intensities of ionic and atomic emission lines from Mg and Fe. The FWHM of the Stark-broadened H<sub>β</sub> line was used to calculate the electron number density, which was also required in the temperature calculations. When the frequency doubled Nd:YAG was used to induce a plasma from the sample with a pulse energy of 100 mJ, an electron density of  $7.36 \times 10^{16} \text{ cm}^{-3}$  was obtained. An average plasma temperature of  $9170 \pm 740 \text{ K}$  was obtained using the Fe lines. The average temperature calculated using the Mg lines was  $9890 \pm 630 \text{ K}$ .

Uebbing *et al.* studied the plasma temperatures produced during double-pulse LIBS analyses of glass and metal samples in a reduced pressure Ar atmosphere in 1991 [43]. A XeCl excimer laser was used to provide the initial laser pulse and the fundamental output of a Nd:YAG laser the second pulse. The energy of each pulse from the XeCl laser was 13 mJ, while the Nd:YAG laser, which was used to re-heat the plasma, produced pulses of 115 mJ. Plasma temperatures, which were measured as a function of time, were calculated using a Boltzmann plot. A few microseconds after the first laser pulse, the plasma temperature was greater than 12000 K. When a second laser pulse was not used, the temperature dropped to approximately 6000 K some 50  $\mu$ s after the start of the laser spark. While elemental emission was still produced at this temperature, it was relatively weak. When a second laser pulse was used to reheat the plasma 40  $\mu$ s after the first pulse, the plasma temperature increased again to 10000 K.

Singh *et al.* in 1993 [34] and Zhang *et al.* in 1995 [33] reported on plasma temperatures produced during LIBS analyses of coal particles in a coal-fired flow facility. A frequency doubled Nd:YAG was used to produce 100 mJ pulses for plasma production. Plasma temperatures were calculated from Boltzmann plots making use of atomic Ti and Fe spectral lines. The temperature calculated from the Ti emission lines was 7010 K. The Boltzmann plot of the Fe emission lines indicated that the plasma temperature was 6020 K.

In their 1995 study, Sabsabi and Cielo measured the plasma temperatures and electron densities produced during LIBS analyses of aluminium alloys [79]. Temperatures were calculated from the Boltzmann plot of atomic Fe emission lines. Electron number densities were calculated using the FWHM of Stark-broadened ionic Al emission lines. When a gate delay of 3  $\mu$ s and 60 mJ pulses from a Nd:YAG laser were used, the calculated temperature was 6730 K. The temperature was observed to drop rapidly in the initial few microseconds of the plasma lifetime. After this time, the plasma temperature decreased at a very slow rate. The maximum electron density was found to be greater than  $10^{18}$  cm<sup>-3</sup> less than 1  $\mu$ s after the start of the laser spark. This decayed to approximately  $10^{17}$  cm<sup>-3</sup> within the first 2  $\mu$ s and remained relatively constant after this time. The temperature and electron density were then used to determine whether the plasma was in local thermodynamic equilibrium.

Panne and coworkers calculated the plasma temperatures and electron densities produced during LIBS analyses of glasses that were used for immobilisation of heavy metals in the ash produced during waste incineration in 1998 [49]. Temperatures were calculated from Boltzmann plots and electron densities via use of the Saha equation. When 75 mJ of energy from a Nd:YAG laser was used to induce the sample plasma, temperatures up to 40000 K were obtained. Calculations of temperatures at different points on the sample surface resulted in variation of up to 15000 K. They proposed that these variations were caused by variable non-stoichiometric ablation. The temperatures and electron densities were used to normalise line ratios in Saha-Boltzmann equilibrium relationships.

Bauer *et al.*, in their 1998 study of standard metal samples using LIBS with an échelle spectrometer, measured plasma temperatures using Boltzmann plots [45]. A Nd:YAG laser was used to induce sample plasmas in an argon atmosphere. A time delay between the start of the laser spark and detection of 2  $\mu\text{s}$  and a detector integration time of 3  $\mu\text{s}$  were used. The same plasma temperature, within the uncertainty of the measurement, was calculated from the Boltzmann plots when using emission lines from several elements in the sample. Under these conditions, the plasma temperature was found to be  $8680 \pm 500$  K.

In their 1998 study of double-pulse LIBS analyses of solid aluminium alloys, St-Onge and coworkers measured time-resolved electron densities and temperatures in the sample plasmas [98]. Temperature was measured from Boltzmann plots of neutral iron emission lines. Electron density was calculated from the Stark-broadened ionic Al emission line at 281.6 nm. When only a single laser pulse was used, the electron density decayed rapidly for 0.5  $\mu\text{s}$  and then more slowly afterwards. When both laser pulses were used, the electron density decayed at the same rate as the single pulse after the second pulse. This suggested that the second pulse, which was produced from the same laser as the first, was absorbed by the existing plasma. Electron density was shown to be slightly lower when using the two pulses than when the single pulse was used. Thus, St-Onge and coworkers were able to conclude that the signal enhancement observed when using double-pulse LIBS was not due to an increase in the electron density. The plasma temperature was found to be higher when the two pulses were used, at delays of 1 and 10  $\mu\text{s}$ . Thus, the increase in temperature may have resulted in the signal enhancement. However, they

proposed that the increase in signal intensity was more likely to be due to increased ablation of the sample.

Liu *et al.* looked at the effects of laser irradiance and delay time on the plasma temperature and electron density during LIBS analyses of silicon samples in 1999 [87]. The electron density was calculated by measuring the FWHM of the Stark-broadened Si emission line at 288.16 nm. The plasma temperature was calculated from the line-to-continuum intensity ratio of the Si emission lines at 288.16 and 263.13 nm. The maximum calculated plasma temperature was 70000 K when a 30 ns delay was used. When a 300 ns delay was used, this temperature had dropped, with a power law dependence, to 20000 K. The electron density, which also experience power law decay, dropped from  $4 \times 10^{19}$  to  $5 \times 10^{18} \text{ cm}^{-3}$  over the same time interval. Plasma temperature and electron density were shown to increase with laser irradiance until the threshold value of  $20 \text{ GWcm}^{-2}$ . After this point, the electron density increased more rapidly with irradiance, while the plasma temperature increased more slowly. The reasons for this behaviour were described in the previous section.

As mentioned earlier in the review of time-resolved LIBS, Setia Budi and coworkers measured the temperatures of plasmas produced from copper samples at a range of time delays after laser-sample interaction in 1999 [88]. The neutral Cu emission lines at 521.8 and 510.5 nm were used in the Boltzmann equation to calculate plasma temperatures. A maximum temperature of 9100 K was obtained for the free plasma at 2 Torr and at 1.2  $\mu\text{s}$  after the start of the laser spark. The maximum temperature of the confined plasma was approximately 300 K cooler and this was achieved 0.4  $\mu\text{s}$  earlier at this pressure. Similar behaviour was observed for the plasmas at 8 Torr, with the maximum temperature of the free plasma found to be 9800 K at 1  $\mu\text{s}$ . The maximum temperature of the confined plasma at this temperature was 9350 K, 0.6  $\mu\text{s}$  after laser-sample interaction.

Gornushkin *et al.* measured the plasma temperature produced during Nd:YAG laser-induced breakdown of steel samples in 1999 [99]. The plasma temperature was calculated from a Boltzmann plot of iron emission lines between 423 and 431 nm. Spectra were obtained with a time delay of 5  $\mu\text{s}$  and a detector integration time of 1  $\mu\text{s}$ . When the laser

energy used was 20 mJ, the plasma temperature was found to be  $7900 \pm 1400$  K. When 100 mJ was used, the temperature was  $8700 \pm 1000$  K.

This literature has shown that both the electron density and temperature of the plasma decrease with increasing time delay. Both electron density and temperature were found to be dependent on several experimental parameters, such as sample type, laser irradiance, and atmospheric environment. Thus, it may be possible to incorporate measurements of the electron density and temperature in a signal normalisation method for LIBS analyses.

#### 2.3.3.6 Line Broadening

In most LIBS experiments, integrated line profiles are used as a measure of the intensity of the elements of interest. Thus, the line shape can have a significant impact on signal response. As mentioned in previous sections of this chapter, the line shape varies with plasma conditions and can be used to measure other properties of the plasma. Hence, it is important to understand the factors that affect the shape of emission lines.

Song and coworkers studied the line profiles of the emission lines produced during time-resolved LIBS analyses of copper samples in 1999 [100]. The third harmonic of a Nd:YAG laser was used to produce between 20 and 100 mJ per pulse in order to induce plasma formation from the copper samples in a 760 torr helium environment. Line narrowing of the copper emission lines at 515.32 and 521.82 nm was observed as the time delay between the start of the laser spark and optical detection was increased. Narrowing of the emission line at 510.55 nm was less dramatic since it was already relatively narrow at short delays. It was proposed that the behaviour of the lines at 515.32 and 521.82 nm was due to Stark broadening and characteristics of the Rydberg-like atomic state. Similar behaviour was observed when these experiments were carried out in both argon and air environments.

Gornushkin *et al.* studied line broadening of emission lines from the laser-induced plasma from calcium carbonate doped with Rb in 1999 [101]. The fundamental output of a Nd:YAG laser was used to induce the sample plasma in argon atmospheres at pressures of between 0.1 and 10 torr. A scanning Ti:Sapphire laser was used to measure the spectral line profiles of Ca, which was a major constituent of the sample matrix, and Rb, which was

present in trace amounts, in the plasma. The main cause of line broadening for the Rb was found to be Doppler broadening. The main broadening mechanism of the Ca emission line monitored was resonance broadening, which is caused by re-absorption of emission from Ca atoms.

### 2.3.3.7 Atmospheric Environment

The nature and pressure of the atmospheric environment in which LIBS is performed are other experimental parameters that can affect plasma production and emission. It is important to understand these effects in order to control and, where applicable, model the ablation process.

Stoffels and coworkers studied the effects of atmospheric environment on LIBS analyses of uranium samples in 1991 [77]. The fundamental wavelength of a Nd:YAG laser was used to provide 10 mJ of energy to samples in order to induce plasmas. As mentioned earlier in the chapter, three maxima in the total emission from the plasma were found on a temporal scale. These maxima were only observable at certain pressures but using any buffer gas. The second maximum was observable between 0.01 and 2 mbar and the third maximum between 0.1 and 1 mbar. The intensity of the laser-induced emission spectrum was found to increase with pressure. The plasma was also found to decay more rapidly when formed in air than when in an argon environment.

Hwang *et al.* looked at the effects of buffer gas in their 1991 study of laser-induced breakdown of metal samples [94]. The plasma emission was measured at a range of laser energies in both air and argon environments at atmospheric pressure. Emission intensity was found to increase with laser energy in both air and argon. Emission intensity from the copper sample was shown to be greater in the argon. The differences between the emission intensities from the four metal samples were greater in argon than in air.

The effects of the atmospheric environment on emission from a laser-induced plasma from metal samples were investigated by Kuzuya *et al.* in 1993 [57]. They tested the use of helium, argon and air at pressures ranging from atmospheric down to 1 torr. The pulse energy of the Nd:YAG laser was also varied from 20 to 95 mJ. Maximum signal intensity was found to occur in an argon environment at 200 torr when high laser energies were

used. Optimum signal-to-background ratios were achieved in helium at 40 torr when the laser pulse energy was low.

As mentioned in previous sections of this chapter, Setia Budi and coworkers studied free and confined laser-induced plasmas from copper samples in air at a range of pressures in 1999 [88]. Copper emission at 521.8 nm in both the free and confined plasmas was found to increase with air pressure up to 15 torr. The intensity of the emission from the confined plasma decreased considerably from 15 to 20 torr. After this point, emission intensity began to increase again. Similar but less drastic behaviour was observed for the free plasma. The spatial and temporal evolution of these plasmas over a range of air pressures is described in a previous section of this chapter.

Also in 1999, Setia Budi and coworkers studied the effects of air pressure during LIBS analyses of zinc plate [89]. The neutral Zn emission line at 481 nm and the ionic Zn emission line at 492 nm were monitored for this purpose. The intensity of the neutral emission line decreased with pressure up to 2 torr. Above this pressure, the intensity of this line increased with pressure until reaching a maximum just above 10 torr. Above 10 torr only a slight decrease in intensity with pressure was observed. The ionic line behaved quite differently. Its intensity remained relatively constant up to 2 torr, above which it increased very slightly with pressure. They proposed that the intensity of the neutral Zn emission line decreased with decreasing pressure because of a reduction of the surrounding gas density, which made excitation less effective. Below 2 torr, emission intensity increased with decreasing pressure because atoms released from the target were more likely to preserve their kinetic energy before colliding with surrounding gas molecules. Thus, these collisions became another excitation mechanism.

The effects of buffer gas and gas pressure on the laser-induced plasmas from pure metal samples were studied by Vadillo *et al.* in 1999 [96]. The average ablation rates (AAR) from Al, Fe and Ti samples at pressures from  $10^{-5}$  to  $10^3$  mbar and at three different laser fluences were investigated. The AAR from each sample and at each fluence was shown to increase as gas pressure was decreased from 1000 to 250 mbar. At pressures at and below 200 mbar, the AAR is relatively constant for each sample, regardless of the laser fluence. For each of the samples, an approximately 300 % increase in fluence resulted in less than a 25% increase in the AAR at these pressures. It was proposed that this was due to the

material that was removed from the samples attenuating the laser beam. On the other hand, the intensity of the Ti emission line at 498 nm was found to increase with gas pressure and fluence. This was a result of the signal intensity being weakened by the rapid expansion of the plasma at lower pressures. The effects of the composition of the buffer gas were also investigated. To this end, the AARs from Ti, W, Fe, Cu and Mo were measured in air at 1 mbar and in both Ar and He at 1000 mbar using 3 different fluences. These results were referenced to those obtained in air at 1000 mbar. When the gas environment was comprised of air at 1 mbar or He at 1000 mbar, the effects were very similar. These experiments resulted in a slight increase in the AAR compared to those in air at 1000 mbar. The Ar atmosphere resulted in a decrease in the AARs of the samples because these plasmas absorbed a higher proportion of the laser beam.

Knight and coworkers reported on their LIBS analyses of soils at reduced pressures and in a simulated Martian environment in 2000 [102]. This research was undertaken in order to demonstrate the feasibility of using LIBS in space exploration. A Nd:YAG laser was used to produce between 80 and 100 mJ per pulse for plasma generation. The results of this work showed that the magnitude of emission intensity and mass ablation were highly dependent on gas pressure. When gas pressure decreased from 590 to between 40 and 100 torr, elemental emission intensity increased by a factor of 3 to 4. When the pressure was lowered further, elemental emission intensity decreased and then levelled off. It was proposed this behaviour was a result of the amount of material ablated from the samples and the frequency of collisions in the plasma. The amount of material ablated increased as pressure decreased from 590 to 100 torr. This was a result of a reduction in the degree of attenuation of the laser beam by the plasma. The mass ablated only increased slightly below 10 torr because the degree of plasma shielding was very low. They also found that the plasma temperature and electron density of the plasma were pressure dependent. Both plasma temperature and electron density were shown to increase with pressure.

In summary, this literature has shown that the atmosphere in which LIBS is carried out has a significant impact on the intensity and signal-to-noise ratios of elemental emission lines in LIBS analyses. Reduced pressure and argon environments have been found to produce the best results in several of these comparative studies. However, undertaking LIBS analyses in such environments negates many of the cost, simplicity, and portability advantages provided by LIBS.

### 2.3.4 Applications of LIBS

In addition to the fundamental research, much work has been done on applying this technique to real samples. This area includes the development of LIBS for remote sensing and the production of portable instruments for on-line and *in situ* analyses. The work done in this field will be reviewed in this section.

#### 2.3.4.1 Remote Sensing Applications

In 1987, Cremers reported on the analysis of metals at a distance using LIBS [47]. The output of a Nd:YAG laser was focussed using a 0.5 m focal length lens onto the surfaces of the metal samples in order to induce plasmas. A fused silica optical fibre was then used to collect plasma emission and transfer it to a spectrograph. The optical fibre had a large acceptance cone angle so that small variation in the spark position did not significantly affect signal response. LIBS experiments were able to be performed at distances up to 2.4 m using this setup. The accuracy of quantitative analyses of the elements in these metal samples was within 5 %. Analytical precision was generally better than 10 %.

In 1995, Cremers and coworkers reported on the remote elemental analysis of Ba and Cr in soils using LIBS [103]. In this study, a fibre optic cable was used to transmit the fundamental output of a Nd:YAG laser to the soil samples. The same fibre was then used to transmit the plasma emission to the spectrograph. Approximately 100 mJ of energy per laser pulse was incident on the end of the optical fibre, with up to 84 mJ reaching the sample surface. Detection limits of 26 and 50 ppm were obtained for Ba and Cr in soil, respectively. These results were comparable to those obtained by direct lens-focussing of the laser beam onto the sample.

Davies *et al.* reported on the remote sensing of several elements in ferrous samples using LIBS in 1995 [104]. As in the study by Cremers and coworkers, an optical fibre was used to deliver the fundamental output of a Nd:YAG laser, which produced 40 to 50 mJ per pulse, to sample surfaces. Pulse energies delivered to the sample surfaces were between 12 and 15 mJ. Although a single fibre could be used for laser light delivery and collection of the plasma emission, it was found to be more efficient to use separate fibres for these purposes. Detection limits between 100 and 380 ppm were obtained for seven trace

elements in the ferrous samples. LIBS experiments were able to be performed at distances up to 100 m using this setup.

Ernst and coworkers looked at the possibility of using remote LIBS to analyse radiation embrittlement in nuclear reactors by measuring copper levels in 1996 [105]. An attempt at using an optical fibre for delivery of the fundamental output of a Nd:YAG laser to the samples was made. However, energy losses from the system meant that insufficient energy was delivered to the sample for plasma formation. Thus, a lens and mirror system was used for laser light delivery in these test analyses. An optical fibre was used for delivery of the plasma light to the spectrometer. These test analyses proved that LIBS could be used for the determination of the Cu content in steel.

Marquardt and coworkers developed a LIBS system for the remote elemental analysis of lead in house paint in 1996 [106]. Four-metre long optical fibres were used to deliver the fundamental or frequency doubled output of a Nd:YAG laser to the dry paint samples. As in the study of steel by Ernst and coworkers, a separate optical fibre was used to collect light from the plasma. Pulse energies between 4.2 and 19.0 mJ were delivered to the sample surfaces. The detection limit for lead in a latex paint was found to be 0.014 % when using this system. The relative standard deviations of the analyses were typically between 5 and 10 %.

In 1998, Marquardt and coworkers developed a fibre optic probe for remote LIBS, Raman spectroscopy, and Raman imaging of solid samples [107]. The fundamental output of a Nd:YAG laser was used for LIBS and an Ar<sup>+</sup> laser for Raman excitation. A microprobe containing 5 optical fibres was developed for laser light delivery and plasma light collection. It was proven during this study that both LIBS and Raman spectra could be obtained using this single probe.

Fichet *et al.* developed a system for the remote elemental analysis of impurities in UO<sub>2</sub> and PuO<sub>2</sub> using LIBS in 1999 [108]. The aim of this study was to develop an instrument for analysis of impurities in PuO<sub>2</sub> powder in hostile nuclear plant environments. A series of three mirrors were used to transport the frequency doubled output of a Nd:YAG laser from the control room to the room which contained the glove box in which the test experiments took place. The 15 mJ beam was then passed through a fused silica window in the glove

box. Two mirrors were used to direct the plasma light outside the glove box and into an optical fibre, which was then used to transport the light back to the control room for analysis. Detection limits of 100 ppm were obtained for 30 impurities in the  $\text{UO}_2$  and  $\text{PuO}_2$  samples.

The aim of the very recent study by Knight and coworkers [102], which was described earlier in this chapter, was to develop a remote LIBS system for space exploration. LIBS experiments were able to be performed at distances up to 19 m using this system. The laser pulses were passed through a Galilean telescope and a beam expander and then focussed onto the sample surface. Plasma light was collected using a lens and then transported to a spectrograph with an optical fibre. This study was able to demonstrate the capability of LIBS to perform remote elemental analysis in Martian and other reduced pressure space environments.

#### 2.3.4.2 Portable Instruments

Therriault and coworkers have reported several times on their development of a portable LIBS instrument for the detection of heavy metal contaminants in soils [69,70,109,110]. In this system, instrument components were truck-mounted. As mentioned earlier in this chapter, the fundamental output of a Nd:YAG laser and the plasma emission were transferred between the truck and the samples using a single optical fibre in a cone penetrometer probe. In this way the instrument facilitated the characterisation of soil samples up to several metres below the surface. When the probe was pressed into the ground, soil was pressed up against the disposable optical window in its housing. This ensures that the focussing conditions of the laser beam, which passed through this window, remained consistent for all analyses. Detection limits equal to or less than the US EPA's site screening levels for Pb, Cd and Cr were obtained using a laboratory mock-up of this portable instrument.

Cremers and coworkers also reported on the development of a transportable LIBS instrument for the analyses of heavy metals in soils in 1996 [40]. However, unlike the instrument by Therriault and coworkers, this instrument was contained within a plastic shipping container and was able to be moved by two or three people. Samples could be analysed in either of two ways; *in situ* with the optical fibre probe or in a sample chamber

in the instrument. When *in situ* measurements were made, a hand-held probe was positioned against the samples. Separate optical fibres were used for laser light delivery and plasma light collection. The authors of this paper concluded that improvement in the calibration and data analysis processes would be required if this instrument was to be used for site characterisation. Also in 1996, this group, in a paper by Yamamoto *et al.*, described the work done in the development of a portable, suitcase-sized LIBS instrument [37]. The outcomes of this work are summarised in an earlier section of this chapter.

In 1998, Miles and Cortes reported on the application of a truck-mounted portable LIBS instrument to the analysis of contaminants in soils [111]. Like the work by Theriault and coworkers, a cone penetrometer probe was used to perform *in situ* analyses. However, in this instrument, the 1.25-inch diameter laser was actually contained in the cone penetrometer probe. In order to prevent damage to the probe window, a recessed window was used so that it was separated from the soil. An optical fibre was used to deliver plasma light to the truck for detection. The successful application of this instrument to the field analysis of Cr and Pb was also reported.

Castle and coworkers reported on the development of a portable, battery powered LIBS instrument in 1998 [41]. Like the instrument developed by Yamamoto and coworkers, this instrument was housed in a suitcase and was relatively lightweight. Again, the laser was incorporated into the sampling probe. Plasma light was transported to the spectrometer using a 2 metre long optical fibre. A miniature, non-gateable spectrometer, which provided a spectral resolution of 0.4 nm was used for detection, with an integration time of 20 ms. Paint, steel, ores, and organic samples were analysed with this system. The detection limits obtained ranged from 0.016 % for Mn in steel to 0.13 % for Ca in the organic samples. Analytical precision was found to be better than 5 % for the steel, ore and organic samples. However, the precision of the Pb in paint analysis was much worse, ranging between 4 and 44 %. This was attributed to the heterogeneity of the paint samples.

As mentioned in a previous section of this chapter, Body and Chadwick developed a portable LIBS instrument and applied it to the analysis of gypsum, black coal, and Latrobe Valley brown coal [38,39]. The instrument components were contained within a metal box that was designed to fit on a laboratory bench. Pressed sample pellets were prepared in sample holders and then loaded into the instrument through an opening in its side. This

system was able to analyse emission over a wide spectral region by using several miniature spectrometers that could be triggered simultaneously. A timing circuit allowed optical detection to be delayed down to a few microseconds after the start of the laser pulse.

### 2.3.5 Signal Normalisation

As mentioned earlier in the chapter, the properties of a laser-induced plasma, including the intensity of elemental emission, are dependent on the sample matrix. Consequently, calibration curves must be constructed for each element in each sample type or some kind of signal correction implemented, in order to ensure accurate quantitative measurements. Even when calibration curves are generated for each sample type, variation in elemental concentrations can affect the behaviour of the laser-induced plasma. Several signal normalisation methods have been employed in an attempt to improve the precision of laser based analytical techniques, including LIBS. These normalisation methods include monitoring laser power [112], monitoring the size of the laser-produced crater [113], internal standardisation [42-46,90,105], plasma temperature normalisation [49], and acoustic signal normalisation [1,50,114,115]. An ideal normalisation method would correct for the matrix effects in any sample over long periods of time.

The most commonly used method of signal normalisation in LIBS analyses is internal standardisation. This process involves taking the ratio of the elemental emission line of interest to an emission line from another element in the sample. Generally this other element is a major component and is homogeneously distributed within the samples being analysed. Ko *et al.* investigated the possibility of using internal standardisation in their LIBS analyses of brass and Fe/Cr binary samples in 1989 [42]. They found that internal standardisation of plasma emission from the Fe/Cr binary samples resulted in data that was very nearly independent of plasma temperature and the state of evaporation of the ablated material. The emission lines used to provide the Fe/Cr ratio were required to be close together in the spectrum to allow for simultaneous detection. The excitation energies of the upper levels of the transitions also had to be similar. Internal standardisation of zinc and copper in the brass samples was found to fail early in the plasma lifetime. Ko *et al.* proposed that this was a result of large differences in the vapour pressures of these elements. Thus they found that internal standardisation should only be used for elements with similar vapour pressures or at long delays after the laser pulse.

Uebbing and coworkers employed internal standardisation as a means of signal normalisation in their 1991 double-pulse LIBS analyses of glass and metal samples [43]. Line ratios were measured at least 4  $\mu\text{s}$  after the second laser pulse to ensure that atomisation inside the plasma was complete. Linear calibration curves were able to be constructed using these ratios. Furthermore, Mg/Mn and Al/Mn line ratios obtained from glass and various metal samples were shown to be independent of the rest of the sample matrix; ratios from all samples fit on the same linear calibration curves that spanned three orders of magnitude in concentration.

Wisbrun and coworkers used Fe emission to normalise emission from other elements in LIBS analyses of steel, sand, and soil samples in 1993 [44]. The precision of the normalised data set was shown to be superior to that of the data set that was not normalised. González *et al.* also used Fe emission to normalise emission from S during analysis of steel samples in 1995 [90]. In this case, the ionic Fe emission line at 186.47 nm was used to normalise the S emission lines at 180.73 and 182.03 nm. These ratios were shown to be independent of the lens-to-sample distance and were linear for sulphur levels between 0.008 to 0.22 %. The S/Fe ratio was also shown to be independent of the other elements in the steel. Ernst and coworkers also used Fe emission to normalise emission from Cu in LIBS analyses of steel in 1996 [105]. The neutral Fe emission line at 330.67 nm was used to normalise the neutral Cu emission line at 324.75 nm. These lines were chosen because their intensities were of the same order of magnitude at high Fe and low Cu concentrations.

In their 1998 study, Bauer *et al.* normalised elemental emission from laser-induced plasmas from aluminium samples using the Al emission line at 266 nm [45]. The ratios of the intensities of elemental emission lines from Cr, Mg, Fe, Cu, Ni, and Ti to this Al line were all shown to increase linearly with concentration. However, some of the data points were shown to deviate from the calibration curves by up to 40 %. Since single-shot measurements were used to construct these curves, these deviations were ascribed to inhomogeneous elemental distributions.

Aragón and coworkers used Fe emission to normalise emission from C, Si, Cr, and Ni during LIBS analyses of steel in 1999 [46]. The reference Fe lines used to normalise

emission lines from the other elements were chosen to arise from the same ionisation state and to have upper energy levels with similar energy to those of the elemental lines of interest. However, an ionic Fe emission line was used to normalise the neutral C emission line because the neutral Fe emission lines in this region of the spectrum were too weak for analysis. Voigt profiles, which are composites of Gaussian and Lorentzian profiles, were fitted to the emission lines chosen. The areas of these profiles were then used as measures of emission intensity. Calibration curves showed non-linear relationships between the normalised emission intensities and elemental concentrations. This non-linearity was a result of self-absorption at high concentrations. The intensity ratios were also shown to vary with both lens-to-sample distance and laser irradiance.

Therefore, while signal normalisation by internal standardisation can be used to improve the precision of data obtained from LIBS analyses, there are several drawbacks associated with its use. Firstly, internal standardisation requires the presence of a uniformly distributed element that varies minimally in concentration. Even when such an element is present, internal standardisation requires that it has emission lines that can be measured simultaneously with those of the elements of interest. It is also preferable that the reference emission lines are in the same ionisation state, arise from energy levels of similar magnitude, and that the elements have similar vapour pressures.

Another signal normalisation method that has been implemented during LIBS analyses involves taking the ratio of the intensity of an elemental emission line to the intensity of background emission. Cremers took the ratios of elemental emission lines to small segments of the background emission that did not contain strong emission lines from the elements being monitored in his 1987 analysis of metals at a distance [47]. This method resulted in the successful identification of the main elements in several metal samples.

Bolger normalised LIBS signals by taking the ratios of the intensities of elemental emission lines to the entire plasma emission in his analysis of mineral drill core samples in 2000 [48]. Samples consisted of unevenly split sections of the drill core samples arranged linearly on sample trays. The height of these rock pieces, and hence the lens-to-sample distance, varied by up to 2 cm. The focal length of the focussing lens was 1000 mm and the lens-to-sample distance was 770 mm in order to minimise the effects of the rock height variations. Normalisation using the integrated emission intensity of the entire measured

spectrum corrected for irregularities in the rock surfaces. The intensities of non-normalised emission lines from identical basalt samples were found to fluctuate by 23 to 26 %. However, when the normalisation procedure was implemented, the relative standard deviations were only 4 to 6 %. Linear calibration curves with high  $R^2$  values were obtained using the normalised data for several elements in drill core samples.

These normalisation methods, which incorporate measurements of background emission levels, also have drawbacks. The method used by Cremers used only a small section of the spectrum as a background measurement. When time-resolved spectra are used, this signal will be very small compared to elemental emission intensities. The small background signals in these spectra would result in a high proportion of noise in the normalised data. The method described by Bolger, while not subject to the same proportion of noise as the Cremers method, will only improve analytical precision when sample composition is reasonably consistent.

The temperature of the laser-induced plasma has also been used to normalise signals during LIBS analyses. In 1998, Panne and coworkers reported on a variation of line ratio normalisation that they used in their analyses of glasses used for immobilisation of heavy metals in the ash produced during waste incineration [49]. They normalised line ratios using Saha-Boltzmann equilibrium relationships that incorporated both electron density and temperature measurements. Linear calibration curves for Mg/Si, Mg/Ca and Mg/Al were constructed. The spread of data points about the calibration curves was found to be greater for the non-normalised line ratios than for the normalised line ratios.

Ciucci *et al.* developed a method for analysing LIBS signals that they proposed rendered it calibration-free in their 1999 study of metallic alloys [116]. They constructed Boltzmann plots using data from the emission lines of the elements of interest. They proposed that the y-intercepts of the linear curves fit through this data were proportional to the logarithms of the concentrations of the ionisation states of the elements. This method was applied to several elements in an aluminium alloy. The results obtained were in good agreement with the nominal concentrations supplied by the producer.

Again, there are drawbacks associated with normalisation methods that are based on plasma temperature calculations. The methods used by Panne and coworkers and Ciucci *et*

*al.* both require the presence of several observable emission lines from each element in a single spectral window. This is a requirement that many samples cannot fulfil.

Peppers and coworkers observed an improvement in the analytical precision of their analyses of Mg in human blood serum when they used the laser energy to normalise the Mg signal in 1968 [112]. They treated the relationship between the spectral signal and laser energy as linear. Hence, normalisation involved simply dividing the spectral signal by the laser energy. However, this type of normalisation only accounts for fluctuations in the laser energy over a very small range. It does not take into account any change in the focussing conditions or surface and matrix effects. Since the relationship between signal intensity and laser energy is not necessarily linear, this method will not improve results when large fluctuations in the laser energy occur.

Morton and coworkers used measurements of the laser-induced craters to normalise signals during laser microprobe analyses of metal samples in 1973 [113]. The diameters and depths of the laser-induced craters were measured using optical microscopy. Craters were assumed to be conical in shape, and so crater volumes were calculated using the formula for a right cone. The masses of material removed were then calculated using the measured or typical densities of the samples. This process typically took several minutes and compared favourably with arc spark analyses when metal samples were interrogated. However, measuring the volume of the laser-induced crater is time-consuming and requires extra equipment. These drawbacks negate many of the advantages of LIBS. This technique also does not take into account the redeposition of material on the sample surface.

Another method that has been used for signal correction involves monitoring the acoustic shock wave produced during laser sample interaction. Chen and Yeung [50] showed in 1988 that the magnitude of the acoustic shock wave was linearly related to emission intensities of major and minor elements in solid metal samples over a range of experimental conditions. Thus, they concluded that it would be possible to use the acoustic signal to normalise for any fluctuations in these parameters. Analytical precision was found to improve by a factor of 2 or more in the laser ablation ICP-AES and ICP-MS analyses of metals by Pang and coworkers in 1991, when acoustic signal normalisation was employed [114].

Kanicky and coworkers reported on the application of acoustic signal normalisation to laser ablation ICP-AES analyses of glass samples in 1998 [115]. They observed a negative relationship between acoustic signal and line intensities from the ICP. They attributed this behaviour to the use of an ultraviolet laser and the ICP. Since Chen and Yeung [50] and Pang and coworkers [114] used 308 nm XeCl excimer lasers and Pang and coworkers obtained good results when normalising ICP-AES data, it is unlikely that these caused the negative correlation.

Chaléard *et al.* showed in 1997 that the acoustic signal was linearly related to elemental emission intensities and the mass of the material removed during LIBS analyses [1]. They used the acoustic signal and a temperature normalisation coefficient to normalise elemental emission line intensities in several different metal samples. They found that the non-normalised emission intensities from Cu in several different types of metal samples did not produce linear calibration curves. However, when the acoustic signal and temperature normalisation method was implemented, a linear calibration curve was obtained for Cu concentrations between 0 and 90 %.

From these studies we can conclude that incorporating acoustic signal measurements seems to be the most promising option for normalisation of LIBS data. It does not increase analysis times, requires little extra instrumentation, has the potential to be applied to all sample types, and corrects for fluctuations in many experimental parameters.

### 2.3.6 Sample Water Content

The water content of solid environmental samples such as coal and soil can affect signal response during analyses by LIBS. The amount of water in these types of samples can vary by up to several percent, leading to a reduction in analytical precision and accuracy. Ideally, the water content of these samples would be measured along with elemental concentrations.

Wisbrun and coworkers reported on the effects of sample water content in their LIBS analyses of sand and soil samples in 1993 and 1994 [78,117]. They observed a decrease in the intensity of LIBS signals with increasing water content. This was because the water increased the energy required for laser-induced breakdown. Wisbrun and coworkers also

found that the magnitude of the effects of the water were different for different samples. The intensities of signals from sand samples were halved when water content increased from 0 to 0.8 %. However, soil samples required water content to increase to 5 % to experience the same signal reduction. They proposed that this was because the soils adsorbed a greater proportion of the water than the sand samples. They suggested that signal variation caused by variation in the water content could be overcome by drying samples prior to analysis.

Jensen and coworkers, and later Langford and Dickinson, reported on the effects of sample moisture in their LIBS analyses of mixtures of  $\text{Eu}_2\text{O}_3$  with granular  $\text{SiO}_2$  in 1995 and 1996 [80,118]. Wet samples were produced by adding distilled water to dry samples that had been analysed previously. The intensity of the emission spectrum from dry samples in the spectral region between 250 and 800 nm was found to be more than 100 times greater than the spectrum from the wet samples. The intensity of the ionic Eu emission lines was also found to decrease relative to the atomic Eu emission lines. Again, this was a result of the water, which has a high heat of vaporisation, using much of the energy delivered to the plasma. Water also has a high ionisation potential, which meant that it did not contribute much to the charged particle densities in the plasma. Jensen and coworkers also proposed that the high electronegativity of the water caused the water vapour to scavenge electrons, which resulted in less intense plasmas.

Rusak and coworkers investigated the effects of water content in their LIBS analyses of  $\text{CaCO}_3$  in 1997 [119]. They found that the intensity of Ca emission decreased linearly as the sample water content increased from 0 to 40 %. An order of magnitude decrease in the signal intensity was observed over this range. Plasma temperatures, which were calculated using Boltzmann plots, were not affected by water content as it increased from 0 to 30 %. However, the electron density of the plasma, which was calculated from the Stark broadened  $\text{H}_\alpha$  line at 656 nm, was found to decrease with increasing sample water content. They proposed that these results were due to the properties of water increasing the energy density required for breakdown and decreasing the charged particle densities in the plasma as water was added. They also proposed that the effects of variation in sample water content could be minimised using internal standardisation or by drying samples prior to analysis.

All of these studies have demonstrated that the water content of solid samples affects the intensity of plasma emission produced during LIBS. The main solutions proposed to overcome the effects of these variations involved internal standardisation or sample drying. However, no attempt was made to make real-time measurements of the water in the samples as elemental analysis took place.

### 2.3.7 Calibration Methods

In order to facilitate quantitative analyses, LIBS generally requires the construction of calibration curves. These curves are usually constructed by relating elemental emission peak intensities/areas or a ratio of peak intensities/areas with elemental concentration, which has been determined by some other analytical method. In general, these curves are produced by fitting a straight line to the data using least squares regression. However, results can sometimes be improved using methods that allow contributions from several spectral features.

Wisbrun and coworkers implemented the generalised linear model (GLM) and principal component regression (PCR) in attempt to improve their quantitative analyses of heavy metals in soil, sand, and sewerage sludge samples in 1994 [78]. The samples used in this work were either standard reference materials or had reference analyses provided by AAS. The GLM method was used to weight the importance of each spectral line for each element analysed. Calibration curves were then produced using these weights and the intensities of the elemental peaks. During PCR analyses, the number of principal components required was determined by plotting the residual Y-variance as a function of the components. Usually, one or two components were able to describe more than 95 % of the variance. Influence plots were used to identify and then remove the data from highly influential peaks. Linear calibration plots were able to be produced using this method. Comparisons between the PCR model and reference analysis results for three soil samples were made. These comparisons showed that the model predictions were in good agreement with the reference analyses for all elements in each of the samples analysed.

Panne *et al.* reported on the implementation of partial least squares (PLS) regression in their 1998 LIBS analyses of glasses used for immobilisation of heavy metals in the ash produced during waste incineration [120]. Normalised intensity ratios were the

independent variables and concentration ratios the dependent variables in the regression. This model found that a single component model produced the best results. Good agreement was obtained in a comparison of the results of the reference analyses and those from the PLS model. The uncertainty of results from this model was between 8 and 20 %. In comparison, the uncertainty in the reference analyses ranged between 3 and 6 %. From this work, they were able to conclude that PLS calibration was superior to simple linear regression.

Sattmann and coworkers employed artificial neural networks to classify LIBS spectra of polymer samples in 1998 [121]. Unlike most LIBS work, the aim of this study was to identify different types of polymers from the spectra, rather than determine elemental concentrations. Eight variables were used as inputs to the neural networks, including emission lines from H, C, C<sub>2</sub>, and Cl. The networks produced had identification accuracies greater than 93 %.

Gornushkin and coworkers applied linear and rank correlation to the classification of metal samples using LIBS spectra in 1999 [122]. They recorded several libraries of LIBS spectra of solid materials. Test samples were then analysed and the resulting spectra compared with the spectral libraries using linear or rank correlation. The test sample was identified as the material with the spectrum that had the highest correlation with the test spectrum. Rank correlation, which was nearly 100 % reliable for the samples tested, was found to provide more reliable classification than linear correlation.

The same group applied linear and rank correlation to the classification of post-consumer plastics from LIBS spectra in 2000 [123]. This method of calibration, which was the same as in their work using metal samples, resulted in the probability of correct sample identification ranging from 0.8 to 1.0.

These studies demonstrated that the use of chemometric methods offers promise in improving LIBS analyses. In particular, the use of multivariate techniques such as PLS and PCR have been found to improve the precision and accuracy of quantitative results.

## *Experimental Design and Optimisation*

### *3.1 Introduction*

Laser-induced breakdown spectroscopy has been used extensively for both the qualitative and quantitative analyses of elemental species in a variety of solid [33-49,124-135], liquid [136-138], gas [139-142] and aerosol [143-144] samples. The LIBS technique involves the interaction of a high-power laser pulse with sample matter. This results in the production of a plasma containing electronically excited species. These species emit radiation at characteristic wavelengths that can subsequently be used to identify and measure the sample constituents, once the plume emission is spectrally resolved.

This chapter details the experimental apparatus and methodology used to undertake LIBS analyses of Latrobe Valley brown coal. Two different instrument arrangements were used during the course of this work; a highly sensitive laboratory-based instrument incorporating an intensified charge-coupled device (ICCD), and a low-cost portable instrument. The optimum experimental conditions for these analyses are also presented here. These conditions were determined by studying the effects of varying experimental parameters on the laser-induced spectra.

### *3.2 Experimental Apparatus*

#### *3.2.1 Laboratory-based System*

The experimental setup for the LIBS system incorporating the ICCD is shown in Figure 3.1. The specifications of the equipment used in this setup are detailed in Table 3.1. The fundamental (1064 nm) output of a Q-switched Nd:YAG (Neodymium: Yttrium Aluminium Garnet) laser, with pulse widths of 5 to 7 ns, was focussed by a 50 mm focal length spherical lens to 200  $\mu\text{m}$  diameter spots at the face of pressed sample pellets. Sample pellets were produced by pressing 10 g of each sample using a hydraulic press (Carver). Latrobe Valley brown coal samples were sieved to produce particle sizes of less than 3 mm diameter and then mixed, prior to being pressed, to provide a more

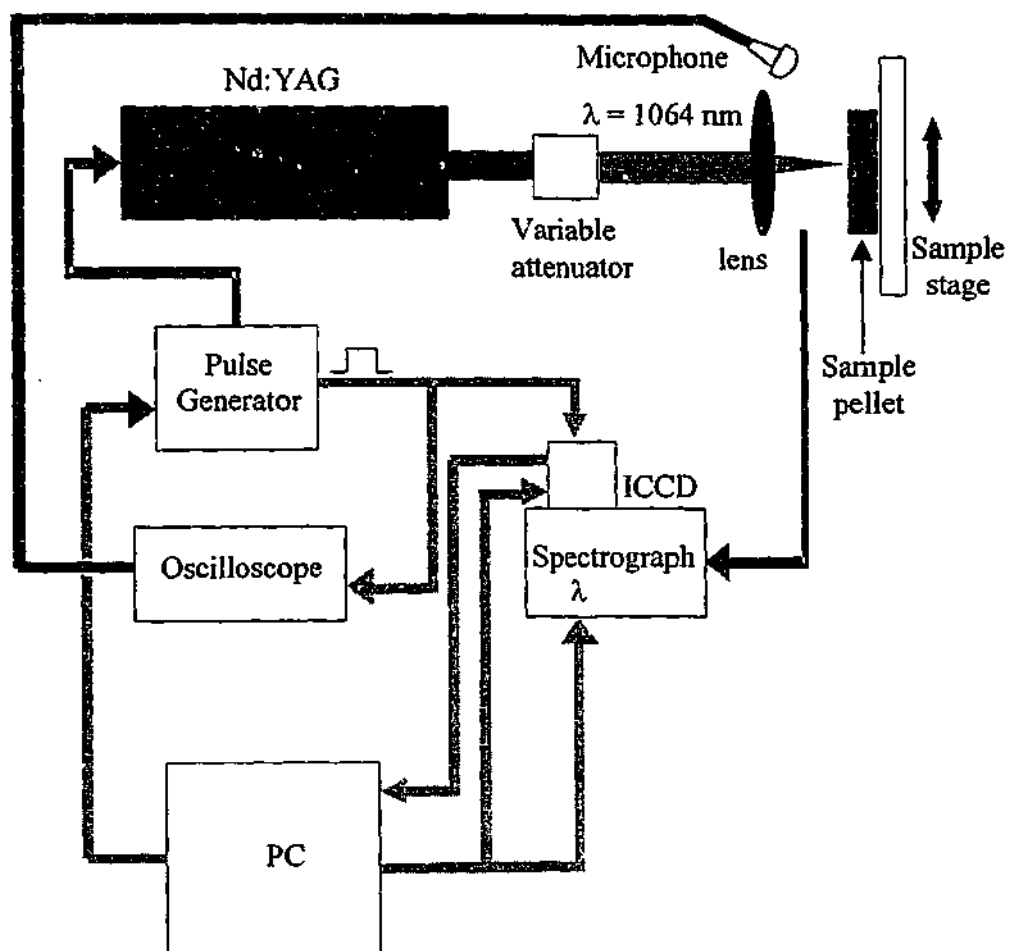


Figure 3.1. Schematic diagram of the laboratory based experimental setup for LIBS analysis of Latrobe Valley brown coal.

Table 3.1. Experimental apparatus and characteristics of the laboratory based setup.

|                          |   |
|--------------------------|---|
| <b>Laser</b>             | Continuum, Surelite   |
| Type                     | Nd:YAG, Q-switched  |
| Wavelength               | 1064 nm   |
| Pulse width              | 5 to 7 ns   |
| Pulse energy             | 10 to 75 mJ/pulse (Max. 385 mJ)   |
| Repetition rate          | 2 Hz to 5 Hz (Max. 10 Hz)   |
| <b>Spectrograph</b>      | Oriel, Multispec (MS257)  |
| Configuration            | Czerny-Turner   |
| Output focal length      | 0.257 m   |
| Diffraction gratings     | 2400 lines/mm, blaze at 250 nm<br>1200 lines/mm, blaze at 250 nm<br>300 lines/mm, blaze at 500 nm |
| Slit width               | 200 $\mu\text{m}$   |
| <b>Detector</b>          | Oriel Instaspec V   |
| Type                     | CCD, three-stage cooling  |
| Size                     | 1024 x 256 pixels, 26 $\mu\text{m}^2$ each  |
| <b>Image intensifier</b> | Oriel Instruments   |
| Diameter                 | 25 mm   |
| Time resolution          | 10 ns   |
| Spatial resolution       | 109 $\mu\text{m}$   |
| <b>Fibre-optic cable</b> | Oriel, Model 77534  |
| Fibre-optic material     | High-grade fused silica   |
| Fibre-optic size         | 200 $\mu\text{m}$ core  |
| Cable input              | ST input  |
| Cable output             | 200 $\mu\text{m}$ x 6.00 mm   |
| Length                   | 2 m   |
| <b>Pulse Generator</b>   | Stanford Research Systems DG535   |

homogeneous distribution of the coal constituents. The moisture content of Latrobe Valley coals ranges from approximately 49 to 70 % on a wet basis [2]. Thus, when high pressures are used to produce sample pellets, the coal may exhibit significant water loss (up to several grams). A pressure of approximately 220 metric ton/m<sup>2</sup> was found to produce stable sample pellets that experienced negligible water loss. Sample pellets of powdered minerals were prepared by mixing boric acid powder (BDH general purpose laboratory reagent) with each sample in a 1 to 4 ratio. In this case a pressure of approximately 1764 metric ton/m<sup>2</sup> was then exerted by the hydraulic press to produce pellets. The purpose of the boric acid was to act as a binder within sample pellets. It is difficult to produce cohesive pellets of powdered mineral samples without such a binder.

Sample pellets were moved by a computer-controlled 2-axis translation stage between laser pulses in order to expose fresh sample to each successive pulse. A third stage was used to optimise depth-of-focus for maximum analytical sensitivity. A 200 µm diameter fused silica fibre and collimating lens were placed 10 cm in front of the sample at a 45° angle to the surface. The collected plasma emission was resolved by a ¼ m spectrograph, which dispersed the light onto a gated, intensified 1024-channel ICCD array. The fibre was placed 10 cm from the sample because fibre contamination by coal particles was unlikely to occur at this distance. The CCD was thermoelectrically cooled with air cooling to -15°C to reduce the dark current.

The maximum collection efficiency of this LIBS system is estimated to be approximately 0.3 % at 350 nm. The usable wavelength region of the system is 200 to 850 nm, with a wavelength range of 40 nm, 80 nm or 300 nm, depending on which of the system's 3 gratings (with line densities of 2400 l/mm, 1200 l/mm or 300 l/mm) are used. A spectral resolution of ~0.2 nm at 500 nm is obtained with the 2400 lines/mm grating used in this investigation. Spatial resolution was measured by taking spectra of a HeAr lamp. Gaussian curves were then fitted to some of the strong peaks from this lamp that were well resolved. The FWHM of the curve that fit the experimental data was taken as a measure of the resolution.

Figure 3.1 indicates that a microphone is part of the laboratory-based experimental setup. Its use will be described in more detail in Chapter 5.

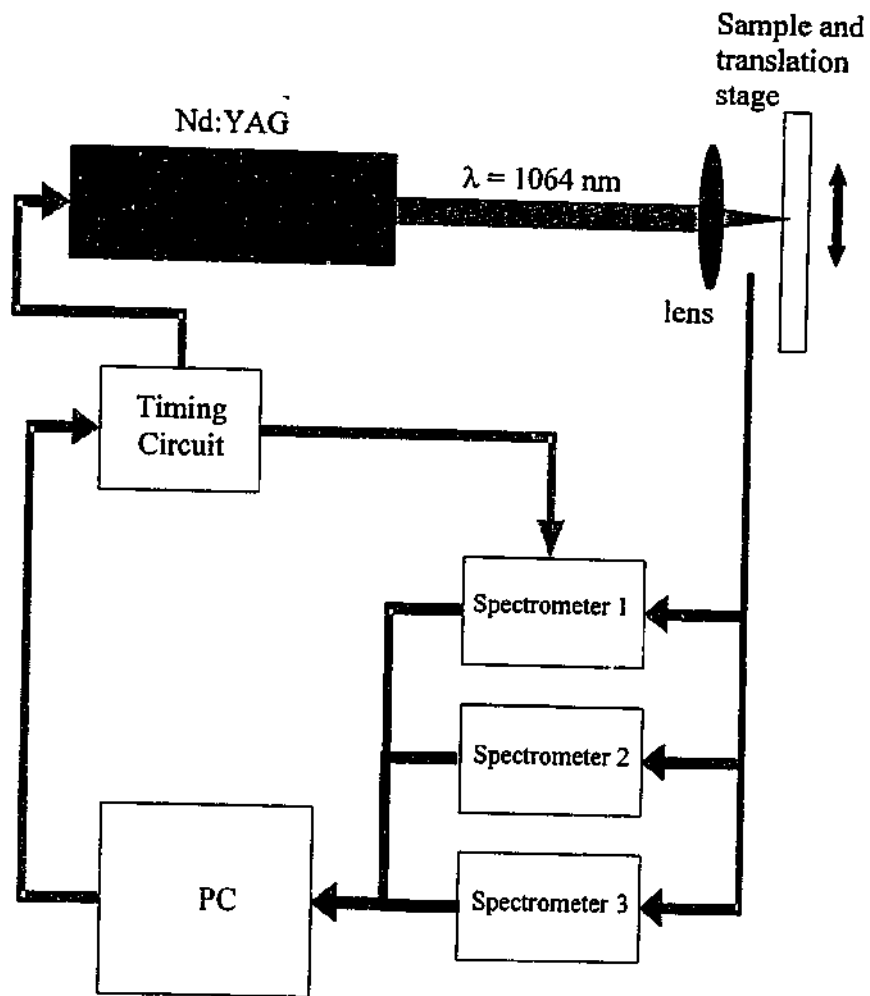


Figure 3.2. Schematic diagram of the Laser Plasma Spectrometer.

Table 3.2. Experimental apparatus and characteristics of the portable Laser Plasma Spectrometer.

|                          |  |
|--------------------------|--|
| <b>Laser</b>             | New Wave Research, Minilase  |
| Type                     | Nd:YAG, Q-switched   |
| Wavelength               | 1064 nm  |
| Pulse width              | 6 to 8 ns  |
| Pulse energy             | 40 mJ (up to 90 mJ)  |
| Repetition rate          | Up to 15 Hz  |
| <b>Spectrographs</b>     | Three Ocean Optics S2000 units   |
| Configuration            | Asymmetric crossed Czerny-Turner   |
| Output focal length      | 0.068 m  |
| Diffraction gratings     | 1. 2400 lines/mm, UV blaze<br>2. 2400 lines/mm, Vis blaze<br>3. 1200 lines/mm, Vis blaze |
| Slit width               | 1. 25 $\mu\text{m}$<br>2. 10 $\mu\text{m}$<br>3. 10 $\mu\text{m}$                        |
| <b>Detectors</b>         | Sony ILX 511   |
| Type                     | CCD  |
| Size                     | 2048 pixels, 14 x 200 $\mu\text{m}$ each   |
| <b>Fibre-optic cable</b> | 1. Optran UV fibre<br>2. Thorlabs, FT1.0-UMT<br>3. Thorlabs FT1.0-UMT                    |
| Fibre-optic material     | Fused Silica   |
| Fibre-optic size         | 1mm core (all fibres)  |
| Cable input              | SMA input  |
| Cable output             | SMA output   |
| Length                   | 1. 0.2 m<br>2. 1 m<br>3. 1 m   |

### 3.2.2 Portable System

The experimental arrangement of the portable low-cost LIBS instrument, the Laser Plasma Spectrometer (LPS), is shown in Figure 3.2. This instrument was initially set up for another project at the CRC for Clean Power from Lignite and was used to collect the data found in Chapter 7 of this thesis. The specifications of the equipment used in this setup are detailed in Table 3.2. In this system, the fundamental output of a Q-switched Nd:YAG laser, with pulse widths of 6 to 8 ns, was focussed by a 38.4 mm focal length spherical lens to the faces of pressed sample pellets. Sample pellets analysed using the LPS were produced using the same method as those analysed by the ICCD system.

Sample pellets were moved by a single-axis translation stage between laser pulses in order to analyse fresh sample with each successive pulse. Three 1mm core fused silica fibres, each coupled to a collimating lens, were placed 5 cm (Spectrometer 1) and 6 cm (Spectrometers 2 and 3) in front of the sample at 45° (Spectrometer 1), 75° (Spectrometer 2) and 90° (Spectrometer 3) to the surface. The collected plasma emission was then resolved by three separate 0.068 m spectrographs, which dispersed the light onto three linear CCD detectors. The wavelength regions of the three spectrographs are 220 to 375 nm, 370 to 490 nm, and 525 to 825 nm. These spectrometers have resolutions of approximately 0.25 nm, 0.17 nm and 0.35 nm respectively. The resolutions of these spectrometers were measured as described previously.

### 3.3 The Effects of Laser Irradiance on Laser-Induced Emission Spectra

The effects of laser irradiance on LIBS analyses of Latrobe Valley brown coals were studied using the apparatus shown in Figure 3.1 and described in Table 3.1. A variable attenuator was used to vary the laser irradiance used in these LIBS experiments. A Joule meter (Scientech, Model 38-1UV5) was used to measure laser energy, which was subsequently used to calculate the irradiance. Irradiances between 5 and 65 GWcm<sup>-2</sup> were tested in order to determine the optimum irradiance to use for LIBS analyses of Latrobe Valley brown coals. A time delay between the start of the laser spark and start of detection of 1.0 μs and a detection integration time of 5 μs were used for all the experiments in this section. A system gain of 0.9 ADC counts/photoelectron was used to intensify plasma

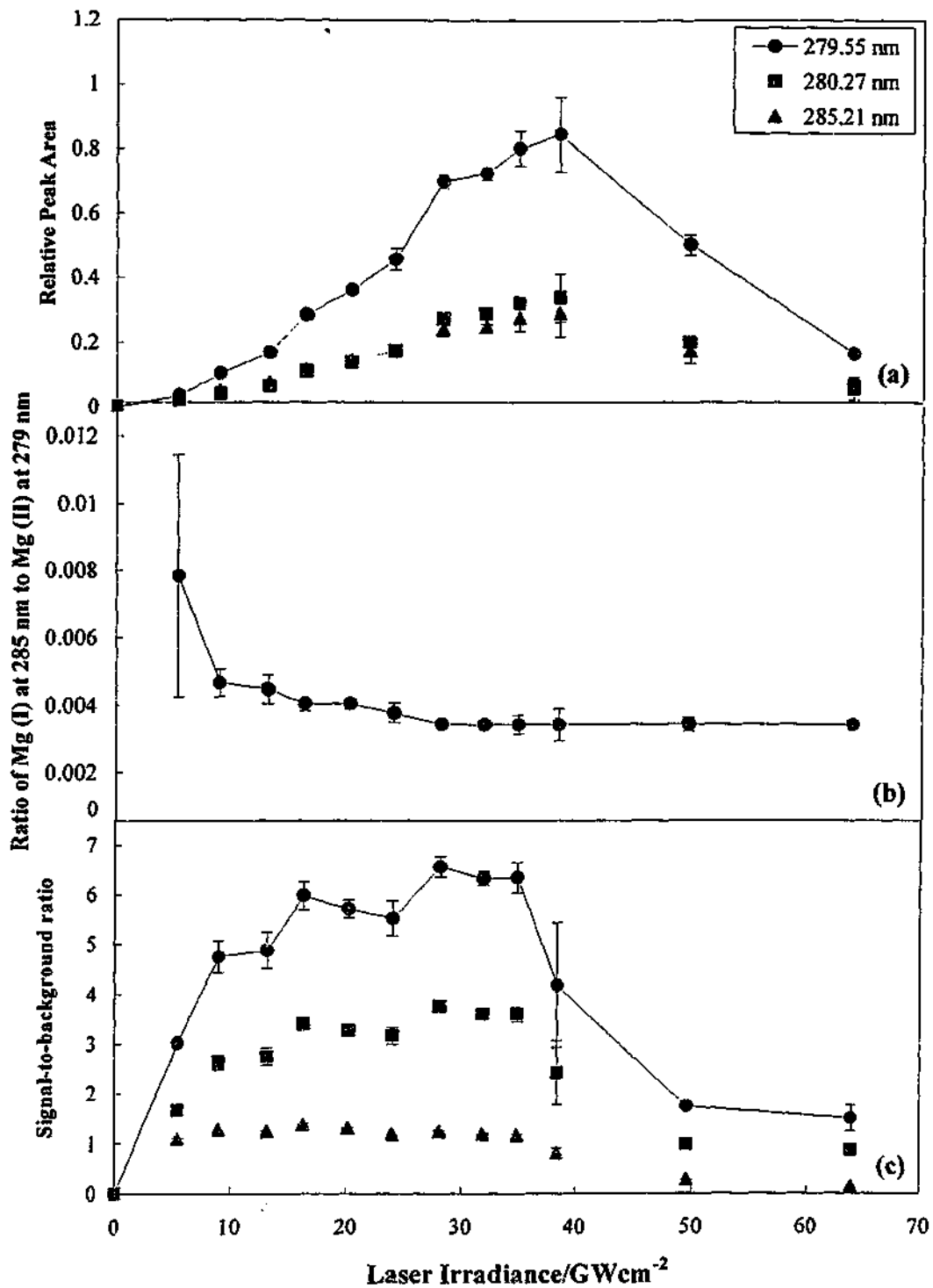


Figure 3.3. Variation of (a) peak area, (b) the ratio of Mg (I) at 285 nm to Mg (II) at 279 nm, and (c) signal-to-background ratio with laser irradiance for Mg in Latrobe Valley brown coal.

emission and 80 nm wide spectra were obtained using the 1200 lines/mm grating. The most intense emission lines from the six major inorganic elements in Latrobe Valley brown coals were used to monitor the effects of irradiance.

The effects of laser irradiance on Mg emission during LIBS analyses of a brown coal from the Loy Yang open cut (sample CRC/8-4-26/64) are shown in Figure 3.3. The standard chemical analysis results for this sample can be found in Appendix A. The variation of the peak areas of Mg (II) emission lines at 279.55 and 280.27 nm and Mg (I) lines at 285.21 nm as a function of laser irradiance are shown in Figure 3.3(a). This plot shows that peak areas increase with irradiance for each of these emission lines to  $\sim 38 \text{ GWcm}^{-2}$ . Above  $38 \text{ GWcm}^{-2}$  the peak areas decreased significantly with increasing irradiance. At these high irradiances it was observed that more sample was removed from the surface of the coal pellets with each laser pulse than at lower irradiances. This meant that there was often overlap between the surface area affected by successive laser pulses, which had an impact on focussing and detection conditions. This led to a significant decrease in the amount of elemental emission produced and detected during LIBS. The error bars in Figure 3.3 to 3.8 represent two standard deviations.

The ratio of the intensity of the atomic Mg emission line at 285.21 nm to the ionic emission line at 279.55 nm as a function of laser irradiance is shown in Figure 3.3(b). This plot shows that the ratio of these lines decreased slightly up until  $28 \text{ GWcm}^{-2}$ . At higher irradiances, the ratio of the intensities of the two Mg emission lines remained relatively constant. Other groups have observed similar trends in neutral-to-ion intensity ratios in laser-induced plasmas [87,89]. The decrease in the intensity ratio of the neutral-to-ionic Mg emission lines with increasing irradiance is caused by an increase in the number of singly charged ions in the laser-induced plasma. However, above approximately  $28 \text{ GWcm}^{-2}$  the ionisation of Mg atoms in the plasma becomes saturated. Hence, the ratio of neutral and ion emission intensities remains constant. Liu and co-workers found that ionisation saturation occurred above  $20 \text{ GWcm}^{-2}$  in their study of Si emission from crystalline silicon [87]. This is slightly lower than the irradiance at which ionisation saturation occurs for Mg in the Latrobe Valley coal. It is likely that this is due to differences in the bulk properties of the two sample types, such as the density, heat of vaporisation and thermal diffusivity [145].

The variation of signal-to-background ratio with laser irradiance for the three Mg emission lines is shown in Figure 3.3(c). The broadband background emission that is observed in LIBS spectra occurs as a result of bremsstrahlung processes, recombination, and Stark broadening and is dependent on variables such as time and laser irradiance [71]. Maximum signal-to-background occurred at approximately  $16.4 \text{ GWcm}^{-2}$  for the Mg (I) emission line at 285.21 nm and at  $28 \text{ GWcm}^{-2}$  for the Mg (II) lines at 279.55 and 280.27 nm. While signal-to-background was at a maximum for the atomic Mg line at  $16.4 \text{ GWcm}^{-2}$ , it varied little from this maximum between 9 and  $35 \text{ GWcm}^{-2}$ . Thus, any irradiance within this range could be used to provide good results for the analysis of Mg in Latrobe Valley brown coal. The irradiance that provides maximum signal-to-background for the two ionic emission lines of Mg is also the point at which ionisation saturation begins to occur, as shown in Figure 3.3(b). Thus, it is likely that maximum signal-to-background occurs at this irradiance because the number of ions in the plasma is at a maximum.

The effects of laser irradiance on the emission induced from Na during LIBS analyses of the brown coal from the Loy Yang open cut are illustrated in Figure 3.4. The variation of the background subtracted peak areas of the Na (I) emission lines (D lines) at 589.0 and 589.6 nm with laser irradiance are shown in Figure 3.4(a). The variation of the combined area of these two emission lines is also plotted in Figure 3.4(a) because they are not completely resolved from one another. Each of these peak areas increased with laser irradiance until approximately  $39 \text{ GWcm}^{-2}$ . At higher irradiances, weaker emission peaks and greater analytical uncertainties are obtained. As in the case of the Mg emission lines, the high laser irradiances remove more material from the surfaces of the sample pellets, which changes the focussing and detection conditions in the experiments.

The variation of the signal-to-background ratio of each of the Na D lines with laser irradiance is shown in Figure 3.4(b). The maximum signal-to-background for each of these lines was obtained using  $32 \text{ GWcm}^{-2}$ . However, signal-to-background values that were little different from this maximum were obtained for irradiances between 20 and  $35 \text{ GWcm}^{-2}$ . Hence any irradiance within this range could be used to analyse Na in Latrobe Valley brown coals.

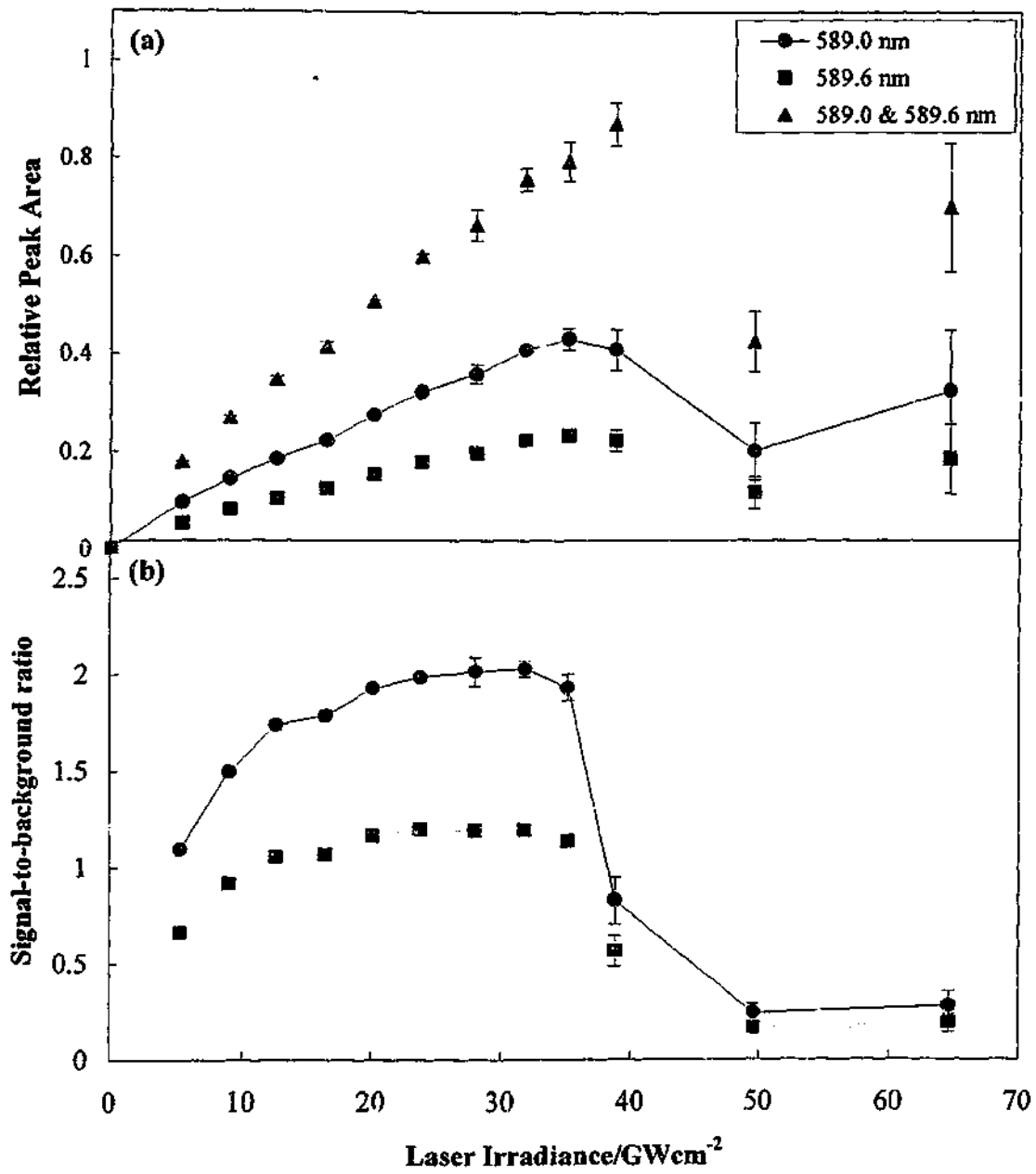


Figure 3.4. Variation of (a) peak area and (b) signal-to-background ratio with laser irradiance for Na emission in LIBS analyses of Latrobe Valley brown coal.

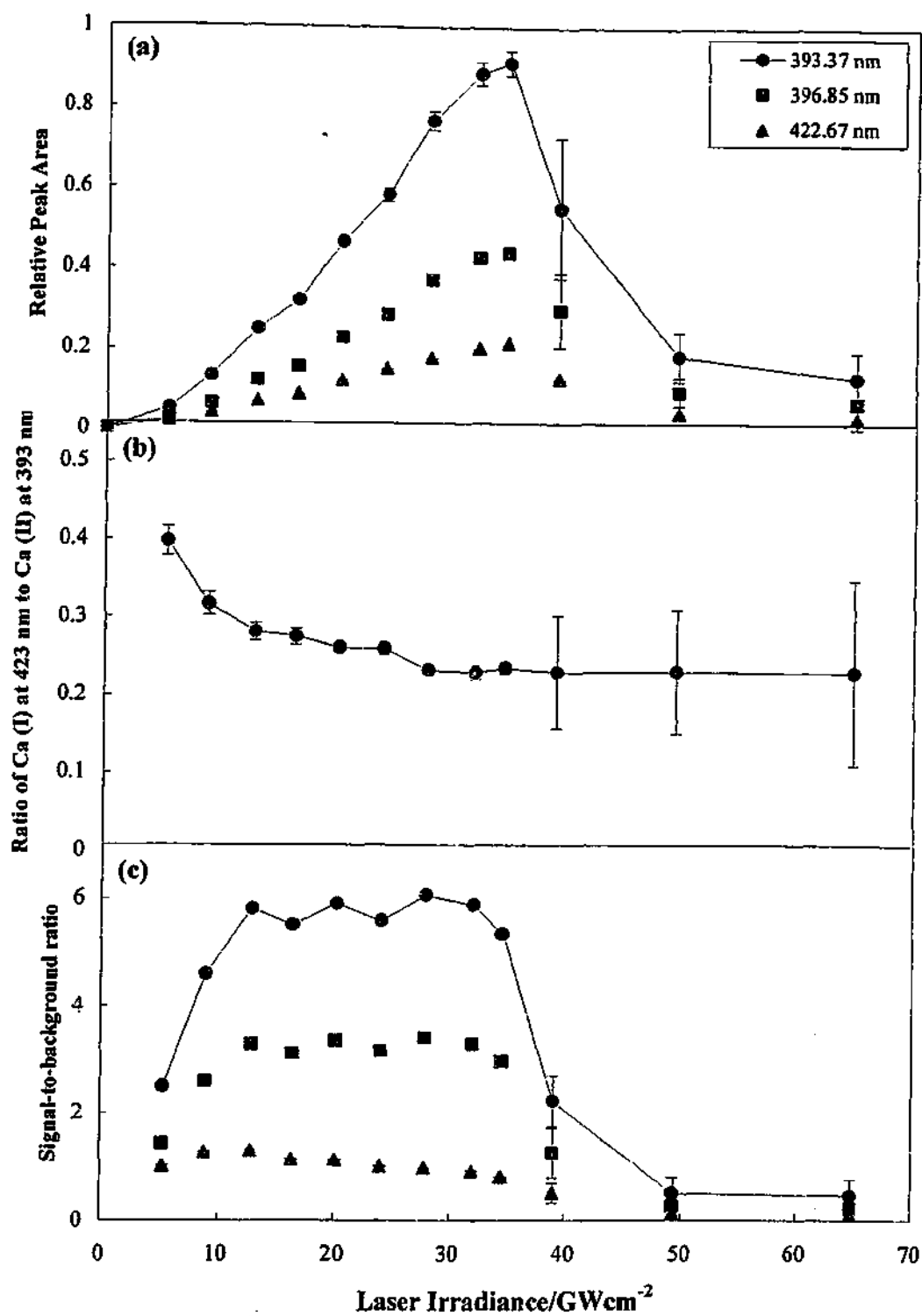


Figure 3.5. Variation of (a) peak area, (b) the ratio of Ca (I) at 423 nm to Ca (II) at 393 nm, and (c) signal-to-background ratio with laser irradiance for Ca in Latrobe Valley brown coal.

The effects of irradiance on the laser-induced emission from Ca in the Loy Yang coal are shown in Figure 3.5. Figure 3.5(a) shows that the peak areas of the Ca (II) emission lines at 393.37 and 396.85 nm and the Ca (I) emission line at 422.67 nm increased with laser irradiance until  $35 \text{ GWcm}^{-2}$ . As for the Mg and Na emission, the magnitude of the Ca emission decreased at higher irradiances because there was overlap between the sample volumes affected by successive laser pulses. This is also the cause of the large degree of uncertainty in these measurements, which is illustrated by the error bars.

The variation of the ratio of the intensities of the Ca (I) emission line at 422.67 nm to the Ca (II) emission line at 393.37 nm with laser irradiance is shown in Figure 3.5(b). This ratio decreased with irradiance until approximately  $28 \text{ GWcm}^{-2}$ . At higher irradiances the ratio remained relatively constant. This behaviour is consistent with that of the atomic-to-ionic line ratio obtained for Mg in the coal. Thus, the levelling off of the Ca line ratio may also be attributed to ionisation saturation.

The variation of the signal-to-background ratio for each of the three Ca emission lines with laser irradiance is shown in Figure 3.5(c). The maximum signal-to-background ratio for the Ca (I) line was obtained at  $13 \text{ GWcm}^{-2}$ , while the maxima for the two ionic Ca lines were obtained at  $28 \text{ GWcm}^{-2}$ . However, good signal-to-background was obtained for the Ca (I) emission line for all irradiances between 9 and  $20 \text{ GWcm}^{-2}$ , and for the Ca (II) lines between 13 and  $32 \text{ GWcm}^{-2}$ . Thus any irradiance within these ranges could be used to analyse Ca in Latrobe Valley brown coals.

The effects of the magnitude of the laser irradiance on Fe emission produced during LIBS analyses of Latrobe Valley brown coal are shown in Figure 3.6. The variation of the peak areas of the Fe (I) emission lines at 372.0 nm, 373.5 and 373.7 nm (combined), 374.6 and 375.0 nm (combined), and 375.8 nm and the Fe (II) emission line at 238.2 nm are shown in Figure 3.6(a). This plot shows that the peak areas of the Fe (I) emission lines increased with irradiances up to  $35 \text{ GWcm}^{-2}$ . The Fe(II) emission line increased with irradiances up to  $32 \text{ GWcm}^{-2}$ . At higher irradiances, the peak areas of the Fe lines decreased as a result of overlap between the sample areas interrogated by successive laser pulses.

The variation of the ratio of the Fe (I) lines at 373.5 and 373.7 nm to the Fe (II) line at 238.2 nm with laser irradiance is shown in Figure 3.6(b). The magnitude of this ratio

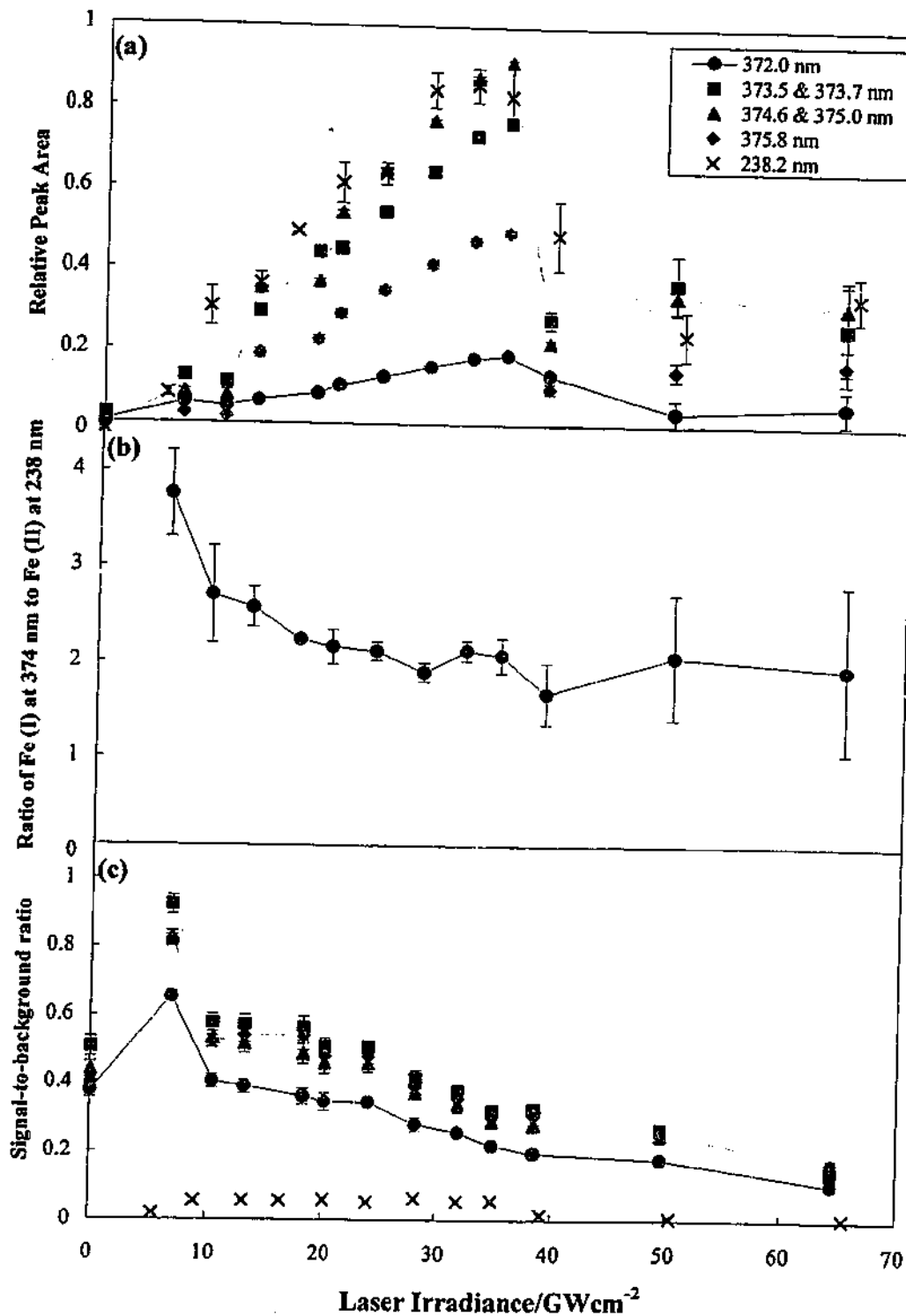


Figure 3.6. Variation of (a) peak area, (b) the ratio of Fe (I) at 373.5 & 373.7 nm to Fe (II) at 238.2 nm, and (c) signal-to-background ratio with laser irradiance for Fe in Latrobe Valley brown coal.

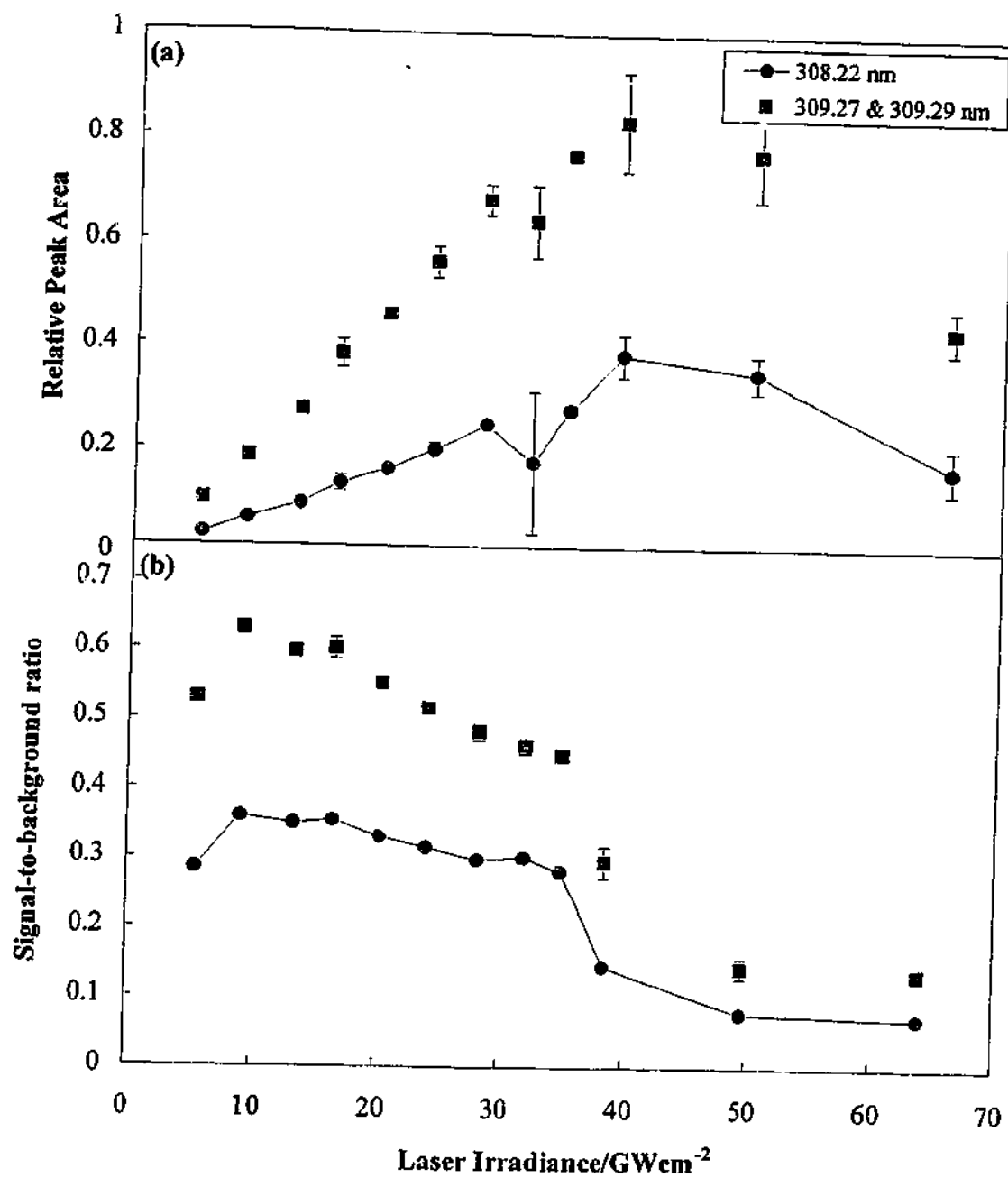


Figure 3.7. Variation of (a) peak area and (b) signal-to-background ratio with laser irradiance for A1 emission in LIBS analyses of Latrobe Valley brown coal.

decreased with irradiance until approximately  $28 \text{ GWcm}^{-2}$ . At irradiances above  $28 \text{ GWcm}^{-2}$ , the ratio remained relatively constant. This levelling off may be attributed to ionisation saturation, as for the neutral-to-ion ratios studied for the Mg and Ca emission from the brown coal.

The variation of the signal-to-background ratio with irradiance for the five Fe peaks is shown in Figure 3.6(c). Maximum signal-to-background for the Fe (I) lines occurred at  $6.8 \text{ GWcm}^{-2}$ , and at  $23 \text{ GWcm}^{-2}$  for the Fe (II) emission line. As was evident for the Mg (II) and Ca (II) emission lines, the maximum signal-to-background for the Fe (II) line was obtained at the irradiance at the onset of ionisation saturation. However, good signal-to-background is obtained for this emission line at any irradiance between 9 and  $35 \text{ GWcm}^{-2}$ . The signal-to-background ratios for the four Fe (I) peaks are significantly higher at  $6.8 \text{ GWcm}^{-2}$  than at any other irradiance studied. However, reasonable signal-to-background is obtained for irradiances up to  $24 \text{ GWcm}^{-2}$ .

The effects of the magnitude of the laser irradiance on Al emission from Latrobe Valley brown coal during LIBS are shown in Figure 3.7. Figure 3.7(a) shows the variation of the peak areas of the Al (I) emission lines at 308.22 nm, and 309.27 and 309.29 nm (combined) with laser irradiance. The area of each of these peaks increased with irradiance up to  $39 \text{ GWcm}^{-2}$ . At irradiances greater than this, decreases in peak areas were observed as a result of the increased crater volume.

The variation of the signal-to-background ratios of the two Al peaks with laser irradiance is shown in Figure 3.7(b). Maximum signal-to-background was obtained for each peak using  $9 \text{ GWcm}^{-2}$ . However, good signal-to-background ratios were also obtained when irradiances between 9 and  $20 \text{ GWcm}^{-2}$  were used.

The effects of laser irradiance on the Si (I) emission line at 288.16 nm during LIBS analyses of the Loy Yang coal sample are shown in Figure 3.8. In Figure 3.8(a) peak area is plotted as a function of laser irradiance. This plot shows that the peak area of the Si emission line increased with irradiance, up to  $35 \text{ GWcm}^{-2}$ . At irradiances greater than this, peak area decreased with increasing irradiance.

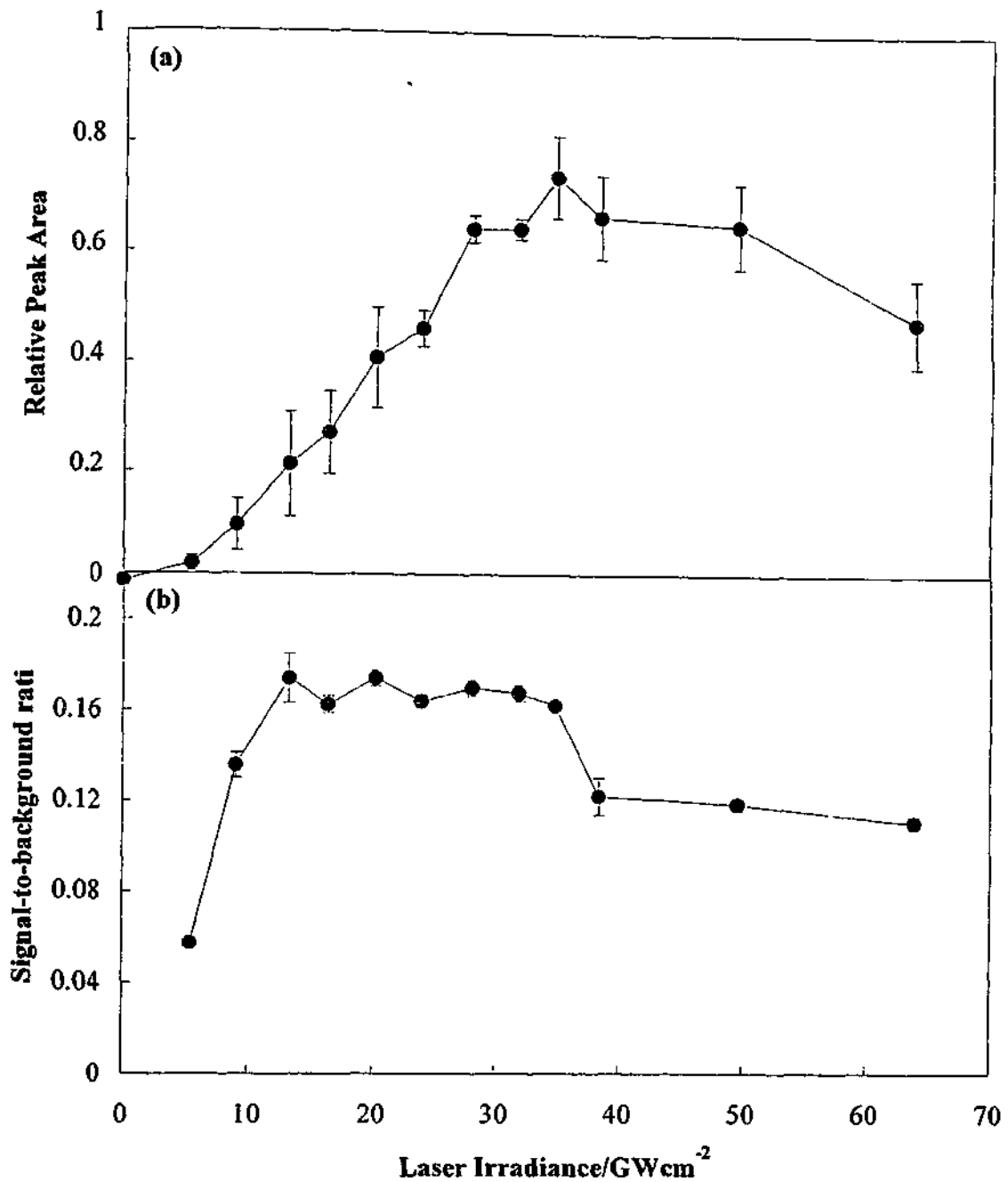


Figure 3.8. Variation of (a) the peak area and (b) the signal-to-background ratio of Si (I) at 288.16 nm with laser irradiance during LIBS analyses of Latrobe Valley brown coal.

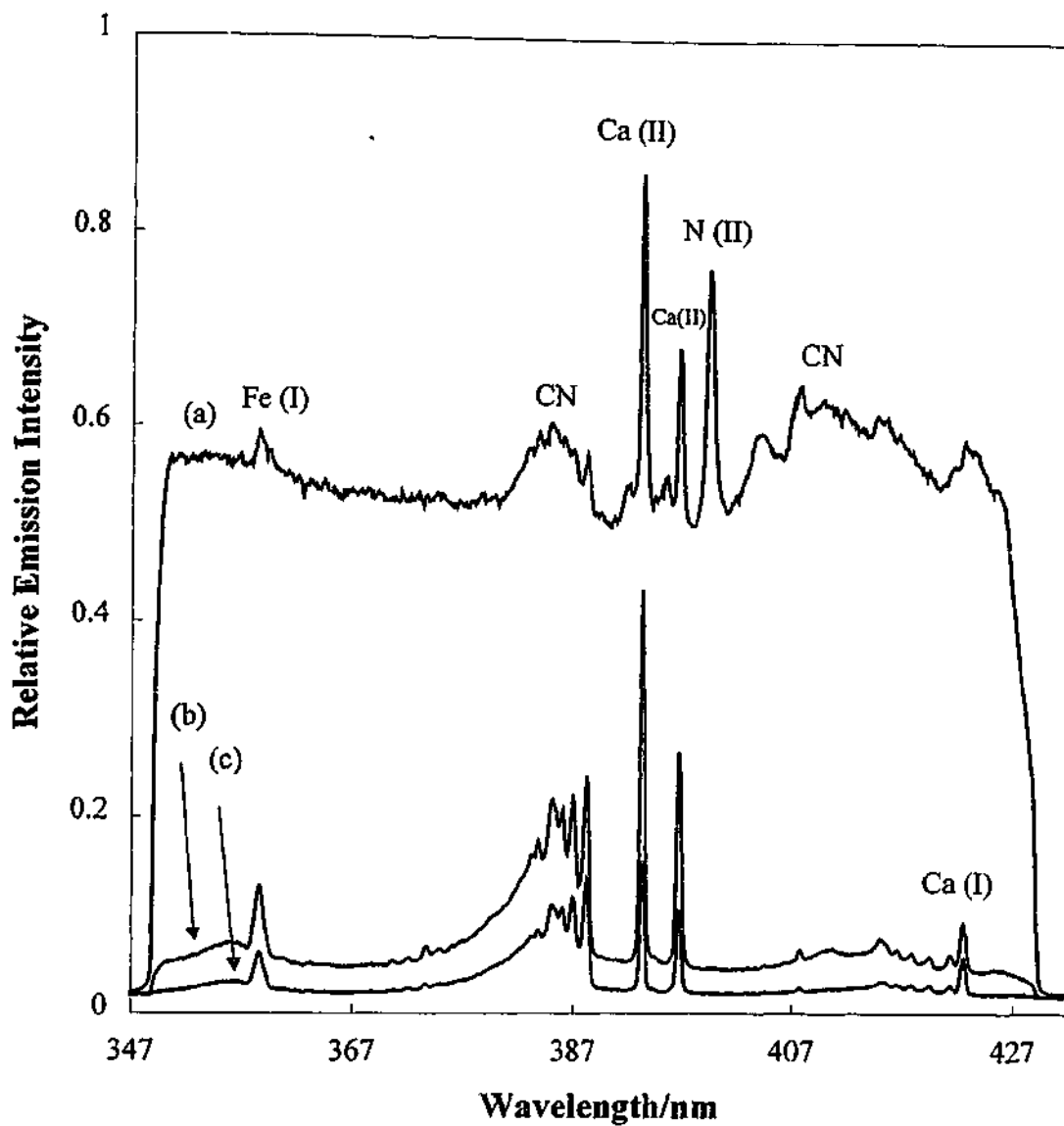


Figure 3.9. LIBS spectra obtained after time delays between the start of the laser spark and optical detection of (a) 0.5  $\mu\text{s}$ , (b) 1.0  $\mu\text{s}$ , and (c) 1.5  $\mu\text{s}$ , with a 5  $\mu\text{s}$  detection window in each case.

The effects of laser irradiance on the signal-to-background ratio of the Si emission line at 288.16 nm are shown in Figure 3.8(b). The maximum signal-to-background ratio for this emission line occurred at 20 GWcm<sup>-2</sup>. However, good signal-to-background was obtained for irradiances between 13 and 35 GWcm<sup>-2</sup>.

The average optimum laser irradiance for the emission lines of the six main inorganic elements in LIBS analyses of Latrobe Valley brown coal was 20 GWcm<sup>-2</sup>. This irradiance produced relatively intense emission and good signal-to-background ratios for all the lines and elements studied. Hence, this value of irradiance will be used in this study to induce elemental emission from Latrobe Valley brown coal during LIBS analyses.

### 3.4 *The Effects of Time-Gating on Laser-Induced Spectra*

The effects of time-gating the detection of the laser-induced plasma were studied using the laboratory-based experimental setup shown in Figure 3.1. Time-gated optical detection is critical in optimising signal response in LIBS experiments [9-13]. A pulse generator was used to externally control the gating of the ICCD with respect to the laser pulse. Time delays of 0 to 5 μs between the start of the laser spark and detection were investigated to optimise the delay, with the integration time of the detector remaining constant at 5 μs. The optimum laser irradiance of 20 GWcm<sup>-2</sup> was used to induce emission from the constituents of Latrobe Valley brown coal. A system gain of 5.9 ADC counts/photoelectron was used to intensify the plasma emission and a 40 nm wide spectral region was covered using the 2400 lines/mm spectrograph grating. Ionisation temperatures were also calculated at various intervals throughout the duration of the plasma by comparing the intensities of emission lines from neutral and ionised forms of the same element (using a smaller 250 ns gate width).

Figure 3.9 illustrates the effect of varying the time delay between the start of the laser spark and detection on a LIBS spectrum of coal in the 347 to 432 nm region. It can be seen in Figure 3.9(a) that at very short delay times the spectrum contains a high proportion of broadband background emission. A singly ionised N emission line is also present above the continuum at 399.5 nm. However, as the time delay is increased in Figure 3.9(b), this background emission decays, the N (II) emission line is no longer observed, and the

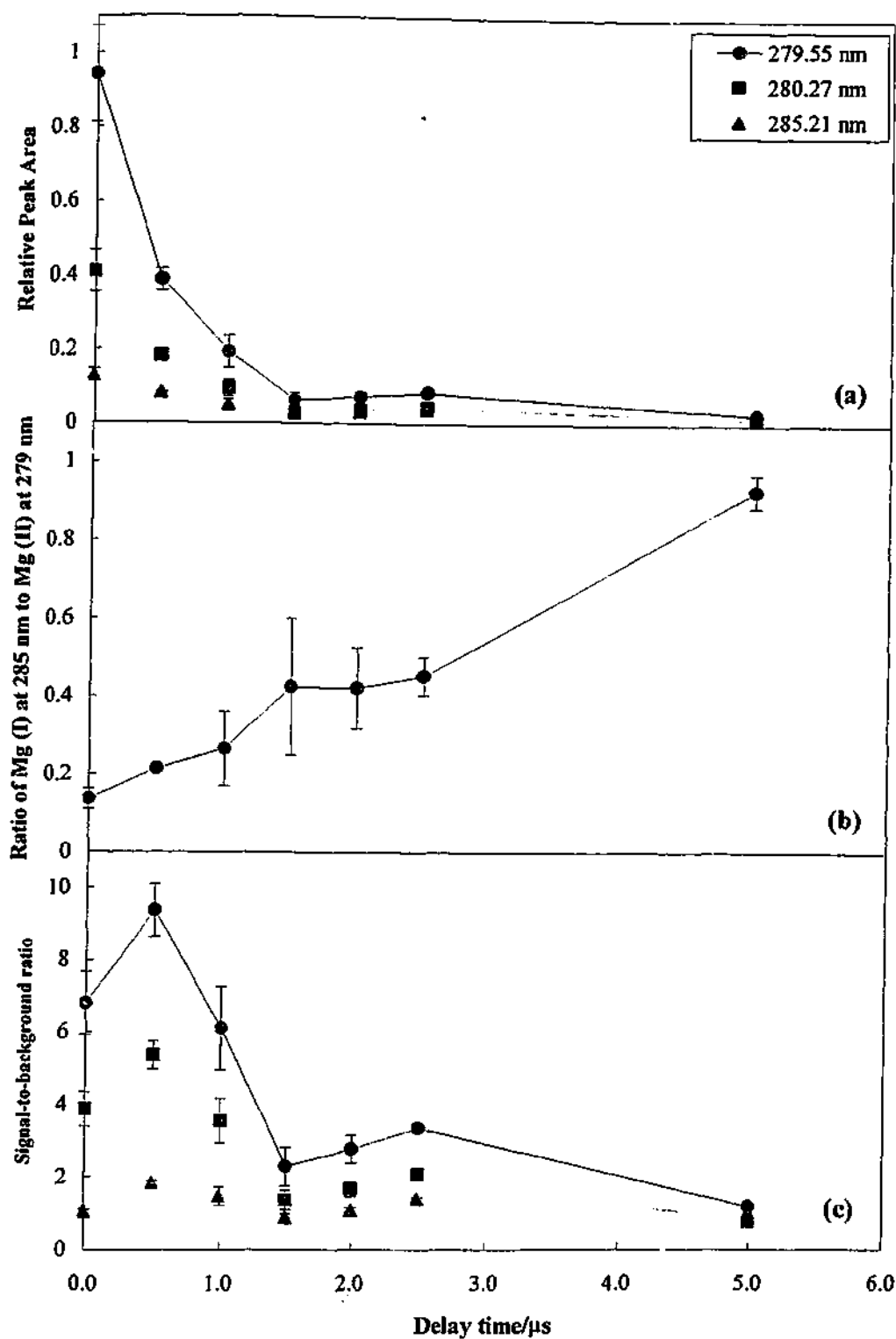


Figure 3.10. Variation of (a) peak area, (b) the ratio of Mg (I) at 285 nm to Mg (II) at 279 nm and (c) the signal-to-background ratio for LIBS analysis of Mg in Latrobe Valley brown coals.

elemental lines of Fe and Ca become the dominant spectral features. As the time delay is further increased in Figure 3.9 (c) and the plasma temperature decreases, the ion-to-neutral species peak ratio decreases. The  $\Delta v = 0$  and  $\Delta v = -1$  sequence bands of the  $B(^2\Sigma) \rightarrow X(^2\Sigma)$  electronic transition of CN also feature in this spectrum at approximately 387 and 420 nm respectively, and their relative intensity with respect to the elemental emission lines increases with the delay after laser excitation.

The effects of the time delay between the start of the laser spark and detection on individual emission lines from the major inorganic elements in Latrobe Valley brown coal were also studied. The most intense emission lines of each of the main inorganic elements were used for this purpose. The results for the Mg emission lines are shown in Figure 3.10. Figure 3.10(a) shows that the emission intensity of the Mg (II) lines at 279.55 and 280.27 nm and the Mg (I) line at 285.21 nm all decreased exponentially with increasing time delay. However, Figure 3.10(b) shows that the ratio of the Mg (II) line at 279.55 nm to the Mg (I) line at 285.21 nm increases linearly with time delay. This indicates that the ionic emission decayed more rapidly than neutral emission. This is to be expected; ionic emission requires more energy than neutral emission and so will decay more rapidly as the laser-induced plasma loses energy to the surrounding environment.

The variation of the signal-to-background ratio of the three Mg emission lines with time delay is shown in Figure 3.10(c). As mentioned earlier, time resolution of the laser-induced plasma can be used to advantage [10]. Figure 3.10(c) shows that a time delay between 0 and 0.5  $\mu\text{s}$  produced the maximum signal-to-background ratio for the ionic Mg emission lines. However, the optimum delay for the neutral emission line was slightly longer, occurring between 0.5 and 1.0  $\mu\text{s}$ . Again, this is the expected behaviour because both the ionic and background emission decay more rapidly than the neutral emission lines in laser-induced plasmas, as shown in Figure 3.9 and in work by other groups [10,74].

The effects of the time delay between the start of the laser spark and optical detection for Na in Latrobe Valley brown coals are shown in Figure 3.11. Figure 3.11(a) shows that the intensities of the Na D lines, like the Mg emission lines, decreased with increasing delay time. The combined peak area of the two lines is plotted as well as their individual areas

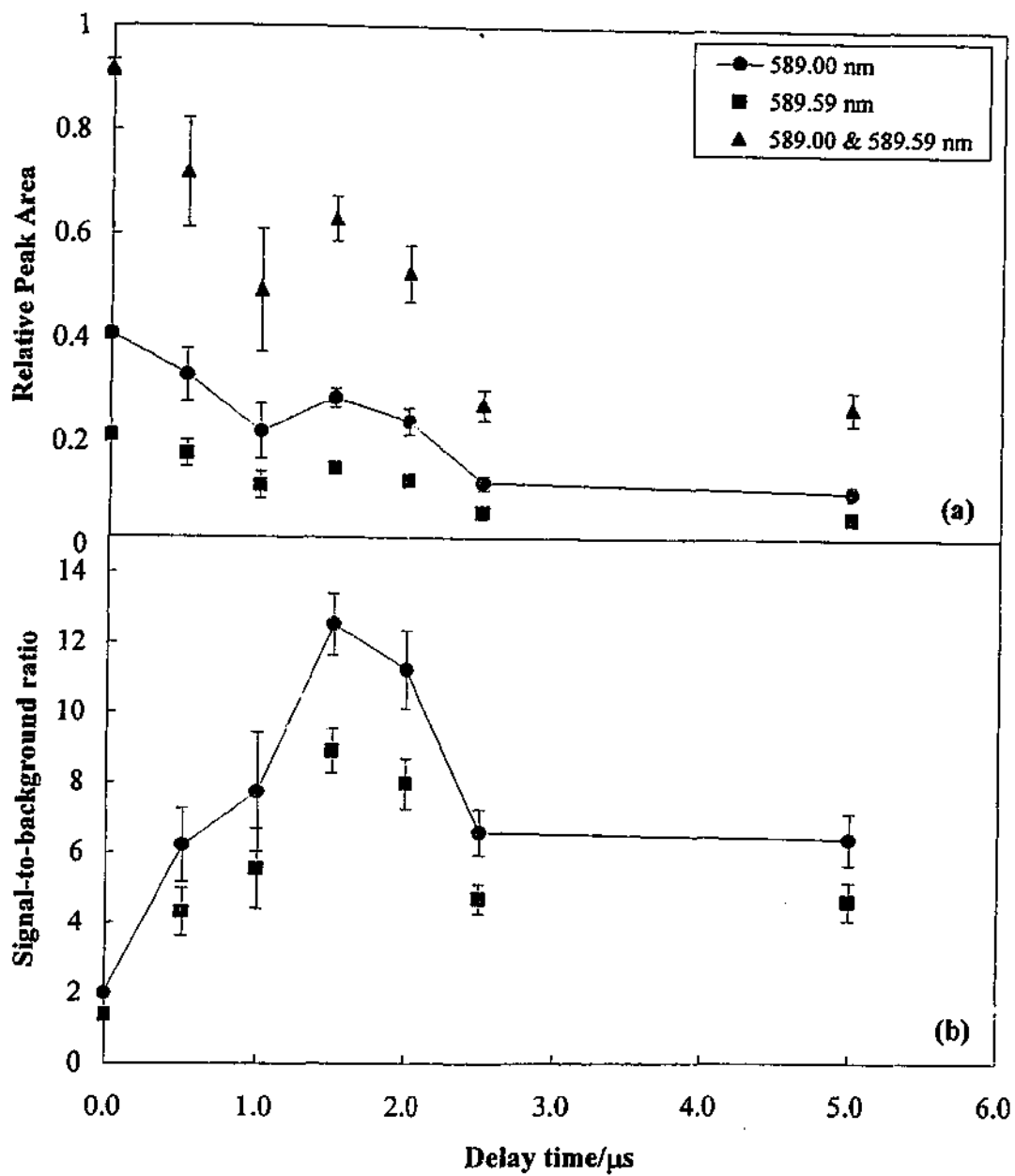


Figure 3.11. Variation of (a) peak area and (b) signal-to-background ratio with time delay for Na in Latrobe Valley brown coals.

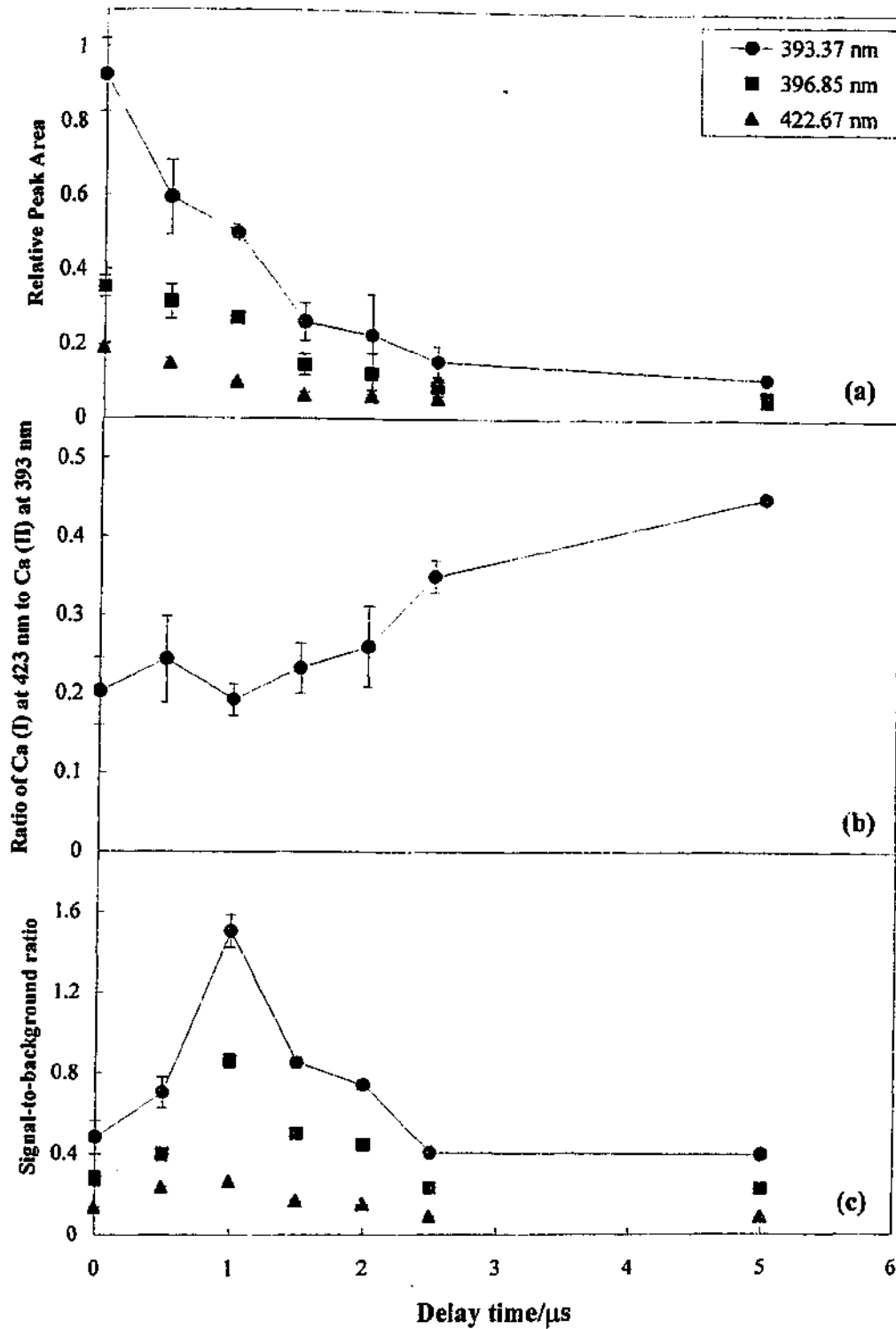


Figure 3.12. Variation of (a) peak area, (b) the ratio of Ca (I) at 423 nm to Ca (II) at 393 nm and (c) the signal-to-background ratio for LIBS analysis of Ca in Latrobe Valley brown coals.

because, as mentioned earlier, the two lines are not completely resolved using this apparatus. The variation of the signal-to-background ratio for each of the two lines is plotted in Figure 3.11(b). This plot shows that optimum time delay for the Na emission lines was approximately 1.5  $\mu\text{s}$ , which is slightly longer than the optimum delay for the neutral Mg emission.

The effects of the time delay on the measurement of Ca emission from Latrobe Valley brown coals are shown in Figure 3.12. Figure 3.12(a) shows that the intensities of the Ca (II) emission lines at 393.37 and 396.85 nm and the Ca (I) emission line at 422.67 nm decreased exponentially with delay time. Figure 3.12(b) shows that the ratio of the neutral emission line at 422.67 nm to the ionic line at 393.37 nm increases with time delay, which is consistent with the data obtained for Mg. Again, this is because more energy is required to produce ionic than neutral emission and, as the plasma cools over time, the number of ions will decrease as it loses energy to its surrounds. Figure 3.12(c) shows that the maximum signal-to-background ratio occurred at 1.0  $\mu\text{s}$  for all three Ca emission lines studied, which lies between the optimum delay times for Mg and Na.

The effects of the time delay between the laser spark and optical detection on the laser-induced emission of Fe in Latrobe Valley brown coals are shown in Figure 3.13. The variation of the peak areas of Fe (I) emission lines at 372.0, 373.5 and 373.7 nm (combined), 374.6 and 375.0 nm (combined), and 375.8 nm and the Fe (II) emission line at 238.2 nm with delay time are shown in Figure 3.13(a). This plot shows that the peak areas of all the Fe emission lines decreased with time delay. Figure 3.13(b) shows that the ratio of the combined peak area of the Fe (I) lines at 373.5 and 373.7 nm to the peak area of the Fe (II) line at 238.2 nm increased with time delay. Again, this is consistent with the results obtained for both Mg and Ca. Figure 3.13(c) shows that the optimum time delay was 2.5  $\mu\text{s}$  for all the neutral emission lines except for the combined peak corresponding to the emission lines at 374.6 and 375.0 nm. The maximum signal-to-background ratio for this peak was obtained when no delay is used. The optimum time delay for the ionic emission line at 238.2 nm was between 0 and 0.5  $\mu\text{s}$ . This is similar to the result obtained for the ionic Mg emission lines.

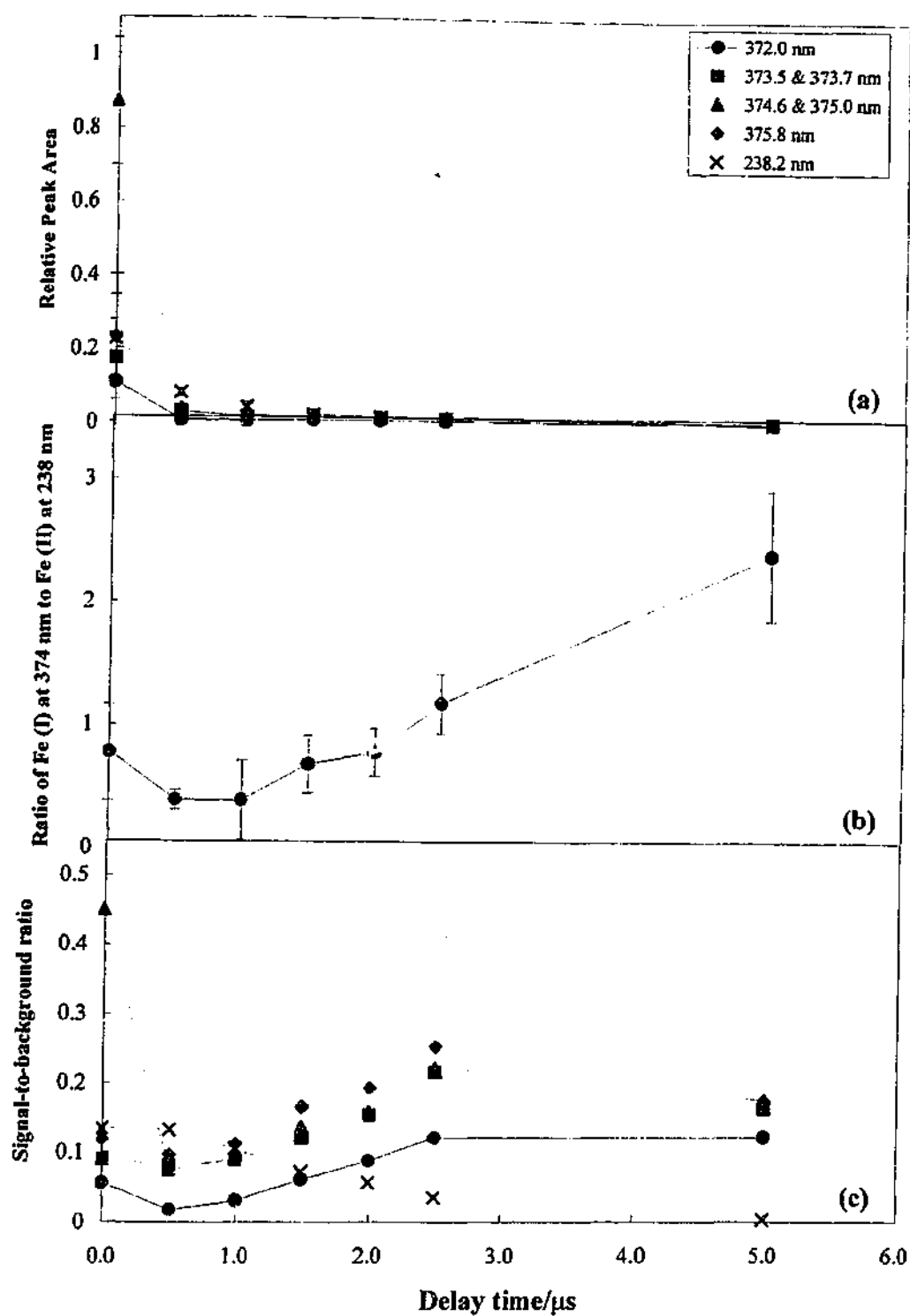


Figure 3.13. Variation of (a) peak area, (b) the ratio of Fe (I) at 373.5 & 373.7 nm to Fe (II) at 238 nm and (c) the signal-to-background ratio for LIBS analysis of Fe in Latrobe Valley brown coals.

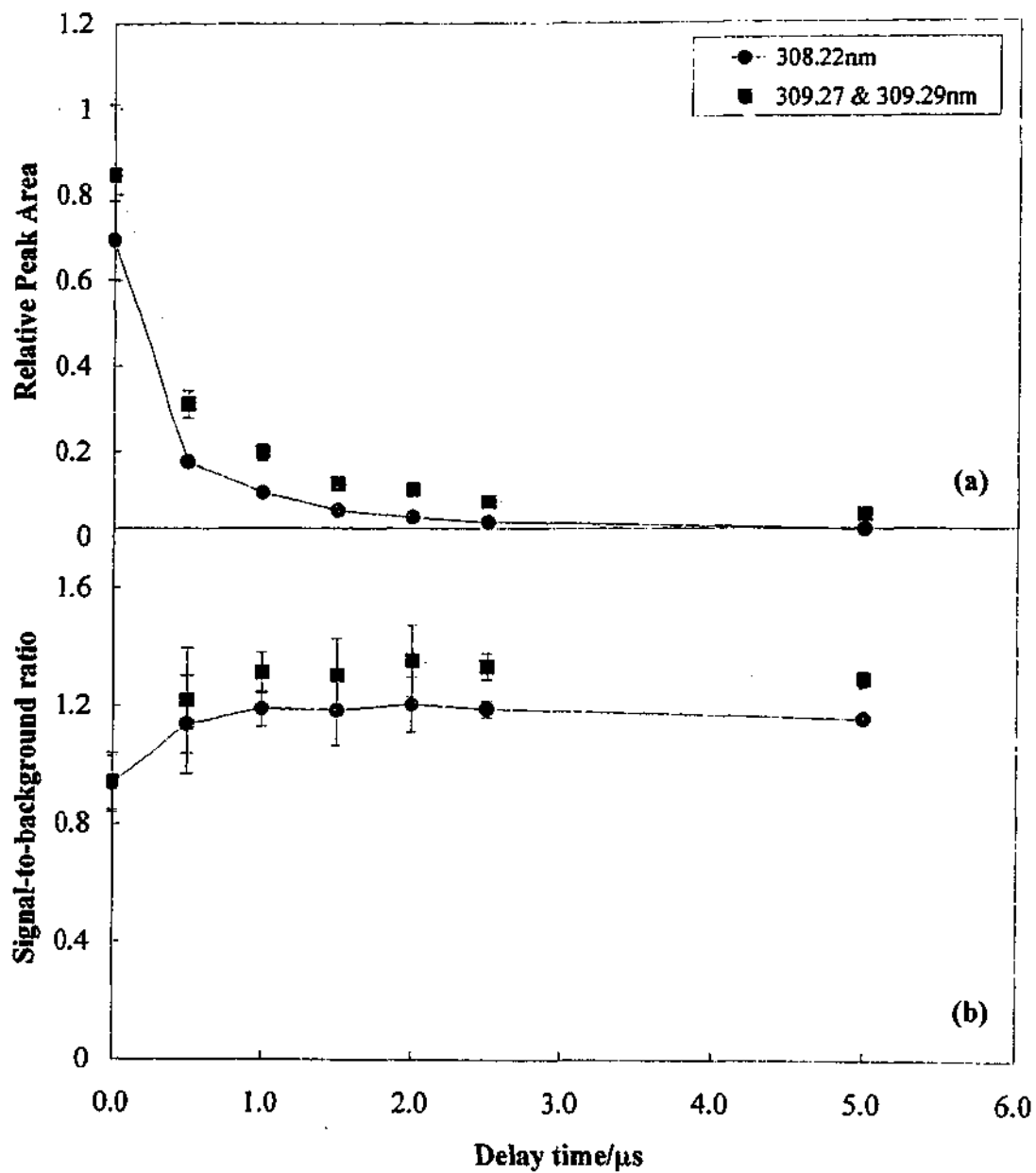


Figure 3.14. Variation of (a) peak area and (b) signal-to-background ratio with time delay for Al in Latrobe Valley brown coals.

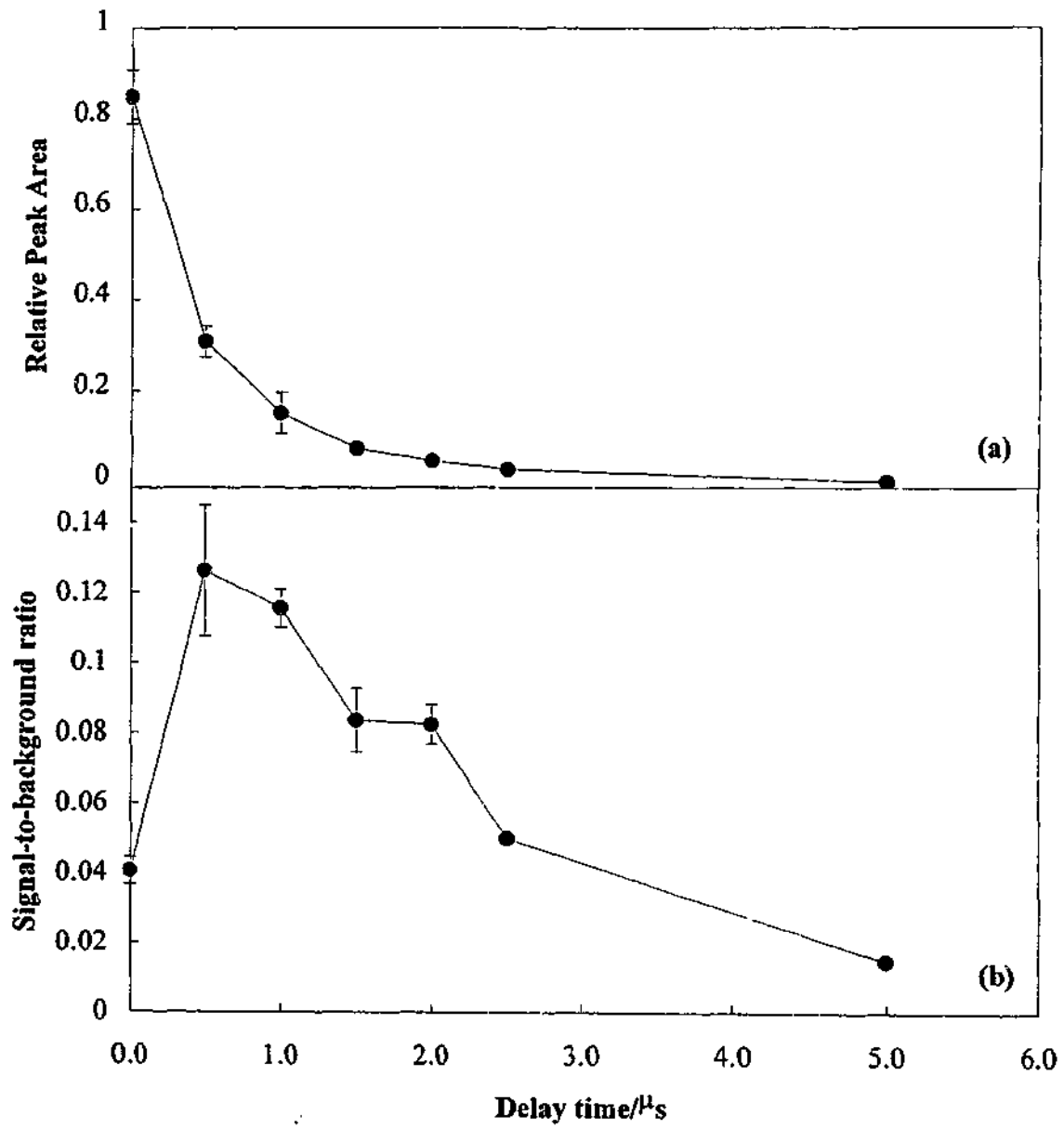


Figure 3.15. Variation of (a) peak area and (b) signal-to-background ratio with time delay for the Si emission line at 288.16 nm.

Figure 3.14 illustrates the effects of delay time on Al emission induced during LIBS analyses of Latrobe Valley brown coal. The intensities of the peak area of the Al (I) emission line at 308.22 nm and the combined area of the Al (I) emission lines at 309.27 and 309.29 nm are shown to decay exponentially with delay time in Figure 3.14(a). Figure 3.14(b) shows that the signal-to-background ratio of each of these lines reached a maximum and remained fairly constant between 1.0 and 2.5  $\mu\text{s}$ . Thus, the optimum delay time between the start of the laser spark and optical detection for Al in Latrobe Valley coals was 1.0  $\mu\text{s}$  because the emission intensity was stronger than when using longer delays.

The effects of the time delay on laser-induced Si emission from Latrobe Valley brown coals are shown in Figure 3.15. As for the other main inorganic elements in Latrobe Valley brown coals, Figure 3.15(a) shows that the peak area of the Si emission line at 288.16 nm decreased exponentially with increasing delay. Figure 3.15(b) shows how the signal-to-background ratio of the 288.16 nm emission line varied with time delay. The maximum signal-to-background ratio and, hence, optimum time delay was reached at approximately 0.5 to 1.0  $\mu\text{s}$ .

The variations observed here in the optimum time delays for different elements, ionisation states and even emission lines of the same element and ionic state is consistent with the results obtained by Castle *et al.* [83]. They observed similar behaviour in their study of ionic and atomic Pb lines in pressed pellets of lead flakes and NIST soil samples. Differences in the optimum delay times for observation of ionic and neutral emission lines of each element are expected because the ionic lines, which require more energy, will decay more rapidly than the neutral lines as the plasma cools. Differences in the optimum delay times of each element are a result of the different chemical properties of these elements.

In the current study, the optimum delay is that which provides good signal-to-background ratios and relatively intense emission for the six major inorganic elements in Latrobe Valley brown coals. The optimum delay times for these elements ranged from 0 to 2.5  $\mu\text{s}$ . However, the average optimum delay time for the emission lines of these elements is approximately 1  $\mu\text{s}$ . Figure 3.9 showed that most of the broadband emission produced by

the plasma decays within the initial microsecond. However, the elemental lines, which are generally more persistent than the broadband emission, can still be detected at longer delays. Therefore a delay time of 1  $\mu\text{s}$  was chosen for use in this study because it results in good signal-to-background and emission intensity for all the inorganic elements studied. A detector integration time of 5  $\mu\text{s}$  is used because it allows for efficient collection of all elemental emission while further ensuring that interference from ambient light is minimised.

Ionisation temperatures for the plasmas produced during LIBS were calculated at several intervals during the plasma lifetimes. To do this, the full width at half-maximum (FWHM) of the Stark broadened hydrogen beta line at 486 nm (see Table 4.1 for transition properties) was measured because it is related to the electron density ( $N_e$ ) of the plasma via:

$$N_e = C(N_e, T) \Delta\lambda_s^{3/2} \quad (3.1)$$

where  $C(N_e, T)$  is a coefficient that is a weak function of  $N_e$  in units of  $\text{\AA}^{-3/2}\text{cm}^{-3}$  and is found in Griem [76], and  $\Delta\lambda_s$  (in  $\text{\AA}$ ) is the full width at half-maximum of the Stark broadened  $H_\beta$  line. The FWHM of the  $H_\beta$  line was measured by fitting the line profiles using a Lorentzian function, which can be used to approximate the shape of Stark broadened emission lines [146]. The experimental data and fitted Lorentzian profiles obtained using delay times of 0.5, 1.0 and 1.5  $\mu\text{s}$  are shown in Figure 3.16. The contributions of Doppler broadening were not considered in these measurements because they are negligible compared to Stark broadening at the electron densities and temperatures that are calculated below. Resonance broadening was also not considered because the  $H_\beta$  line is not a resonance line.

The electron density, along with the intensities of emission lines from neutral and ionised forms of the same element, is required to calculate the degree of ionisation of this atom using the Saha equation [76]. The  $H_\beta$  line is used to calculate the electron density because atomic hydrogen is subject to a large linear Stark effect. This means that the relative accuracy of the measurement of the FWHM is greater than for narrower lines. The

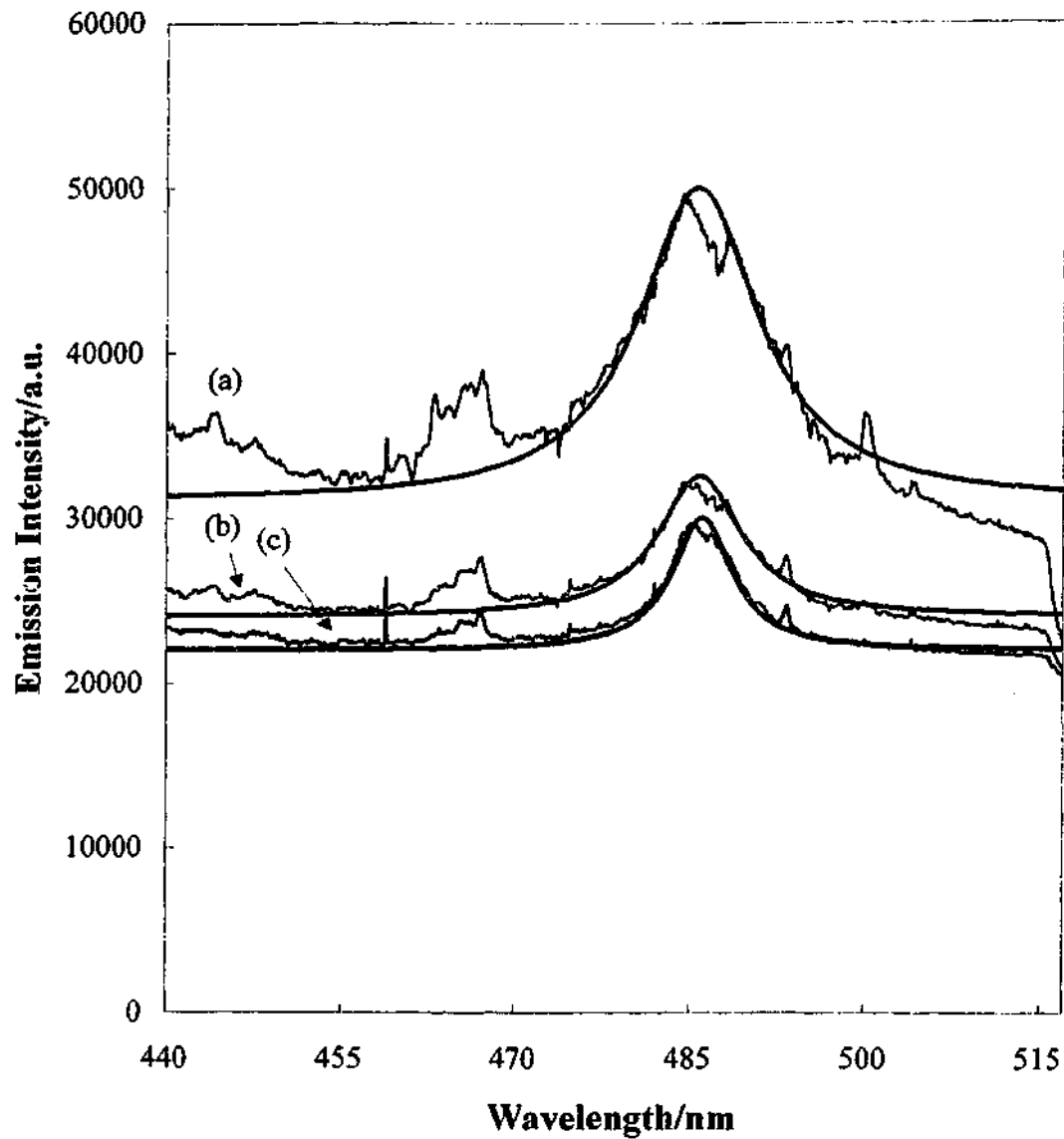


Figure 3.16. The  $H_{\beta}$  emission lines obtained at delay times of (a)  $0.5 \mu\text{s}$ , (b)  $1.0 \mu\text{s}$ , and (c)  $1.5 \mu\text{s}$  after the start of the laser spark. The thin lines represent the experimental data and the thick lines the Lorentzian fits.

accuracy of electron density calculations from the  $H_{\beta}$  line has also been reported to be greater than for the other H lines [76].

The form of the Saha equation used in this work is:

$$\frac{N_e N_m^z}{N_n^{z-1}} = \frac{2g_m^z}{g_n^{z-1}} \left( \frac{mkT}{2\pi\hbar^2} \right)^{3/2} \exp\left( \frac{-\Delta E}{kT} \right) \quad (3.2)$$

where  $N_m^z$  is the number density of species in the upper energy level of the transition of the ionised element selected for analysis;  $N_n^{z-1}$  is the number density of species in the upper energy level of the chosen transition of the neutral element;  $g_m^z$  is the statistical weight of the upper energy level of the ion transition;  $g_n^{z-1}$  is the statistical weight of the upper level of the neutral transition;  $m$  is the mass of an electron;  $k$  is the Boltzmann constant;  $T$  is the ionisation temperature;  $\hbar$  is Planck's constant divided by  $2\pi$ ; and  $\Delta E$  is the difference between the upper energy levels of the two transitions [76].

It was not possible to measure the  $H_{\beta}$  line and the lines from the other elements selected for analysis in a single spectrum with sufficient resolution. Hence the average of the FWHM measurements of the  $H_{\beta}$  line at each time interval, under the experimental conditions described earlier, were used in the temperature calculations. For these temperature measurements, detector integration times of 250 ns were used. Ca (I) and Ca (II) were chosen to calculate the ionisation temperatures of the plasmas produced during LIBS because they had strong emission lines able to be imaged in 40 nm wide spectra of Latrobe Valley brown coal. The Ca (I) emission line at 422.67 nm and Ca (II) emission line at 393.37 nm were used for this purpose. Local thermodynamic equilibrium (LTE) must hold in order to describe the temperature of the plasma using the Saha equation. LTE exists when collisional and energy transfer processes in the plasma are rapid. These conditions usually exist in plasmas with high electron densities and which have been induced by Q-switched lasers, such as those produced in this work [60]. The measured FWHM of the  $H_{\beta}$  line, intensity ratios of Ca (II) to Ca (I), electron densities, and ionisation temperatures calculated at delay times of 0.5, 1.0 and 1.5  $\mu$ s are given in Table 3.3.

Table 3.3. Calculated Plasma Properties.

| Time Delay<br>( $\mu\text{s}$ ) | FWHM of $H_{\beta}$<br>(nm) | Ca (II)/Ca (I) | Electron Density<br>( $\text{cm}^{-3}$ ) | Ionisation<br>Temperature<br>(K) |
|---------------------------------|-----------------------------|----------------|--|----------------------------------|
| 0.5                             | $12.0 \pm 0.2$              | $4.1 \pm 0.9$  | $(3.8 \pm 0.1) \times 10^{17}$           | $14\,900 \pm 800$                |
| 1.0                             | $8.7 \pm 0.2$               | $5.2 \pm 0.5$  | $(2.43 \pm 0.07) \times 10^{17}$         | $14\,600 \pm 600$                |
| 1.5                             | $6.3 \pm 0.2$               | $4.3 \pm 0.6$  | $(1.48 \pm 0.07) \times 10^{17}$         | $13\,500 \pm 600$                |

The ionisation temperatures measured at a 1.0  $\mu\text{s}$  delay in this work are higher than those obtained by Zhang and coworkers [33] at the same delay and at a higher irradiance in their laser-induced breakdown studies of coal particles. However, the results in this study of Latrobe Valley brown coal are similar to those obtained during the laser-induced breakdown of graphite performed by Chen and Mazumder [97]. A laser irradiance of 0.7  $\text{GWcm}^{-2}$ , which is significantly lower than the irradiance used in this work, was used to produce the plasma in the graphite work. However, it is possible that the high water content of the Latrobe Valley coal lowered the temperatures in the laser-induced plasmas produced from these samples. This possibility will be investigated in Chapter 6.

### 3.5 Summary

The experimental apparatus and methodology used in the analysis of Latrobe Valley brown coal by laser-induced breakdown spectroscopy have been described in this chapter. Two experimental setups were described; a sensitive laboratory-based system which incorporated an ICCD, as well as a lower-cost portable system. The optimum experimental conditions for the analysis of the six main inorganic elements in the brown coal using the ICCD system are summarised here.

The effects of the magnitude of the laser irradiance used during LIBS on atomic and ionic emission from the six main inorganic elements in Latrobe Valley brown coals were investigated. The peak areas, atomic-to-ionic peak ratios, and signal-to-background ratios were measured over a range of irradiances for the major observable emission lines from each of the main inorganic elements within the coal. The optimum laser irradiance was

found to vary between elements and also to depend on their ionisation states. The average optimum laser irradiance for all the inorganic elements was found to be  $20 \text{ GWcm}^{-2}$ . This irradiance produced good signal-to-background ratios and emission intensities for all the peaks studied.

Table 3.4. Optimum delay times and laser irradiances for the elemental emission lines.

| <i>Element</i> | <i>Emission Line (nm)</i> | <i>Optimum Delay Time (<math>\mu\text{s}</math>)</i> | <i>Optimum Irradiance (<math>\text{GWcm}^{-2}</math>)</i> |
|----------------|---------------------------|--|---|
| Mg (II)        | 279.55                    | 0.5  | 28.0  |
|                | 280.27                    | 0.5  | 28.0  |
| Mg (I)         | 285.21                    | 0.5  | 16.4  |
| Na (I)         | 589.00                    | 1.5  | 32  |
|                | 589.59                    | 1.5  | 32  |
| Ca (II)        | 393.37                    | 1.0  | 28.0  |
|                | 396.85                    | 1.0  | 28.0  |
| Ca (I)         | 422.67                    | 1.0  | 13.0  |
| Fe (II)        | 238.20                    | 0.5  | 28.0  |
| Fe (I)         | 371.99                    | 2.5  | 6.8   |
|                | 373.49 & 373.71           | 2.5  | 6.8   |
|                | 374.56 & 374.95           | 0  | 6.8   |
|                | 375.82                    | 2.5  | 6.8   |
| Al (I)         | 308.22                    | 1.0  | 9.0   |
|                | 309.27 & 309.29 nm        | 1.0  | 9.0   |
| Si (I)         | 288.16 nm                 | 0.5  | 20.0  |

The effects of time-gating optical detection in LIBS analyses of Latrobe Valley brown coal were also detailed in this chapter. Peak areas, atomic-to-ionic peak ratios, and signal-to-background ratios of the six main inorganic elements were measured at a range of delays between the start of the laser spark and detection. The optimum time delay, which varied between elements, ionisation states and emission lines of the same element and ionic state, ranged between 0 and  $2.5 \mu\text{s}$ . The average optimum delay time for these elemental

emission lines was found to be approximately 1  $\mu$ s. This delay ensured good signal-to-background and emission intensity for all the elements studied. The optimum delay times and laser irradiances for each of the emission lines studied are summarised in Table 3.4.

The electron densities and ionisation temperatures of the laser-induced plasmas at delay times of 0.5, 1.0, and 1.5 ms after the start of the laser spark were also measured and have been presented in Table 3.3. As expected, both temperature and electron density decreased with time delay.

---

## *Analysis of the Inorganic Content of Latrobe Valley Coal Using Laser-Induced Breakdown Spectroscopy*

### *4.1 Introduction*

The efficiency of coal power generation can be adversely affected by variations in the chemical composition of the fuel. Specifically, variation in the concentrations of the inorganic ash-forming components may result in reduced thermal efficiency and operation time of the power station boilers. Thus, determining the inorganic content of the coal, prior to its utilisation, would allow the implementation of strategies to minimise such problems.

The major inorganic elements found in Latrobe Valley brown coals are Na, Mg, Ca, Fe, Al, and Si. These elements occur within the coal as soluble salts, discrete minerals, or exchangeable cations associated with the carboxyl groups that form part of the organic coal matter. As mentioned in previous chapters, there is currently no commercially available portable instrument capable of performing complete chemical analyses of low-ash brown coal with sufficient accuracy for reliable use. There is a requirement for such a system to provide reliable detection of low concentrations of the inorganic species present in Latrobe Valley coals. The system currently used for on-line coal analyses in Australia is CSIRO's prompt gamma neutron activation analysis instrument COALSCAN [4]. However, this instrument lacks the sensitivity required for the reliable detection of the low levels of inorganics present in Latrobe Valley coals. On-line x-ray fluorescence (XRF) instruments, which have also been used for coal monitoring [7,30], also lack the sensitivity needed for this application. Hence, the use of LIBS for the analysis of the inorganic content of Latrobe Valley brown coal was chosen as a subject for investigation.

In this chapter, the results of the application of laser-induced breakdown spectroscopy (LIBS) to the chemical analysis of Latrobe Valley low-ash brown coal are presented. A Nd:YAG laser was used to induce emission from the ash-forming components of coal, which was then spectrally resolved and analysed. The reproducibility of LIBS analyses of the 6 major inorganic components of Latrobe Valley brown coal between sample pellets

was investigated. Following this, calibration curves were produced from a study of 30 coal samples, each of which was interrogated by 300 laser pulses. Detection limits for each of the 6 elements were then calculated from these calibration curves. A comparison between LIBS and standard chemical methods for analysing the inorganic elements in Latrobe Valley coals was also undertaken.

## **4.2 *Experimental Apparatus and Methodology***

A comprehensive description of the experimental apparatus used in this work can be found in Chapter 3. In this section of work, the laser was operated with a 5 Hz repetition rate to produce an irradiance of  $20 \text{ GWcm}^{-2}$  at the sample surface. The detector delay and integration times used were the optimum 1 and 5  $\mu\text{s}$  respectively, while a gain of 5.9 ADC counts/photoelectron was used to intensify spectra. The spectrograph grating with a line density of 2400 lines/mm was chosen to produce spectra covering a 40 nm region. Sample pellets were produced by pressing 10 g quantities of as-mined coal, which had been sieved to produce particle sizes of less than 3 mm diameter, using 220 metric ton/m<sup>2</sup> pressure.

## **4.3 *Spectra of Latrobe Valley Brown Coals***

Typical laser-induced emission spectra of Latrobe Valley brown coals from the Yallourn, Loy Yang and Morwell open cuts were obtained using the experimental apparatus and conditions described in Chapter 3 and the previous section. A composite spectrum from the Yallourn coal (sample CRC/8-4-26/68) is shown in Figure 4.1. This spectrum and the spectra for the Loy Yang and Morwell coals were obtained using a spectrograph grating with a line density of 1200 lines/mm. The entire spectrum between 200 and 840 nm for each coal was obtained by adding together eight 80 nm wide spectra. This spectrograph grating was used rather than one with a broader spectral coverage (ca. 300 nm) in order to achieve the resolution required for the identification of all the major spectral features ( $\sim 0.4 \text{ nm}$ ).

The main spectral features seen in LIBS of Yallourn coal are labelled in Figure 4.1. This sample is characterised by moderate levels of ash-forming elements, relative to other

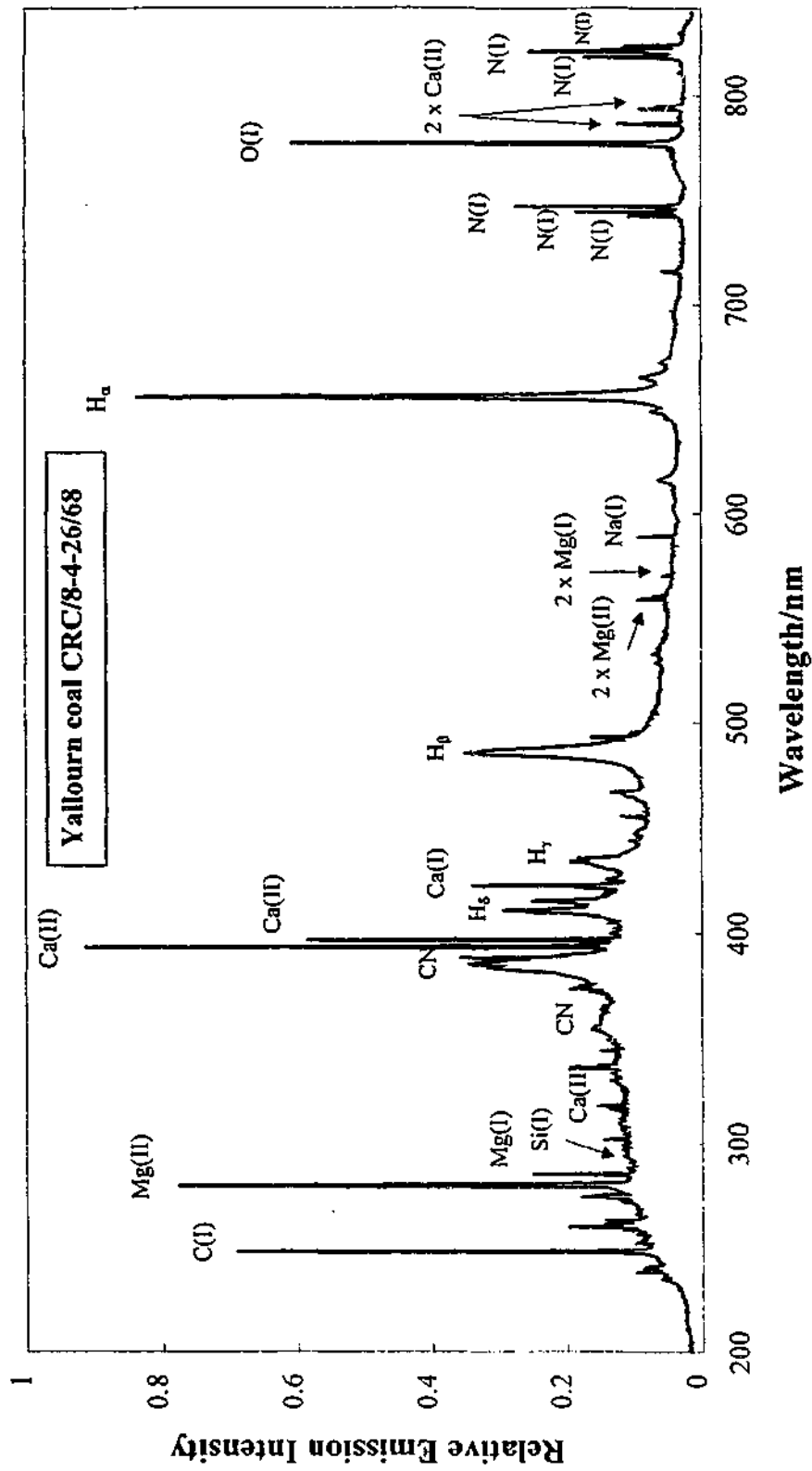


Figure 4.1. Spectrum of brown coal from the Yallourn open cut between 200 and 840 nm.

Latrobe Valley coals (see Appendix A). The intensities of the strongest emission lines from the inorganic elements are comparable to the intensities of the most intense C, H and O lines. Most of the spectral features are the result of elemental emission. However, the  $\Delta v = +1$  and  $\Delta v = 0$  sequence bands of the  $B(^2\Sigma) \rightarrow X(^2\Sigma)$  electronic transition of CN, which have band heads between 358 and 359 nm, and 385 and 388 nm, also feature in the spectrum.

The composite LIBS spectrum of a Loy Yang coal (sample CRC/8-4-26/70) between 200 and 840 nm is shown in Figure 4.2. This coal is characterised by low-levels of the ash-forming elements (see Appendix A). In this spectrum, emission lines from C, H and O are the most intense. Again, most of the spectral features are a result of elemental emission. The two sequence bands of CN mentioned previously also appear in this spectrum

The laser-induced spectrum from a Morwell coal (sample CRC/8-4-26/69) is shown in Figure 4.3. This sample is characterised by levels of ash-forming elements that are considered high for Latrobe Valley brown coals. In particular, like much of the coal from the Morwell open cut, this sample contains very high levels of Ca. As expected, the intense Ca (II) emission lines at 393.37 and 396.85 nm dominate the spectrum shown in Figure 4.3. As with the spectra of the Yallourn and Loy Yang coals, most of the spectral features are due to elemental emission.

The properties of the emission lines observed in the spectra of these three coals are listed in Table 4.1 [147,148].

#### ***4.4 Reproducibility of LIBS Analyses of the Inorganic Content of Latrobe Valley Brown Coals***

In order for LIBS to be successfully applied as an analytical tool in coal science, sufficient reproducibility between pellets from a single coal sample must be demonstrated. To do this, three coal samples were selected for the F testing for equality of means [149,150]. A coal sample with a high clay content and another with a high sand content were selected for analysis because these types of samples are likely to be more heterogeneous than

Table 4.1. Properties of emission lines observed in LIBS spectra of Latrobe Valley brown coals [147,148].

| Wavelength (nm) | Element | $E_i \leftarrow E_k$ ( $\text{cm}^{-1}$ ) | Configurations                    | $A_{ki}$ ( $10^8 \text{ s}^{-1}$ ) | $g_i \leftarrow g_k$ |
|-----------------|---------|---|-----------------------------------|------------------------------------|----------------------|
| 238.2           | Fe (II) | 0 - 41968                                 | $3d^6(^5D)4s - 3d^6(^5D)4p$       | 3.8                                | 10 - 12              |
| 247.86          | C (I)   | 21648 - 61982                             | $2s^22p^2 - 2s^22p(^2P^o)3s$      | 0.34                               | 1 - 3                |
| 251.43          | Si (I)  | 0 - 39760                                 | $3s^23p^2 - 3s^23p4s$             | 0.61                               | 1 - 3                |
| 251.61          | Si (I)  | 223 - 39955                               | $3s^23p^2 - 3s^23p4s$             | 1.21                               | 5 - 5                |
| 251.92          | Si (I)  | 77 - 39760                                | $3s^23p^2 - 3s^23p4s$             | 0.46                               | 3 - 3                |
| 252.41          | Si (I)  | 77 - 39683                                | $3s^23p^2 - 3s^23p4s$             | 1.81                               | 3 - 1                |
| 252.85          | Si (I)  | 223 - 39760                               | $3s^23p^2 - 3s^23p4s$             | 0.77                               | 5 - 3                |
| 259.94          | Fe (II) | 0 - 38455                                 | $3d^6(^5D)4s - 3d^6(^5D)4p$       | 2.2                                | 10 - 10              |
| 279.55          | Mg (II) | 0 - 35761                                 | $3s - 3p$                         | 2.6                                | 2 - 4                |
| 280.27          | Mg (II) | 0 - 35669                                 | $3s - 3p$                         | 2.6                                | 2 - 2                |
| 285.21          | Mg (I)  | 0 - 35051                                 | $3s^2 - 3s3p$                     | 4.95                               | 1 - 3                |
| 288.16          | Si (I)  | 6299 - 40992                              | $3s^23p^2 - 3s^23p4s$             | 1.89                               | 5 - 3                |
| 308.22          | Al (I)  | 0 - 32436                                 | $3s^2(^1S)3p - 3s^2(^1S)3d$       | 0.63                               | 2 - 4                |
| 309.27          | Al (I)  | 112 - 32437                               | $3s^2(^1S)3p - 3s^2(^1S)3d$       | 0.74                               | 4 - 6                |
| 309.29          | Al (I)  | 112 - 32436                               | $3s^2(^1S)3p - 3s^2(^1S)3d$       | 0.12                               | 4 - 4                |
| 315.89          | Ca (II) | 25192 - 56839                             | $3p^6(^1S)4p - 3p^6(^1S)4d$       | 3.1                                | 2 - 4                |
| 317.93          | Ca (II) | 25414 - 56839                             | $3p^6(^1S)4p - 3p^6(^1S)4d$       | 3.6                                | 4 - 6                |
| 357.01          | Fe (I)  | 7377 - 35379                              | $3d^7(^4F)4s - 3d^7(^4F)4p$       | 0.677                              | 9 - 11               |
| 358.12          | Fe (I)  | 6928 - 34844                              | $3d^7(^4F)4s - 3d^7(^4F)4p$       | 1.02                               | 11 - 13              |
| 371.99          | Fe (I)  | 0 - 26875                                 | $3d^64s^2 - 3d^6(^5D)4s4p(^3P^o)$ | 0.16                               | 9 11                 |
| 385-388         | CN      |   |                                   |                                    |                      |

|                         |                        |                              |   |          |                      |
|-------------------------|------------------------|------------------------------|---|----------|----------------------|
| 393.37                  | Ca (II)                | 0 - 25414                    | $3p^6(^1S)4s - 3p^6(^1S)4p$             | 1.47     | 2 - 4                |
| 394.40                  | Al (I)                 | 0 - 25348                    | $3s^2(^1S)3p - 3s^2(^1S)4s$             | 0.493    | 2 - 2                |
| 396.15                  | Al (I)                 | 112 - 25348                  | $3s^2(^1S)3p - 3s^2(^1S)4s$             | 0.98     | 4 - 2                |
| 396.85                  | Ca (II)                | 0 - 25192                    | $3p^6(^1S)4s - 3p^6(^1S)4p$             | 1.4      | 2 - 2                |
| 410.17                  | H (I)                  | 82259 - 106632               | 2p - 6d                                 | 0.008575 | 4 - 4                |
| 422.67                  | Ca (I)                 | 0 - 23652                    | $4s^2 - 4s4p$                           | 2.18     | 1 - 3                |
| 434.05                  | H (I)                  | 82259 - 105292               | 2p - 5d                                 | 0.09425  | 4 - 6                |
| 486.13                  | H (I) ( $H_{\beta}$ )  | 82259 - 102824               | 2p - 4d                                 | 0.2062   | 4 - 6                |
| 589.00                  | Na (I)                 | 0 - 16973                    | 3s - 3p                                 | 0.622    | 2 - 4                |
| 589.59                  | Na (I)                 | 0 - 16956                    | 3s - 3p                                 | 0.618    | 2 - 2                |
| 656.27 & 656.28         | H (I) ( $H_{\alpha}$ ) | 82259 - 97492                | 2p - 3d                                 | 0.6465   | 4 - 6                |
| 742.36                  | N (I)                  | 83284 - 96751                | $2s^22p^2(^3P)3s - 2s^22p^2(^3P)3p$     | 0.0595   | 2 - 4                |
| 744.23                  | N (I)                  | 83318 - 96751                | $2s^22p^2(^3P)3s - 2s^22p^2(^3P)3p$     | 0.124    | 4 - 4                |
| 746.83                  | N (I)                  | 83365 - 96751                | $2s^22p^2(^3P)3s - 2s^22p^2(^3P)3p$     | 0.193    | 6 - 4                |
| 777.19, 777.41 & 777.54 | O (I)                  | 86630 - 86632, 86628 & 86626 | $2s^22p^3(^4S^0)3s - 2s^22p^3(^4S^0)3p$ | 0.369    | 5 - 7, 5 - 5 & 5 - 3 |
| 818.49                  | N (I)                  | 83318 - 95532                | $2s^22p^2(^3P)3s - 2s^22p^2(^3P)3p$     | 0.0858   | 4 - 6                |
| 818.80                  | N (I)                  | 83284 - 95494                | $2s^22p^2(^3P)3s - 2s^22p^2(^3P)3p$     | 0.127    | 2 - 4                |
| 821.63                  | N (I)                  | 83365 - 95532                | $2s^22p^2(^3P)3s - 2s^22p^2(^3P)3p$     | 0.223    | 6 - 6                |
| 822.31                  | N (I)                  | 83318 - 95475                | $2s^22p^2(^3P)3s - 2s^22p^2(^3P)3p$     | 0.264    | 4 - 2                |
| 824.24                  | N (I)                  | 83365 - 95494                | $2s^22p^2(^3P)3s - 2s^22p^2(^3P)3p$     | 0.136    | 6 - 4                |

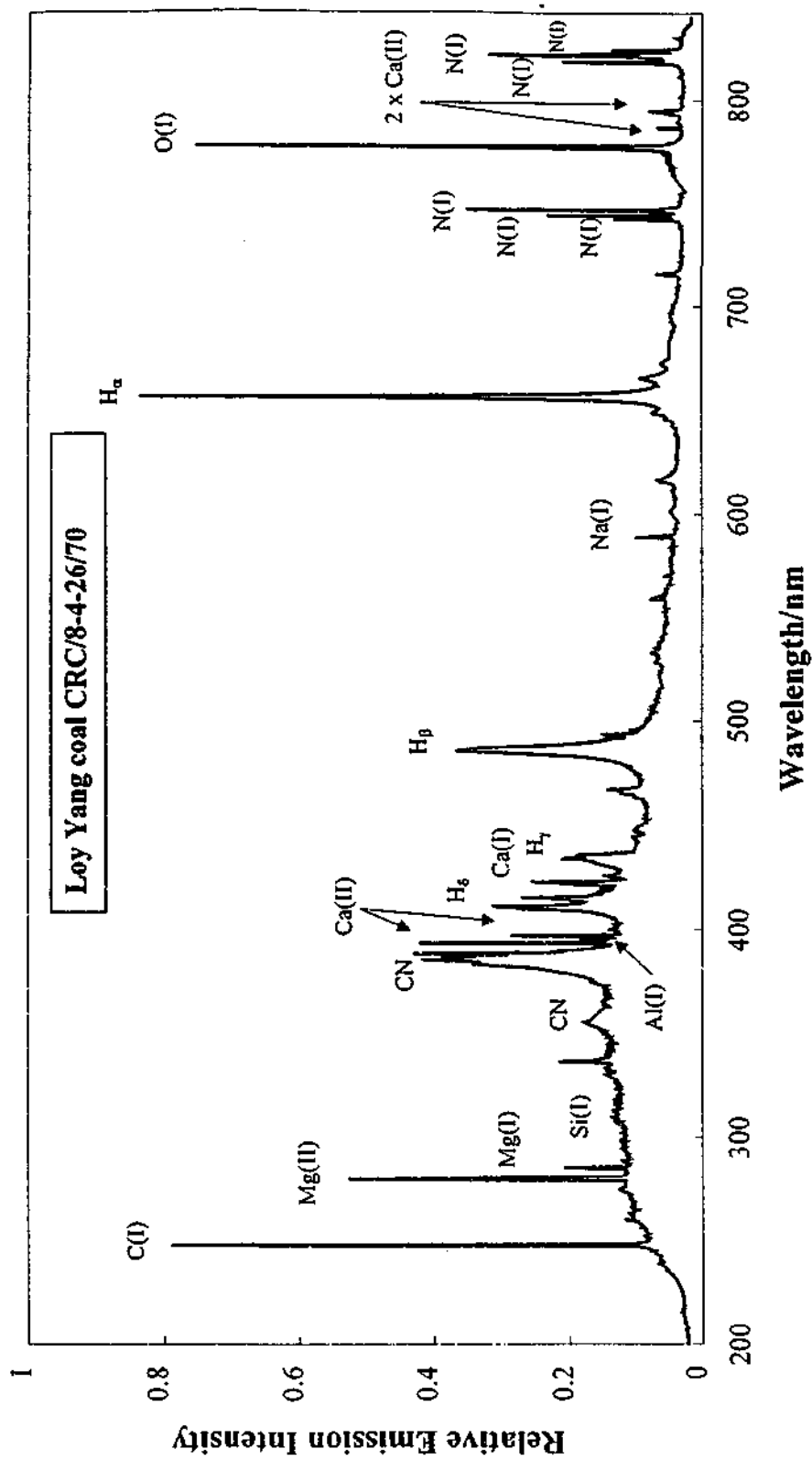


Figure 4.2. Spectrum of brown coal from the Loy Yang open cut between 200 and 840 nm.

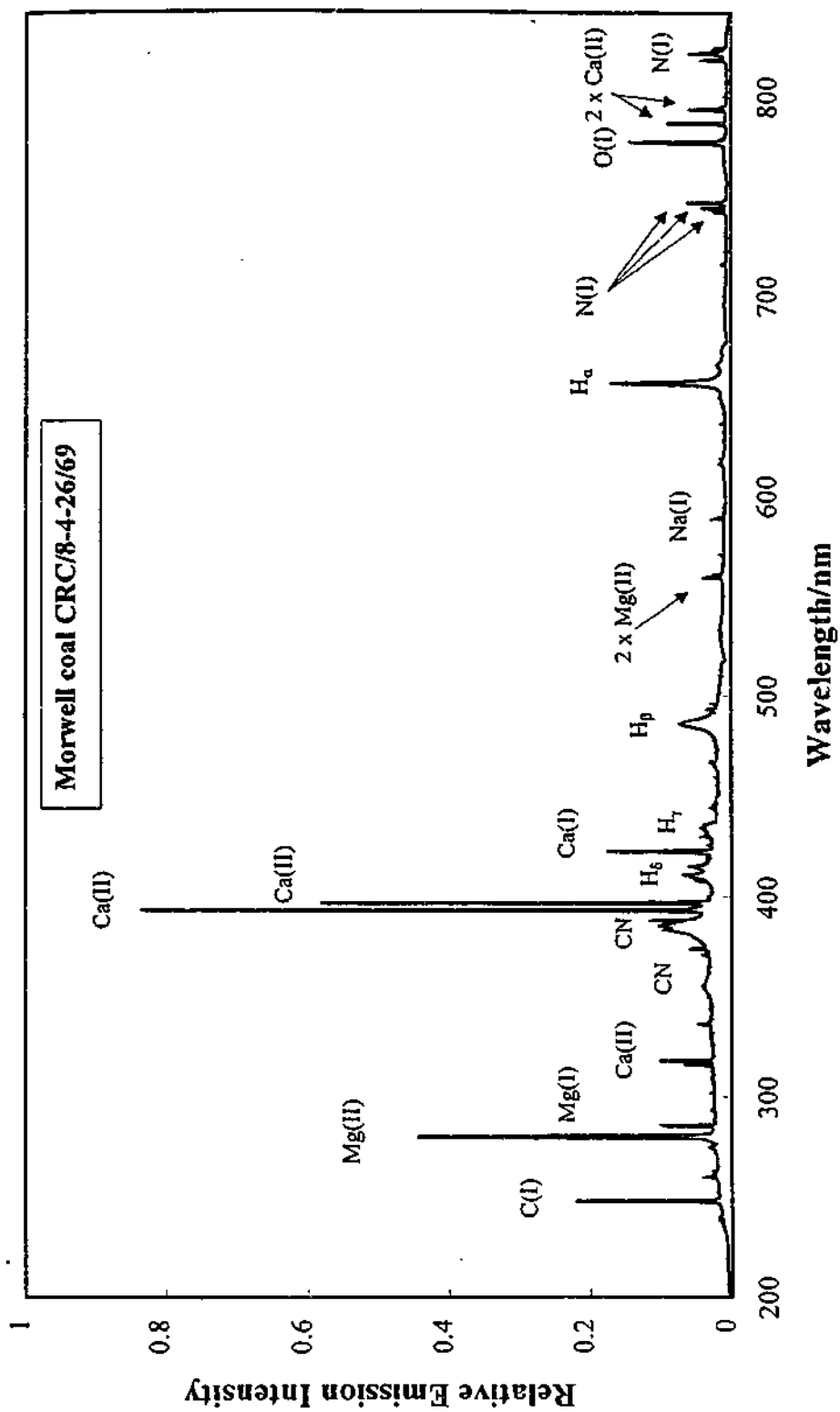


Figure 4.3. Spectrum of brown coal from the Morwell open cut between 200 and 840 nm.

typical Latrobe Valley low-ash coals. A sample with inorganic species concentrations typical of many Latrobe Valley coals was also chosen for analysis.

To gauge the level of reproducibility achieved by this LIBS system, five pellets each of the three coal samples were prepared and analysed for a range of inorganic species using the ICCD based experimental setup described in Chapter 3. One hundred spectra, each obtained from a single laser shot, were co-added for every spectral region analysed. The 100 co-added spectra comprised one measurement, which was then repeated 3 times for each spectral range, each time with the use of a different (fresh) section of the pellet for analysis. In this way a measurement mean and standard deviation were obtained.

Baseline-corrected peak areas were then determined from the spectra using an integration algorithm employing the trapezoidal rule. The results obtained for the pellets from each sample were then compared using an F test for equality of means. An F test is a procedure used to test the statistical significance of the differences among the obtained means of two or more random samples from a given population. In this case, the test was used to determine if there was no significant difference between the results obtained from each pellet produced from a single coal sample, i.e. if this LIBS analysis was reproducible. The F values obtained for the inorganic and mineral elements in each sample are shown in Tables 4.2 (a) and (b).

The critical F value (above which it can be concluded that the sample means are different) is 3.48, at a 95% level of confidence. An examination of the data in Tables 4.2 (a) and (b) shows that the use of ionic emission lines tends to produce higher F values than the use of neutral emission lines. The most likely explanation is that processes more highly dependent on the amount of energy delivered to the plasma are required to produce ionic emission. Hence, these transitions will be more sensitive to fluctuations in experimental parameters. The F testing shows that analyses of neutral emission is reproducible between sample pellets, in most cases. The only exceptions to this were the results obtained for Mg and Na analyses in the coal sample with high sand content and Si in the sample with "typical" elemental concentrations. It will be shown later that the concentration of Si in Sample 3 is actually lower than the detection limit for LIBS analyses of Si, which explains the poor reproducibility of its analysis in this instance. As expected, analyses of the

Table 4.2. Emission lines used in analysis and F values obtained in reproducibility studies for (a) neutral emission lines and (b) ionic emission lines.

(a)

| Element | Emission line<br>(nm) | Sample 1 (high clay)   |         | Sample 2 (high sand)   |         | Sample 3 (typical)     |         |
|---------|-----------------------|------------------------|---------|------------------------|---------|------------------------|---------|
|         |                       | Concentration<br>(ppm) | F value | Concentration<br>(ppm) | F value | Concentration<br>(ppm) | F value |
| Mg      | 285.21                | 1500                   | 3.0     | 500                    | 7.2     | 2100                   | 0.3     |
| Na      | 589.00 & 589.59       | 1200                   | 0.7     | 200                    | 12.4    | 2100                   | 0.2     |
| Fe      | 371.99                | 1300                   | 0.8     | 1800                   | 0.3     | 90                     | 0.3     |
|         | 373.49 & 373.71       | 1300                   | 25.6    | 1800                   | 0.6     | 90                     | 1.5     |
|         | 374.55 & 374.95       | 1300                   | 3.8     | 1800                   | 1.1     | 90                     | 0.6     |
| Al      | 375.82                | 1300                   | 8.4     | 1800                   | 0.9     | 90                     | <0.1    |
|         | 308.22                | 15700                  | 0.7     | 4600                   | 2.5     | 260                    | 0.2     |
|         | 309.27 & 309.29       | 15700                  | 4.6     | 4600                   | 2.1     | 260                    | 0.4     |
| Si      | 288.16                | 11800                  | 0.8     | 28700                  | 2.9     | 130                    | 5.0     |
| Ca      | 422.67                | 1400                   | 3.1     | 200                    | 3.3     | 1900                   | 2.9     |

(b)

| Element | Emission line<br>(nm) | Sample 1 (high clay)   |         | Sample 2 (high sand)   |         | Sample 3 (typical)     |         |
|---------|-----------------------|------------------------|---------|------------------------|---------|------------------------|---------|
|         |                       | Concentration<br>(ppm) | F value | Concentration<br>(ppm) | F value | Concentration<br>(ppm) | F value |
| Mg      | 279.55                | 1500                   | 7.4     | 500                    | 23.1    | 2100                   | 0.6     |
|         | 280.27                | 1500                   | 8.5     | 500                    | 21.4    | 2100                   | 0.6     |
| Ca      | 393.37                | 1400                   | 18.3    | 200                    | 10.3    | 1900                   | 5.1     |
|         | 396.85                | 1400                   | 15.3    | 200                    | 4.8     | 1900                   | 5.5     |
| Fe      | 238.20                | 1300                   | 10.5    | 1800                   | 3.2     | 90                     | 0.6     |

sample containing typical levels of inorganics were more reproducible than analyses of the other two samples. Sand and clay particles are typically distributed through coal samples as discrete particles, leading to increased heterogeneity and reduced analytical reproducibility.

#### ***4.5 Calibration of LIBS Analyses of the Inorganic Elements in Latrobe Valley Brown Coal***

Calibration curves for each of the major inorganic elements in Latrobe Valley brown coal were generated by measuring the peak area of the characteristic spectral features and correlating these with the results from the standard chemical analyses. To do this, a total of 30 samples of raw coal originating from the Yallourn, Loy Yang and Morwell coalfields in the Gippsland basin were collected. Inductively coupled plasma (ICP) spectroscopy and atomic absorption spectrophotometry were used to analyse the acid extracted cations (Na, Ca, Mg, Al<sub>sol</sub> and Fe<sub>NP</sub><sup>a</sup>) and the constituents of the coal ash extract (Si, Na, Ca, Mg, Al and Fe).

These samples were then pelletised and analysed using the LIBS technique under the conditions described earlier. The baseline-corrected areas of the peaks of interest were measured subsequent to data collection and then correlated with the results from the standard chemical analyses. The peak areas used in these correlations were the averages obtained from the three analyses performed on each sample pellet.

The calibration curve constructed for Na content in Latrobe Valley brown coal is shown in Figure 4.4. The combined peak area of the Na D lines at 589.00 and 589.59 nm was correlated with Na concentration to produce this curve. The combined peak area was used because these lines were unable to be completely resolved from each other. The R<sup>2</sup> value obtained for the linear regression through this data was 0.97, while the standard prediction error obtained for this curve was 200 ppm. The error bars shown in Figure 4.4 represent two standard deviations for each point. The standard prediction error is a measure of the standard error of the predicted y-value for each x in the regression. The method for calculating this error is described in Appendix B.

<sup>a</sup> Fe<sub>NP</sub> refers to non-pyritic iron and Al<sub>sol</sub> to acid-soluble aluminium

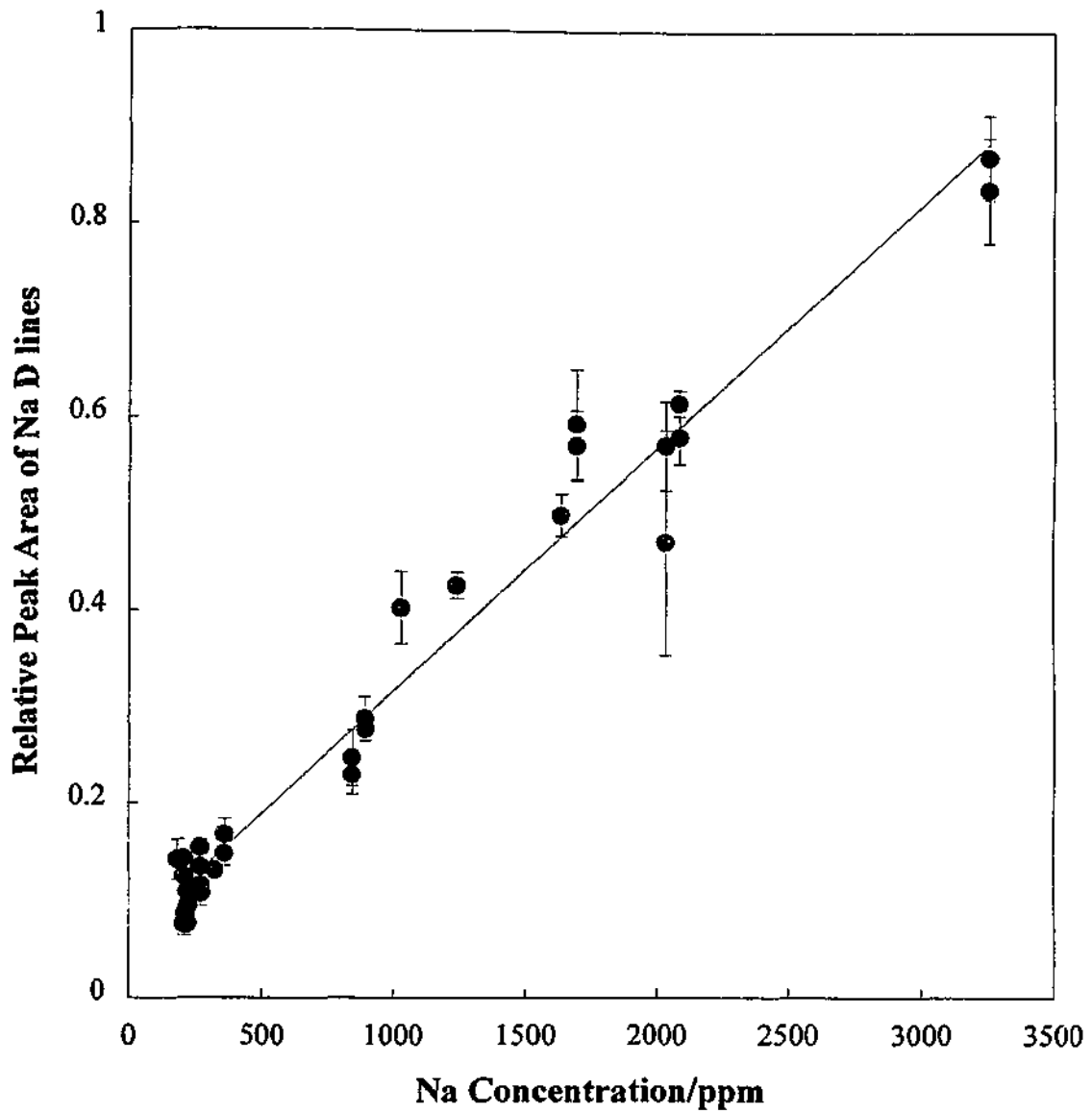


Figure 4.4. Calibration curve for Na in low-ash Latrobe Valley brown coal constructed from LIBS analyses of 30 coal samples.

There does not appear to be any significant self-absorption of the Na emission over this concentration range. The self-absorption of resonance lines, such as the Na D lines, is usually indicated when the calibration curve for the emission line being measured begins to plateau. The calibration curve in Figure 4.4 remains linear over the concentration range studied. However, the regression line fitted through the Na data does not pass through the origin; it has a positive intercept on the Y-axis. It is possible that this is caused by interference by some other unobservable spectral feature with the Na D lines. This interference could be caused by a weak emission line from another element or the  $\Delta v = -2$  sequence band of the  $A(^3\Pi) \rightarrow X(^3\Pi)$  electronic transition of  $C_2$ , which has band heads occurring between 590 and 619 nm [151]. It is most likely that the  $C_2$  emission is interfering with the Na peaks because it will be present and remain relatively constant in all samples and at all Na concentrations.

The calibration curve for Mg in Latrobe Valley brown coal is shown in Figure 4.5. The peak area of the Mg (I) emission line at 285.21 nm was correlated with the Mg concentration measured by ICP to produce this curve. In contrast to the Na data, there appears to be significant self-absorption of the Mg emission at Mg concentrations above approximately 1500 ppm. The regression line fitted through this data has an  $R^2$  value of 0.91 and a standard prediction error of 200 ppm. The following function has a better fit than a straight line through data from emission that undergoes significant self-absorption:

$$I = A_0 - A_1 \exp(-A_2 c) \quad (4.1)$$

where  $I$  is the relative emission intensity and  $c$  is elemental concentration. A least squares fit of Equation 4.1 to the Mg data resulted in an  $R^2$  value of 0.96 and a standard prediction error of 100 ppm, which is a significant improvement over the linear regression model.

The calibration data collected for Ca in Latrobe Valley brown coal is shown in Figure 4.6. As for the Mg transition, the Ca emission line at 422.67 nm appears to experience a significant amount of self-absorption above approximately 1000 ppm. Both a straight line and Equation 4.1 were fitted through the data in an attempt to construct an appropriate calibration curve. The linear regression through the Ca data resulted in a low  $R^2$  value of 0.85 and a standard prediction error of 400 ppm. When Equation 4.1 was fitted through

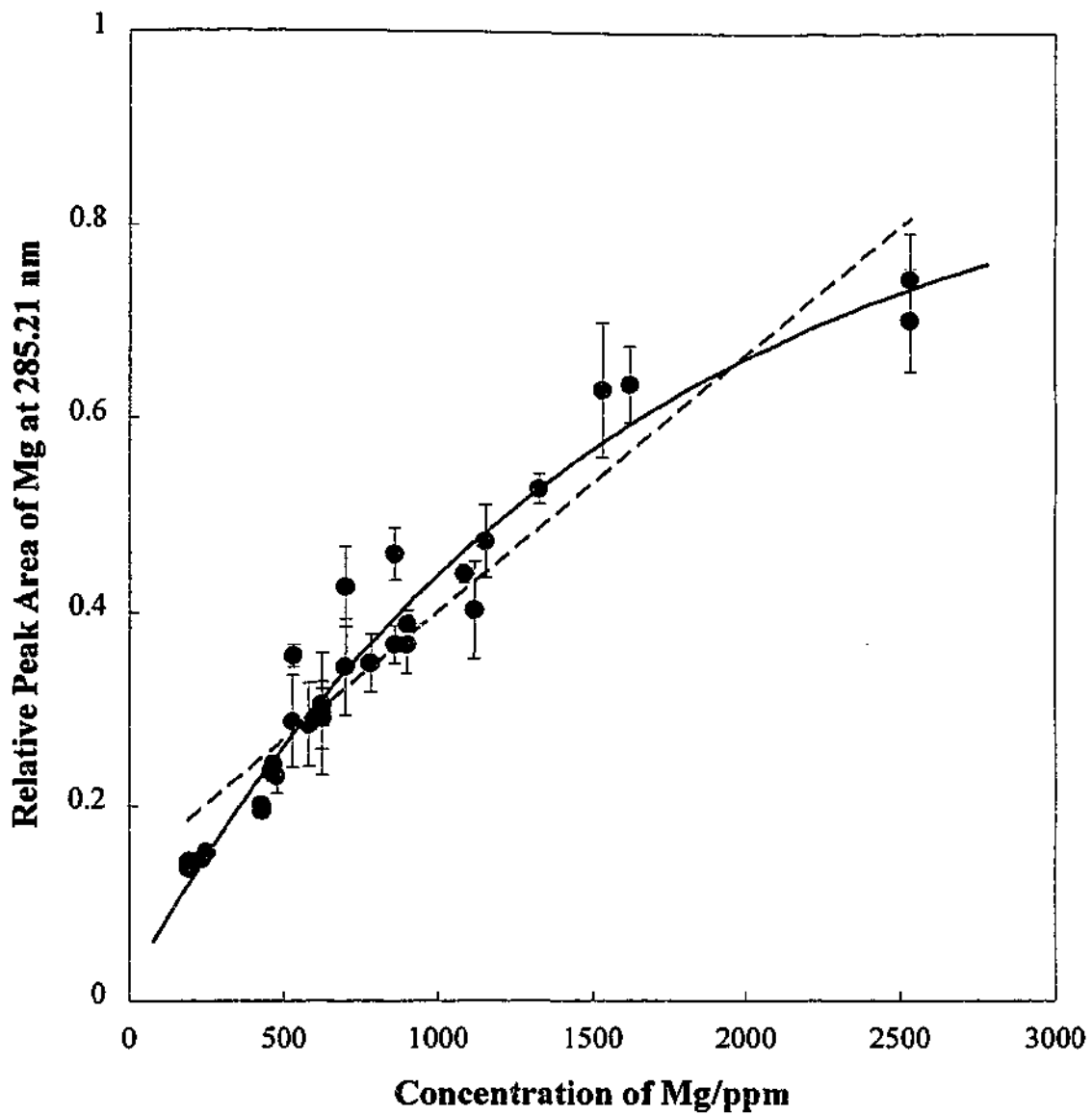


Figure 4.5. Calibration curves for LIBS analyses of Mg in low-ash Latrobe Valley brown coal using linear regression (---) and Equation 4.1 (—).

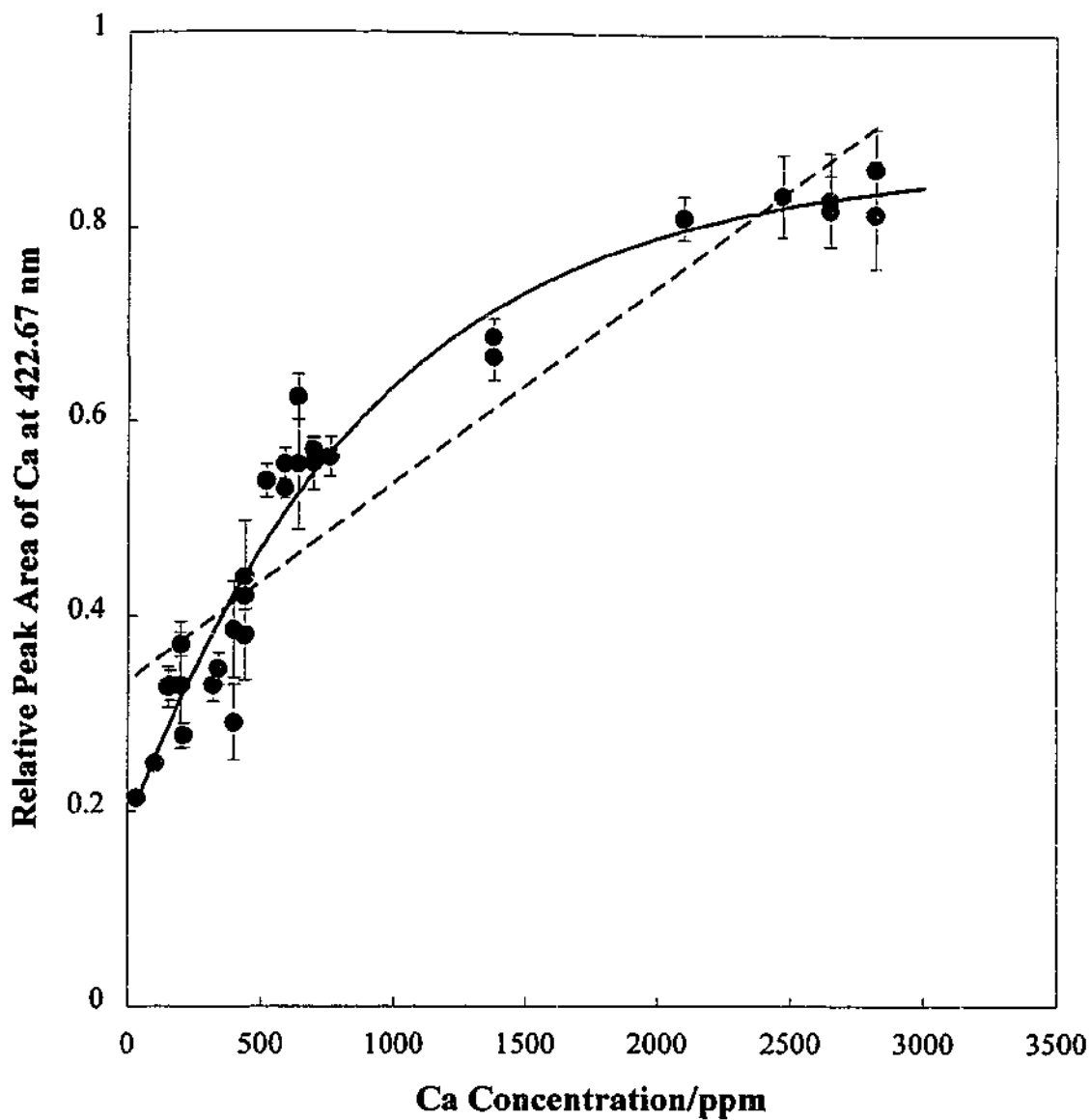


Figure 4.6. Calibration curves for LIBS analyses of Ca in low-ash Latrobe Valley brown coal using linear regression (---) and Equation 4.1 (—).

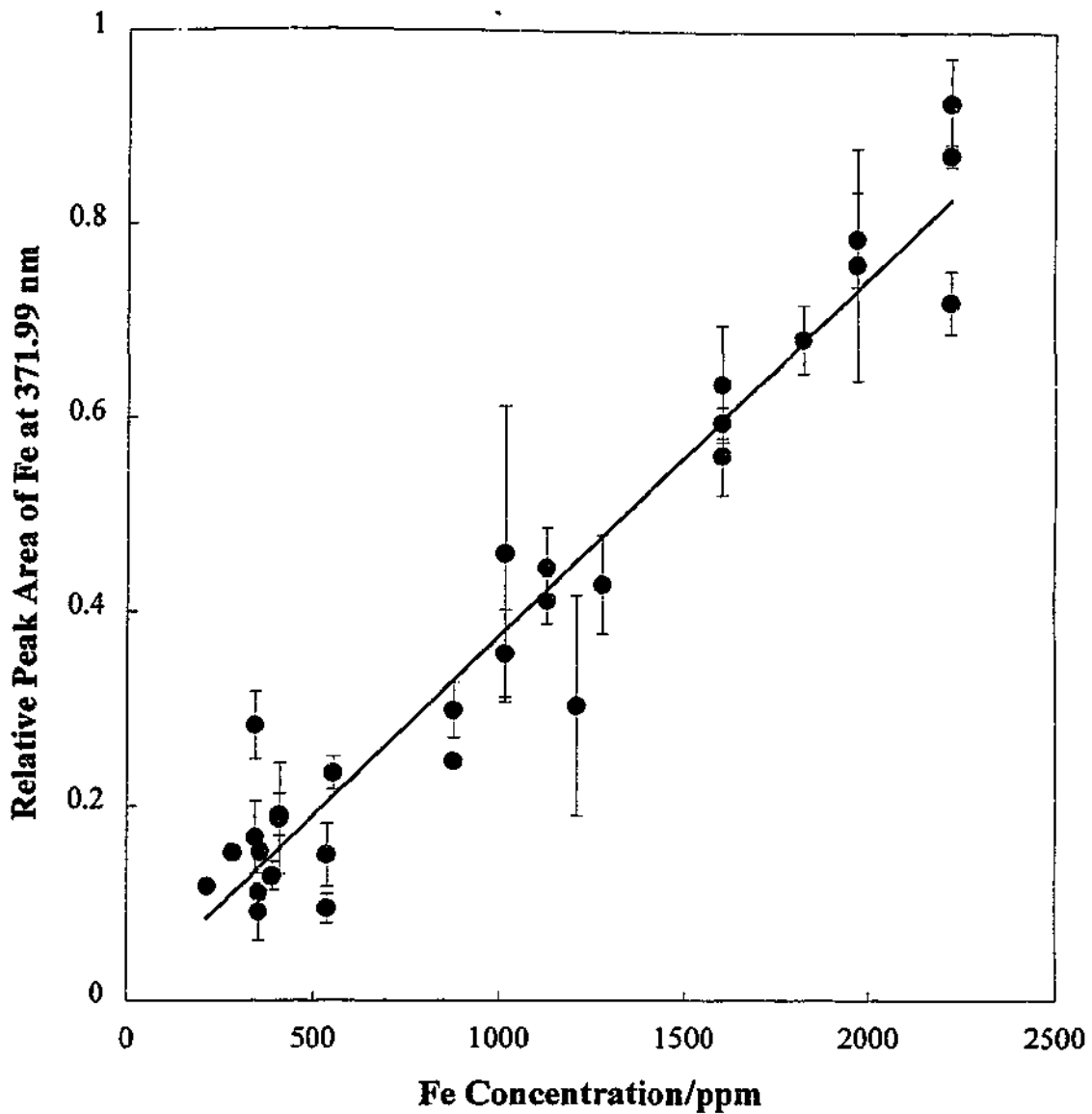


Figure 4.7. Calibration curve for Fe in low-ash Latrobe Valley brown coal constructed from LIBS analyses of 30 coal samples.

the data, an  $R^2$  value of 0.95 and a prediction error of 200 ppm were obtained. Thus, the curve with the functional form of Equation 4.1 was used for calibration. Neither of the regression lines fit through the Ca data pass through the origin. It is possible that this offset is caused by spectral interference from the  $\Delta v = -1$  sequence band of the  $B(^2\Sigma) \rightarrow X(^2\Sigma)$  electronic transition of CN, which has band heads between 415 and 422 nm [151].

The calibration curve constructed for Fe in Latrobe Valley brown coal, using the emission line at 371.99 nm, is shown in Figure 4.7. There does not appear to be a significant amount of self-absorption at high Fe concentrations. Thus, only a linear regression line was fitted through the data. This regression line has an  $R^2$  value of 0.94 and a standard prediction error of 200 ppm. The error bars in Figure 4.7 represent two standard deviations, as in Figures 4.4 to 4.6. However, the relative standard deviations for these points appear to be larger than those for Na, Mg and Ca. It is likely that this is because the Fe emission line used for calibration is much less intense than the emission lines used in the calibration of the other three elements.

The calibration curve for Al in Latrobe Valley brown coal is shown in Figure 4.8. The combined peak area of the Al emission lines at 309.27 and 309.29 is plotted against Al concentration using linear scales on the axes in Figure 4.8(a). Figure 4.8(a) shows that the combined peak area of these lines increases linearly with the Al concentration tested. The  $R^2$  value for this regression is 0.99 and the standard prediction error for Al is 300 ppm. The concentration of Al in Latrobe Valley brown coal varies over such a wide range because of its chemical form in the coal. Al is present in Latrobe Valley coals as a monovalent hydroxy complex that is exchanged onto carboxyl groups as well as in minerals, including kaolinite ( $Al_2Si_2O_5(OH)_4$ ) and muscovite ( $KAl_2(AlSi_3)O_{10}(OH)_2$ ). These minerals are inhomogeneously distributed throughout the coal, meaning that some samples will be very rich in minerals and consequently Al, while others will have extremely low mineral content. This results in a wide range of Al concentrations in Latrobe Valley brown coal samples.

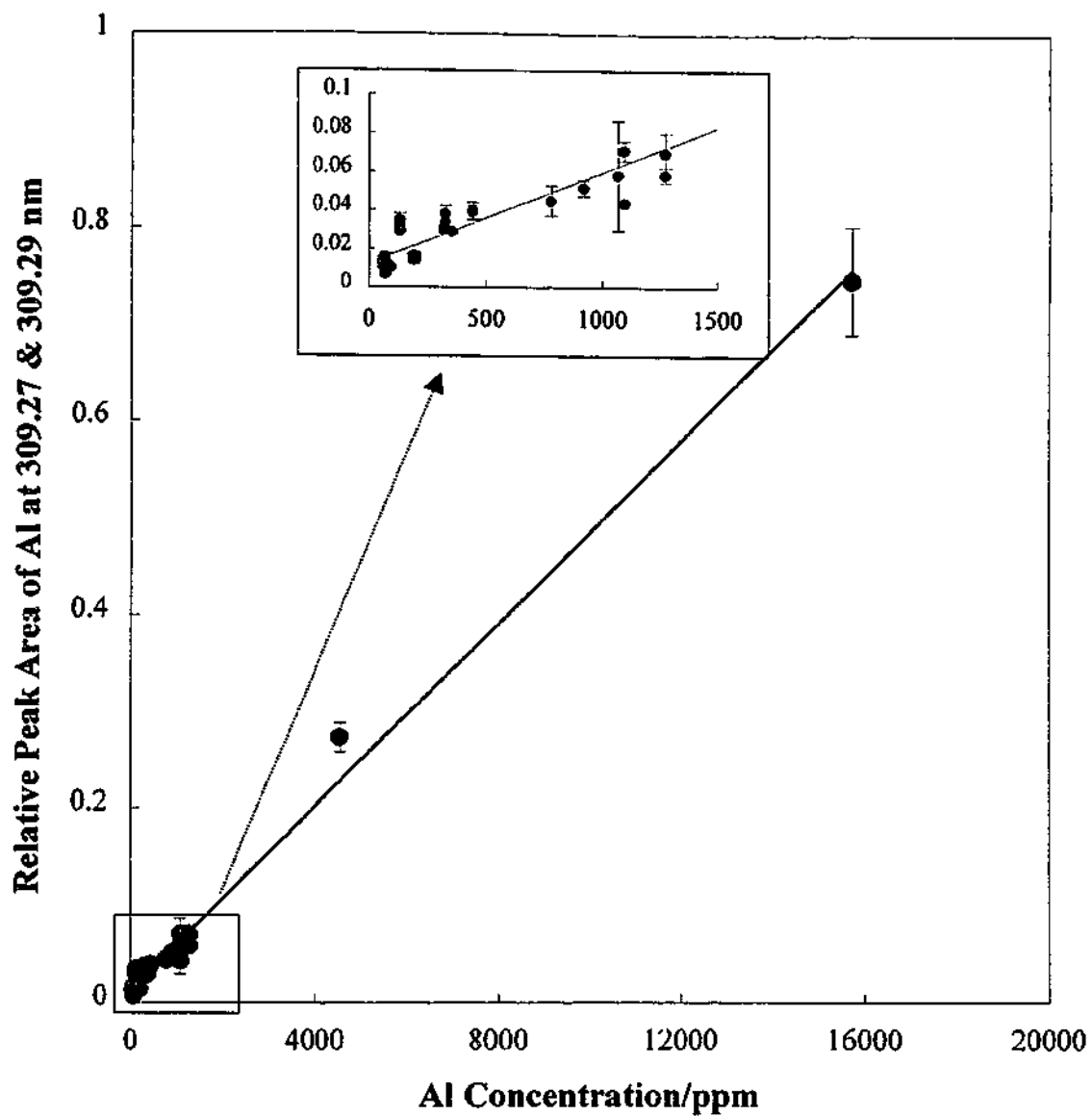


Figure 4.8. Calibration curve for Al in Latrobe Valley brown coal constructed from LIBS analyses of 30 samples.

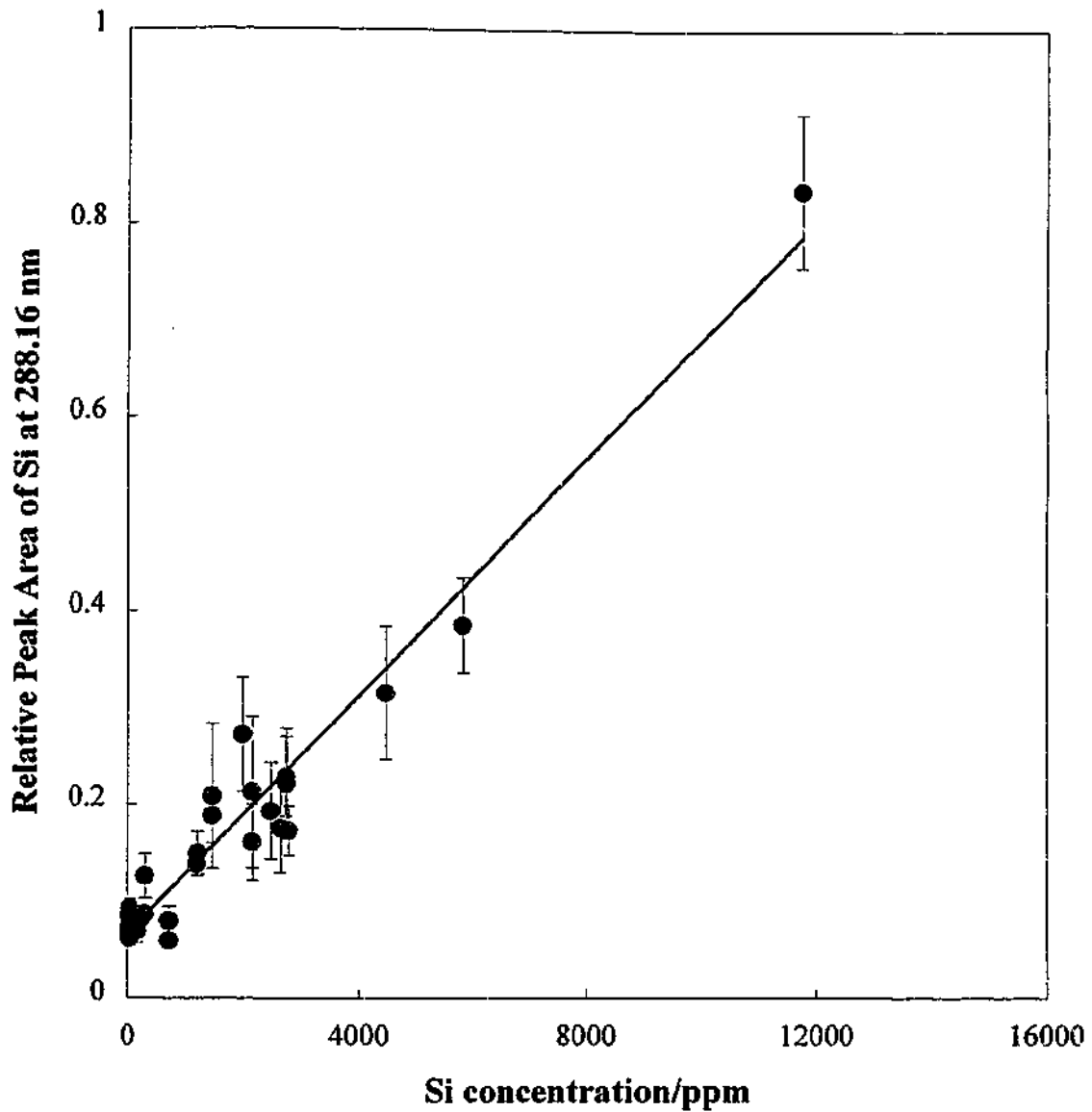


Figure 4.9. Calibration curve for Si in low-ash Latrobe Valley brown coal constructed from LIBS analyses of 30 coal samples.

The calibration curve for Si in Latrobe Valley brown coals, constructed using the Si (I) emission line at 288.16 nm, is shown in Figure 4.9. There does not appear to be any significant self-absorption of this emission at high Si concentrations. This is to be expected, since this line is not a resonance line. The regression line has an  $R^2$  value of 0.95 and results in a standard prediction error of 500 ppm for Si in Latrobe Valley brown coal. The standard prediction error and the relative magnitudes of the error bars, which represent two standard deviations of each measurement, are larger than for the analyses of the other 5 major inorganic elements in the coals. This is likely to be due to the heterogeneous nature of the Si in the coal. Si is present in Latrobe Valley brown coals in discrete mineral particles, including quartz, kaolinite and muscovite. Thus there can be significant variation in the amount of Si in the sample volume, even between consecutive laser pulses.

Detection limits ( $C_L$ ) for each species were calculated from each of the calibration curves using the equation:

$$C_L = 3s_{ave}/m \quad (4.2)$$

where  $s_{ave}$  is the average of the standard deviations of the measurements for the samples with the five lowest elemental concentrations, and  $m$  is the slope of the linear calibration curve. It is sufficient to use the slope of the linear calibration curves for calculation of the detection limits because emission intensity will increase linearly with elemental concentration at low concentrations.

Detection limits obtained for each inorganic species using the LIBS technique, under the conditions described earlier, are reported in Table 4.3. These detection limits are comparable to those obtained for LIBS studies of pulverised bituminous and sub-bituminous coal particles. For example, Ottesen *et al.* obtained detection limits of approximately 100 ppm for Li, Na, K, Mg, Ca, Ba, Sr, Al, Si, Ti, Mn and Fe in pulverised medium to high-ash coal particles obtained from a variety of mines in the USA [36]. Analyses of elements in complicated sample matrices, such as coal or soil, are often not as sensitive as analyses of samples with less complex matrices. Thus, the detection limits of such analyses will be higher.

Table 4.3. Detection limits of the inorganic elements in Latrobe Valley coal calculated from calibration curves constructed from LIBS analyses of 30 coal samples.

| Element | Emission line (nm) | Detection limit (ppm) | R <sup>2</sup> | Standard prediction error (ppm) | Self-absorption (Y/N) |
|---------|--------------------|-----------------------|----------------|---------------------------------|-----------------------|
| Mg(I)   | 285.21             | 40                    | 0.96           | 100                             | Y                     |
| Na(I)   | 589.00 & 589.59    | 70                    | 0.97           | 200                             | N                     |
| Ca(I)   | 422.67             | 130                   | 0.95           | 200                             | Y                     |
| Fe(I)   | 371.99             | 110                   | 0.94           | 200                             | N                     |
| Al(I)   | 309.27 & 309.29    | 60                    | 0.99           | 300                             | N                     |
| Si(I)   | 288.16             | 200                   | 0.95           | 500                             | N                     |

#### 4.6 Comparison of LIBS and Standard Analyses of Latrobe Valley Brown Coal

A test coal of unknown composition was analysed independently using LIBS and ICP (Spectro Flame Modula E). The results from each analysis, shown in Table 4.4, were then compared. The error margins quoted for the LIBS analyses are the standard errors of prediction noted earlier for each calibration curve. Table 4.4 shows that the LIBS and ICP analyses for the six main inorganic and mineral elements in the coal are in good agreement. The differences between the results were less than the error margin of the LIBS analysis in all cases. In most instances, the difference between the values measured using the two analytical methods was considerably less than the standard error of prediction.

The low concentration of Ca in the unknown sample means that the standard error of prediction in the LIBS analysis is the same magnitude as the measurement. The main reason for this is that the concentration of Ca in this coal is below the LIBS detection limit (see Table 4.3). The concentration of Ca in Latrobe Valley brown coals is generally higher than the concentration in this sample (the average concentration of Ca in Latrobe Valley coals is 1100 ppm [2]). Thus, there will not usually be such a high relative uncertainty.

Table 4.4. Comparison of LIBS and ICP analyses of an unknown coal sample.

| Element | LIBS analysis (ppm) | ICP analysis (ppm) |
|---------|---------------------|--------------------|
| Mg      | 500 ± 100           | 460 ± 70           |
| Na      | 1600 ± 200          | 1630 ± 70          |
| Ca      | 200 ± 200           | 110 ± 40           |
| Fe      | 400 ± 200           | 280 ± 40           |
| Al      | 800 ± 300           | 920 ± 70           |
| Si      | 2400 ± 500          | 2800 ± 100         |

#### 4.7 Conclusions

The application of laser-induced breakdown spectroscopy (LIBS) to the chemical analysis of the inorganic and mineral content of Latrobe Valley brown coal has been investigated. Laser-induced emission spectra recorded between 200 and 840 nm of brown coal samples from the Yallourn, Loy Yang, and Morwell open cuts have been obtained. These spectra showed that differences in the content of the ash-forming elements in these samples were reflected in the laser-induced plasma. Differences in the concentrations of specific inorganic elements in the coals were also mirrored in the laser-induced spectra. These spectra demonstrate the possibility of using LIBS for analysis of the inorganic and mineral content of Latrobe Valley brown coal.

The reproducibility of LIBS analyses of the mineral and inorganic ash-forming elements in Latrobe Valley brown coal was also investigated. The variation in the analysis results of five pellets of the same coal sample was examined using an F test for equality of means. This test was performed on each of three coal samples; a high sand content coal, a high clay content coal, and a coal with inorganic concentrations typical of many Latrobe Valley brown coal samples. The results of this study showed that analysis of neutral emission caused by laser-sample interaction is reproducible between sample pellets at a 95% confidence level in most cases. However, ionic emission was found to be less reproducible. This means that LIBS analyses of the inorganic and mineral content of Latrobe Valley brown coal should be limited to neutral emission lines where possible.

Calibration curves were constructed for each of the six major inorganic elements in the brown coal by correlating elemental emission peak areas with the results from standard chemical analyses. Linear calibration curves were obtained for Na, Fe, Al, and Si for concentrations between 200 and 3300, 200 and 2200, 60 and 16000, and 40 and 12000 ppm respectively. Non-linear calibration curves were found to have a better fit through the Mg and Ca emission data, which experienced self-absorption at high elemental concentrations. These curves covered Mg and Ca concentrations between 190 and 2530, and 40 and 2820 ppm, respectively. The standard errors of prediction for each of the six calibration curves were 100 (Mg), 200 (Na, Ca, Fe), 300 (Al), and 500 ppm (Si). Detection limits between 40 ppm and 200 ppm were obtained, on a wet basis, from the calibration curves for all the major inorganic elements (Na, Mg, Ca, Al, Fe and Si) present in low-rank coal.

A Latrobe Valley brown coal of unknown chemical composition was analysed for its inorganic and mineral content independently using LIBS and ICP. The results of these analyses showed that the LIBS analyses were in good agreement with ICP analyses. The differences between the two sets of results were less than the error margin of the LIBS analyses for all six elements.

The work in this chapter proved that LIBS could be used for the qualitative and quantitative analyses of Latrobe Valley brown coal. Good agreement with standard analyses and reasonable error margins were obtained. However, it was to be hoped that these results could still be further improved. To this end, the effects of implementing signal normalisation in these LIBS analyses will be investigated in Chapter 5. The effects of multivariate analyses of LIBS data will also be tested in Chapter 7.

---

*Acoustic Wave Normalisation of Laser-Induced  
Breakdown Spectroscopic Analyses*

*5.1 Introduction*

The magnitude of emission signals produced in LIBS is often dependent on the sample matrix [78]. Thus, calibration must be performed for each sample type or some form of signal correction implemented in order to ensure accurate quantitative measurements. Several methods of signal normalisation have been used by others in an attempt to improve the precision of laser based analytical techniques. These include monitoring laser power [112], monitoring the size of the laser-produced crater in the sample [113], internal standardisation [42-46,90,105], measuring the plasma temperature [49], and acoustic signal normalisation [1,50,114,115]. Ideally a normalisation procedure able to correct for matrix effects in any sample would be used.

In this chapter, the results presented are those obtained using three methods for normalisation of elemental emission signals produced during laser-induced breakdown spectroscopy. These normalisation procedures, two of which incorporated a measurement of the laser-produced acoustic signal, were first validated experimentally. This was done by investigating the relationships between the acoustic signal and laser irradiance, elemental emission intensity and laser-induced mass loss. The variation of the acoustic signal with sample matrix was also studied. One of the three normalisation methods tested used only the acoustic signal for normalisation, another method used a temperature normalisation coefficient, while the third method incorporated both the acoustic signal and temperature normalisation coefficient. A wide range of coals and powdered minerals were used as samples. The main aim of this study was to implement an appropriate normalisation process for laser-induced emission signals from coal and mineral samples that is independent of sample type.

## 5.2 *Experimental Apparatus and Methodology*

A detailed description of the experimental set-up used in this work may be found in Chapter 3. The pressed pellet samples used in this study were produced in two ways. For coal samples, 10 g quantities of as-received coal with particle sizes of less than 3 mm diameter were pelletised using a hydraulic press (Carver, Model C). A pressure of approximately 220 metric ton/m<sup>2</sup> was applied to produce these pellets, resulting in negligible water loss from the coals. Mineral samples were prepared by mixing boric acid powder with each sample in a 1:4 ratio. A pressure of approximately 1764 metric ton/m<sup>2</sup> was then exerted by the hydraulic press to produce pellets.

The acoustic signal produced during laser-sample interaction was measured using an electret microphone. A circuit diagram of the microphone system built to measure the acoustic signal is shown in Figure 5.1. The signal trace from the microphone was displayed on an oscilloscope (LeCroy) and averaged over the number of laser shots required in each experiment. The average signal trace was then transferred to the PC, where the absolute value of each point was calculated using a Visual Basic for Applications (VBA) macro. The absolute value of each point in the trace was then integrated to produce a value representative of the magnitude of the acoustic signal. The integrated signal was baseline corrected by subtracting the value of the positive offset of the acoustic signal (see Figure 5.2).

## 5.3 *Validity of Acoustic Wave Normalisation*

A typical acoustic signal trace obtained during single-shot laser-induced breakdown of Victorian brown coal is shown in Figure 5.2. A laser irradiance of 20 GW cm<sup>-2</sup> was used to produce this signal. The trace shows that the first peak of the signal occurred 0.65 ms after the start of the laser pulse. Given that the speed of sound in air at 20°C and 1 atm is 343 ms<sup>-1</sup>, this corresponds to the sound travelling 22 cm, which was precisely the distance between the microphone and the point at which laser-sample interaction occurred. The remaining peaks represent the interference pattern of the original sound wave and the reflections off the sides of the box that surrounds the apparatus. Initially the acoustic signal was measured by using a boxcar integrator to integrate the signal over only a single

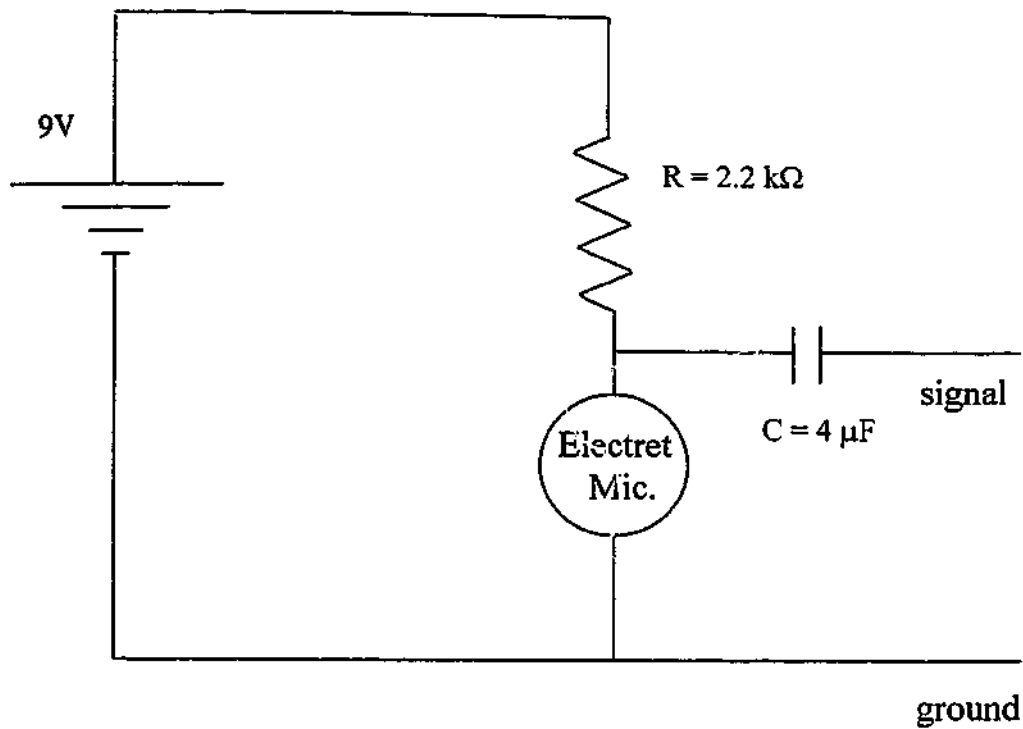


Figure 5.1. Circuit diagram of the microphone system used to measure the acoustic signal during LIBS experiments.

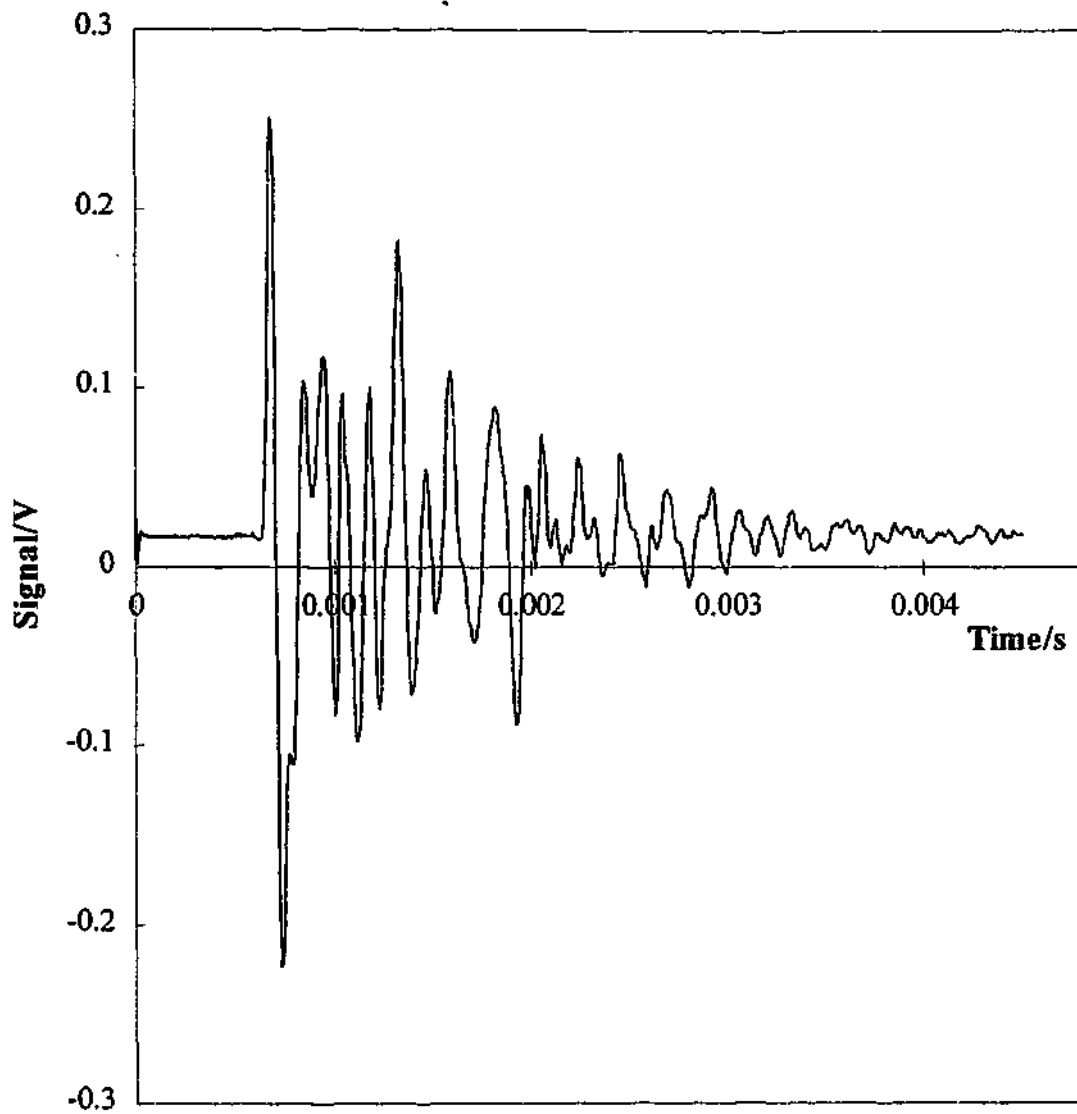


Figure 5.2. A typical trace of a laser-induced acoustic signal of Latrobe Valley brown coal, obtained using a laser irradiance of  $20 \text{ GW cm}^{-2}$ .

peak in the trace. However, as laser irradiance increased, the start of the acoustic signal moved closer to the start of the laser spark in time. It is likely that, when high laser irradiances are used, the acoustic shock wave is produced sooner than when low irradiances are used because the amount of energy required to produce the shock wave is acquired sooner. The method of signal integration detailed above did not vary linearly with either laser irradiance or elemental emission intensity in this instance because the maximum measurement interval able to be observed by the boxcar (20  $\mu$ s) was smaller than the peak width. Thus the entire acoustic signal was integrated in order to minimise the effects of changes in peak position.

In order to confirm the validity of using the acoustic shock wave for emission signal normalisation in LIBS analyses, the acoustic signals produced during laser-induced breakdown of Victorian brown coal were measured at a range of laser irradiances. One hundred plasma emission spectra, each from a single laser shot, were obtained for each spectral region analysed. Baseline corrected peak areas were measured from each spectrum and subsequently averaged. The associated acoustic signal was also averaged over these 100 laser shots. This was repeated 3 times at each of the laser irradiances used. The laser energy, which was measured immediately prior to each experiment by a Joule meter (Scientech, Model 38-1UV5), varied between 10 and 70 mJ/pulse. This resulted in laser irradiances ranging from 5.31 to 37.1 GW cm<sup>-2</sup>.

The effects of laser irradiance on the magnitude of the integrated acoustic signal are shown in Figure 5.3. The integrated, background subtracted acoustic signal increases linearly with laser irradiance. The error bars represent the 95 % confidence limits and an R<sup>2</sup> value of 0.98 was obtained. Thus, from this plot it seems possible that the acoustic wave could be used to measure and correct for fluctuation in the laser irradiance during sample breakdown.

Figure 5.4 shows how sample mass loss varies with laser irradiance in laser-induced breakdown of Latrobe Valley brown coal. It is difficult to measure mass loss simply and with a great deal of accuracy. In this instance the sample was simply weighed before and after each set of 200 laser shots. Even using such a simple technique, it appears that there is a linear relationship between mass loss and laser irradiance.

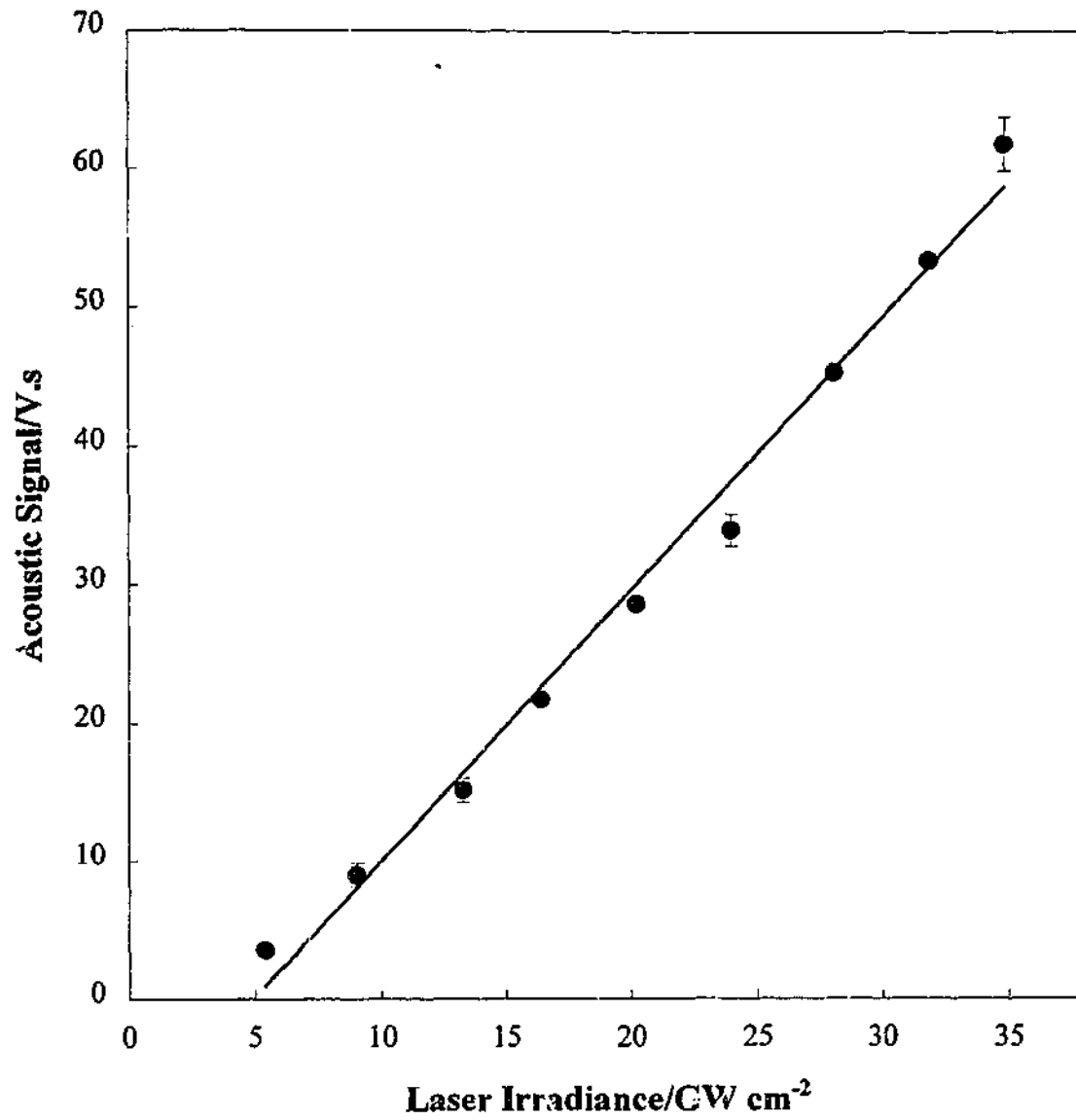


Figure 5.3. Laser-induced acoustic signal from a sample of Latrobe Valley brown coal as a function of laser irradiance.

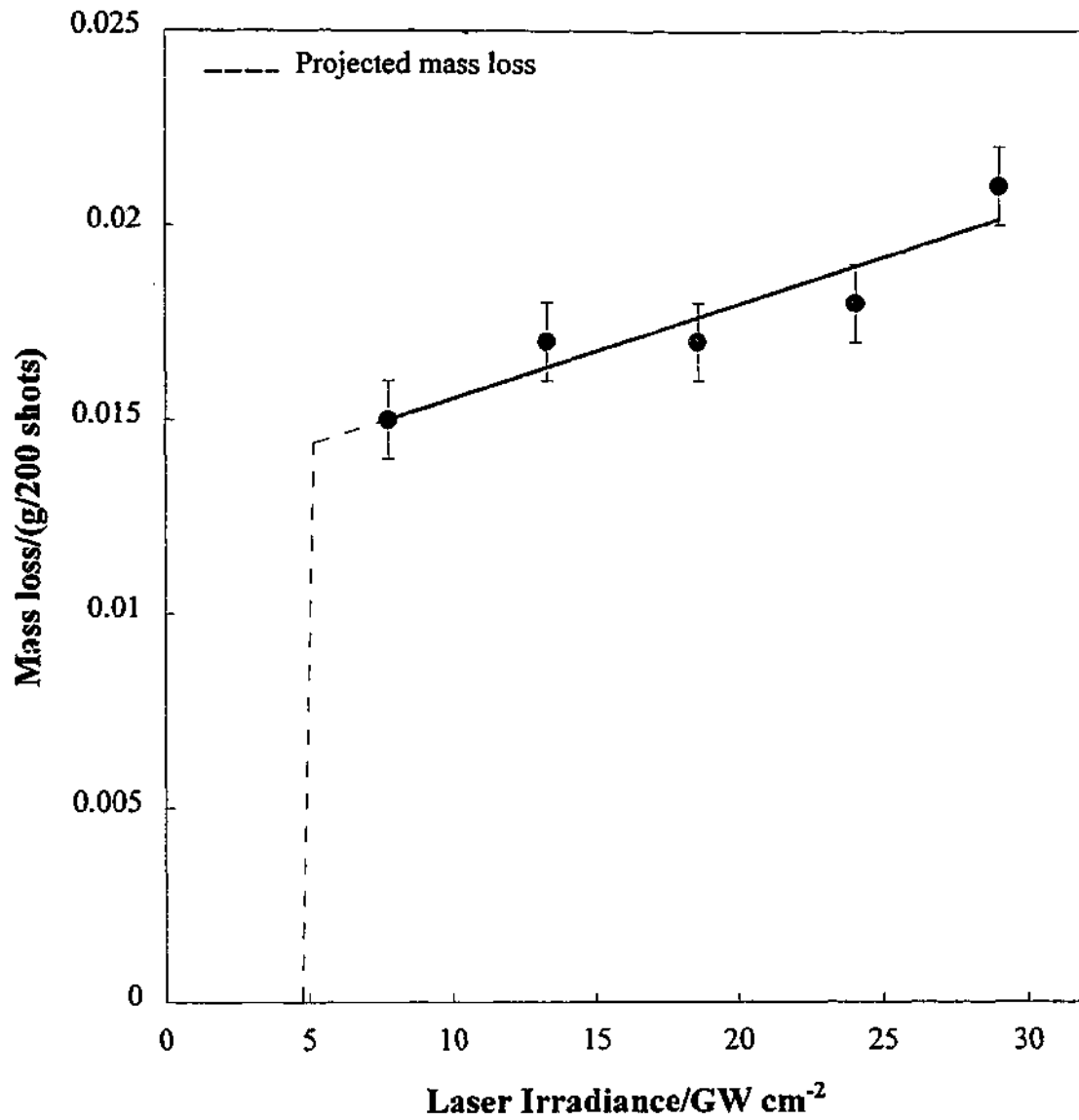


Figure 5.4. Laser-induced mass loss from Latrobe Valley brown coal as a function of laser irradiance.

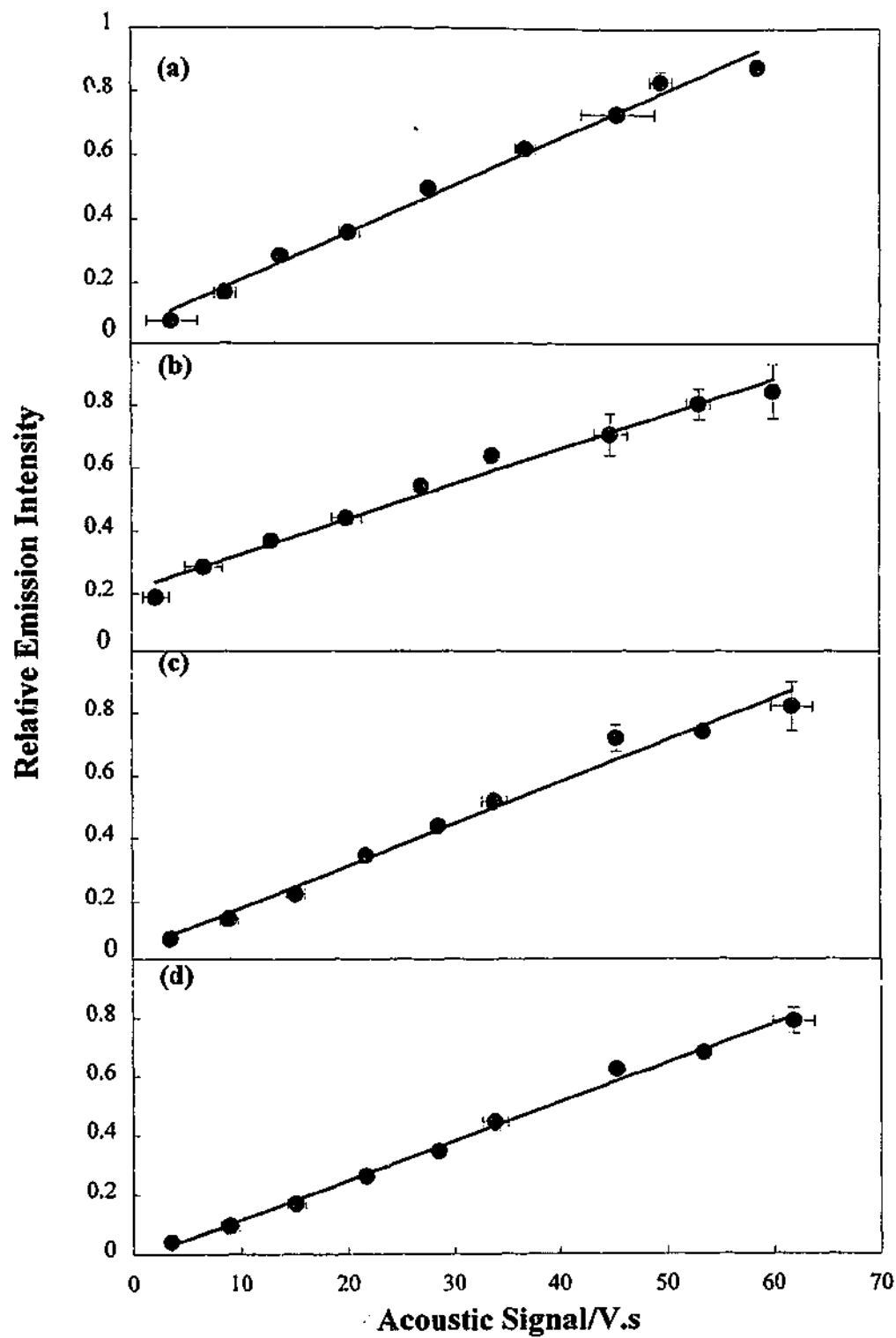


Figure 5.5. Elemental emission intensity as a function of acoustic signal for (a) Ca at 422.7 nm, (b) Na D lines, (c) Mg at 285.2 nm, and (d) C at 247.9 nm.

The regression lines in Figures 5.3 and 5.4 do not pass through the origin. The reason for this is that a minimum irradiance is required for laser-induced breakdown and, hence, mass loss. This threshold value is dependent on the sample density, heat of vaporisation and thermal diffusivity. Therefore, below the threshold irradiance, there will be no observable mass loss or acoustic signal. Once this threshold is reached, it is expected mass loss will increase with laser irradiance. See Figure 5.4 for predicted mass loss behaviour.

The variation of elemental emission intensity with background subtracted acoustic signal is shown in Figure 5.5. It can be seen that Mg, Na, Ca and C neutral emission peak areas all increase linearly with the integrated acoustic signal until the latter is approximately 50 Volt seconds. The Mg, Ca and Na lines experience some self-absorption above this point, which is indicated by the non-linear relationship between emission intensity and acoustic signal. This phenomenon is to be expected because these transitions terminate in the ground state – i.e. they are resonance lines. It should be noted that the acoustic signal measurements used in these plots are each the average of 3 traces from the CRO that were, in turn, the average signals from 100 laser pulses.

#### *5.4 The Effect of Sample Matrix on Acoustic Signal Levels*

Twelve samples were analysed using the experimental configuration shown in Chapter 3 to determine whether different sample matrices resulted in different acoustic signal levels at constant laser irradiance. These samples consisted of a black coal, a brown coal, a fused XRF pellet (10% mineral, 90% LiBO<sub>2</sub>), a standard copper alloy, two cement samples, and six cement ingredients (gypsum, ironstone, limestone, fly ash, clay from Birdwood (South Australia) and clay from Moculta (South Australia)). Sample pellets were produced using the methods described earlier. Acoustic signals were then obtained from laser interaction with each sample. The measurements were repeated twice for each sample. The laser energy remained at 15 mJ/pulse for each analysis. The variation of acoustic signal with sample matrix is shown in Figure 5.6.

It can be seen that different sample matrices give rise to different acoustic signal levels. The two cement samples and three of the cement ingredients all produced acoustic signals of similar magnitude. Since these samples all contained 20% orthoboric acid and the two cements were partially comprised of the three ingredients, this is not unexpected. The

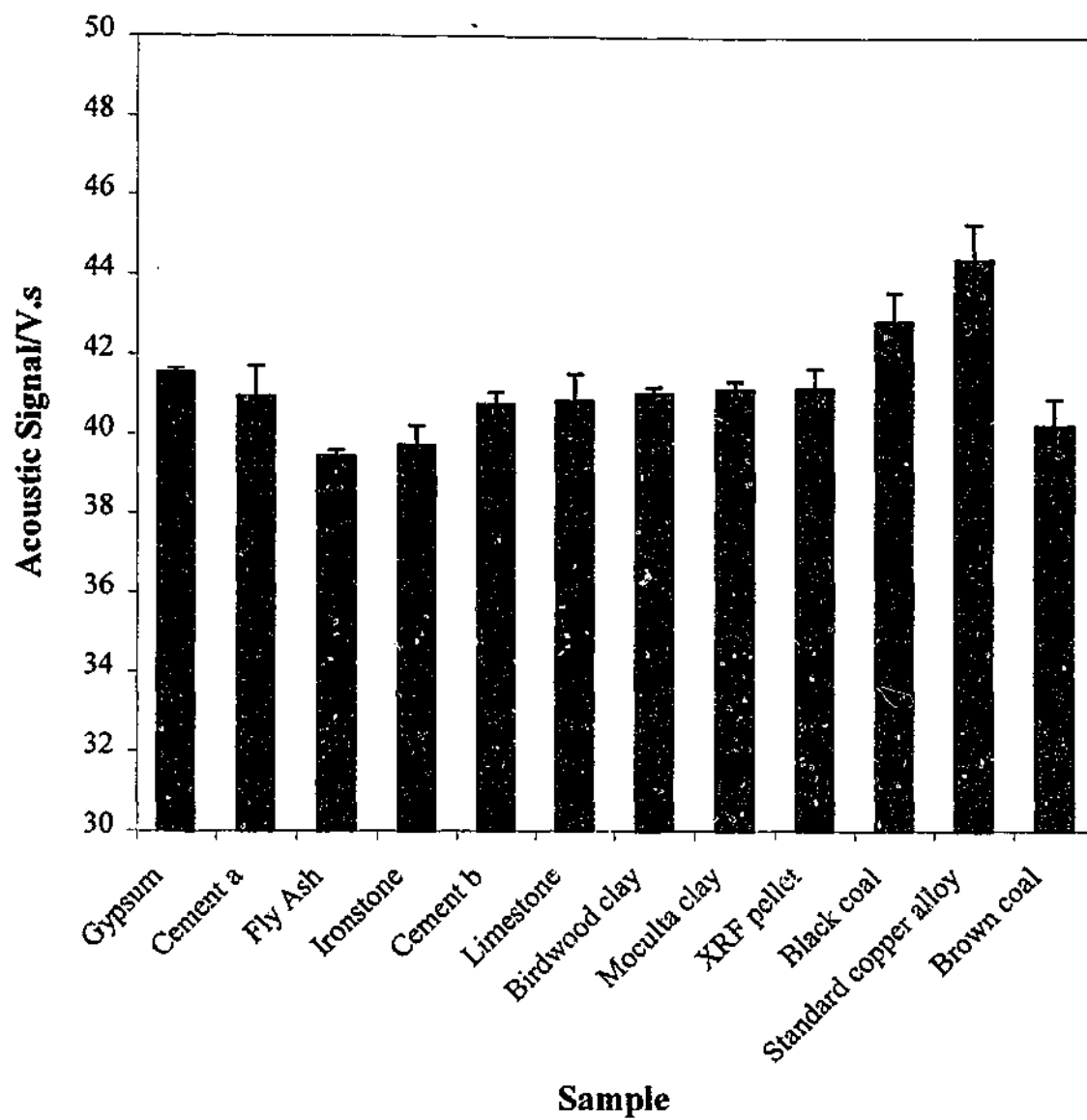


Figure 5.6. Variation of the acoustic signal with sample matrix.

chemical compositions of these samples, which are listed in Table 5.1, show that these five samples were similar and particularly characterised by high levels of Si. The copper alloy produced the largest acoustic signal. This is likely to be due to the thermal conductivity of the alloy, which would be higher than for the other samples. This means that the breakdown threshold for this sample is lower and more energy remains for plasma formation. The variation of acoustic signal with sample matrix indicates that it may be possible to correct for matrix effects in LIBS using this signal.

Table 5.1. Chemical composition of samples that produced similar acoustic signals.

|           | Cement a | Cement b | Birdwood<br>clay | Moculta<br>clay | Limestone |
|-----------|----------|----------|------------------|-----------------|-----------|
| Mn (wt %) | 0.01     | 0.02     | 0.01             | -               | -         |
| Ca (wt %) | 36.60    | 45.30    | 0.30             | 0.20            | 32.60     |
| Na (wt %) | 0.60     | 0.20     | 0.10             | 0.10            | 0.10      |
| Mg (wt %) | 1.10     | 0.90     | 0.20             | 0.10            | 0.60      |
| K (wt %)  | 0.50     | 0.40     | 0.50             | 0.40            | 0.20      |
| Ti (wt %) | 0.40     | 0.20     | 0.80             | 0.70            | 0.10      |
| Fe (wt %) | 2.50     | 2.40     | 2.20             | 3.50            | 0.70      |
| Al (wt %) | 5.20     | 2.70     | 13.80            | 9.10            | 0.80      |
| Si (wt %) | 13.30    | 9.80     | 22.60            | 30.90           | 4.90      |
| S (wt %)  | -        | -        | 0.08             | -               | -         |

Thus, the use of the laser-produced acoustic shock wave for signal normalisation in LIBS appears extremely promising. The magnitude of this acoustic signal is dependent upon laser irradiance and sample matrix and varies with elemental emission intensity. Hence it shows the attributes that would be required for signal normalisation. In the next section the ability of the acoustic signal to normalise LIBS data will be investigated.

### 5.5 Comparison of Normalisation Methods

Three signal normalisation methods were applied to the results for 4 elements found in the cements and their ingredients; Ca, Fe, Mg and Si. These elements were chosen for

investigation because they possessed emission lines with the necessary properties to perform the normalisation (see below) or appeared in the same spectral region as elements with these properties. Aluminium, despite being a major element in most of these samples, was not studied because it did not have emission lines with the necessary properties.

The first normalisation procedure tested involved using the method described by Chaléard *et al.* [1]. They normalised the emission signals obtained in their work by dividing the emission intensity by a factor comprised of the integrated acoustic signal ( $A_s$ ) and a temperature normalisation coefficient ( $r$ ) according to:

$$\frac{I}{A_s e^{-E_u/r}} \quad (5.1)$$

where:

$$r = \frac{E_2 - E_1}{\ln \frac{I_1}{I_2} + \ln \frac{g_2 A_2}{g_1 A_1}}$$

and  $E_1$  and  $E_2$  are the upper energy levels of the two emission lines used in the calculation of the  $r$  value,  $I_1$  and  $I_2$  are the intensities of the two lines,  $g_1$  and  $g_2$  are the degeneracy factors of the atomic states,  $A_1$  and  $A_2$  are the emission rates for the two transitions.  $E_u$  is the upper energy level of the line being used for calibration. Therefore, this normalisation process requires that one of the elements within the spectral region being analysed has two emission lines in this region that originate from different energy levels. The emission line being normalised can be one of those used to calculate  $r$  or from another element with lines in the spectral region being measured. The emission lines used and their properties are detailed in Table 5.2.

In the second normalisation method, the peak area of the elemental line of interest was simply divided by the integrated acoustic signal:

$$\frac{I}{A_s} \quad (5.2)$$

In the final normalisation technique only the temperature normalisation coefficient is used:

$$\frac{I}{e^{-E_u/r}} \quad (5.3)$$

Thus, the individual and combined effects of acoustic signal and temperature normalisation may be measured and compared.

Table 5.2. Elemental emission lines used in acoustic normalisation studies and their properties.

| Element | Wavelength/nm | $E_k/\text{cm}^{-1}$ | $A_{ki}/10^8\text{s}^{-1}$ | $g_k$ |
|---------|---------------|----------------------|----------------------------|-------|
| Ca      | 422.67        | 23652                | 2.18                       | 3     |
|         | 430.25        | 38552                | 1.36                       | 5     |
| Si      | 263.13        | 53387                | 0.97                       | 3     |
|         | 288.16        | 40992                | 1.89                       | 3     |
| Mg      | 285.21        | 35051                | 0.27                       | 3     |
| Fe      | 438.35        | 34782                | 0.50                       | 11    |

### 5.5.1 Normalisation of Ca emission

Ca was chosen for normalisation because it has two emission lines originating from different energy levels in a 40 nm spectral region (see Table 5.2), within the width of the spectral window obtained using the highest resolution grating in the ICCD setup. Only seven of the samples were chosen for normalisation; the two cements, limestone, gypsum, fly ash, ironstone and the black coal. Figure 5.7 shows the ratios of peak areas of the 430.25 nm line to the 422.67 nm line for each sample. It can be seen that similar values are obtained for the seven samples used in the normalisation process. Most of these samples are characterised by high Ca levels. The ratios of the samples with low Ca (less than 1 %) cover a wide range of values, varying from 0.2 to 0.73. As the Ca line at 430.25 nm is relatively weak, it is likely that at low concentrations its intensity is more sensitive to background noise, resulting in some anomalous results. Thus, the normalisation processes

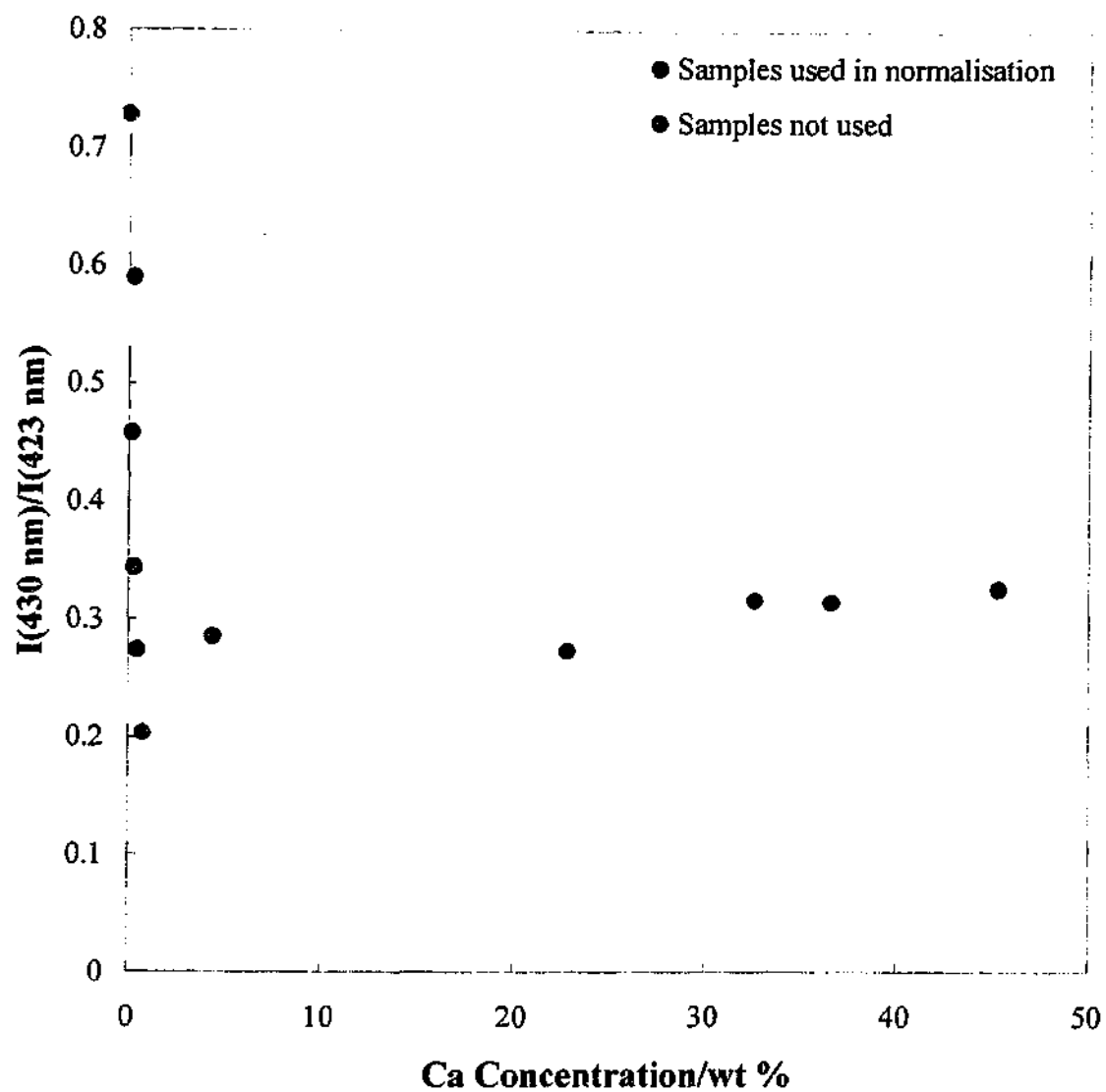


Figure 5.7. Variation of the intensity ratio of the 430.25 nm emission line of Ca to the 422.67 nm emission line with Ca concentration.

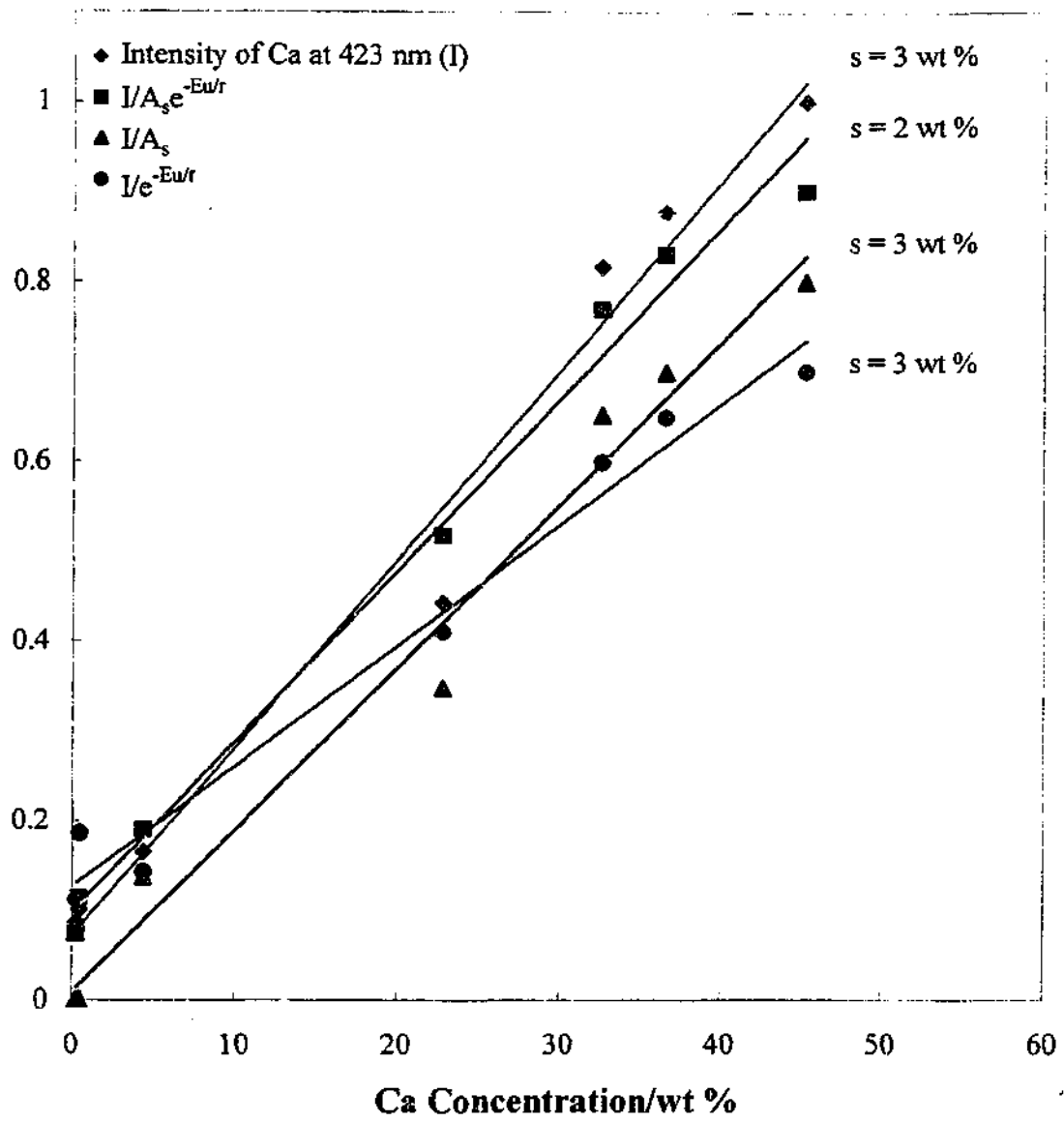


Figure 5.8. Results of the normalisation of Ca at 422.67 nm.

are restricted to samples whose peak area ratios are close to 0.3 in value. The results of the use of the three normalisation procedures for the Ca emission line at 422.67 nm as well as the original data are shown in Figure 5.8. Note that the intensity values have been scaled for the purposes of comparison.

The standard errors of prediction ( $s$ ) are shown beside each of the regression lines for both the uncorrected and normalised data in Figure 5.8. These error values indicate that the normalisation method proposed by Chaléard *et al.* [1] does improve the predictive abilities of the calibration curves. Furthermore, there is no perceivable improvement in the data when using only the acoustic signal or the temperature normalisation coefficient for normalisation.

### 5.5.2 Normalisation of Fe emission

Fe was chosen for normalisation because it has emission lines in the same 40 nm spectral region as the two Ca lines. For this reason it was possible to use the Ca lines to calculate the temperature normalisation coefficient ( $r$ ). Six of the seven samples used for Ca normalisation were also used here for the reasons detailed in the previous section. However, the black coal was not used here because its low iron level meant that the Fe line was not observable above the background noise. The normalised and original data for Fe at 438.35 nm are shown in Figure 5.9. Again the normalisation method proposed by Chaléard *et al.* [1] improves the precision of the calibration curve. In this instance, using only the acoustic signal to normalise the data also results in a slight improvement. The differences between the original and normalised Ca and Fe data are not great because there is already a relatively linear relationship between the raw signals and elemental concentrations. The data set also does not cover the entire concentration range; most of the samples have Fe concentrations below 5 wt %, while ironstone has 43.60 wt % iron. However, even the small improvement observed in this data set is beneficial when using LIBS for elemental quantification.

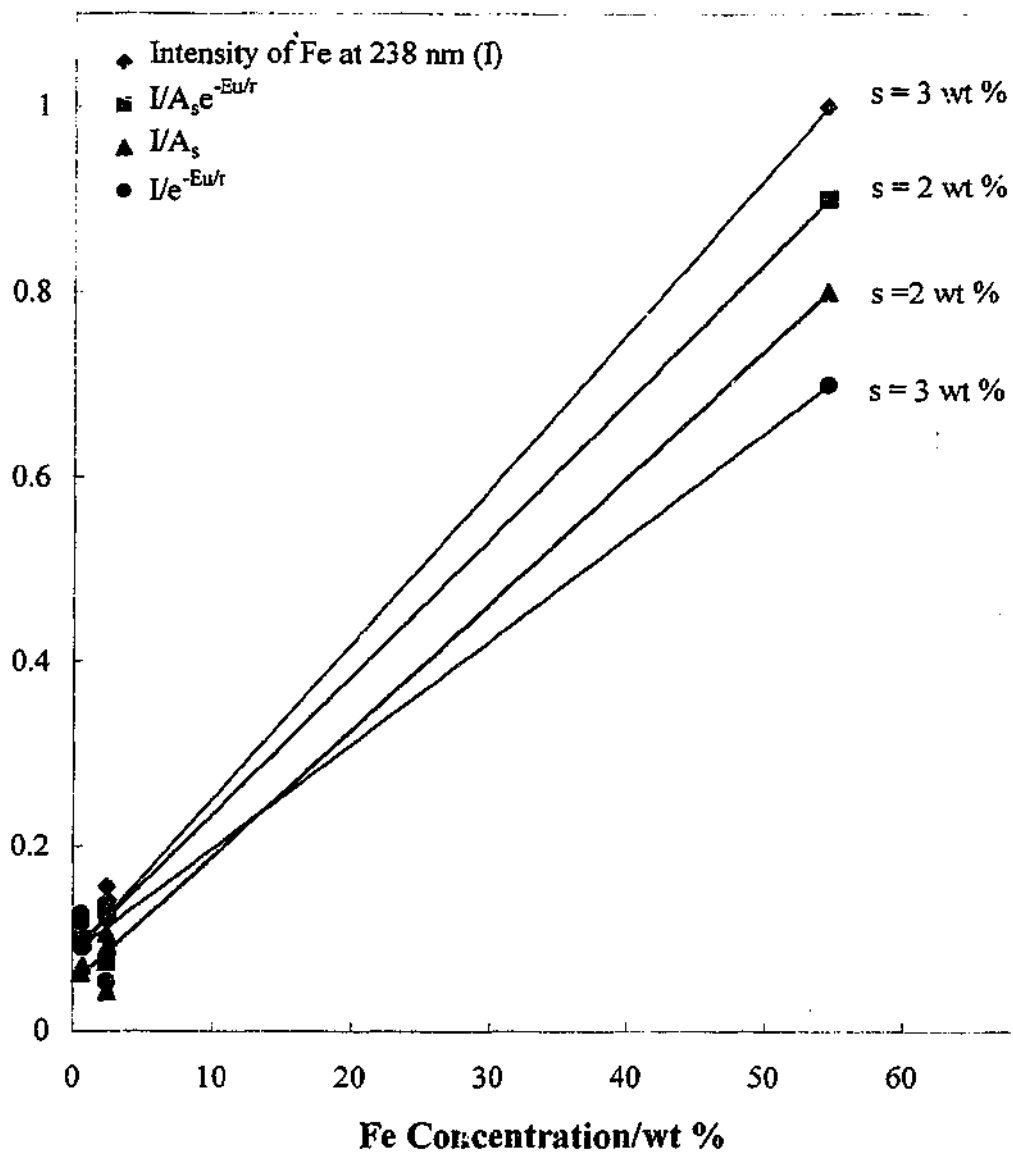


Figure 5.9. Results of the normalisation of Fe at 438.3 nm.

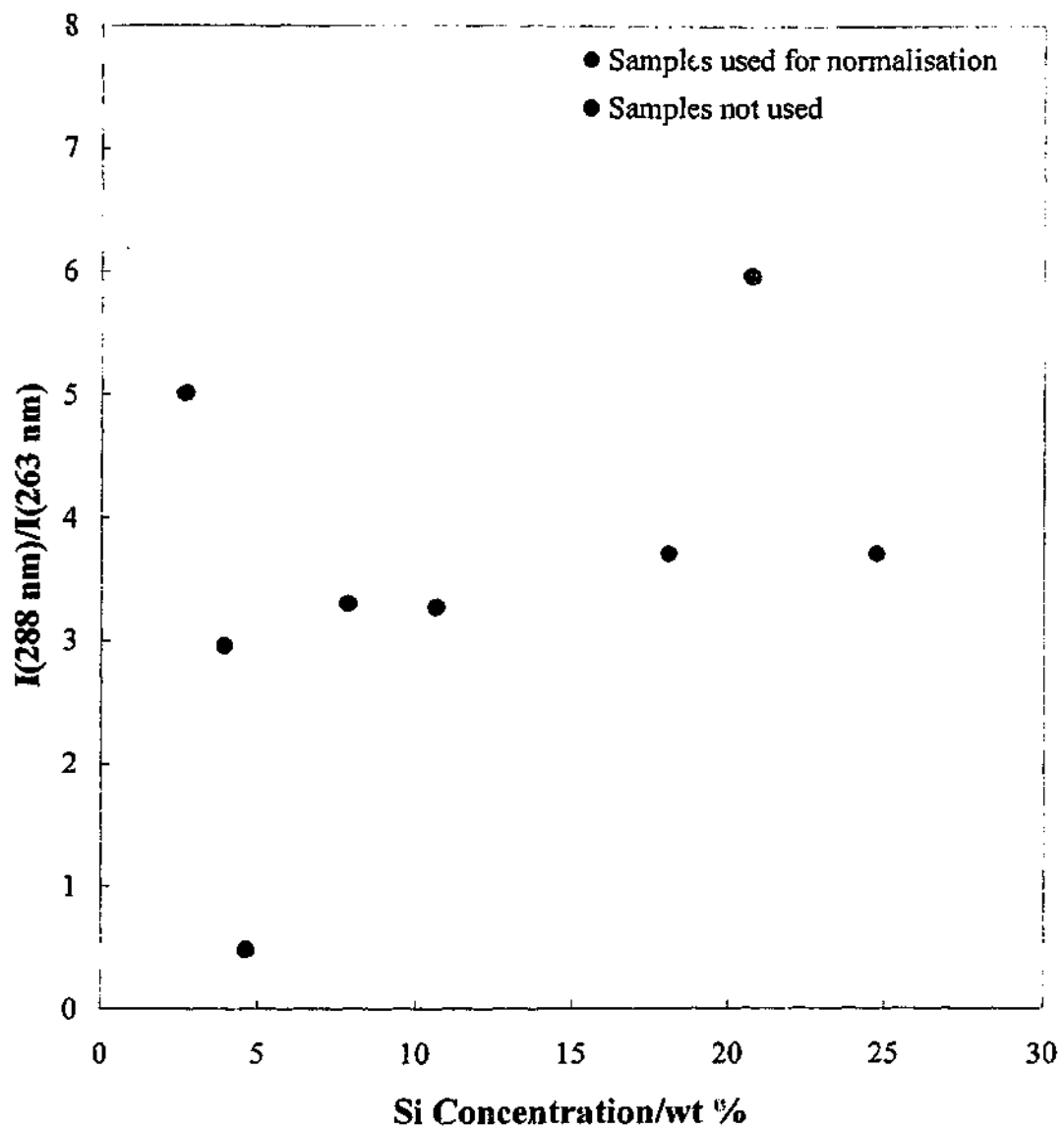


Figure 5.10. Variation of the intensity ratio of the 288.16 nm emission line of Si to the 263.13 nm emission line with Si concentration in cement and cement ingredients.

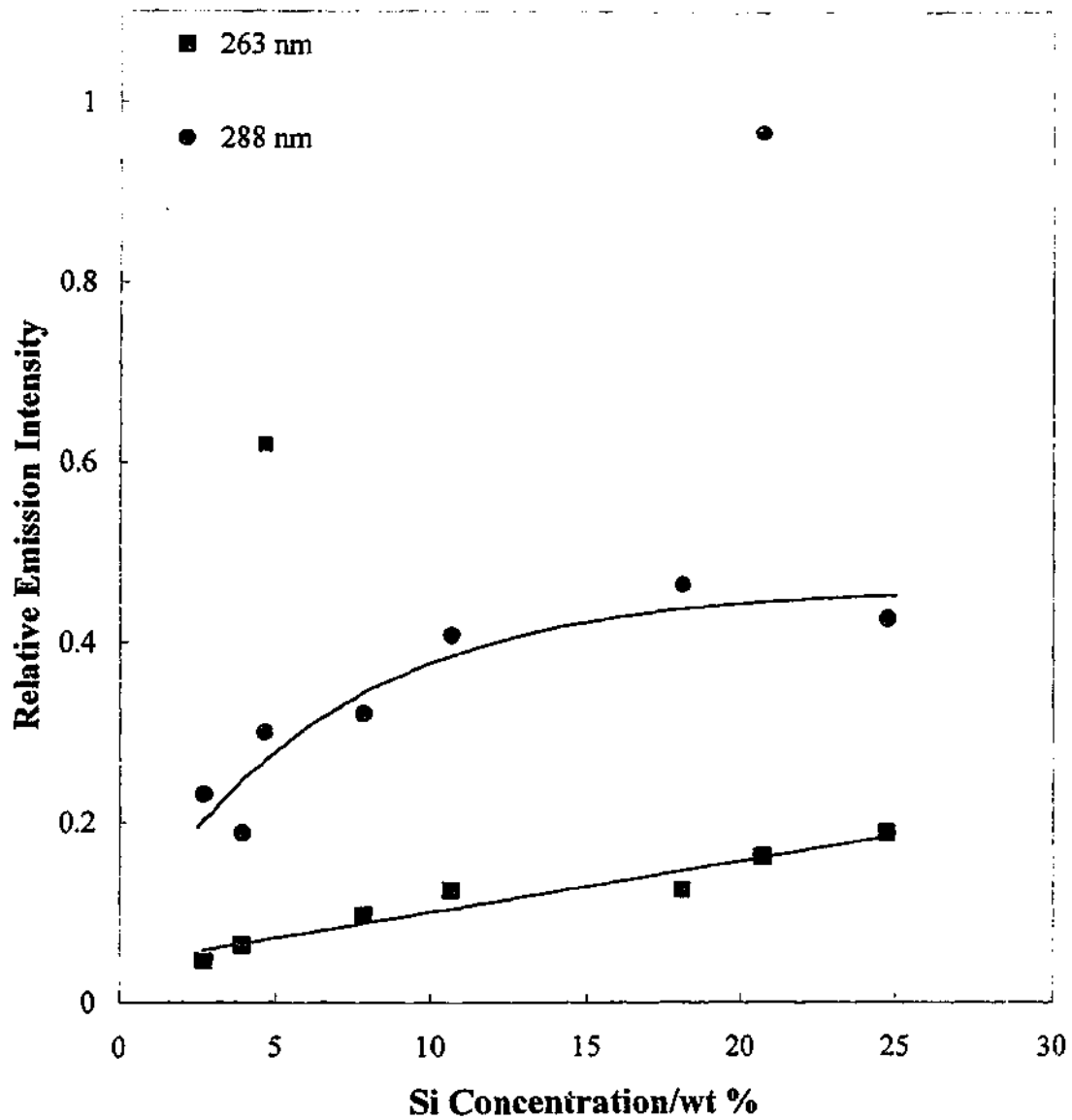


Figure 5.11. Variation of the emission intensities of the Si lines at 263.13 nm and 288.16 nm with Si concentration in cement and cement ingredients.

### 5.5.3 Normalisation of Si emission

Si was chosen for normalisation because, like Ca, it has two emission lines within a 40 nm range that have different upper energy levels. These lines and their properties are listed in Table 5.2. Only the cements and their ingredients were used for this study. The Si levels in the other samples were too low to observe the relatively weak emission line at 263.13 nm. The ratio of the 288.16 nm emission line to the 263.13 nm emission line is plotted against Si concentration for the cements and their ingredients in Figure 5.10. It can be seen that there are large differences in the value of this ratio, up to a two-fold difference between the average and maximum values. The emission intensities of the two lines are plotted against Si concentration in Figure 5.11. The reasons why the large variation in the line ratio occurred can be seen in this plot.

In the data set shown in Figure 5.11 there appear to be three anomalous points, where the intensity of one of the lines does not follow the trend indicated by the other points. These differences could conceivably be due to either spectral interference or matrix effects. It is more likely that the differences are caused by spectral interferences because it is unlikely that such variations in line ratios and hence plasma temperatures would occur under the conditions used. One of the anomalous points, with a Si concentration of 4.64 wt %, is the result from the ironstone spectrum. It is likely that the extremely high levels of Fe in this sample caused the numerous Fe emission lines in the region of 263 nm to interfere with the Si line at 263.13 nm, resulting in the abnormally high emission intensity. The anomalous point from the 288.16 nm emission line with a Si concentration of 20.72 wt % corresponds to the spectrum of fly ash. This sample contains high levels of Al (see Appendix A), so it is possible that the Al II emission line at 288.15 nm is interfering with the Si line at 288.16 nm. The emission intensity of the 288.16 nm line is also abnormally high with respect to the 263.13 nm line for the gypsum sample (with 2.696 wt % Si). This sample contains very high levels of Ca and so it is possible that the Ca (III) emission line at 288.18 nm is interfering with the Si line. All of these samples must be removed from the study in order to obtain meaningful results.

It also appears that the emission line at 288.16 nm suffers from self-absorption above approximately 20 wt %. Conversely, the relationship between Si concentration and the line at 263.13 nm seems to remain linear over this concentration range. While the 288.16

nm line is not a resonance line, its lower energy level lies at  $6299\text{ cm}^{-1}$  while the lower level of the 263.13 nm line lies considerably higher at  $15394\text{ cm}^{-1}$ . The self-absorption of the 288.16 nm emission line leads to a decrease in its ratio with respect to the 263.13 nm line at high Si concentrations. Thus, the data point with 24.72 % Si (the Moculta clay) should also be removed from the normalisation procedure. This leaves only four samples that can be used to test the signal normalisation procedures; the two cements, the limestone and the Birdwood clay. The uncorrected and normalised Si data are shown in Figure 5.12. The original data shows that the sample with the highest Si content, the Birdwood clay, suffers from either a small amount of self-absorption or matrix effects. However, the normalisation procedure proposed by Chaléard *et al.* [1] seems to correct for this effect. The linear regression line has a much better fit through the normalised data than the original results. The standard error of prediction is also dramatically. Again, using both the acoustic signal and then temperature normalisation coefficient is more effective than using either on its own.

#### 5.5.4 Normalisation of Mg emission

Mg was chosen for normalisation because some of its emission lines lie in the same spectral region as the Si lines used above. For the reasons discussed in the previous section, only four of the samples could be used in the normalisation study. These four samples were the two cements, limestone, and Birdwood clay. The original and normalised Mg data are shown in Figure 5.13. The original Mg data appears to suffer from self-absorption and/or matrix effects above approximately 0.5 wt %. Again, the normalisation process proposed by Chaléard *et al.* [1] seems to correct for these effects. Figure 5.13 shows that the linear regression line has a better fit through the normalised data than the original data. This is also indicated in the improvement in the standard errors of prediction when the data is normalised using both the acoustic signal and the temperature normalisation coefficient. The normalisation method incorporating both the acoustic signal and the temperature normalisation coefficient also results in a better  $s$  value than using either of these methods alone.

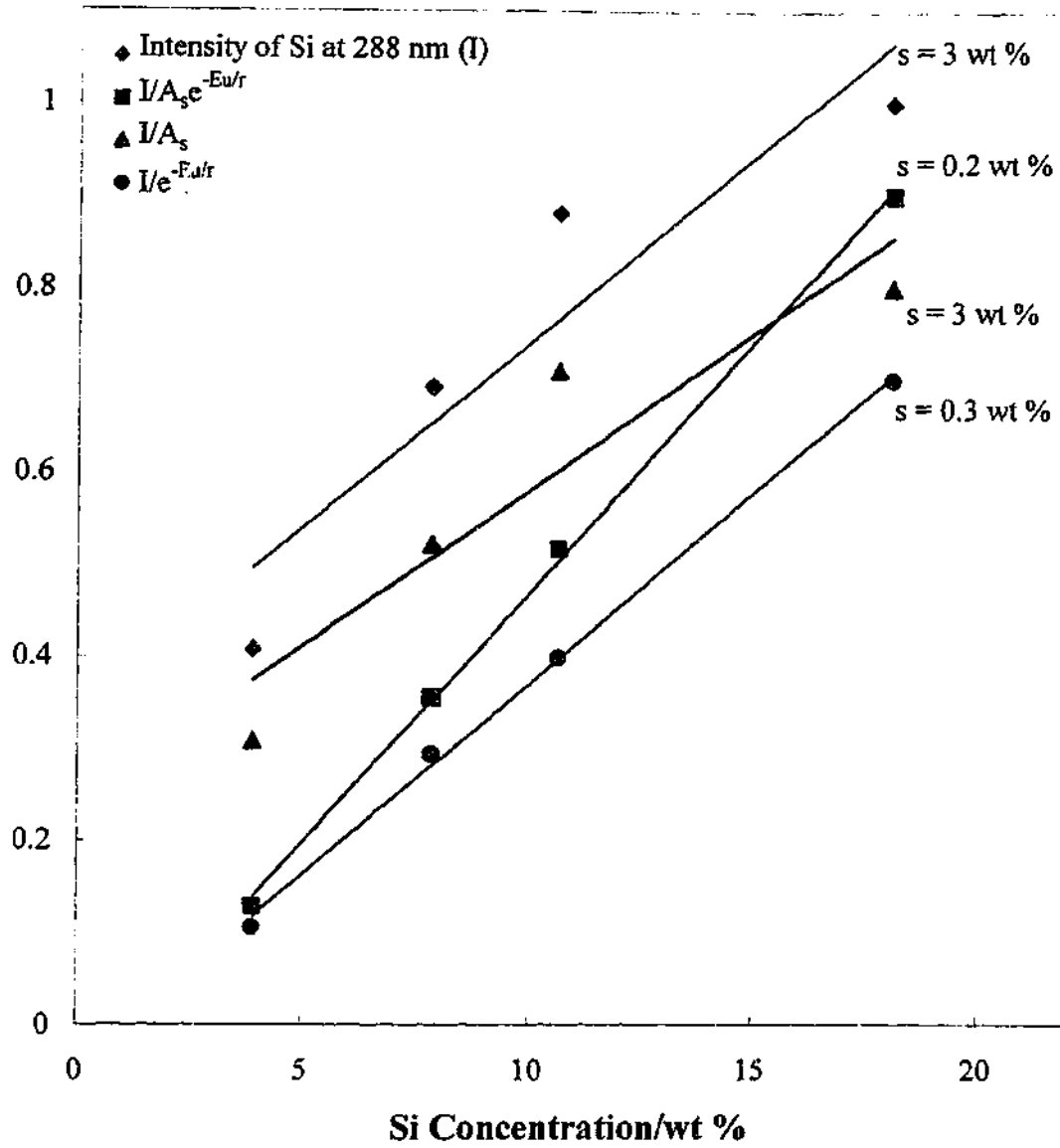


Figure 5.12. Results of the normalisation of Si at 288.16 nm.

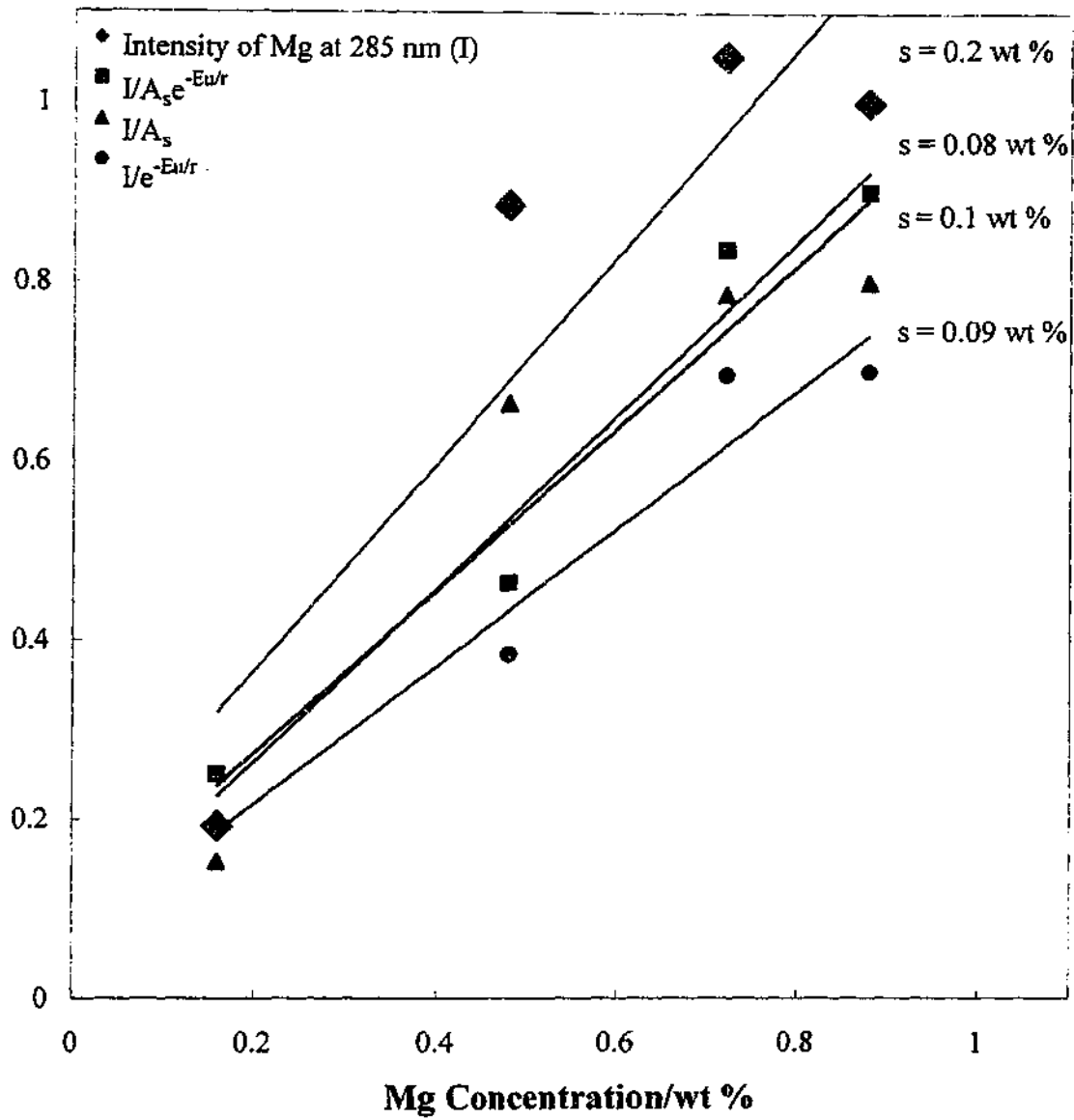


Figure 5.13. Results of the normalisation of Mg at 285.21 nm.

## 5.6 Conclusions

The effectiveness of three methods of signal normalisation in improving the results of elemental analysis obtained using LIBS has been investigated in this chapter. One of the three normalisation methods tested used the laser-induced acoustic signal, while another method incorporated a temperature normalisation coefficient. The third method, which was proposed by Chaléard *et al.* [1], incorporated both the acoustic signal and temperature normalisation coefficient.

The validity of using the laser-produced acoustic shock wave for LIBS signal normalisation was first determined experimentally. To this end, the relationships between the acoustic signal and laser irradiance, elemental emission intensity, and laser-induced mass loss were investigated. It was demonstrated that the magnitude of the laser-induced acoustic shock wave is linearly related to laser irradiance, elemental emission intensity and laser-induced mass loss. The effect of sample matrix on the laser-induced acoustic shock wave was also studied by measuring the acoustic signals produced from a number of different samples. These samples included a black coal, a brown coal, a fused XRF pellet, a standard copper alloy, two cement samples, and six cement ingredients. The acoustic signal was found to vary significantly with sample matrix. The copper alloy produced the largest acoustic signal of all the samples. It is likely that this was a result of its high thermal conductivity, which resulted in a relatively low breakdown threshold. Sample matrices with similar chemical composition were found to produce signals of similar magnitude upon laser ablation. These results suggest that it is valid to use the laser-induced acoustic shock wave as a means of signal normalisation in LIBS analyses.

The three signal normalisation methods were applied to the results of the LIBS analyses of four elements found in the cements and their ingredients; Ca, Fe, Mg, and Si. The most effective normalisation process for each of these elements was found to be that proposed by Chaléard *et al.* and which incorporates a temperature normalisation coefficient as well as the acoustic signal [1]. This method successfully normalised samples with Ca concentrations between 0.3 and 45 wt %, Fe concentrations between 0.7 and 55 wt %, Si concentrations between 4 and 18 wt %, and Mg concentrations between 0.16 and 0.88 wt %. The standard errors of prediction obtained improved from 3 to 2 wt % for Ca and Fe, 3

to 0.2 wt % for Si, and 0.2 to 0.08 wt % for Mg, when this normalisation procedure was implemented. The normalisation procedure was particularly encouraging for Si, with the standard error of prediction decreasing by an order of magnitude after normalisation.

Hence, it may be concluded that signal normalisation incorporating a measurement of the laser-induced acoustic shock wave as well as a temperature normalisation coefficient can be used to improve the precision of LIBS analyses. This method is independent of sample type and should be effective even when the focussing and detection conditions of the instrument used for analysis fluctuate.

---

*Determination of Coal Moisture Content and its Effects on  
LIBS System Response*

**6.1 Introduction**

Latrobe Valley brown coals are characterised by high levels of moisture, typically averaging between 49 and 70 % on a wet basis [2]. As moisture content has been shown to be inversely related to the specific energy of this coal [2], the high moisture content has been a major drawback to its use. Despite this, the five Latrobe Valley brown coal fired power stations currently provide approximately 85 % of Victoria's power [2].

Moisture content varies between and within coalfields and even a small decrease will result in a significant increase in the specific energy of the coal. Hence it is important to determine moisture levels in coal, prior to utilisation, to ensure that the efficiency of power generation is optimised. The current standard analytical methods used to measure coal moisture levels, azeotropic distillation and oven drying, are time consuming and labour intensive. On-line methods, including nuclear and microwave instruments, have also been used to determine moisture content in Latrobe Valley coals [4]. As mentioned in Chapter 2, there are disadvantages associated with using either of these instruments. Nuclear instruments do not provide the sensitivity required while microwave instruments cannot be used to monitor other properties of the coal. As mentioned in previous chapters, LIBS is time efficient, requires little sample preparation and can also be used to monitor the levels of the inorganic and mineral elements in Latrobe Valley brown coal. Hence, the exploration of its use for monitoring is desirable.

This chapter details the effects of coal moisture content on LIBS analyses of the inorganic constituents of Latrobe Valley brown coals. Sub-samples of a single coal were dried to produce a set of coals identical in composition except for moisture content. The intensities of elemental emission lines obtained during the laser-induced breakdown of these samples were then measured and compared. The intensities of elemental emission lines from different coal samples covering a wide range of moisture levels were also measured and compared.

The effects of coal moisture content on the intensities of C and H emission lines are also detailed within this chapter. Again, partially dried sub-samples of a single coal were used to monitor the variation of the intensity of C and H emission lines with coal moisture content. A sample set covering a wide range of coal moisture levels was also used in this analysis. The aim of this study was to develop a method for measuring the moisture content of Latrobe Valley brown coals from laser-induced emission spectra.

## 6.2 *Experimental Apparatus and Methodology*

A detailed description of the experimental set-up used in this work may be found in Chapter 3. For this section of work, the Nd:YAG laser was operated at 2 Hz and with an irradiance of  $20 \text{ GW cm}^{-2}$ , except where indicated otherwise. The detector delay and integration times used were the optimal 1 and 5  $\mu\text{s}$  respectively, as determined in Chapter 3, while a gain of 0.9 ADC counts/photoelectron was used to intensify the CCD response. The spectrograph grating with a line density of 1200 lines/mm and that provides 80 nm wide spectra was used except where indicated. A pressure of approximately 220 metric ton/m<sup>2</sup> was applied to 10 g quantities of coal with particle sizes of less than 3 mm to produce the sample pellets.

Samples identical in all respects except moisture content were produced using an oven drying method. Sixty gram quantities of a single coal were transferred to each of two 115 mm diameter petri dishes and weighed. The two samples were then placed in a nitrogen flushed drying oven at 105 °C for 10, 15, 25, 35 or 45 minutes. Samples were produced using each of these drying times to generate a set covering a range of moisture levels. After drying, each of the samples was weighed. One of each of the two-sample sets was then returned to the oven for 3 hours. These samples were subsequently re-weighed and returned to the oven for another 1 hour. This process was repeated until a constant weight was obtained for each sample. The mass loss from these samples after the initial 10, 15, 25, 25 or 45 minutes was then used to calculate the moisture content of their duplicate samples, which were stored in airtight containers for subsequent LIBS analyses.

### 6.3 *Effects of Coal Moisture Content on Inorganic Analyses using LIBS.*

Samples identical in all properties but moisture content were first analysed to determine the effects of moisture content on inorganic elemental emission intensity. Samples CRC/8-4-26/68, a Yallourn coal, and CRC/8-4-30/55, a blend of Yallourn, Loy Yang and Morwell coals, were used for this purpose. Analysis results for these samples using ICP can be found in Appendix A. The background subtracted peak areas of Na and Mg emission lines observed during LIBS are plotted against moisture content in Figure 6.1 for the Yallourn coal sample. The results from the blended coal sample are illustrated in Figure 6.2. The error bars in these plots represent the 95 % confidence intervals. Na and Mg were chosen for analysis because, as previously mentioned, they are two of the main inorganic elements found in Latrobe Valley brown coals. Figure 6.1(a) shows that the combined area of the Na D lines at 589.00 and 589.59 nm increases linearly with decreasing moisture content. The area of the Mg line at 285.21 nm also increases approximately linearly with decreasing moisture content until moisture levels fall below 58 %. Below this point the Mg emission intensity remains fairly constant.

It can be seen in Figure 6.2 that the Na and Mg emission intensities in the blended coal sample also increase linearly with decreasing moisture content until moisture levels reach approximately 50 %. Again, below this point, the emission intensities appear to plateau. It is possible that these trends are a result of the water affecting the laser-induced plasma chemistry or merely acting as a diluent. These possibilities will be discussed later in the chapter.

In order to investigate whether the water acts as a diluent, Na and Mg emission intensities were plotted against elemental concentrations on a wet basis for each of the two samples studied. The results for the Yallourn sample are shown in Figure 6.3, while the results for the blended coal sample may be found in Figure 6.4. Again, the error bars in these Figures represent the 95 % confidence intervals. From Figures 6.3 and 6.4 it can be seen that emission intensity increases with elemental concentration for both Na and Mg in both of the coals tested. The intensities of the emission peaks associated with Na and Mg in the blended coal and Mg in the Yallourn coal all plateau at high elemental concentrations.

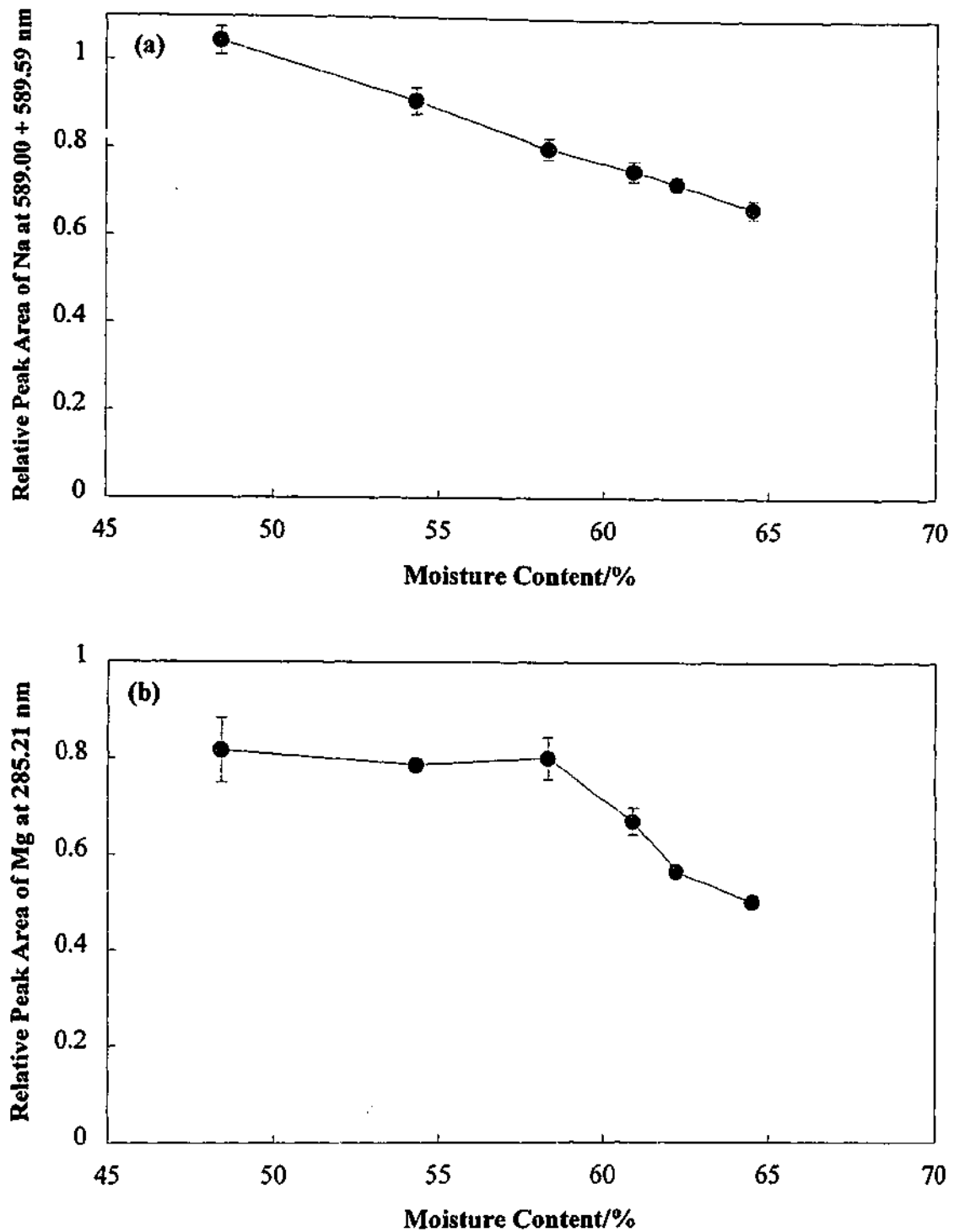


Figure 6.1. Variation of elemental peak area with moisture content in Yallourn coal sample CRC/8-4-26/68 for (a) the Na D lines (589.0 and 589.6 nm) and (b) Mg at 285.21 nm.

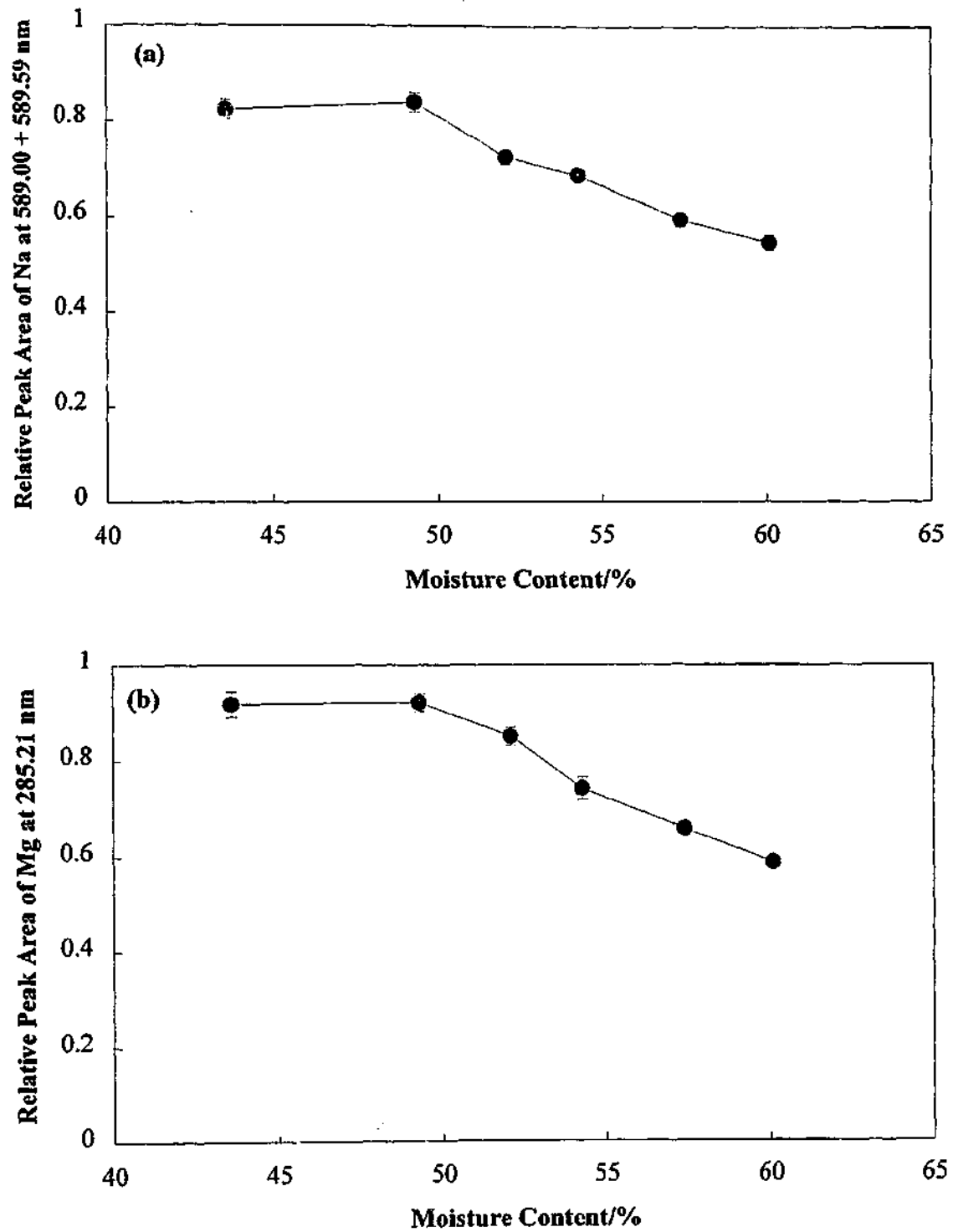


Figure 6.2. Variation of elemental peak area with moisture content in blended coal sample CRC/8-4-30/55 for (a) the Na D lines and (b) Mg at 285.21 nm.

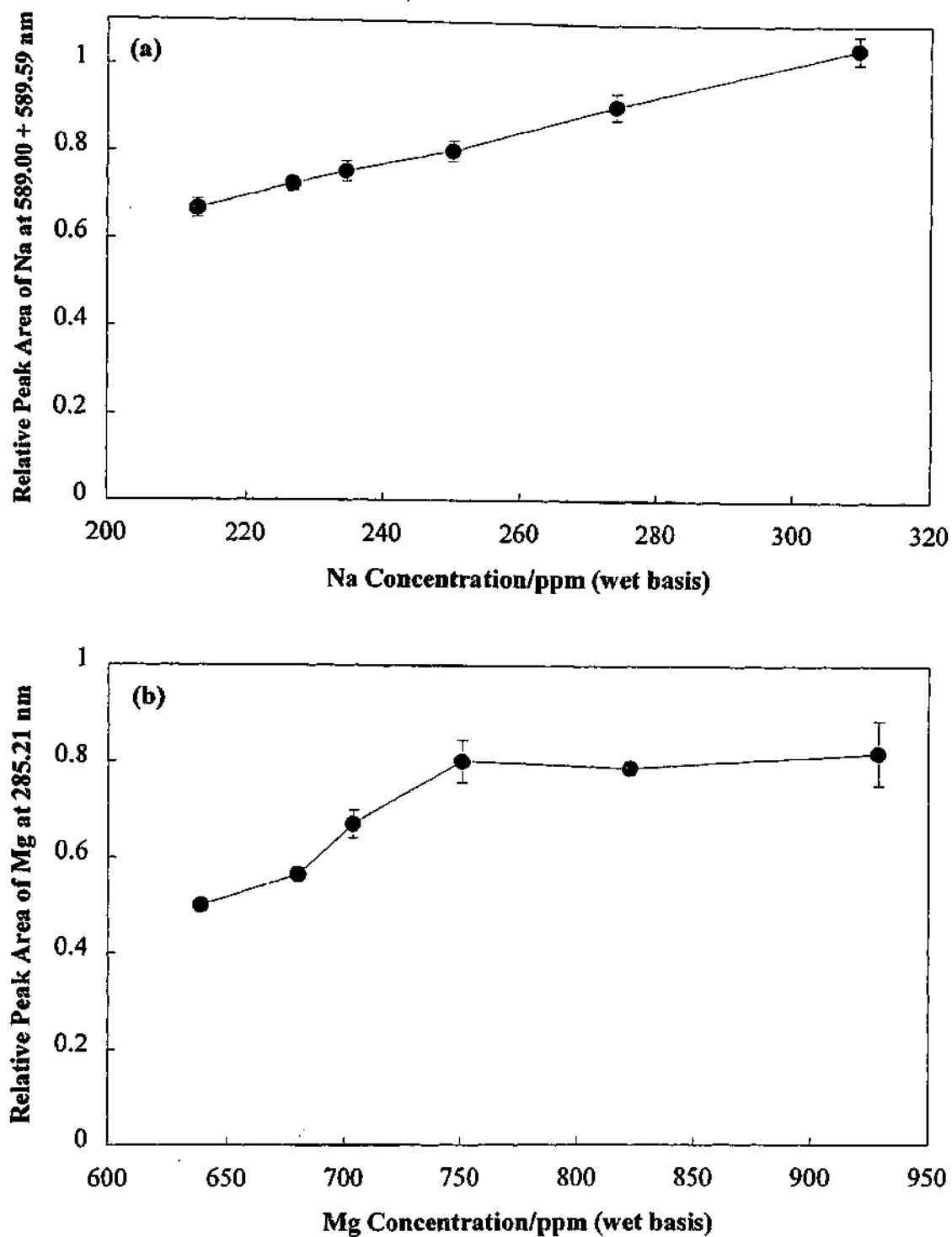


Figure 6.3. Variation of peak area with elemental concentration for Yallourn coal sample CRC/8-4-26/68 for (a) the Na D lines and (b) Mg at 285.21 nm.

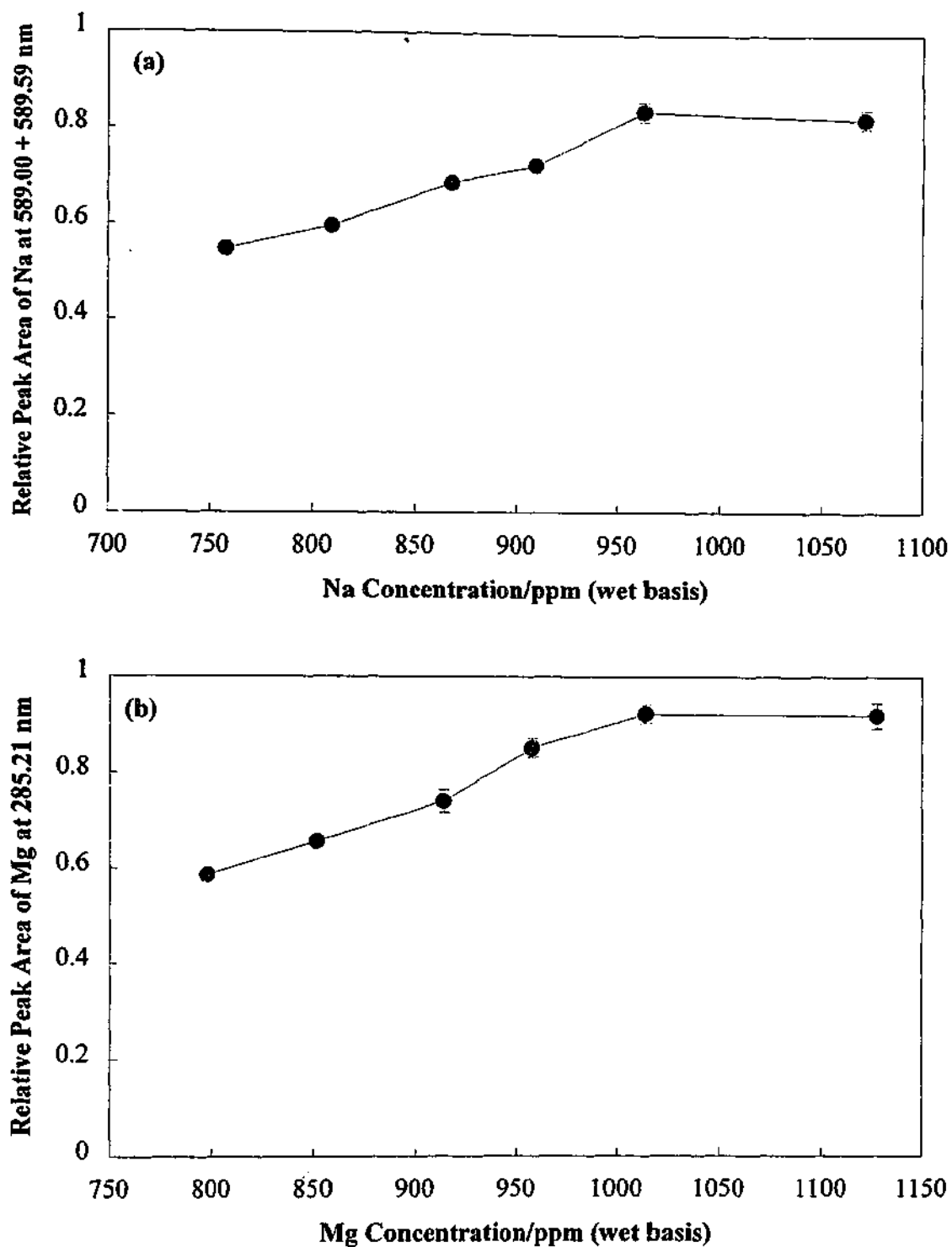


Figure 6.4. Variation of peak area with elemental concentration for blended coal sample CRC/8-4-30/55 for (a) the Na D lines and (b) Mg at 285.21 nm.

Similar trends are observed for some of the elemental calibration curves in Chapter 4 as a result of atomic self-absorption. Thus, it is possible that this effect is also the reason for the curves reaching a plateau here.

To determine the effects of moisture content on the measurement of inorganic elements in Latrobe Valley coals, 8 coal samples (CRC/8-4-26/58, 60-62, 64, 65, 68, 69) with different moisture content were analysed using LIBS. Figure 6.5 shows how emission intensity varies with elemental concentration for Na and Mg in these 8 samples. Note that the elemental concentrations are plotted on a wet basis, which factors in the diluting effects of the water in the coal. The error bars represent the 95 % confidence intervals for each point.

The plots in Figure 6.5 indicate that emission intensity, which in this case is measured using the background subtracted areas of the emission peaks, is linearly related to elemental concentration. The  $R^2$  value of the regression line fitted through the Na data is 0.94, while that for the regression line fit through the Mg data is 0.97. A key point is that the moisture content of the samples, which varies from 54.3 % to 64.5 %, does not appear to affect significantly the intensity of elemental emission.

These results agree with those obtained by Rusak and co-workers [119]. They found that the intensity of the Ca (II) line at 393 nm increased linearly with decreasing water content in LIBS analyses of  $\text{CaCO}_3$  powder. They postulated two possible causes for the reduction of emission intensity with increasing sample moisture. The first of these explanations was that increasing the water content of a sample increased the energy density required for breakdown. Krokhin [31] proposed that the minimum irradiance required for the laser-induced breakdown of a sample could be determined using the following equation:

$$F_{\min} = \rho L_v a^{1/2} t_e^{-1/2} \quad (6.1)$$

where  $F$  is the irradiance ( $\text{Wm}^{-2}$ ),  $\rho$  is the density of the sample ( $\text{kgm}^{-3}$ ),  $L_v$  is the heat of vaporisation of the sample ( $\text{Jkg}^{-1}$ ),  $a$  is the thermal diffusivity of the sample ( $\text{m}^2\text{s}^{-1}$ ) and  $t_e$  is the duration of the laser pulse (s). Like  $\text{CaCO}_3$  powder, when Latrobe Valley brown coals are dried, air-filled voids are formed [2]. Hence the bulk density, heat of

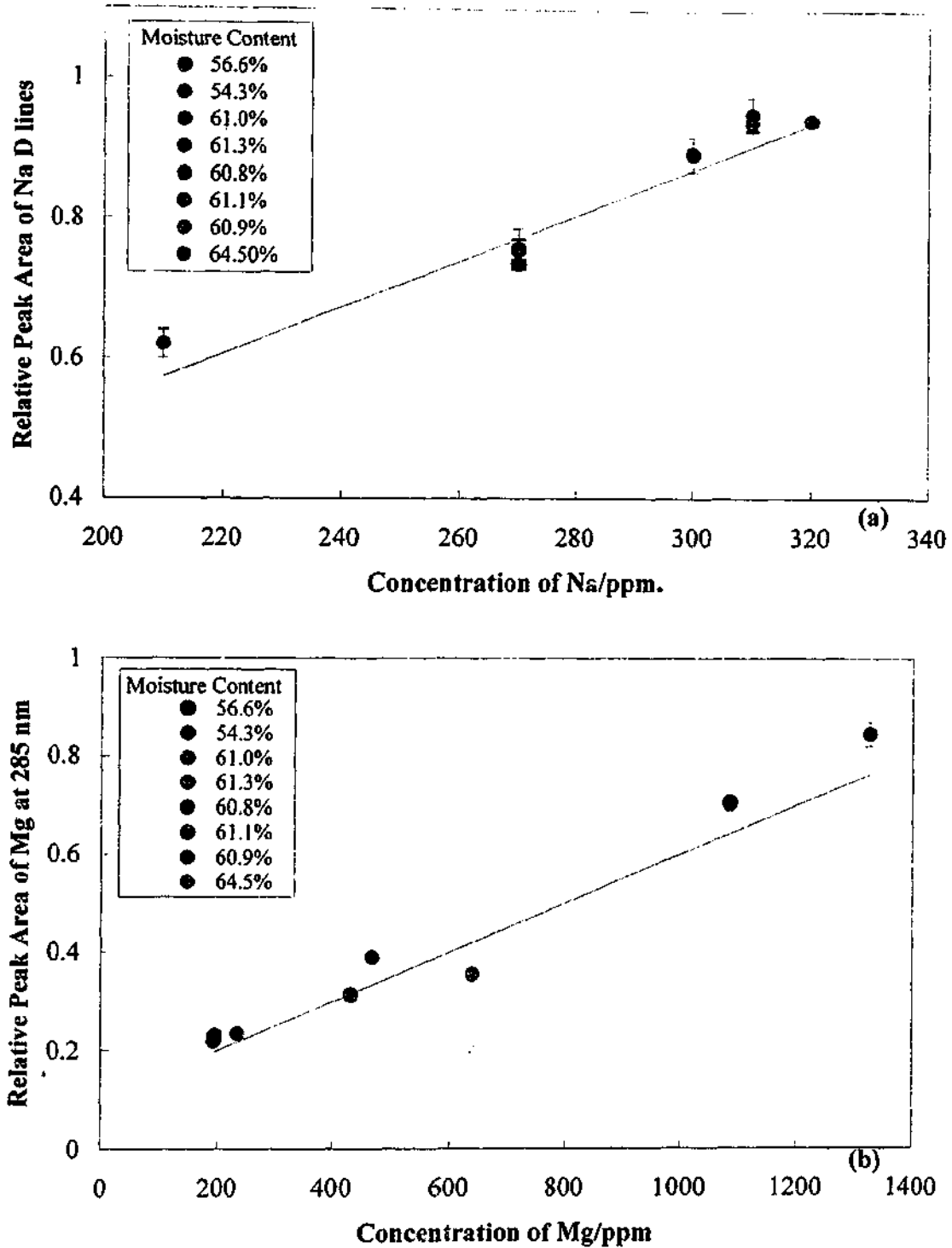


Figure 6.5. Variation of emission intensity with elemental concentration for 8 Latrobe Valley coal samples for (a) the Na D lines and (b) Mg at 285.21 nm.

vaporisation and diffusivity of the coals should decrease as water is replaced by air in the pores of the coals. The results of this are a decreased breakdown threshold and increased elemental emission intensity for a given laser irradiance.

The other explanation proposed by Rusak and coworkers [119] for the decrease of Ca (II) emission intensity with increasing sample moisture was that water comprises an increasing proportion of the sampling volume as its levels are increased. In other words, the water dilutes the concentration of the solid sample. This section of work proves that the water does dilute the concentration of the inorganic matter in the sample volume. However, it is unclear from this study of the inorganics whether the moisture content of Latrobe Valley coals also affects the bulk properties of the coals and, hence, the chemistry of the laser-induced plasma.

#### **6.4 *Effects of Coal Moisture on Carbon and Hydrogen Emission***

Samples identical in all properties except for moisture content were first analysed to determine the effects of moisture content on C and H emission intensity. The Yallourn and blended coals used in the previous section were also used here. Figure 6.6 shows how the intensity of the strongest H emission line, the H $\alpha$  line at 656.3 nm, varies with coal moisture content for the Yallourn and blended coals when using a laser irradiance of approximately 20 GWcm<sup>-2</sup>. The error bars indicate the 95 % confidence intervals. The way in which this emission line varies with moisture content is somewhat unexpected. At high moisture levels (> 58 %) the intensity of the H emission line decreases with increasing moisture content. Between approximately 50 and 58 % moisture the intensity of the H emission line is relatively constant. Below 50 % the intensity of H emission begins to decrease slightly with decreasing moisture content in the blended coal. Given that an increase in water content results in an increase in the amount of H in the sample, it might be expected that H emission intensity would increase with coal moisture content. However, these results seem to suggest that the increase in water content produces an increase in the sample breakdown threshold and hence a decrease in emission intensity for the reasons described in the previous section.

The variation of C emission intensity at 248 nm with coal moisture content is shown in

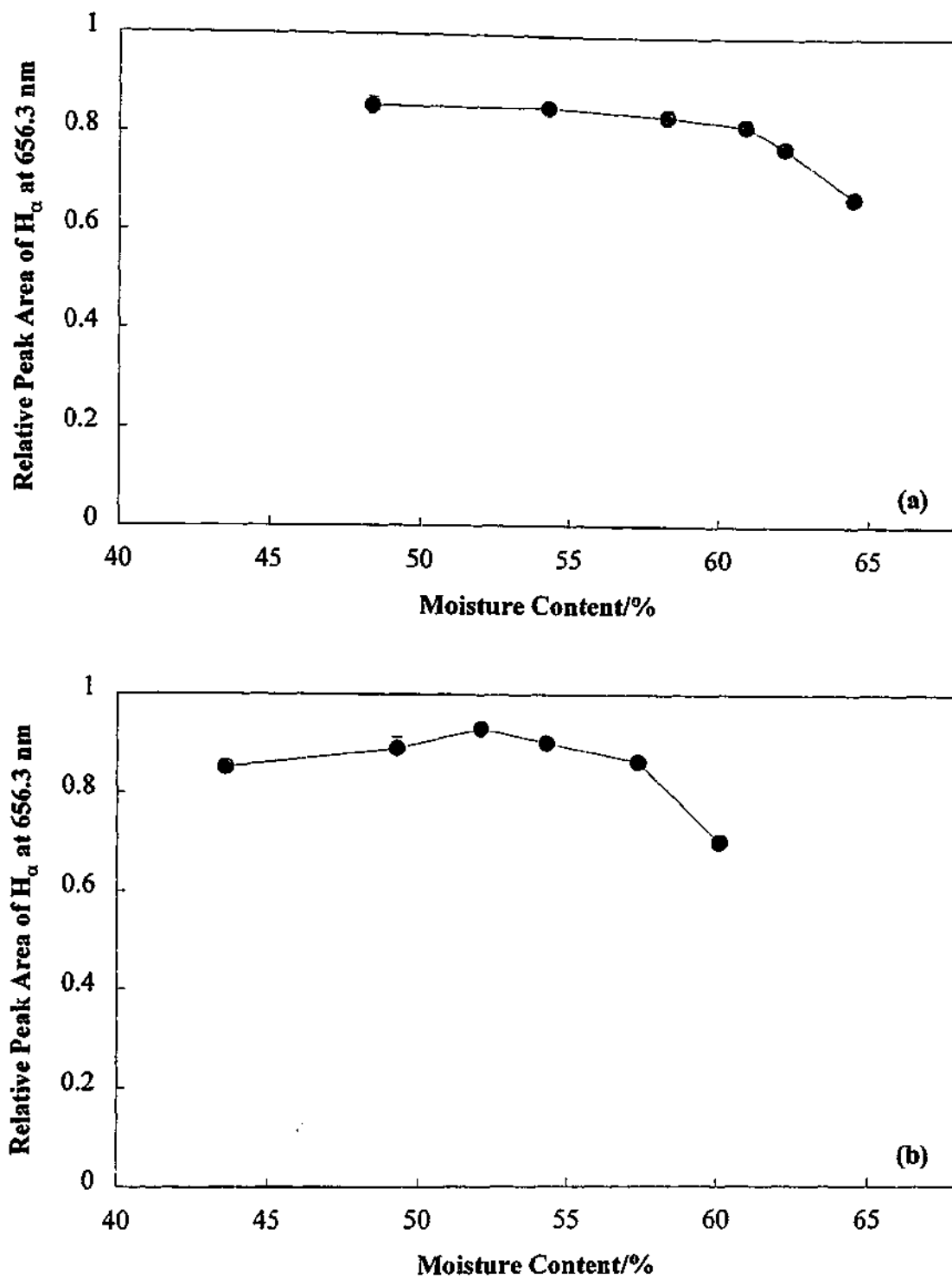


Figure 6.6. Variation of the  $H_{\alpha}$  emission line at 656.3 nm with coal moisture content for (a) a Yallourn coal and (b) a blended coal.

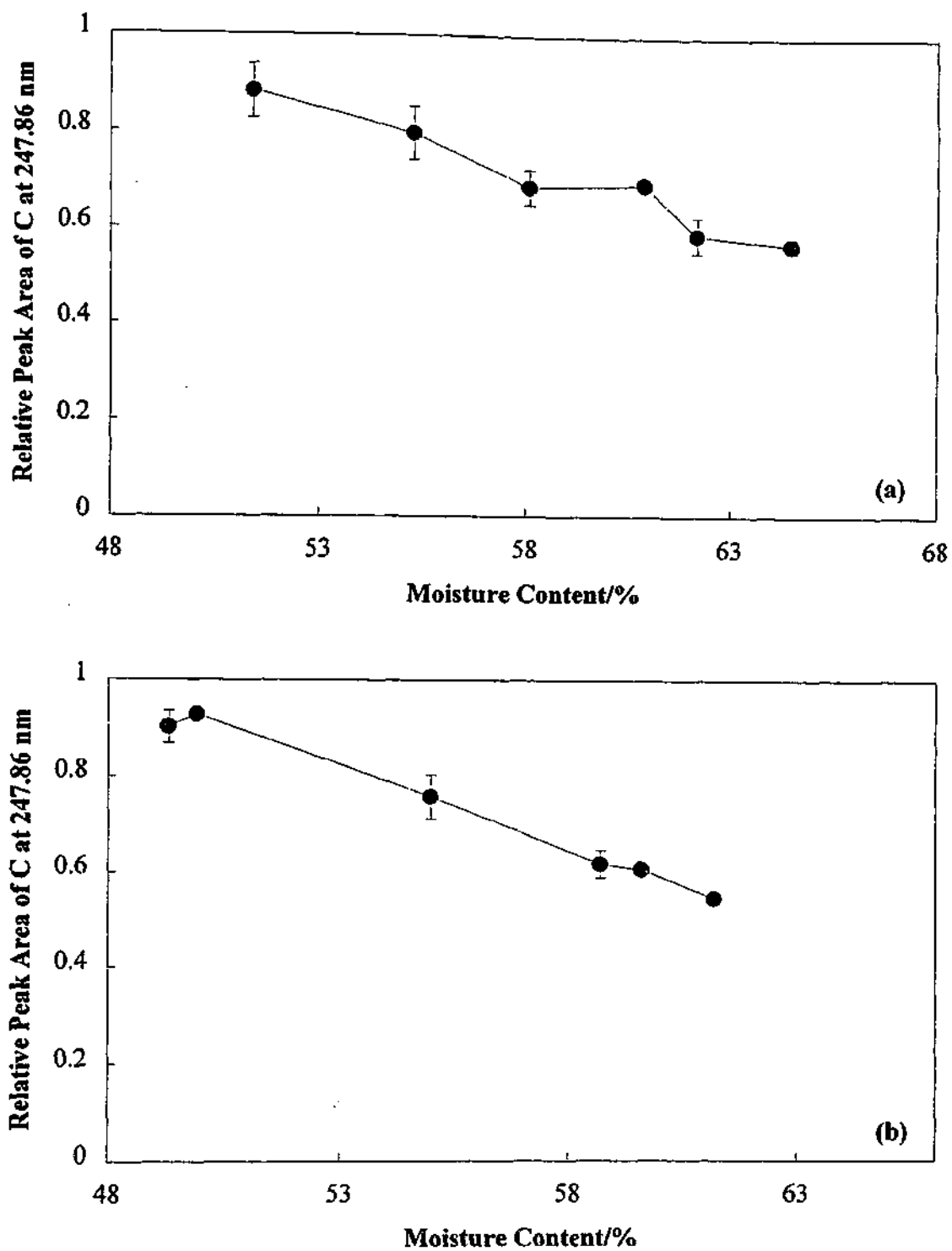


Figure 6.7. Variation of the C emission line at 247.86 nm with coal moisture content for (a) a Yallourn coal and (b) a Loy Yang coal.

Figure 6.7 for the Yallourn coal and a Loy Yang coal (sample CRC/8-4-26/70). The C emission line was chosen for investigation because its concentration expressed on a dry-basis remains relatively constant between samples and is generally evenly distributed throughout the coal because it is present in such large quantities (typically 65 to 70 % d.b.) [2].

The plots in Figure 6.7 show that C emission intensity decreases linearly with increasing coal moisture content. Again this trend is consistent with the water diluting C in the sample, increasing the breakdown threshold, or a combination of both effects.

As mentioned in Chapter 2, the ratios of emission line intensities to the intensity of an emission line from a major element in a sample of interest are often taken in order to factor out experimental fluctuations in the breakdown process. This was not a feasible option for the inorganic analyses described in the previous chapters because the only detectable line from the major element of coal, C, is at the lower end of the spectral range able to be obtained with our ICCD-based instrument. This meant that the latter was unable to be measured at the same time as all of the inorganic elemental emission lines with sufficient resolution, which is a requirement for this type of normalisation. However, the  $H_{\beta}$  emission line, located at 486.13 nm (the second most intense H line), and the C line at 247.86 nm are able to be measured simultaneously using the spectrograph grating with a line density of 300 lines/mm and that provides a spectral coverage of 300 nm. Measurement of these two lines required only a low-resolution grating because the wavelengths of the C and  $H_{\beta}$  lines are sufficiently removed from other emission lines that interference does not occur. In this manner it may be possible to factor out the effects on H emission intensity of the changes in the bulk properties of the coal caused by the evaporation of water by measuring the ratio of the  $H_{\beta}$  line to the C emission line.

The variation of the peak area of the  $H_{\beta}$  line with moisture content in the Yallourn and Loy Yang coals at 4 different laser irradiances is shown in Figure 6.8. This data shows that the  $H_{\beta}$  line behaves differently to the  $H_{\alpha}$  line. While the intensity of the  $H_{\alpha}$  emission line varies with moisture content (see Figure 6.6), the intensity of the  $H_{\beta}$  line remains fairly constant for each irradiance used over the range of moisture levels investigated. It is possible that the differences in the variation of intensity with moisture content for these

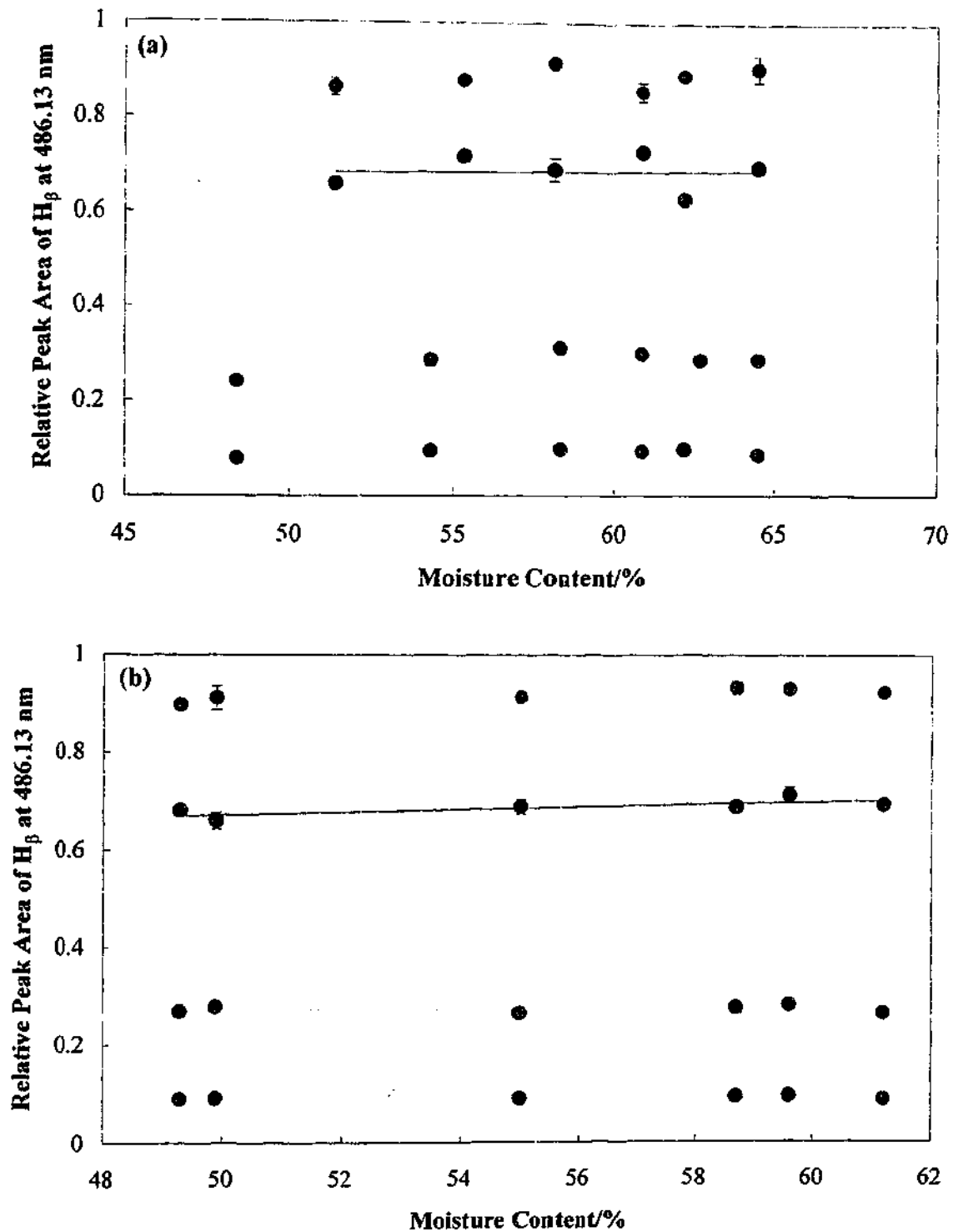


Figure 6.8. Variation of the peak area of H $\beta$  at 486.13 nm at (●) 8 GWcm<sup>-2</sup>, (○) 13 GWcm<sup>-2</sup>, (●) 20 GWcm<sup>-2</sup>, and (○) 24 GWcm<sup>-2</sup> for (a) a Yallourn coal and (b) a Loy Yang coal.

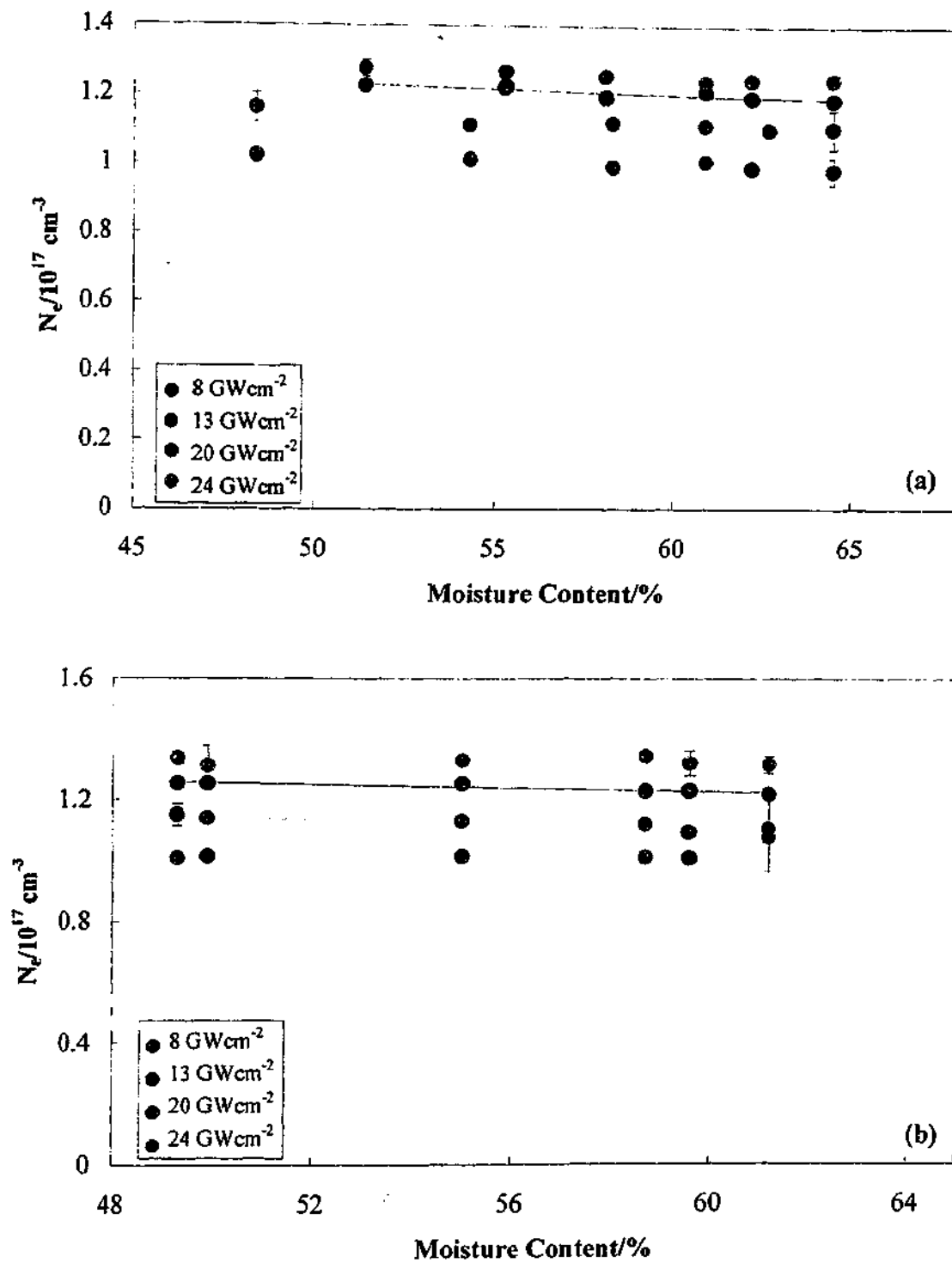


Figure 6.9. Variation of the electron number density ( $N_e$ ) of the laser induced plasma with moisture content in (a) a Yallourn coal and (b) a Loy Yang coal.

two H lines are due to the difference in their sensitivities to plasma temperature. While the line width of the  $H_\beta$  line is largely independent of the laser-induced plasma temperature, the width of the  $H_\alpha$  line is somewhat sensitive to temperature [152]. Thus, it may be that the changes in the bulk properties of the coal caused by variation in the moisture content result in variation in the plasma temperatures. The fact that the peak area of the  $H_\beta$  emission line remains constant over the range of moisture levels investigated suggests that its full width at half maximum (FWHM) is also relatively constant. The FWHM of the Stark broadened  $H_\beta$  line is related to the electron number density ( $N_e$ ) as follows:

$$N_e = C(N_e, T) \Delta\lambda_s^{3/2} \quad (6.2)$$

where  $C(N_e, T)$  is a coefficient that is weak function of  $N_e$  ( $\text{\AA}^{-3/2} \text{cm}^{-3}$ ) and is found in Griem [76], and  $\Delta\lambda_s$  is the full width at half maximum of the Stark broadened  $H_\beta$  line ( $\text{\AA}$ ). Thus, if the FWHM of the  $H_\beta$  line remains constant,  $N_e$  is also constant over the range of moistures. Figure 6.9 shows how  $N_e$ , as calculated by the above method, varies with moisture content in the Yallourn and Loy Yang coal samples at four different laser irradiances. The error bars represent the 95 % confidence limits. As expected,  $N_e$  remains constant over the moisture range for each irradiance used. Figure 6.10 shows how the FWHM of the  $H_\alpha$  line varies with moisture content in the Yallourn and blended coals at an irradiance of  $20 \text{ GWcm}^{-2}$ . In contrast to the results from the  $H_\beta$  line, the FWHM of the  $H_\alpha$  line does vary with coal moisture content. The FWHM of the  $H_\beta$  line has been shown to have little dependence on the plasma temperature, while the FWHM of the  $H_\alpha$  line is sensitive to temperature fluctuations [152]. Since it was shown in Figure 6.9 that  $N_e$  remains relatively constant over the moisture ranges studied, the variation in the FWHM of the  $H_\alpha$  line must be a result of variation in the plasma temperature. These results are inconsistent with those obtained by Rusak and coworkers [119]. They reported that the excitation temperature remained constant as sample water content varied, while  $N_e$  decreased. The average plasma temperature here can be roughly estimated from the FWHM of the  $H_\alpha$  line and the data in Griem [76]. These calculations indicate that the plasma temperature for the Yallourn coal is greater than 20000 K for all the partially dried samples and less than 5000 K for the raw coal which has 64.5 % water.

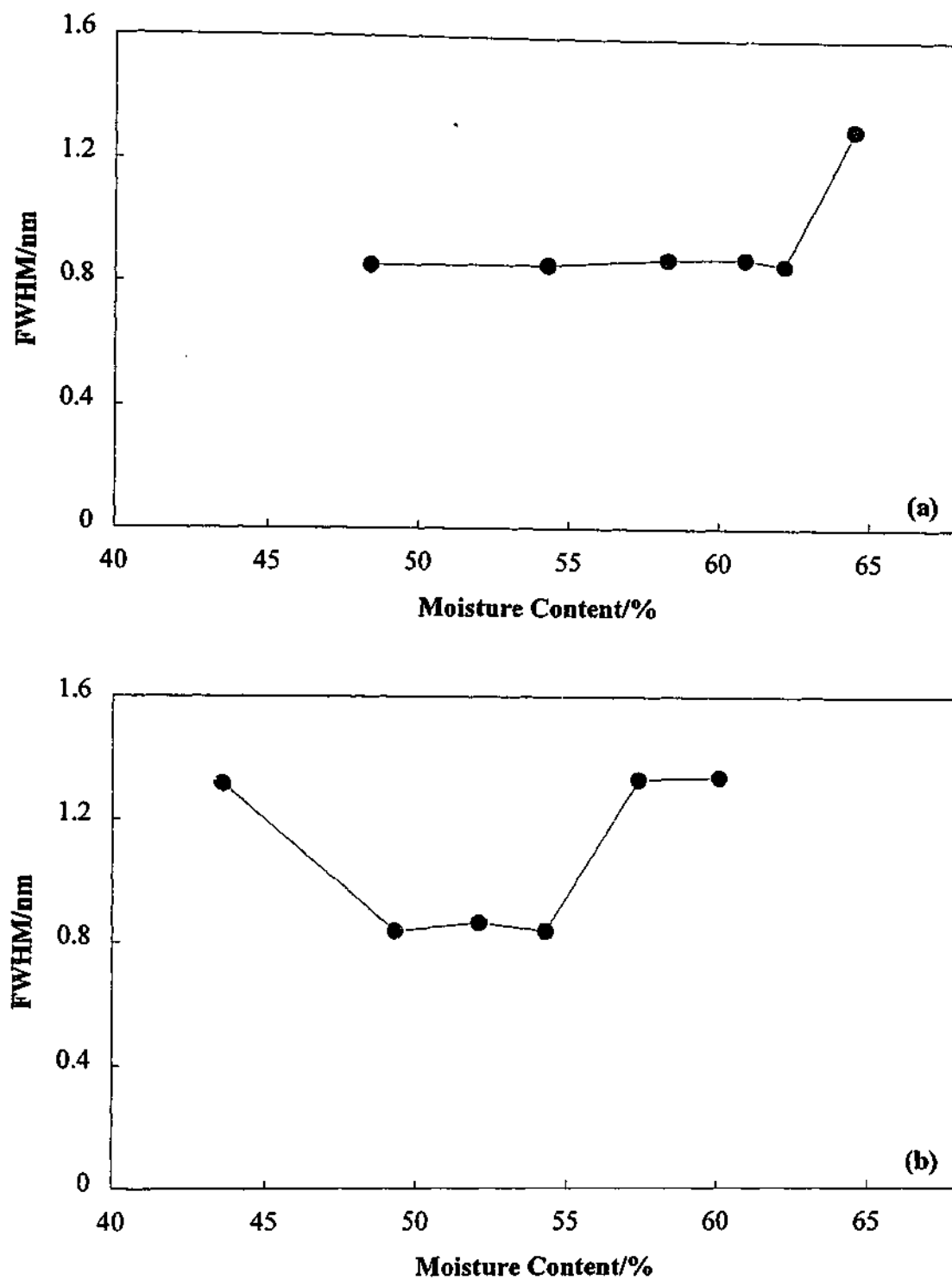


Figure 6.10. Variation of the FWHM of the H $\alpha$  line at 656.3 nm with moisture content in (a) a Yallourn coal and (b) a blended coal.

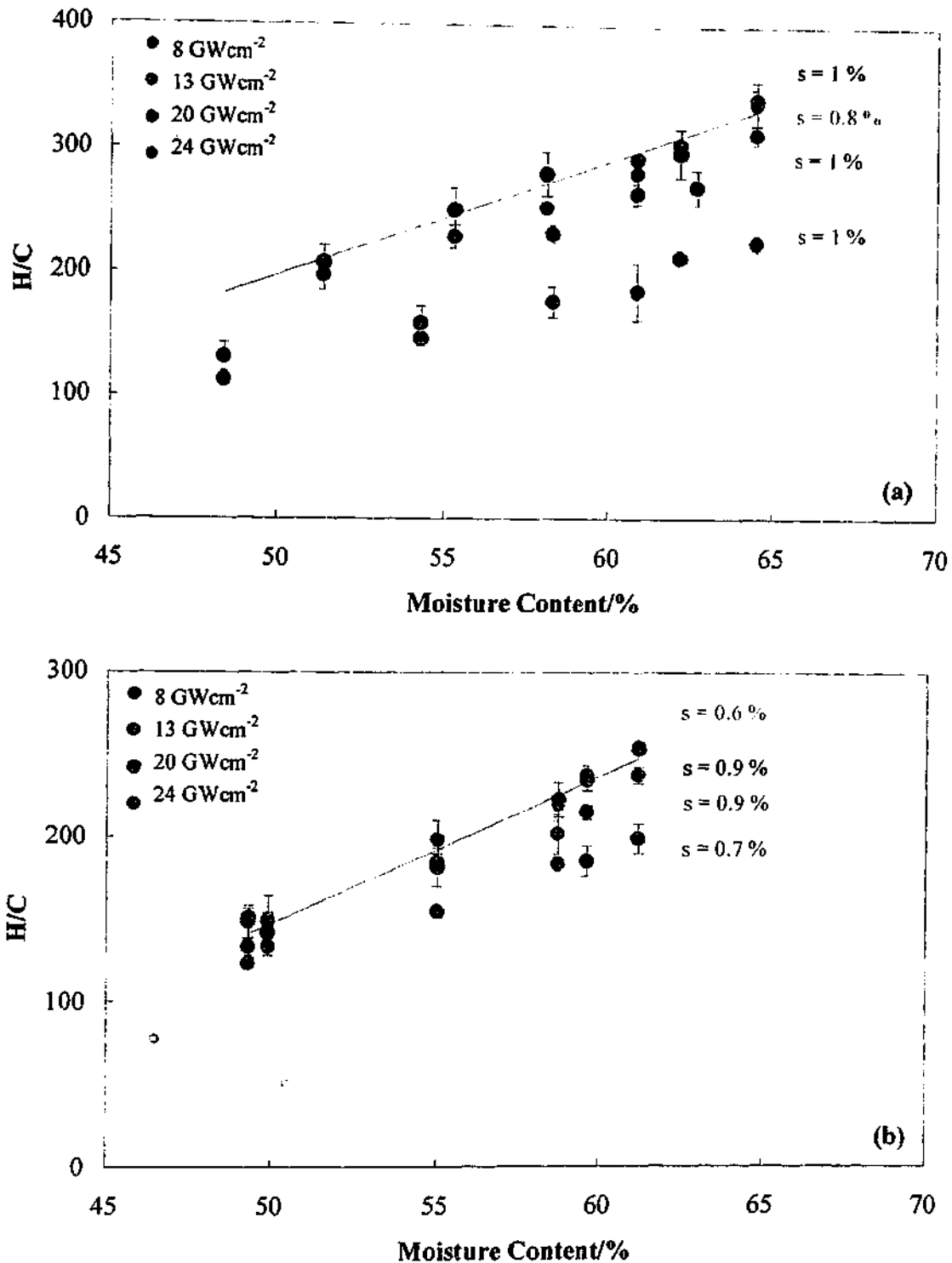


Figure 6.11. Variation of the ratio of H $\beta$  line at 486.13 nm to the C line at 247.86 nm with coal moisture content at four laser irradiances for (a) a Yallourn coal and (b) a Loy Yang coal.

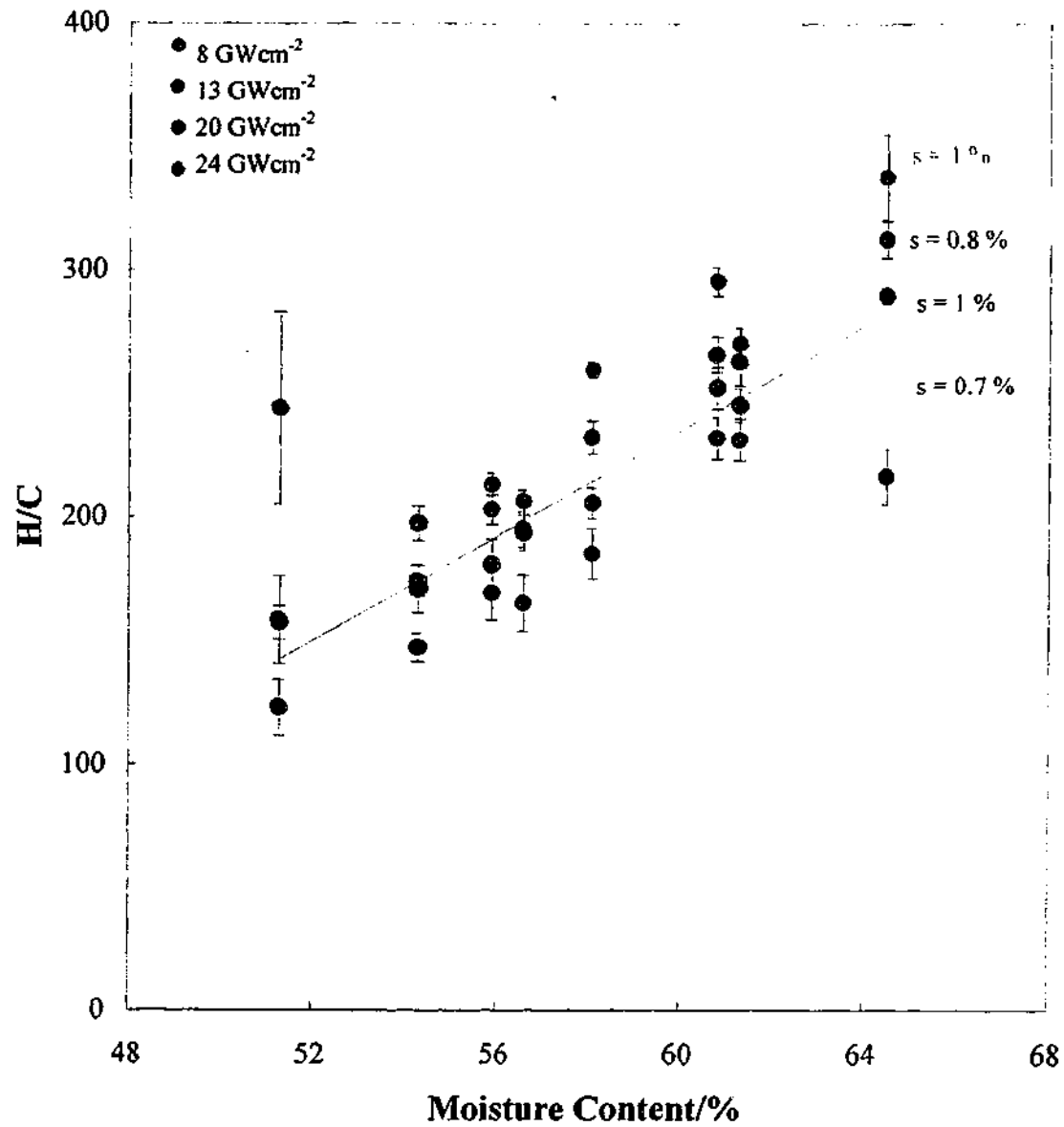


Figure 6.12. Variation of the ratio of H $\beta$  at 486.13 nm to C at 247.86 nm with moisture content in 8 Latrobe Valley coal samples at four laser irradiances.

The variation of the H-to-C ratio with moisture content in the Yallourn and Loy Yang coals at four different laser irradiances are shown in Figure 6.11. These plots show that the H-to-C ratio increases linearly with coal moisture content for both coals and at each irradiance used. Hence, it seems likely that using this ratio adequately corrects for changes in the bulk properties of the coal samples caused by variation in the moisture content. The H-to-C ratio decreases as water is removed from the samples because the number of H atoms is also decreased. Thus, it appears possible to measure the moisture content of Latrobe Valley coals using the H-to-C ratio in LIBS spectra.

Hydrogen is present in Latrobe Valley coals as part of the organic matter as well as in the coal moisture. While the amount of organic H in these coals is small (approximately 4.5 to 5.0 % dry basis [153]) compared to the water content, it can vary between samples. To ascertain whether this variation has a significant impact on the spectral H-to-C ratio, 8 different Latrobe Valley coal samples were analysed using LIBS. Figure 6.12 shows how the H-to-C ratio varies with moisture content for these 8 samples at 4 different laser irradiances. This plot shows that the H-to-C ratio increases linearly with moisture content for the 8 samples and each of the irradiances used. Good  $R^2$  values ( $> 0.93$ ) are obtained for the regression lines through the data obtained at each irradiance used. The standard errors of prediction (s) are shown beside each of the regression lines. However, one data point was omitted from each of the regression analyses for the 8  $\text{GWcm}^{-2}$  and 24  $\text{GWcm}^{-2}$  data. The data from the sample with the lowest moisture content was removed from the 24  $\text{GWcm}^{-2}$  regression because its H/C value seemed abnormally high. During analysis it was observed that more sample was removed from the surface of this coal with each laser pulse than coals with higher moisture levels. The water in the coal acts as a binder in the sample pellets. Hence, when less water is present, the pellets are more brittle and a greater volume of sample can be removed from the surface with each laser pulse. This means that sometimes overlap can occur between the area affected by successive laser pulses, impacting focussing and detection conditions. This can lead to an increase in the errors associated with the analysis. Figure 6.12 shows that the error in the point omitted from the regression analysis of the 24  $\text{GWcm}^{-2}$  data is much larger than the errors in the other points. Thus, in this instance it is possible that these effects have led to an increased H/C value.

The data from the sample with the highest moisture content was also removed from the regression analysis of the data obtained at  $8 \text{ GWcm}^{-2}$ . It is unclear why this point does not fit the trend followed by the other samples. This sample produced results consistent with those of the other samples for the other irradiances used. The  $8 \text{ GWcm}^{-2}$  data in Figure 6.11(a) also remains linear at moisture levels similar to that of this sample. Thus, it is likely that the cause of the low H/C value for this sample is simply experimental error.

The standard errors of prediction of the moisture content by measurement of the H-to-C ratio are less than or equal to 1 % for each sample and irradiance tested. This is not significantly different to the results obtained from the coals identical in all properties but moisture content. Hence it would seem that organic hydrogen levels in the coal have little impact on the spectral H-to-C ratio.

The uncertainties obtained using the spectral H-to-C ratio are comparable to those obtained using on-line nuclear instruments and slightly poorer than those from microwave instruments [4]. However, as mentioned previously, the microwave instruments are unable to measure the inorganic content of the coal and nuclear instruments do not provide the sensitivity required for the analysis of the inorganics in low-ash brown coal. Thus, it is preferable to use LIBS based instruments for these purposes.

## 6.5 Conclusions

The effects of moisture content on the LIBS analyses of the inorganic elements in Latrobe Valley brown coal were investigated in this chapter. Coal samples identical in all properties but moisture content were used to determine the effects of moisture content on the emission intensity of lines from Na and Mg. The peak areas of the Na and Mg emission lines studied were found to increase linearly with decreasing moisture content and wet basis elemental concentrations, until threshold moisture levels were reached. Below these thresholds, emission intensity remained relatively constant. It is possible that this levelling off was due to atomic self-absorption, like that observed in Chapter 4 of this thesis, or water-induced changes to the plasma chemistry. It was concluded that the trends observed were at least partly the result of the sample acting as a diluent. It was possible

that the results observed were also due to the water affecting the chemistry of the laser-induced plasma.

Eight coal samples with moisture contents covering a wide range were then analysed using LIBS to determine if the water was affecting the plasma chemistry or just acting as a diluent. The peak areas of the Na and Mg emission lines analysed were found to increase as wet basis elemental concentrations increased. Wet basis concentrations were used because they account for the diluting effects of the water. The diluting effects of the sample moisture were again observed for this data. However, it was still unclear whether the water also affected the chemistry of the plasma.

The effects of sample moisture content on the intensity of emission from carbon and hydrogen in Latrobe Valley brown coal produced during LIBS analyses were also investigated. Again, samples identical in all properties but moisture content were used in these experiments. At high moisture levels ( $> 58\%$ ), the area of the  $H_{\alpha}$  emission line at 656 nm was found to decrease with increasing moisture content. When the moisture content was between approximately 50 and 58 %, the intensity of this emission line was relatively constant. Below 50 % sample moisture, the intensity of the  $H_{\alpha}$  line was found to decrease with decreasing moisture content. While an increasing sample moisture content means an increase in the number of H atoms in the sample, these results suggested that this moisture increase resulted in an increase in the breakdown threshold of the coal. This, in turn, resulted in a decrease in the energy of the laser-induced plasma and, hence, emission intensity.

The effects of coal moisture content on the intensity of the  $H_{\beta}$  emission line at 486 nm were also studied. This line was found to behave differently to the  $H_{\alpha}$  line as the moisture content varied. Its peak area remained relatively constant as moisture content was varied between 48 and 65 %. While the intensity of this line increased with laser irradiance, it remained constant for all moisture levels at each irradiance. It is possible that the differences in the behaviours of the two H emission lines were due to the difference in their sensitivities to plasma temperature. The FWHM of the Stark broadened  $H_{\beta}$  line, which is largely independent of plasma temperature and remained constant over the sample moisture range, was used to calculate the electron density of the laser-induced plasmas.

The electron density, which was found to increase with laser irradiance, remained relatively constant over the moisture range studied. Conversely, the FWHM of the  $H_{\alpha}$  line, which has a greater dependence on plasma temperature than the  $H_{\beta}$  line, was found to vary with coal moisture content. Since it was shown that the electron density of the plasma remained relatively constant over the entire moisture range, it is likely that this variation was due to fluctuation in the plasma temperature. This is borne out by rough estimates of the plasma temperature from the FWHM of the  $H_{\alpha}$  line. These results indicate that increasing the sample moisture both affects the plasma chemistry and dilutes elemental concentrations.

The intensity of the carbon emission line at 248 nm was found to decrease linearly with increasing coal moisture content in LIBS experiments. Again, it is possible that this trend was due to both dilution and a water-induced increase in the breakdown threshold of the sample.

The effects of the moisture content on the intensity ratio of the  $H_{\beta}$  line to the C emission line at 248 nm in LIBS analyses of Latrobe Valley brown coal were investigated in both samples identical in all respects except moisture content and different samples covering a range of moisture levels. This was done at four different laser irradiances. This ratio was found to increase linearly with the moisture content of Latrobe Valley brown coal at each irradiance. The H-to-C ratio was also found to increase with irradiance below 20  $\text{GWcm}^{-2}$ . The organic H content of the coal was found to have a negligible impact on the spectral H-to-C ratio. Thus, this ratio may be used to measure moisture levels in the coal, provided that the laser irradiance is relatively constant or above 20  $\text{GWcm}^{-2}$ . The standard errors of prediction of the coal moisture were less than or equal to 1 % over a 48 to 64 % moisture range at each of the irradiances when using the H-to-C ratio.

The standard error of prediction obtained when using the spectral H-to-C ratio is comparable to those obtained using on-line nuclear instruments and slightly poorer than those obtained using on-line microwave instruments [4]. However, the on-line microwave instruments cannot be used to analyse the inorganic and mineral content of the coal. Hence, it may be preferable to use LIBS based instruments for such analyses.

## *The Modelling of Coal Constituents by Principal Component Regression*

### *7.1 Introduction*

This chapter presents models that can be used to improve elemental concentration predictions from spectral data obtained from LIBS analyses of Latrobe Valley brown coals. In Chapter 4 the concentrations of elements that comprised the ash-forming inorganics and minerals within the coals were predicted simply by measuring the areas of spectral peaks corresponding to each element. In Chapter 5 this method was refined by implementing acoustic signal normalisation. In the present chapter, principal component regression (PCR) is applied to the acoustic wave normalised spectra of 50 Latrobe Valley brown coals and models are developed for 10 variables describing the coals; Na, Mg, Ca, Fe, Si, Al, Cl, S, moisture content, and total ash yield.

### *7.2 Principal Component Regression*

Principal component analysis (PCA) is a multivariate technique that can be used to reduce the number of variables in a large data set [154-156]. When large numbers of independent variables are present within a data set there is often extensive correlation between many of them. This means that much of the data within the set is redundant. PCA reduces the data to its essentials by transforming the original set of variables to a new set of variables that are linear combinations of the original variables. These new variables are called principal components. Each principal component is derived in decreasing order of influence on the sample set and is orthogonal to the others. Hence, the first principal component will explain the greatest proportion of variance within the sample set and be uncorrelated with any of the other principal components. When there is correlation between some of the original variables, the number of principal components needed to describe the variance within the sample data will be less than the number of original variables. Generally, only the first few principal components contain significant information, the remainder describe the noise within the data set.

Principal component regression (PCR) performs a multi-linear regression on the principal components determined from PCA to produce a model that describes the relationship between the dependent and independent variables. This model can subsequently be used to predict the value of the independent variable in unknown samples.

In this work, PCR was applied to spectral data obtained from 50 samples of Latrobe Valley brown coal, using the LPS instrument (see Chapter 3). These samples were obtained from the Yallourn, Morwell and Loy Yang coalfields and cover a wide range of inorganic, mineral and moisture levels. See Appendix A for the complete standard chemical analyses of these 50 coals.

The fundamental wavelength of the Nd:YAG laser operating at 15 Hz and producing approximately 40 mJ/pulse was used to induce sample breakdown. In these experiments a time delay between the start of the laser spark and detection of approximately 2  $\mu$ s ( $\pm$  50 ns) was found to produce optimum signal-to-background levels in the spectra. A detector integration time of 2 ms, which is the minimum integration time allowed by the LPS, was used for signal collection.

The spectra used for PCR were each the average of 50 spectra obtained from different sections of the sample pellets. Each spectrum consisted of data obtained from the 3 detector channels, each of which contained 2048 pixels. After collection, this averaged data was normalised using the integrated acoustic signal. Hence each coal was, in effect represented by 6144 measurements, many of which were unnecessary to measure the composition of the coal. Thus, PCR was applied to identify the specific pixels/wavelengths required to predict each of the constituents of interest. The commercially available computer package *Unscrambler* [157] was used in this work.

### 7.3 Model Optimisation

The first step in producing prediction models using PCR was to examine the data set for outliers. To do this, PCR was performed on the spectra separately for each of the coal constituents. The resulting influence plot was then examined for outliers. An example of an influence plot is shown in Figure 7.1. An influence plot displays the residual

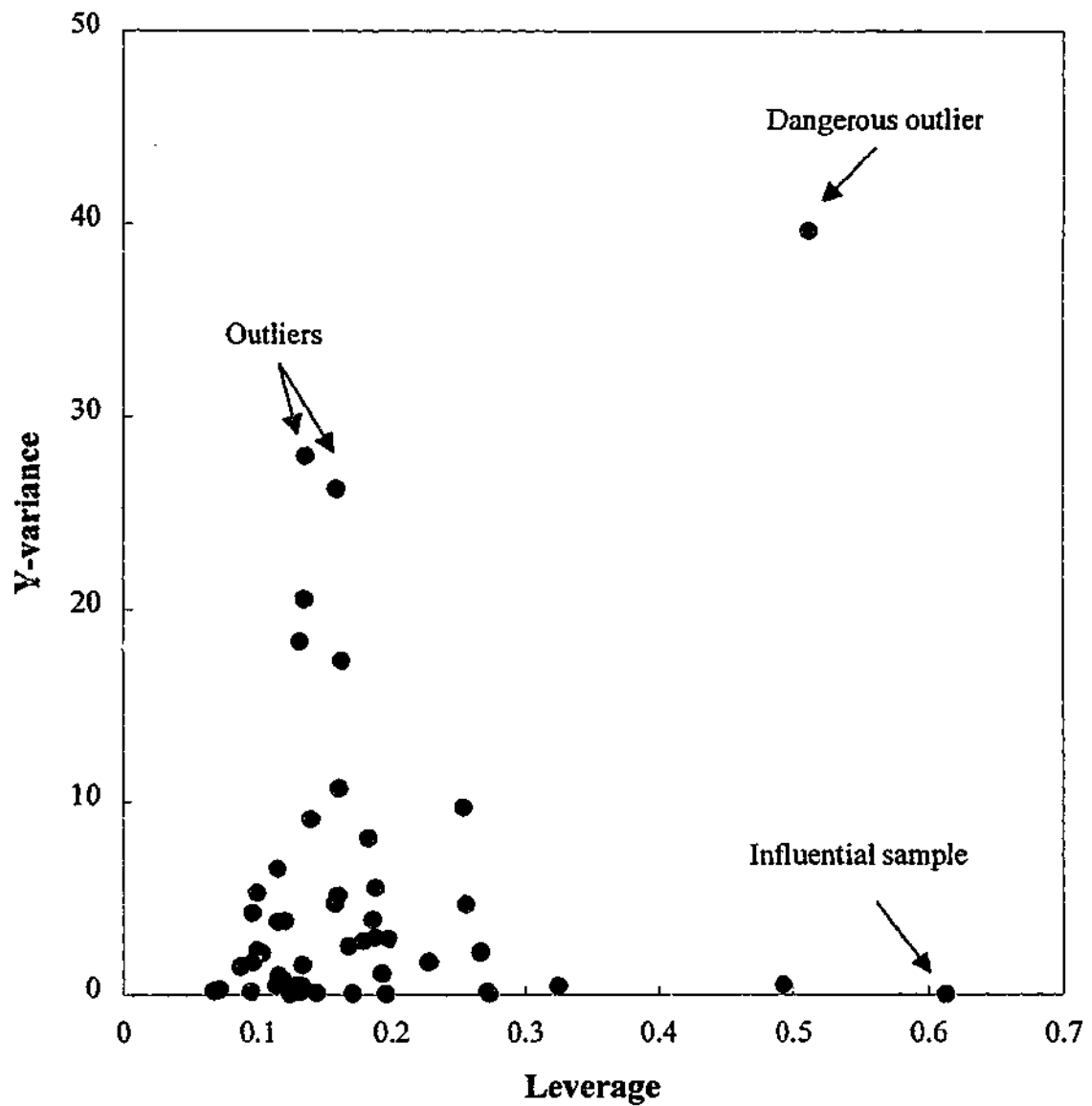


Figure 7.1 Influence plot from the initial PCR model for moisture content in Latrobe Valley brown coals, illustrating outliers, influential samples and dangerous outliers.

Y-variances (variances of the dependent variable) against leverage values. The leverage is a measure of the difference between the Y-value of a sample and the average Y-value for the complete data set. Samples at the top of the plot away from most of the other samples and, hence with high residual variance, are prone to be outliers or samples which the model does not accurately describe. Samples lying on the far right of the influence plot also have high leverage. These samples are not necessarily outliers, they merely possess more influence on the regression model than the other samples. However, if a sample has both a high residual Y-variance and high leverage it can severely distort the regression model. Thus, when dealing with a fixed number of samples, such as in this study, these highly influential samples or "dangerous outliers" are removed from the data set and another regression model fitted.

Two outliers were removed from nine of the models and three from the model for chlorine content. The outliers were different for each of the coal constituents modelled. Following the outlier removal, the PCR models were re-calculated. These new models were able to more accurately describe the remaining samples.

Table 7.1. Comparison of correlation coefficients and RMSEPs in PCR models, before and after outliers were removed.

| Coal<br>Constituent | All Samples  |         | Outliers Removed |         |
|---------------------|--------------|---------|------------------|---------|
|                     | Corr. coeff. | RMSEP   | Corr. Coeff.     | RMSEP   |
| Mg                  | 0.932        | 300 ppm | 0.955            | 200 ppm |
| Na                  | 0.957        | 300     | 0.966            | 200     |
| Ca                  | 0.961        | 300     | 0.962            | 300     |
| Fe                  | 0.973        | 300     | 0.987            | 200     |
| Al                  | 0.794        | 600     | 0.946            | 200     |
| Si                  | 0.771        | 800     | 0.769            | 600     |
| Cl                  | 0.908        | 400     | 0.916            | 300     |
| S                   | 0.514        | 900     | 0.926            | 600     |
| Total ash yield     | 0.840        | 0.4 %   | 0.931            | 0.3 %   |
| Moisture            | 0.959        | 3 %     | 0.974            | 3 %     |

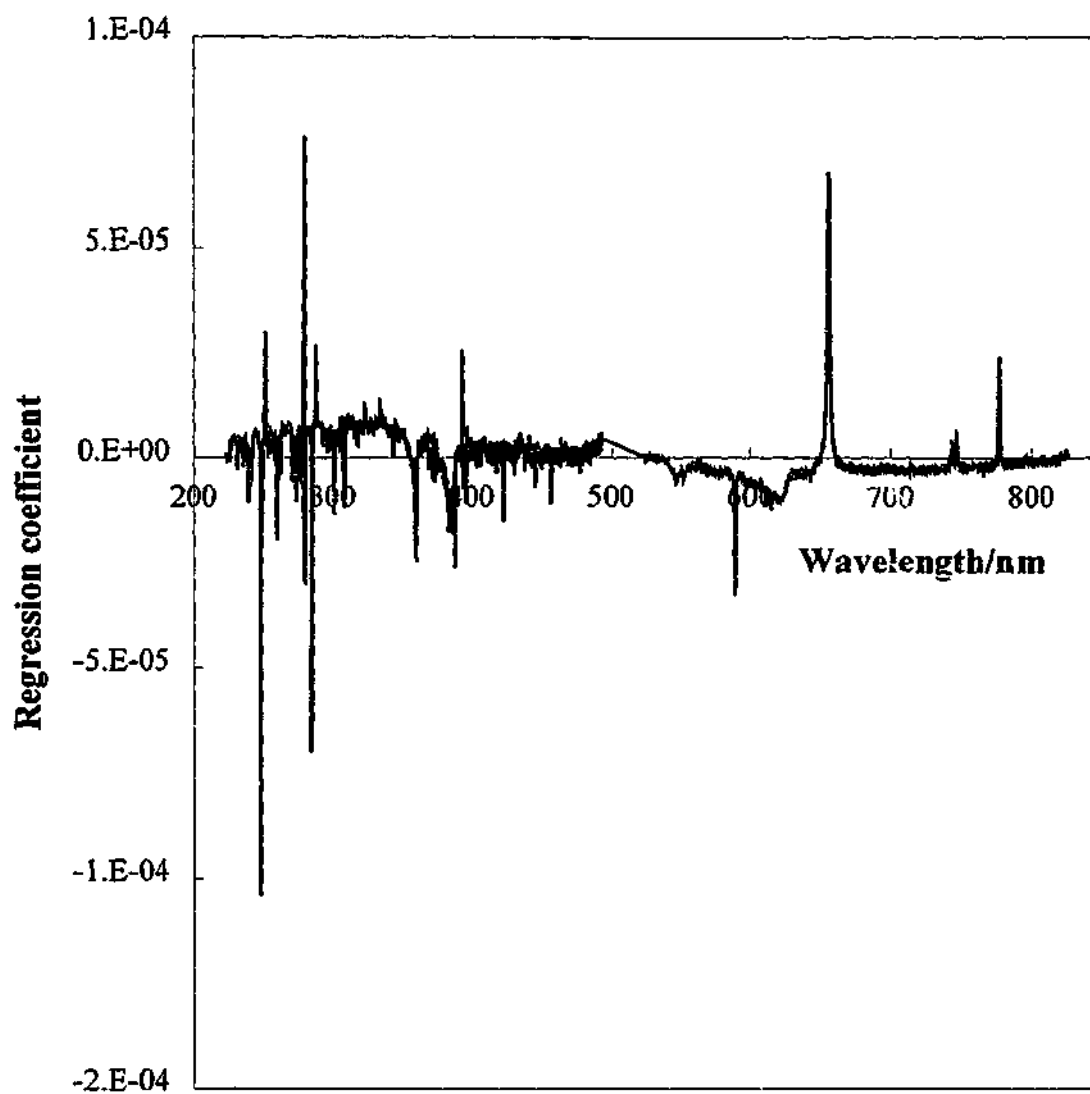


Figure 7.2. Regression plot obtained from analysis of coal moisture content.

This was indicated by improved correlation between the predicted and measured dependent variables and a decrease in the root mean square error of prediction (RMSEP). This is illustrated in Table 7.1. The RMSEP is the average uncertainty expected on future predictions, providing the new samples are similar to the ones used for calibration. The RMSEP is calculated using a validation set, which is a set of samples that have not been used for calibration. The samples within the validation set should also have properties similar to the set used for calibration.

#### **7.4 Model Simplification**

Having improved the models by removing outliers, the next step was to simplify them. This was done by identifying the independent variables (pixels) that contributed most to each model. Plotting the regression coefficients of the independent variables allowed for easy identification of these pixels. An example of a regression plot is shown in Figure 7.2. Independent variables which correlate positively with the coal component of interest have positive regression coefficients, while those which correlate negatively will have negative regression coefficients. The concentration of the dependent variable of interest is calculated by summing the products of the regression coefficients and the values of their associated independent variables. The regression coefficients were derived using only the useful principal components in each model. A plot of the RMSEP against the number of principal components used in the model for coal moisture content is shown in Figure 7.3. The numbers of useful principal components in each model were determined using plots such as that shown in Figure 7.3. The optimum number of principal components for the moisture content model is 8 because this number corresponds to the minimum RMSEP. Generally, elements with strong emission lines required fewer principal components to predict their concentrations. All of the pixels having high regression coefficients in the models corresponded to atomic or molecular emission lines within the coal spectra. In general, emission lines corresponding to the element being modelled were positively correlated with its concentration.

The data sets were reduced for each of the coal constituents to between 4 and 15 pixels from the 6144 original pixels. This was done by only including in the model the independent variables that were strongly correlated with the coal component being

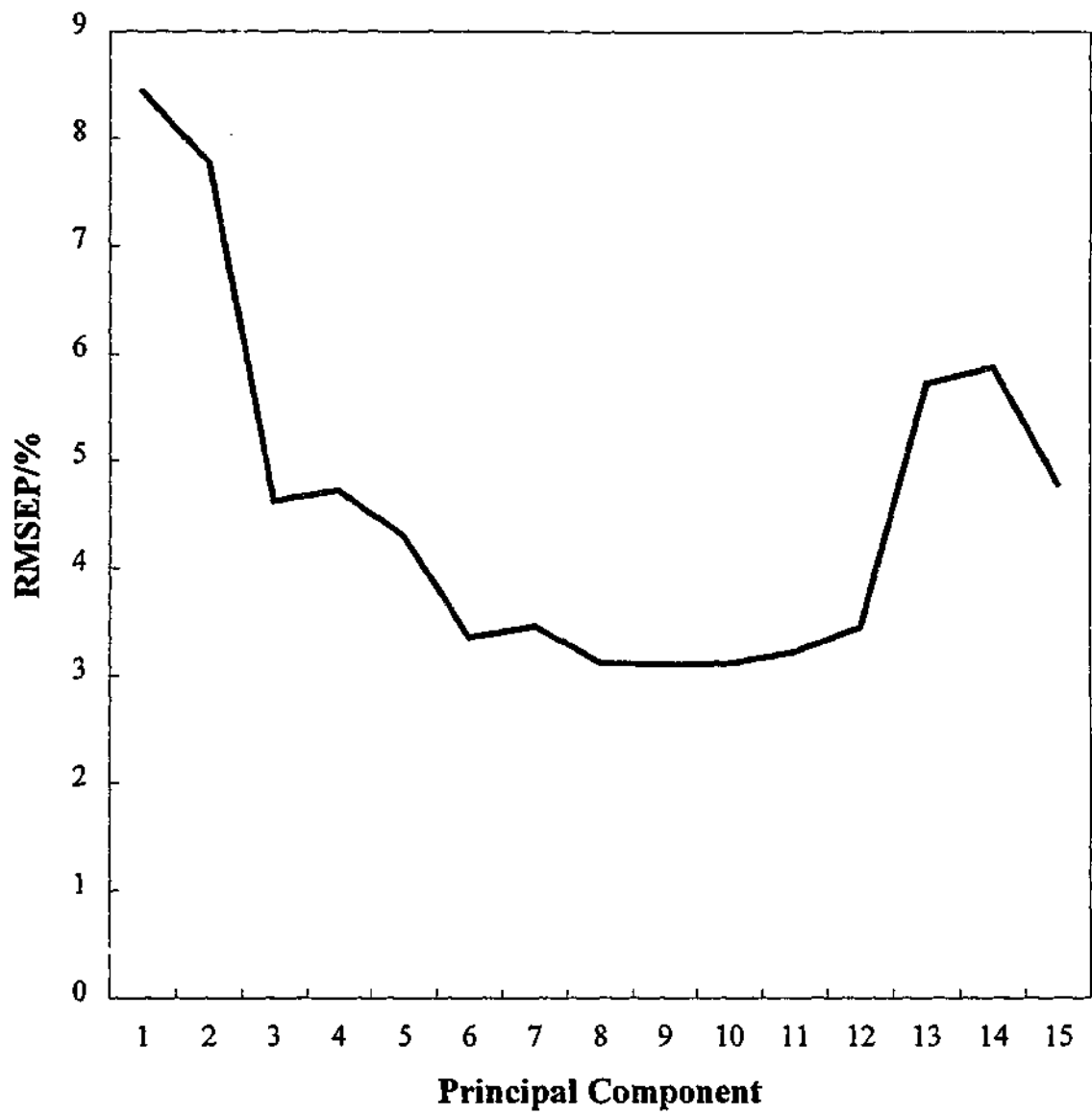


Figure 7.3. Variation of the RMSEP with the number of principal components used in PCR model for coal moisture content.

modelled. Thus there was little difference in the predictive abilities of the original and simplified models.

Following the simplification of the models, the RMSEPs were calculated. In this work, 9 out of the remaining 48 samples (47 for Cl) were used for validation. This was repeated five times for each model, with different samples used in the validation set each time. Thus five RMSEP values were calculated for each of the models. The average RMSEP values for the models are shown in Table 7.2. In general, the RMSEP will not be lower than twice the precision of the reference methods. From Table 7.2 it can be seen that the RMSEP values for the inorganic elements are approximately twice the 100 ppm uncertainty quoted in the standard ICP and AAS analyses in Appendix A.

Table 7.2. The root mean square errors of prediction for the simplified PCR models of ten constituents of Latrobe Valley brown coals.

| Coal constituent | RMSEP   |
|------------------|---------|
| Mg               | 200 ppm |
| Na               | 200 ppm |
| Ca               | 200 ppm |
| Fe               | 200 ppm |
| Al               | 100 ppm |
| Si               | 600 ppm |
| Cl               | 300 ppm |
| S                | 400 ppm |
| Total ash        | 0.2 %   |
| Moisture         | 3 %     |

### 7.5 Linear PCR Models

Linear PCR models were developed for 10 variables describing Latrobe Valley brown coals; Mg, Na, Ca, Fe, Al, Si, Cl, S, total ash, and moisture. As described in Chapter 4, Mg, Na, Ca, Fe, Al, and Si concentrations are able to be directly determined using the background subtracted peak area of single emission peaks. Moisture content is also able to

be predicted using the ratio of the peak areas of the hydrogen emission line at 486.13 nm and the carbon emission line at 247.86 nm, as was demonstrated in Chapter 6. PCR models for these elements were developed in an attempt to improve the precision and accuracy of these predictions. PCR models were also developed for S, Cl, and total ash values, which were previously unable to be predicted using LIBS. Sulphur and chlorine levels were previously unable to be predicted because of a lack of intense emission lines in the spectral regions analysed. A recent study by Lancelin and coworkers used the chlorine and sulphur emission lines at 837.6 and 921.3 nm, respectively for LIBS analyses of these elements in organohalogenated molecules [142]. However, these emission lines are outside the wavelength region examined in this work.

### 7.5.1 Model for Magnesium

The simplified model developed for Mg, using the method described above, is shown in Figure 7.4. It should be noted that the wavelengths given in the model do not exactly correspond with literature values for the atomic transitions with which they are associated [147]. This is a result of the imperfect wavelength calibration of the LPS spectrometers.

Pixels corresponding to the main Mg emission lines at 279.55, 280.27 and 285.21 nm are, as expected, present within the regression model. However, there are a number of other elements that have emission lines, which contribute to this model. Both the C line at 247.86 nm and the H line at 656.27 nm are quite strongly negatively correlated with Mg concentration. In general, coals with higher moisture levels will have lower inorganic levels (the water acts as a diluent). Hence, the negative correlation between Mg concentration and H emission is to be expected. Similarly, coals with low levels of ash-forming elements will have a greater proportion of organic matter, explaining the negative correlation between Mg levels and C emission intensity.

The regression model for Mg also indicates a positive correlation with the Na emission line at 589 nm. This may be due to the fact that both Mg and Na occur within the coal primarily as exchangeable cations associated with carboxyl groups [2]. Mg and Na also tend to exhibit similar concentration gradients within coal seams. Brockway and Borsaru [15] found that  $\text{Na}^+$  and  $\text{Mg}^{2+}$  possessed similar relative rates of movement in bed-moist brown coal under the influence of a net water movement resulting from surface

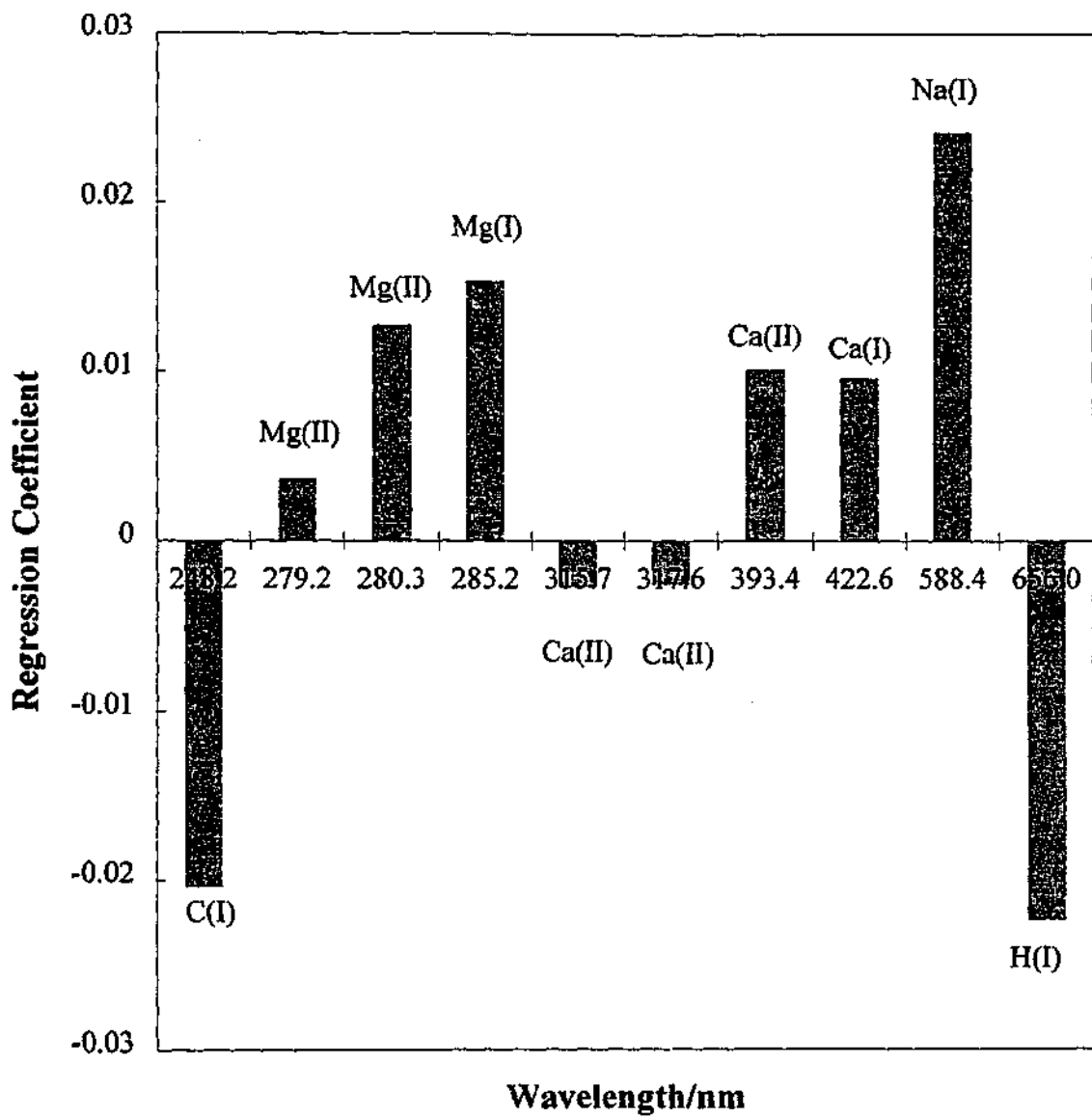


Figure 7.4. PCR model for Mg concentrations in Latrobe Valley brown coals.

evaporation. They also found that these rates were independent of the source of the coal and its lithotype. Hence, it would be expected that the levels of Mg and Na would vary similarly within a coal seam. Pixels corresponding to Ca emission lines at 315.89, 317.93, 393.37 and 422.67 nm also contribute to the model for Mg. However, while the 315.89 and 317.93 nm lines are negatively correlated with Mg, the other Ca lines show a positive correlation.

In the original PCR model produced from all 6144 pixels, the plot of regression coefficients as a function of wavelength showed that there was a small contribution from the  $\Delta v = -2$  sequence band of the  $A(^3\Pi) \rightarrow X(^3\Pi)$  electronic transition of  $C_2$ , which has band heads between 590 and 619 nm [151]. It is interesting to note that this band is not readily observed in the LIBS spectra of brown coal. However, this model indicates that despite this fact,  $C_2$  is still involved in the plasma chemistry.

### 8.5.2 Model for Sodium

The simplified regression model for Na in Latrobe Valley brown coals is shown in Figure 7.5. As with Mg, the main Na emission lines in the LIBS spectra at 589.00 and 589.59 nm are positively correlated with the Na concentration in the coal. Again there are contributions from the emission lines of other elements. The C line at 247.86 nm and the H line at 656.27 nm are once again negatively correlated with Na concentration.

The Mg lines at 279.55 and 285.21 nm are also present in the regression model. The Mg (II) line at 279.55 nm shows a negative correlation with Na concentration, while the Mg (I) line at 285.21 nm shows a positive correlation. The intensities of these Mg lines are plotted against Na concentration in Figure 7.6. It can be seen that the intensities of both these lines increase with Na concentration, despite the scatter in the data. This is to be expected, as discussed for the Mg model. The intensity ratio of the two Mg lines, also shown in Figure 7.6, remains constant over the Na concentration range. Therefore there does not seem to be any physical explanation for the negative correlation between Na levels and the Mg (II) line at 279.55 nm. It should be noted that removing this line from the regression model has a detrimental effect on the prediction of Na levels in coal.

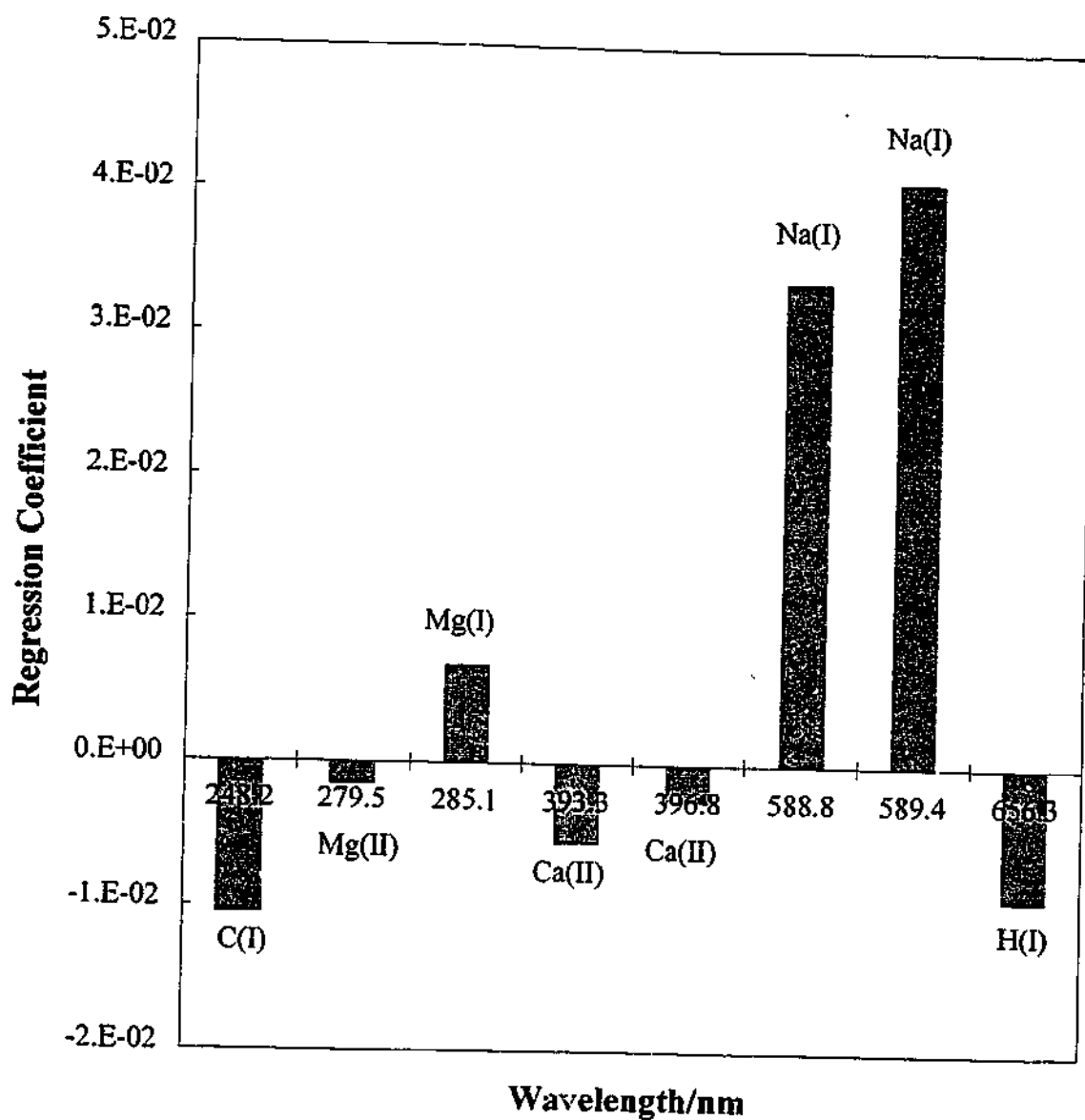


Figure 7.5. PCR model for Na concentration in Latrobe Valley brown coals.

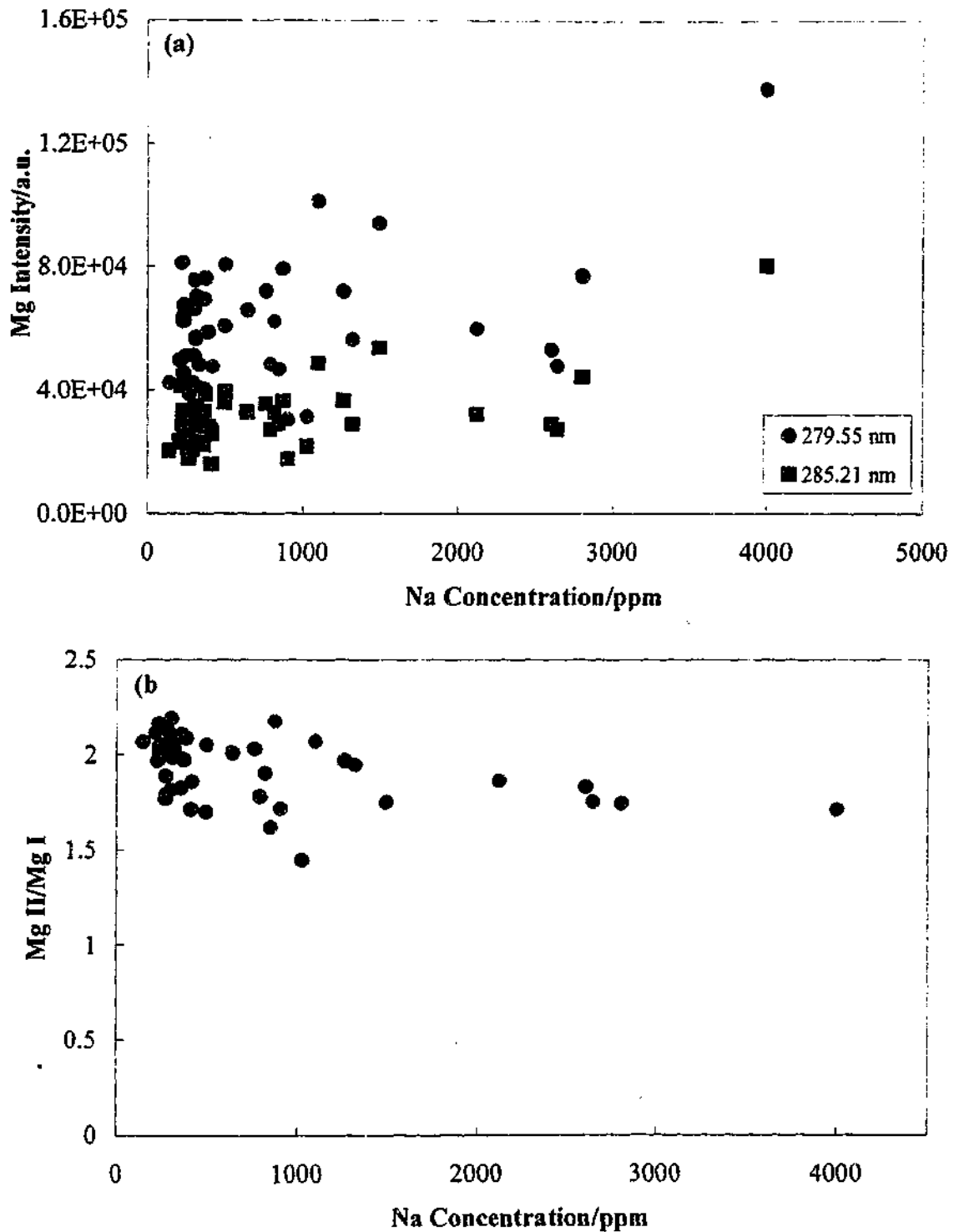


Figure 7.6. Variation of Mg emission intensity with Na concentration in Latrobe Valley coals; (a) for the Mg (I) line at 285.21 nm and the Mg (II) line at 279.55 nm, and (b) for the Mg (II)/Mg (I) ratio.

Ca (II) emission lines at 393.37 and 396.85 nm also contribute to the Na model. The model indicates that there is a negative correlation between these lines and the Na concentration. Again, most of the Ca and Na within the coal occur are associated with the carboxyl groups [2]. Unlike for Na and Mg, which are usually concentrated at the top of coal seams, Ca is often most concentrated somewhere in the middle of the seam. Thus, as Na concentration falls with depth, Ca concentration will increase until its maximum is reached. This may account for the negative correlation between Ca emission lines and Na concentration within the regression model.

### 7.5.3 Model for Calcium

The PCR model for Ca in Latrobe Valley brown coal is presented in Figure 7.7. As with the Mg and Na models, all the main Ca emission lines that are present within the laser-induced spectra at 315.89, 317.93, 393.37, 396.85 and 422.67 nm are positively correlated with Ca concentration. The C emission line at 247.86 nm is also negatively correlated with Ca concentration.

The Ca regression model shows a negative correlation between Ca concentration and the Mg (II) emission peaks at 279.55 and 280.27 nm. As mentioned previously, Mg is concentrated at the top of coal seams because  $Mg^{2+}$  moves relatively quickly through coal. The maximum concentration of Ca tends to be somewhere in the middle of a coal seam, closer to the bottom than the top. Thus we may expect Mg levels to decrease as Ca levels increase.

The model also reveals a positive correlation between the concentration of Ca and the intensity of Na emission at 589.00 and 589.59 nm. This is somewhat surprising, considering that some of the Ca (II) lines are negatively correlated with Na concentration in the previous model. The Ca concentration is plotted against the Na concentration for the coal samples used to produce the regression models in Figure 7.8. It can be seen that samples which are high in Na are low in Ca, while samples high in Ca are low in Na. However, samples with low Na or Ca concentrations can also have either high or low Ca or Na levels. On the basis of Figure 7.8 there is no clear linear relationship between Na and Ca levels in the coals. This may be the reason why the Na and Ca models indicate different relationships between the two elements.

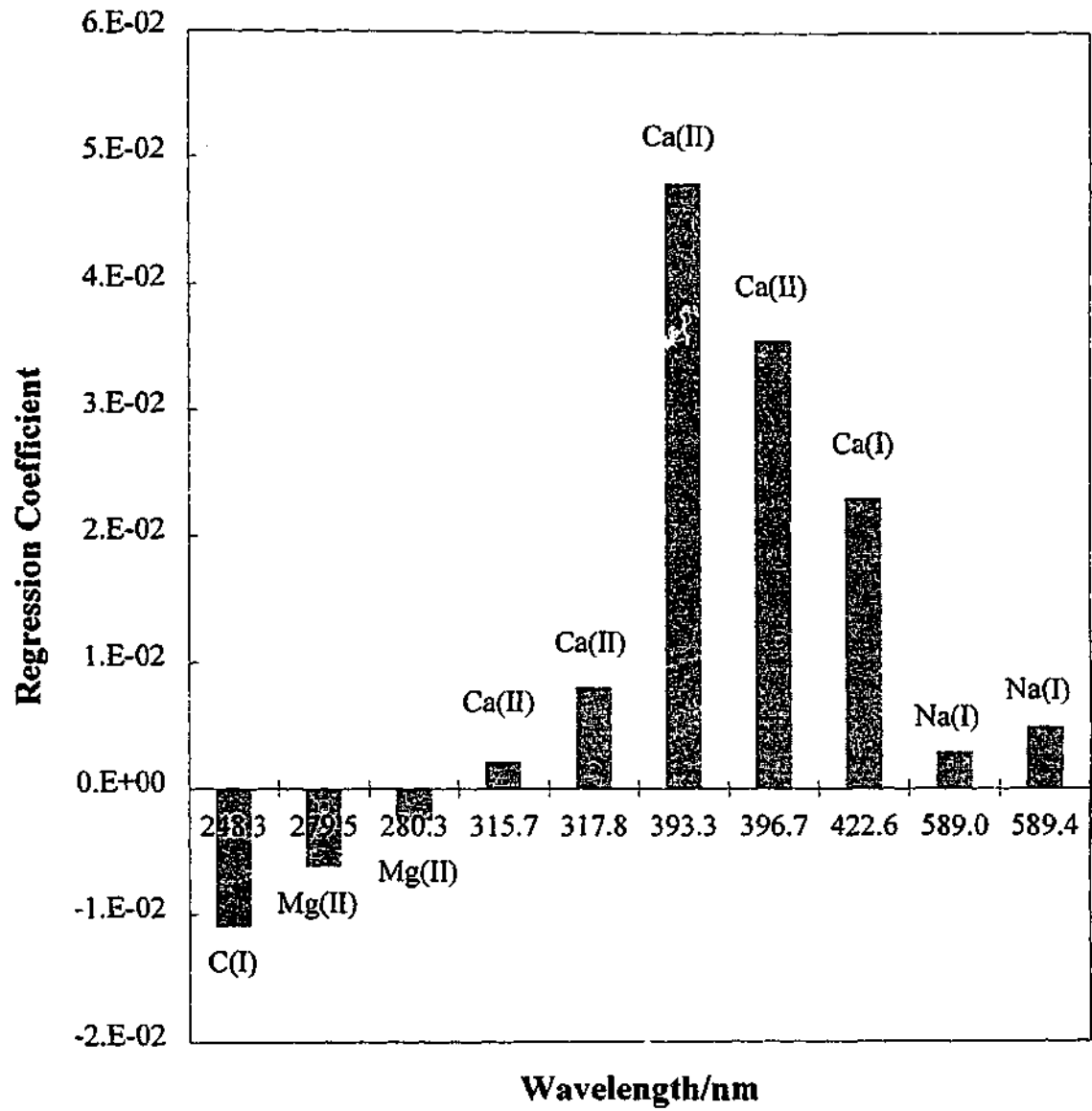


Figure 7.7. PCR model for Ca concentration in Latrobe Valley brown coals.

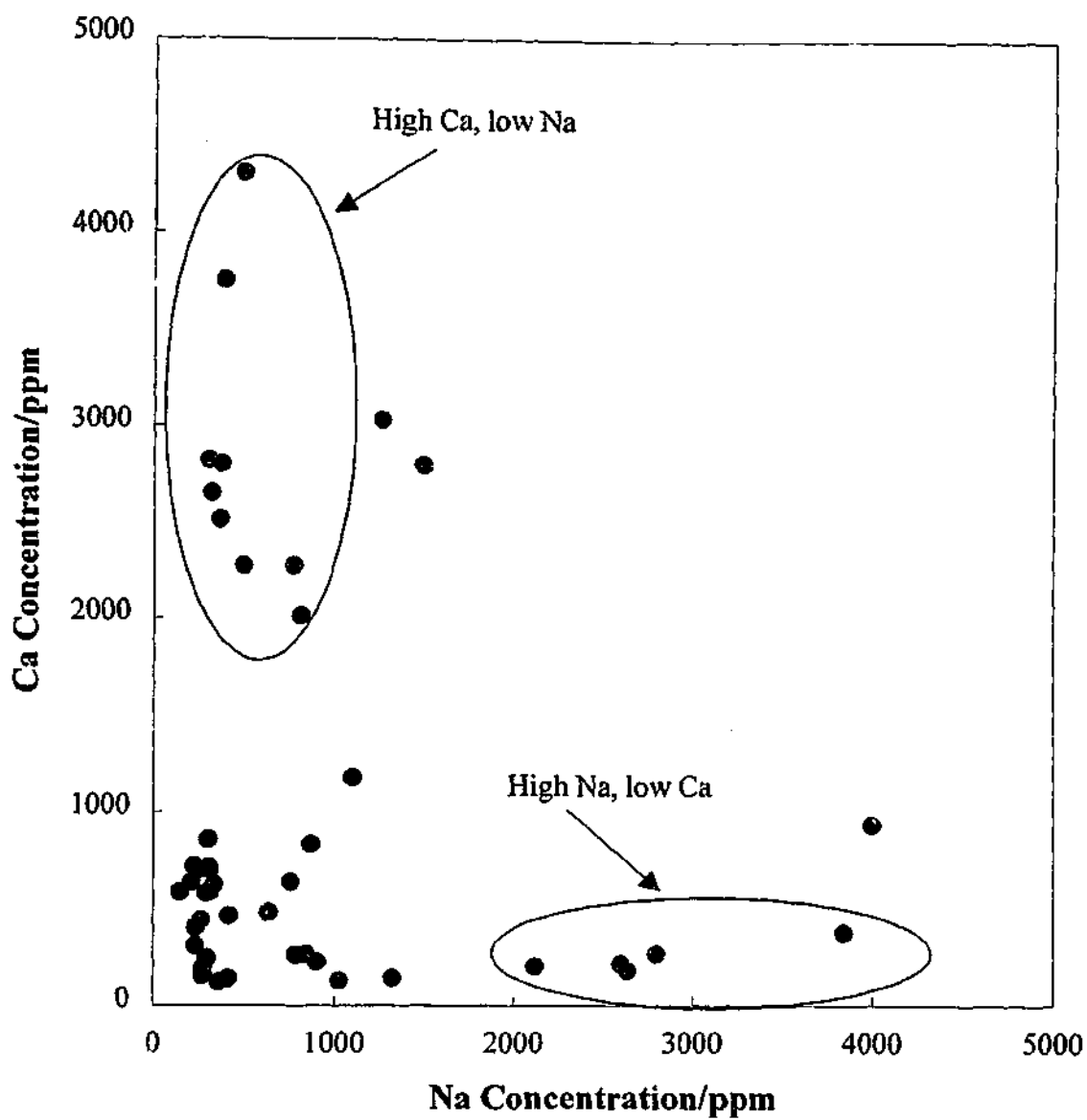


Figure 7.8. Variation of Ca concentration with Na concentration in the Latrobe Valley brown coals used to produce regression models. Ca and Na concentrations were determined by standard chemical methods.

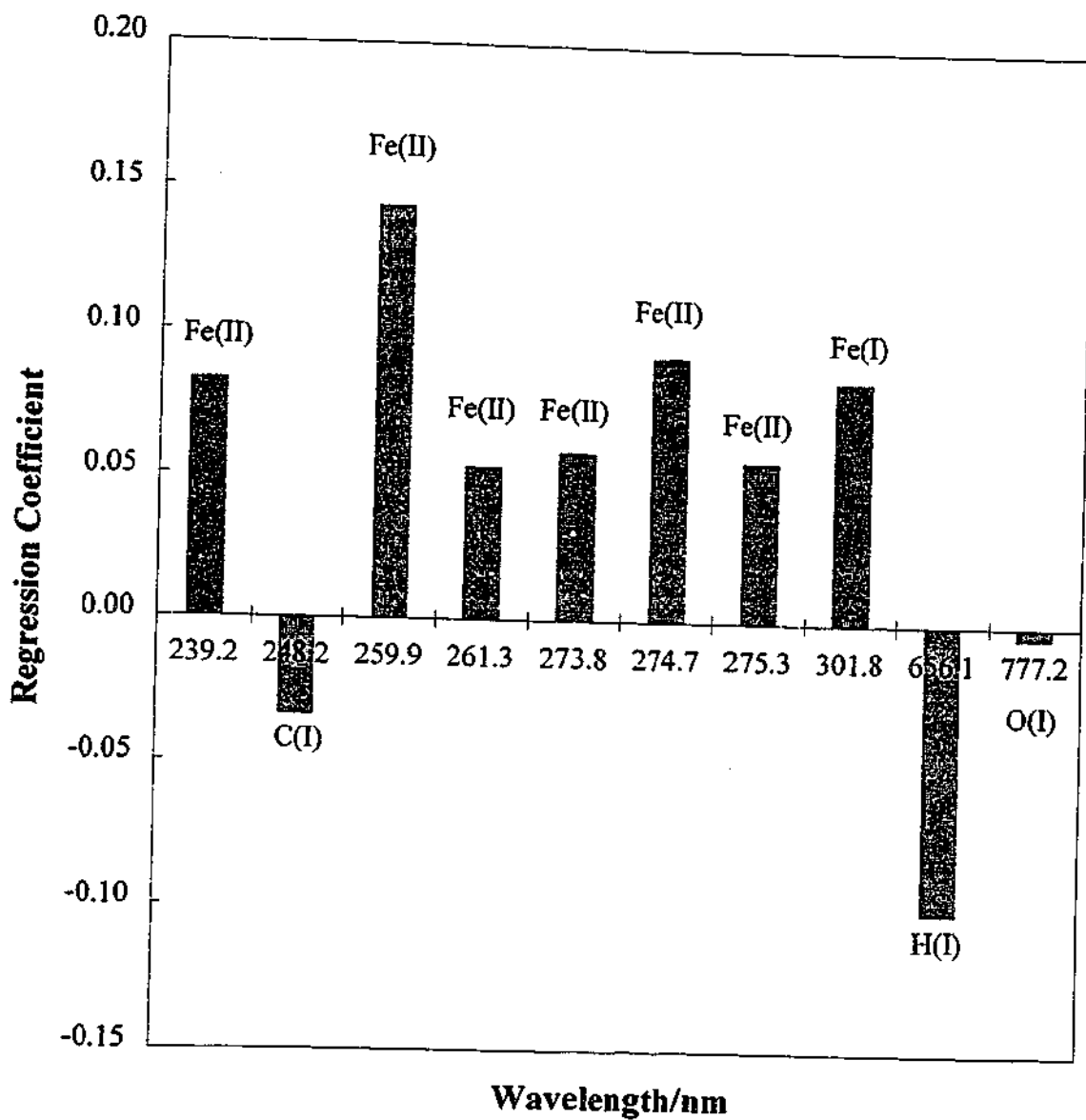


Figure 7.9. PCR model for Fe concentration in Latrobe Valley brown coals.

#### 7.5.4 Model for Iron

The wavelengths and regression coefficients used in the model for total Fe concentration in Latrobe Valley coal are shown in Figure 7.9. As for the other inorganic elements, Fe concentration is correlated with some of its emission lines; 239.56, 259.94, 261.19, 273.95, 274.93, 275.57 and 302.11 nm. Interestingly, these were not the strongest Fe emission lines observed in the spectra of coal. One explanation could be that the stronger lines suffer from spectral interferences more than these lines. In this model Fe concentration is also negatively correlated with C at 247.86 nm, H at 656.27 nm and O at 777.19 nm. Again, these correlations may be attributed to variations in the organic and moisture levels with respect to the inorganic levels within the coals.

#### 8.5.3 Model for Aluminium

The wavelengths and regression coefficients comprising the PCR model for Al are shown in Figure 7.10. This model consists of contributions solely from Al and Si. The Al lines at 308.22, 309.27 and 309.29 (unresolved), 394.40 and 396.35 nm are all positively correlated with Al concentration. Conversely, the Si lines at 251.61 and 288.16 nm are negatively correlated with Al concentration. This is somewhat surprising, considering that both Al and Si are present in some of the minerals found in Latrobe Valley coals, including kaolinite ( $\text{Al}_2\text{Si}_2\text{O}_5(\text{OH})_4$ ) and muscovite ( $\text{KAl}_2(\text{AlSi}_3)\text{O}_{10}(\text{OH})_2$ ). However, while Si is also present in another mineral, quartz, the other main source of Al is a monovalent hydroxy complex that is exchanged onto carboxyl groups. In general, the concentration of minerals in the coal is low, increasing near interseam sediments and overburden deposits. However, Higgins *et al.* [158] reported that occasionally quartz replaces woody cells within the coal. When this is the case, the concentrations of the other constituents of the coal will decrease. This may explain the negative correlation between the Si emission lines and Al concentration in the regression model.

#### 8.5.4 Model for Silicon

The regression model developed to predict Si concentrations in Latrobe Valley coals is shown in Figure 7.11. The main Si emission lines in the laser-induced spectra of Latrobe

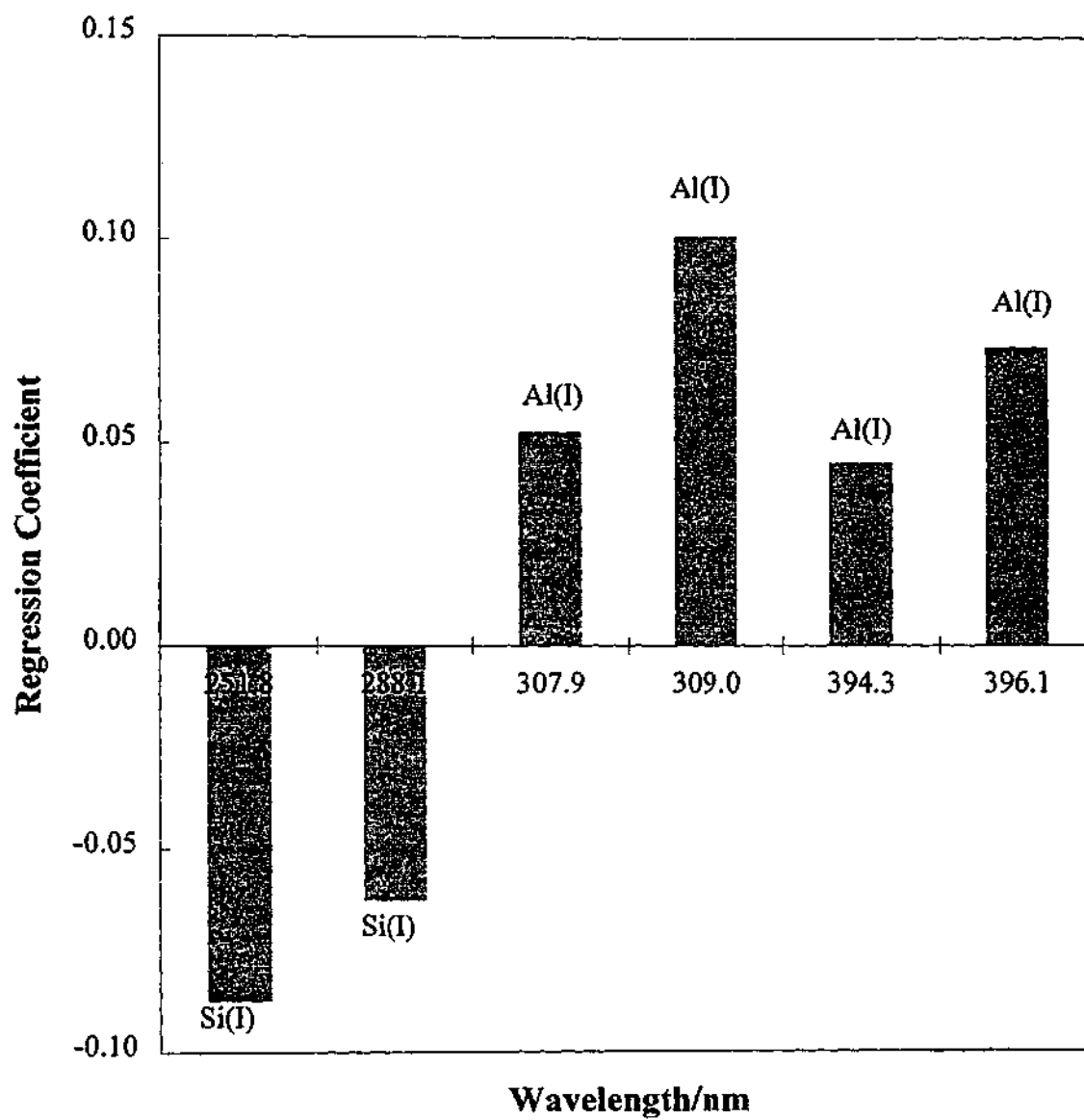


Figure 7.10. PCR model for Al concentration in Latrobe Valley brown coals.

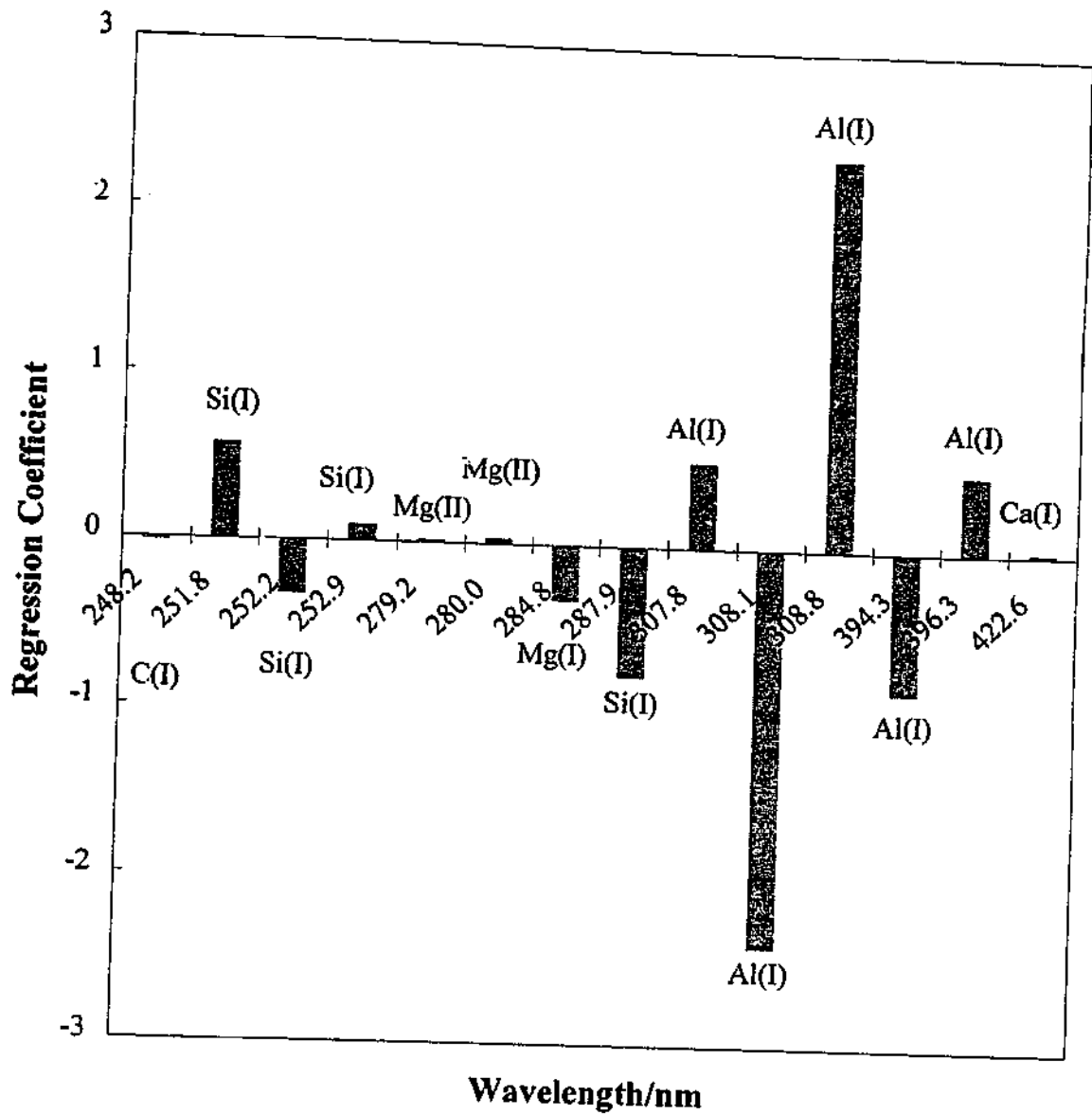


Figure 7.11. PCR model for Si concentration in Latrobe Valley brown coals.

Valley coals at 251.61, 252.41, 252.85 and 288.16 nm contribute to the regression model, as expected. However, some of these lines are positively correlated with Si concentration, while others are negatively correlated.

Emission lines from Mg (279.55, 280.27 and 285.21 nm), Al (308.22, 309.27 and 309.29, 394.40 and 396.15 nm) and Ca (422.607 nm) are also present in the model. The Mg and Al lines, like the Si lines, are both positively and negatively correlated with Si concentration. The inconsistency of the correlations within this model may be a result of the increased heterogeneity of mineral rich coals. Minerals, and hence Si, occur within the coal as discrete particles. As mentioned in Chapter 4, each laser pulse only samples a small (typically < 100 µg) amount of the coal. Thus, the measurement of Si is less precise than the measurement of many of the other elements. Even though average spectra were used to produce the model, the lack of measurement precision may have been the cause of these anomalies.

#### *7.5.7 Model for Chlorine*

Figure 7.12 shows coefficients of the regression model for Cl concentration in Latrobe Valley brown coals. As mentioned previously, Cl cannot be measured directly from the spectra obtained using the method described in Chapter 4. The main reason for this was that Cl emission lines present within the detection window of the system described in Chapter 3 were not strong enough to be observed. Clearly the only way that Cl can be measured by that system is by correlating its levels in the coal with other features in the laser-induced spectra.

The model in Figure 7.12 shows that Cl concentration can be correlated with emission lines from Ca (422.67 nm) and Na (589.00 and 589.59 nm). The positive correlation between Na lines and Cl is to be expected; dissolved NaCl is present within the in-seam moisture in Latrobe Valley brown coals. Cl, like Na, is found concentrated at the top of coal seams as a result of the high mobility of the ion through coal. This means that Na and Cl will vary similarly throughout the coal seam. As discussed for the Na model, the maximum Ca concentration is found somewhere in the middle of the coal seam because  $\text{Ca}^{2+}$  is less mobile than both Na and Cl. Hence the Ca emission line at 422.67 nm is

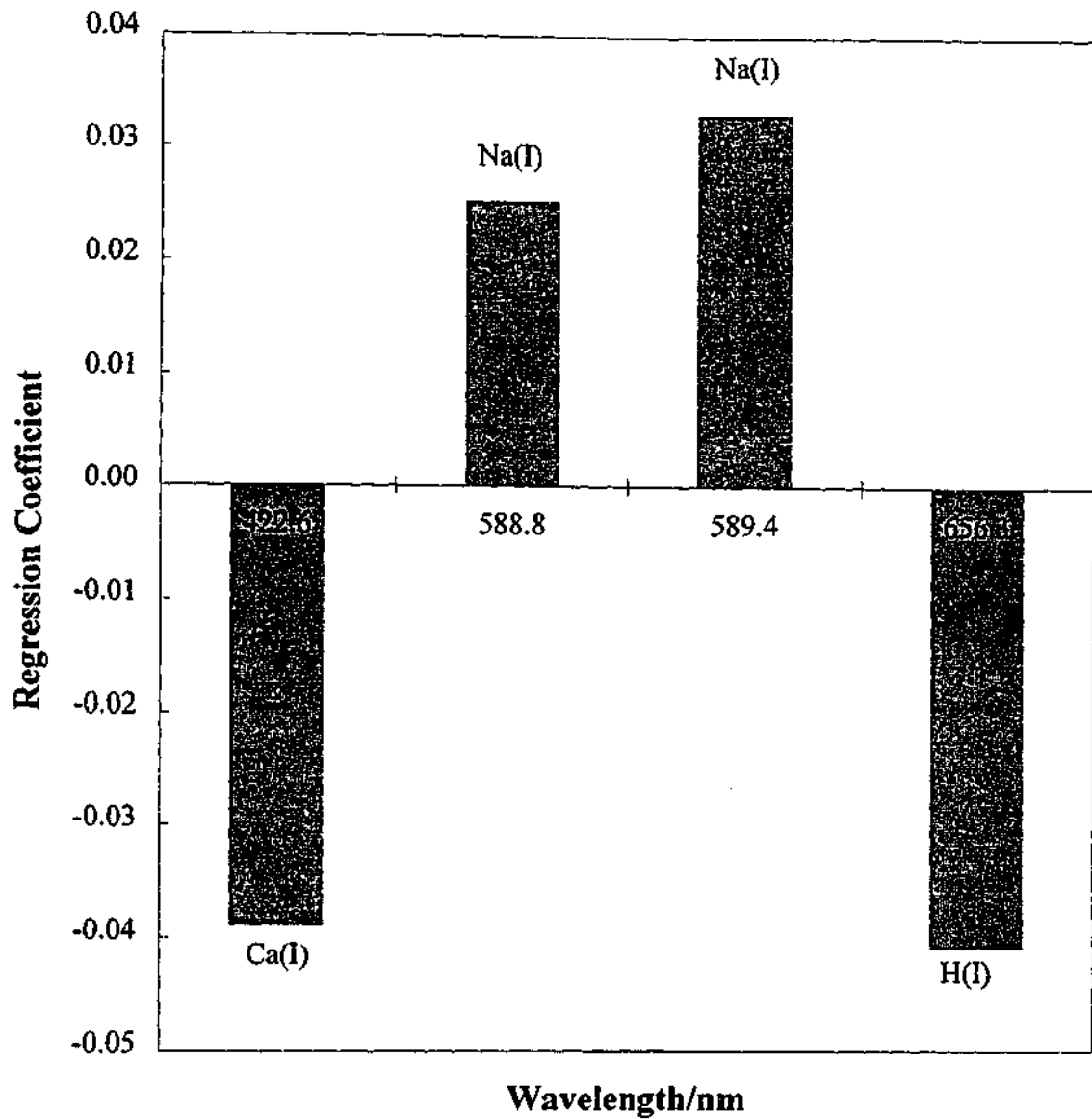


Figure 7.12. PCR model for Cl concentration in Latrobe Valley brown coals.

negatively correlated with Cl concentration. As with many of the other elements, Cl is negatively correlated with the H line at 656.27 nm. The RMSEP of the model for Cl concentration is also similar to those obtained for the other elements, despite the absence of Cl emission lines in the LIBS spectra.

### 7.5.8 Model for Sulphur

The PCR model developed for S in Latrobe Valley coals is shown in Figure 7.13. Like Cl, S was unable to be measured directly from the laser-induced spectra of coal in Chapter 4. This was a result of the lack of intense emission lines in the region of the electromagnetic spectrum being monitored. Again, the only way to predict S from these spectra is to correlate its concentration with other features of the spectra.

Sulphur is mainly present in Latrobe Valley coals as organic sulphur [2]. Thus it is not surprising that its concentration is positively correlated with the C emission line at 247.86 nm in the regression model. Sulphur is also present in Latrobe Valley coals as pyrite ( $\text{FeS}_2$ ). While the regression model does not show any strong correlation between S concentration and Fe emissions, S concentration is positively correlated with the Al lines at 308.22, 309.27 and 309.29, 394.40 and 396.15 nm, and the Mg lines at 280.27 and 285.21 nm. Since Al is also present in the coal in a mineral form, both S and Al levels may be elevated in coals with a high mineral content, resulting in the positive correlation indicated in the model. The correlation between the Mg emission lines and S concentration does not seem attributable to elemental variation within the coals. It may be that matrix effects in LIBS are the cause for the correlation; S levels may contribute to Mg emission intensities.

A negative correlation is observed between the intensities of Si lines at 251.61, 251.92, 252.41 and 288.16 nm and S levels. When there are high levels of minerals within the coal there are increased levels of Si. However, this also means that the concentration of organic matter in the coal is decreased. If S is mainly present in its organic form, an increase in Si will lead to a decrease in S, which may explain the negative correlation.

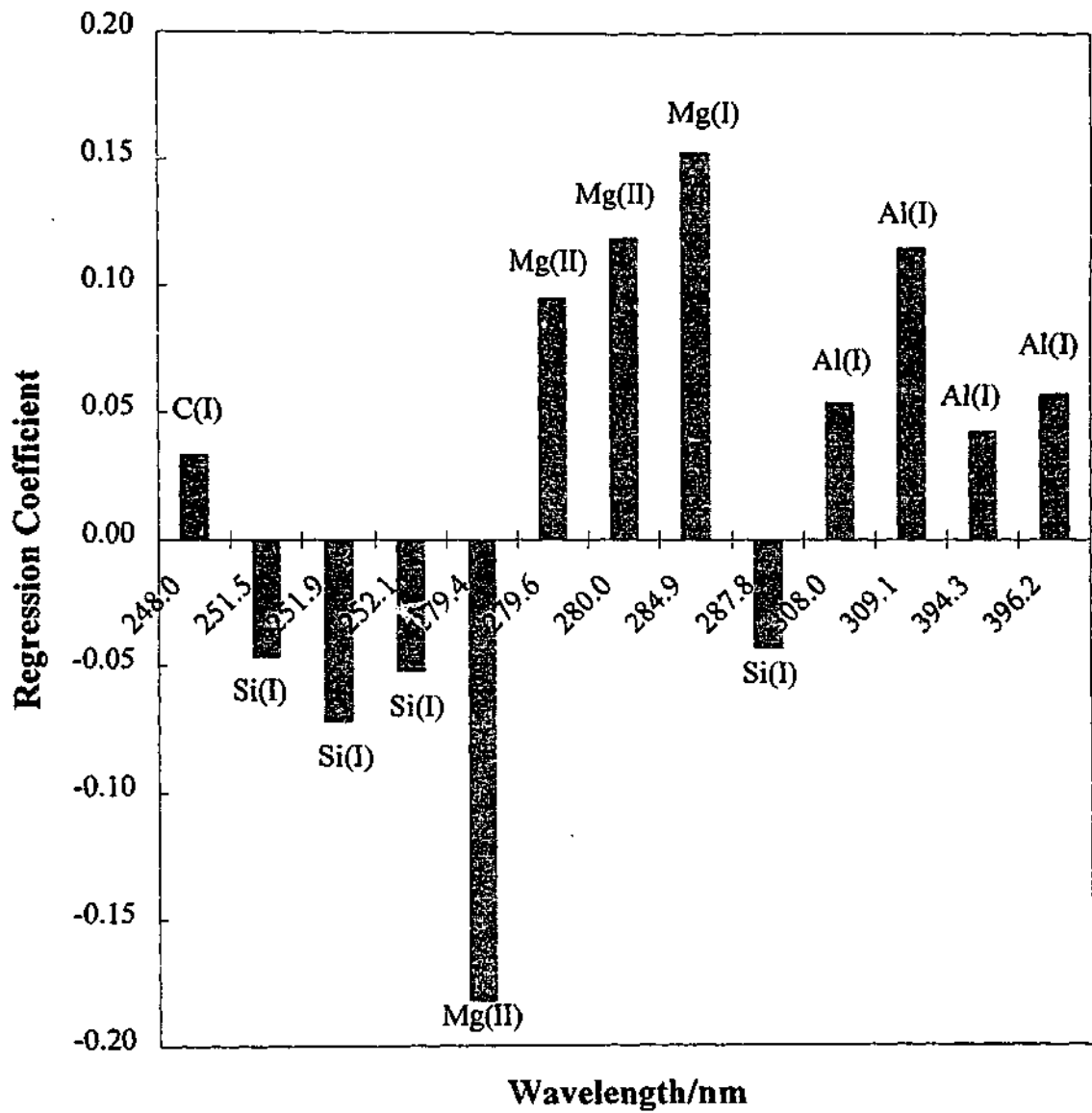


Figure 7.13. PCR model for S concentration in Latrobe Valley brown coals.

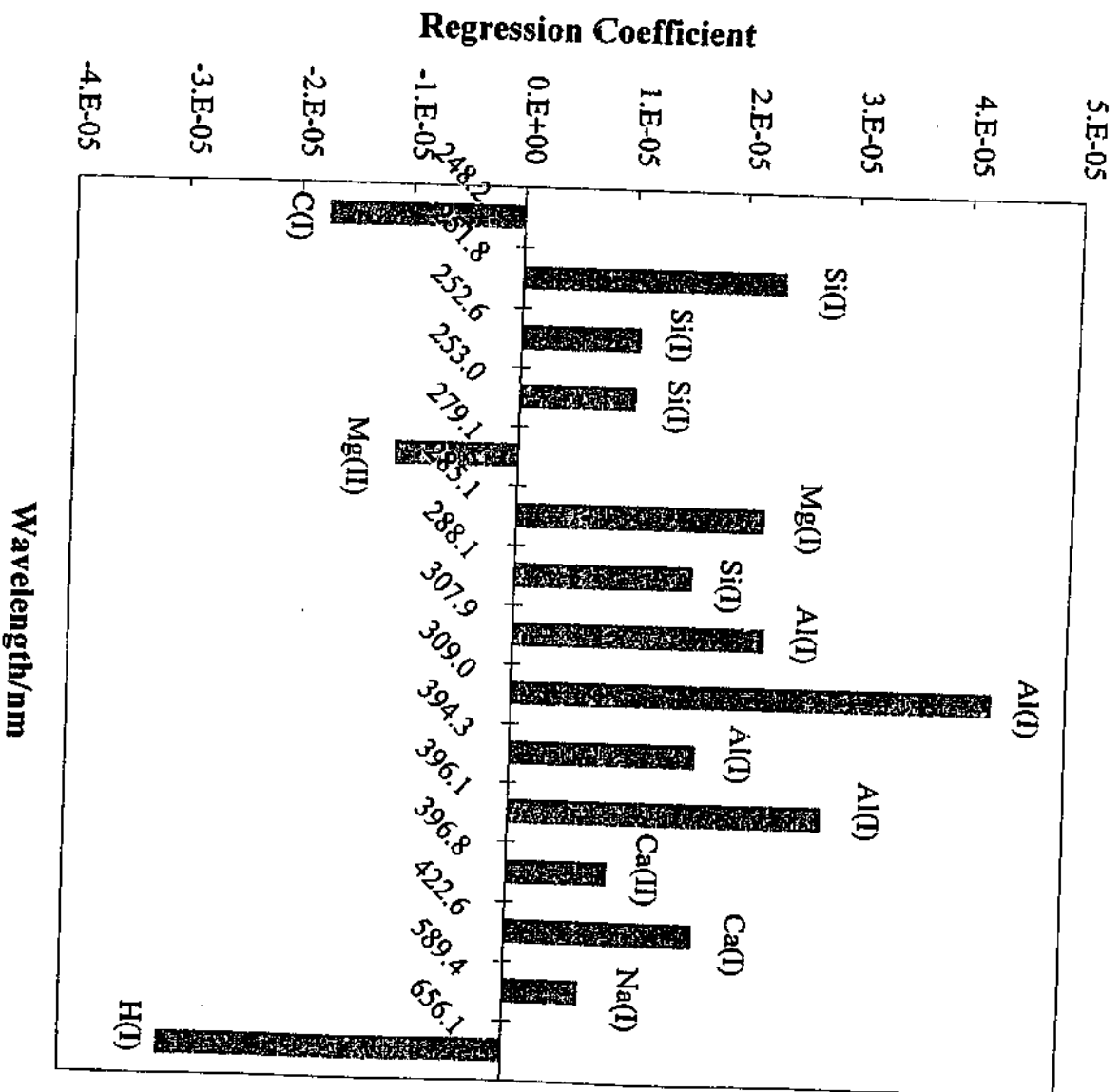


Figure 7.14. PCR model for total ash yield in Latrobe Valley brown coals.

### 7.5.9 Model for Total Ash Yield

The regression model for the total ash yield of Latrobe Valley coals is shown in Figure 7.14. The total ash yield is often employed as an indicator of coal quality. It is a measure of the amount of ash produced by the inorganics, organic sulphur and oxygen in coal during combustion. The ash yield of a particular coal depends primarily on sulphur retention. In laboratory testing, sulphur retention is set to a maximum so that repeatable results may be observed [2]. Obviously a larger set of emission lines from laser-induced spectra are required to adequately predict the total ash yield because the ash is comprised of many elements. The main ash-forming elements also vary from mine-to-mine.

Figure 7.14 shows that the intensities of the lines from most of the main inorganic elements present in Latrobe Valley coals contribute to the PCR model for total ash yield. The inorganic elemental emission lines contributing to this model are the Si lines at 251.92, 252.85 and 288.16 nm, Mg lines at 279.55 and 285.21 nm, Al lines at 308.22, 309.27 and 309.29, 394.40 and 396.15 nm, Ca lines at 396.85 and 422.67 nm, and the Na line at 589.59 nm. All of these lines except that for Mg (at 279.55 nm) are positively correlated with ash yield. Total ash increases with an increase in inorganic element levels, so this finding is to be expected. It is possible that the negative correlation between Mg at 279.55 nm and total ash yield is an anomaly. The total ash yield, like the concentrations of many of the inorganics, is also negatively correlated with the C line at 247.86 nm and the H line at 656.27 nm.

### 7.5.10 Model for Coal Moisture Content

Finally, Figure 7.15 presents the regression model developed for coal moisture content. As expected, the moisture levels in Latrobe Valley coals show a strong positive correlation with the intensity of the H emission line at 656.27 nm. There is also a negative correlation between moisture content and the intensity of the C line at 247.86 nm. Again, this is to be expected; as the moisture content increases the concentration of organic material decreases. Moisture content is also strongly negatively correlated with peaks in the  $\Delta v = 0$  sequence region of the  $B(^2\Sigma) \rightarrow X(^2\Sigma)$  electronic transition of CN, which has band heads situated

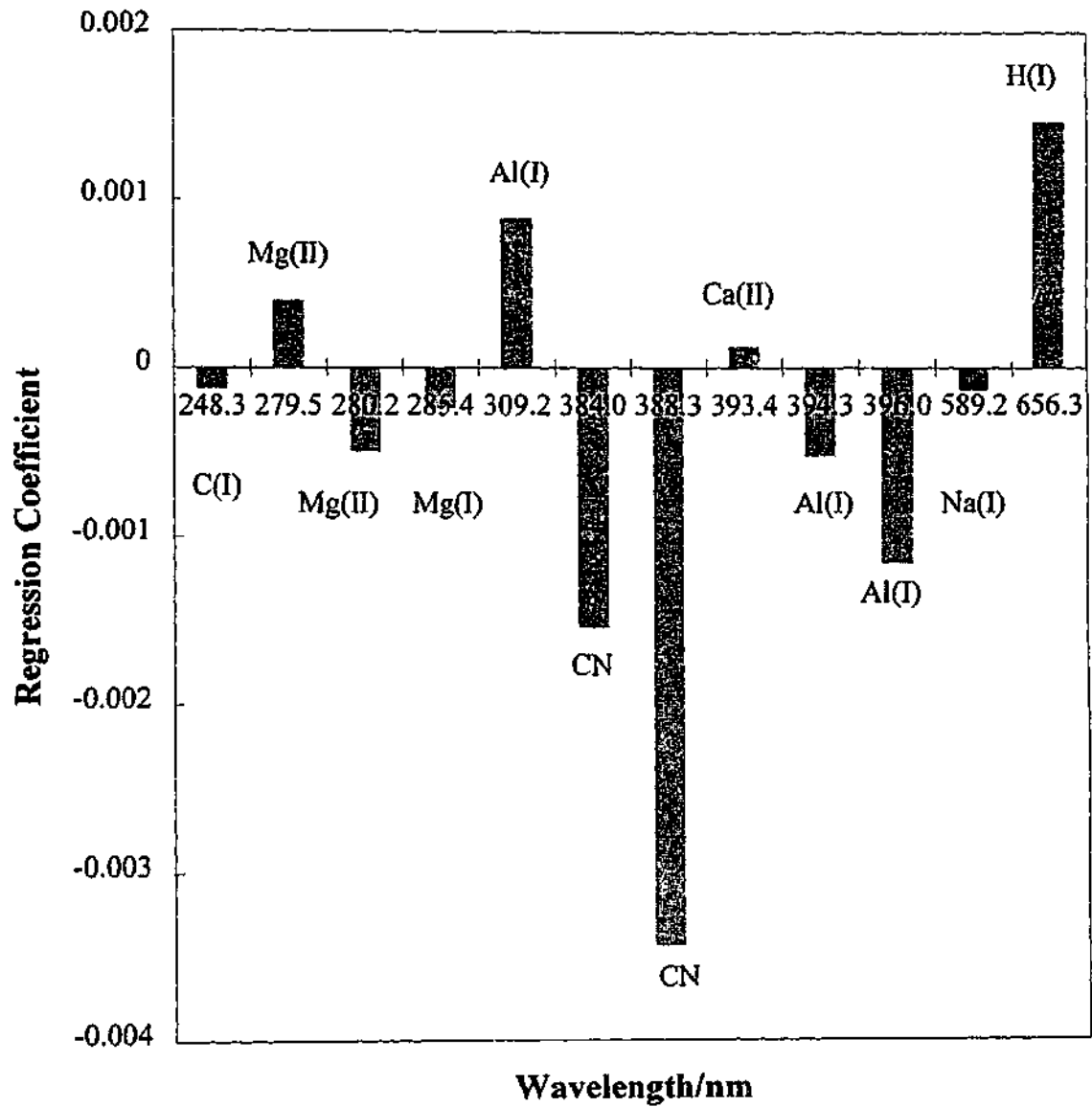


Figure 7.15. PCR model for moisture content in Latrobe Valley brown coals.

between 385 and 388 nm [151]. Emission in this region arises from electronic excitation of CN, likely produced from a reaction of C in the coal with N in the atmosphere. Thus, we would also expect the magnitude of the peaks in this band to decrease as moisture levels increase.

Emission lines from Mg (279.55, 280.27 and 285.21 nm), Al (309.27 and 309.29, 394.40 and 396.15 nm), Ca (393.37 nm) and Na (589.59 nm) are also represented in the model for moisture content. As expected, most of these lines are negatively correlated with moisture content. The exceptions to this are the Al line at 309.27 and 309.29 nm, the Ca line at 393.37 nm and the Mg line at 279.55 nm.

### **7.6 *Non-linear Models***

Having produced simple linear regression models for each of the ten coal constituents of interest, the dependent variables were tested for non-linear contributions from the emission lines. To do this, each of the independent variables remaining in the models was squared and then these values added to the data set as independent variables. Regression models were then calculated as for the linear models. While this resulted in improved regression coefficients between the predicted and measured values for some of the inorganic elements, the RMSEP only improved for the Cl model (300 to 200 ppm). Therefore it can be concluded that there is little value in adding complexity to the models by including quadratic terms.

### **7.7 *Conclusions***

Principal component regression was applied to LIBS spectral data from fifty Latrobe Valley brown coal samples in this chapter in order to produce predictive models for ten of the variables describing the coal. The coal constituents modelled were the Na, Mg, Ca, Fe, Si, Al, Cl and S concentrations, the moisture content, and the total ash yield. The emission spectra used in this work were obtained using three 2048 element CCD detectors and covered the wavelength region between 220 and 830 nm.

The PCR models were first optimised by removing outliers from the data. This process resulted in improvements in the correlations between the predicted and measured dependent variables and, hence, decreases in the RMSEPs of most of the models. Following this optimisation, the PCR models were simplified by selecting the independent variables that contributed most to each model and discarding the remainder of the variables. This process simplified the models without lessening their predictive abilities. Both the RMSEPs and correlation coefficients obtained using these simplified models were little different to those of the optimised models.

The RMSEPs obtained using these simplified models were 100 (Al), 200 (Mg, Na, Ca, Fe), 300 (Cl), 400 (S), and 600 ppm (Si). The RMSEP obtained using the PCR model for coal moisture content was 3 %, while that obtained for the total ash yield model was 0.2 %. The main achievements of the work in this chapter were the development of predictive models for S, Cl, and total ash yield because these variables were not able to be measured from individual emission peaks or ratios of peaks in the spectra. PCR modelling was also able to improve the error margins in predictions of the Al levels in Latrobe Valley brown coal from LIBS spectra. The standard error of prediction obtained from the calibration curve for Al in Chapter 4 of this thesis was 300 ppm. The 100 ppm prediction error obtained using the PCR model is a significant improvement. The prediction errors obtained when using the PCR models for the other inorganic and mineral elements were approximately the same as those obtained in Chapter 4. The prediction error obtained from the PCR model for the coal moisture content was worse than that obtained using the H to C ratio method described in Chapter 6.

The abilities on non-linear PCR models to predict the concentrations of the ten coal constituents from laser-induced emission spectra were also investigated. However, it was found that the predictive capabilities of only the Cl model were improved using the non-linear model. Thus, it was concluded that adding the complexity of non-linear terms to the models was not justified.

In summary, it was concluded that PCR models could be used for the prediction of Cl, S, Al, and total ash from LIBS spectra of Latrobe Valley brown coal. However, single peak calibration curves were found to provide predictions with similar precision to the PCR models for Na, Mg, Ca, Fe, and Si. Hence, single peak calibration is preferable because of

its simplicity. Measuring the intensity ratio of H-to-C in the spectra was also found to be preferable to using the PCR model for moisture content because its precision was superior to that of the latter.

## General Conclusions

In this thesis, laser-induced breakdown spectroscopy has been applied to the analysis of the inorganic, mineral and moisture content of Latrobe Valley brown coal. Experimental parameters such as the laser irradiance and time gating of the optical detection were first optimised for this sample matrix. The six major inorganic and mineral elements, Na, Mg, Ca, Fe, Al and Si, were then analysed using LIBS. These analyses were found to be reproducible and in good agreement with standard analysis methods. The effects of coal moisture levels on these analyses and a method for measuring the moisture content of coal have also been studied. Signal normalisation and multivariate analyses were implemented in order to improve these analyses.

The experimental apparatus and methodology used to undertake LIBS analyses of Latrobe Valley brown coal were detailed in Chapter 3 of this thesis. Two different experimental systems were used in this work. The first, which was a sensitive bench-top system that incorporated an ICCD, was used for the work in Chapters 4 to 6. The other system, a lower-cost portable instrument, was used to provide spectra for the multivariate analyses in Chapter 7. The optimum conditions for the analysis of the six major inorganic and mineral elements in the coal were determined experimentally for the ICCD system. The effects of the laser irradiance used to induce the sample plasma on the atomic and ionic emission from the inorganic and mineral elements were first investigated. To this end, the peak areas, atomic-to-ionic peak ratios, and signal-to-background ratios were measured over a range of irradiances for the major emission lines observed from each of the main inorganic and mineral elements within the coal. The optimum laser irradiance was found to depend on the element being analysed as well as its ionisation state. An irradiance of  $20 \text{ GWcm}^{-2}$  was found to produce good signal-to-background and emission intensities for all the peaks studied.

The effects of time-gating the optical detection in LIBS analyses of the brown coal using the ICCD system were also investigated. The peak areas, atomic-to-ionic peak ratios, and signal-to-background ratios of emission lines from the six major inorganic and mineral elements were measured at a range of time delays between the start of the laser pulse and detection. The optimum time delay was found to vary between elements, ionisation states,

and emission lines from the same element and ionisation state. A time delay of 1  $\mu$ s provided good signal-to-background and emission intensity for the lines studied. The electron density and temperature were also measured over a range of time delays. As expected, both the temperature and electron density were found to decrease with increasing time delay.

The application of LIBS to the chemical analysis of the inorganic and mineral content of Latrobe Valley brown coal was pursued in Chapter 4. Laser-induced emission spectra between 200 and 840 nm from coal samples from the Yallourn, Loy Yang, and Morwell open cut mines were obtained. These spectra indicated that the differences in the ash-forming content of the coals were reflected in the emission from laser-induced plasmas. Hence, the possibility of using LIBS from the analysis of the inorganic and mineral elements in Latrobe Valley brown coal was demonstrated.

The reproducibility of LIBS analyses of the six major inorganic and mineral elements in the coal was then investigated. The results of these experiments showed that most of the analyses of neutral emission from the laser-induced plasma were reproducible at a 95 % confidence level. However, the intensity of ionic emission was found to be less reproducible than the neutral emission. Thus, it was concluded that LIBS analysis of the inorganic and minerals in Latrobe Valley brown coal should be restricted to neutral emission lines, where possible.

Calibration curves were constructed for the LIBS analysis of each of the six major inorganic and mineral elements in the coal by correlating emission peak areas with the results from standard chemical analyses. These calibration curves were found to be linear for Na, Fe, Al, and Si for concentrations between 200 and 3300, 200 and 2200, 60 and 16000, and 40 and 12000 ppm, respectively. However, linear calibration curves were found to fit poorly through the data obtained for Ca and Mg in the coal as a result of atomic self-absorption at high concentrations. Thus, non-linear curves were fitted through this data, which spanned the concentration range from 190 to 2530 ppm for Mg, and 40 to 2820 ppm for Ca.

The standard errors of prediction obtained when using these calibration curves were 100 (Mg), 200 (Na, Ca, Fe), 300 (Al), and 500 ppm (Si). Detection limits were also calculated from the calibration curves. These ranged between 40 and 200 ppm for the six inorganic and mineral elements.

A Latrobe Valley brown coal sample with an unknown chemical composition was analysed for its inorganic and mineral content independently using LIBS and ICP. The results of these independent analyses showed that the LIBS measurements were in good agreement with those made using ICP. For each of the six elements, the difference between the results of the two analysis methods was less than the uncertainty in the LIBS measurement.

The use of signal normalisation to improve the results of LIBS elemental analyses was investigated in Chapter 5. Three different signal normalisation methods were tested. The first of these used a measurement of the laser-induced acoustic shock wave. Another of these methods incorporated a temperature normalisation coefficient. The third method, which had been proposed previously by Chaléard *et al.* [1] in a study of metal samples, used both the acoustic signal and the temperature normalisation coefficient.

The validity of using a measure of the acoustic shock wave for signal normalisation was first investigated. The results of a series of experiments showed that the magnitude of the acoustic signal was linearly related to the laser irradiance, elemental emission intensity and laser-induced mass loss. Hence, it was concluded that this measurement could be used to correct for fluctuations in the laser irradiance and any other parameters which caused the laser-induced mass loss and emission intensity to vary. The effects of sample matrix on the magnitude of the acoustic shock wave were also investigated. To achieve this, the acoustic signals produced during laser interaction with a black coal, a brown coal, a fused XRF pellet, a standard copper alloy, two cement samples, and six cement ingredients were measured. The magnitude of the acoustic signal was found to vary significantly with sample matrix. The copper alloy produced the largest acoustic signal of the samples tested. It was proposed that this was likely to be a result of its relatively high thermal conductivity. Samples with high thermal conductivities have relatively low breakdown thresholds. Hence, more energy remains for plasma formation. In general, when more energy is provided for plasma formation, a larger acoustic shock wave will be produced. Samples with similar chemical matrices were found to produce similar acoustic signals.

Hence, these results proved that it is valid to use a measure of the laser-induced acoustic shock wave as a means of signal normalisation in LIBS experiments.

The three methods of signal normalisation were tested on the results of LIBS analyses of Ca, Fe, Mg and Si in the two cements and six cement ingredients. The normalisation method proposed by Chaléard *et al.* [1] was found to be the most effective for correcting for fluctuations in experimental parameters in this study. This normalisation procedure was found to be effective for samples with Ca concentrations between 0.3 and 45 wt %, Fe concentrations between 0.7 and 55 wt %, Si concentrations between 4 and 18 wt %, and Mg concentrations between 0.16 and 0.88 wt %. Hence, this method is applicable over large concentration ranges for Ca, Fe, and Si. It is possible that it may also be applied to samples with Mg concentrations outside the range listed. However, such samples were not investigated in this thesis.

The standard errors of prediction obtained from the calibration curves improved from 3 to 2 wt % for Ca and Fe, 3 to 0.2 wt % for Si, and 0.2 to 0.08 wt % for Mg, when the normalisation procedure incorporating the acoustic signal and temperature normalisation coefficient was implemented. Thus, it was concluded that this method of signal normalisation could be used to improve the results from LIBS analyses. The advantages of this normalisation method over other methods are that it is independent of sample type and will be effective even when experimental parameters, such as laser focussing, vary.

Chapter 6 described studies of the effects of moisture content on LIBS analyses of the inorganic elements in Latrobe Valley brown coal. Coal samples identical in all properties but moisture content, as well as a set of different samples covering a range of coal moistures, were used in this study. The peak areas of the Na and Mg emission lines studied were found to increase linearly with decreasing moisture content and wet basis elemental concentrations, until threshold moisture levels were reached. Below these thresholds, emission intensity remained relatively constant. It was concluded that there were two possible causes of this behaviour. Firstly the sample water was acting as a diluent. Hence, as coal moisture decreased, the concentrations of the inorganics increased. In Chapter 4, atomic self-absorption was observed at high elemental concentrations. Consequently, it is possible that this was the cause of the levelling off of the intensities of

the Na and Mg lines. Alternatively, it is possible that changes in the water content of the samples caused changes in the plasma chemistry that resulted in this levelling off.

The effects of sample moisture content on the intensity of emission from carbon and hydrogen in Latrobe Valley brown coal produced during LIBS analyses were also investigated in Chapter 6. It might be expected that the increase in the number of H atoms in the sample caused by increasing its moisture content would result in an increase in the emission intensity of hydrogen. However, this was not the case. At high moisture levels (> 58 %), the area of the  $H_{\alpha}$  emission line at 656 nm was found to decrease as moisture content increased. When sample moisture was between 50 and 58 %, the intensity of this emission line remained relatively constant. At moisture levels below 50 %, the intensity of the  $H_{\alpha}$  line was found to decrease with decreasing coal moisture content. Therefore it was concluded that as coal moisture increased, the breakdown threshold of the sample increased. This resulted in a decrease in the energy used to form the plasma and, consequently, emission intensity.

The effects of coal moisture content on the intensity of the  $H_{\beta}$  emission line at 486 nm were also investigated. Unlike the  $H_{\alpha}$  line, the peak area of this line remained relatively constant as moisture content varied between 48 and 65 %. It is possible that the different behaviours of the two lines were a result of differences in their sensitivities to plasma temperature. The FWHM of the Stark broadened  $H_{\beta}$  line, which is largely independent of plasma temperature and which remained constant as sample moisture varied, was used to calculate the electron density in the laser-induced plasma. These calculations indicated that the electron density remained relatively constant as coal moisture content varied. Unlike the FWHM of the  $H_{\beta}$  line, that of the  $H_{\alpha}$  line was found to vary with coal moisture content. Since the electron density was found to remain constant as coal moisture varied, it is likely the FWHM of the  $H_{\alpha}$  line varied as a result of changes in the plasma temperature. These results demonstrate that increasing sample moisture content affects both plasma chemistry and dilutes elemental concentrations in Latrobe Valley brown coals.

The area of the carbon emission line at 248 nm was found to decrease linearly as coal moisture increased in the LIBS experiments. As found above, it is likely that this trend is a

result of the water diluting the concentration of carbon in the coal as well as reducing the energy in the laser-induced plasma.

The effects of the moisture content of the Latrobe Valley coal on the intensity ratio of the  $H\beta$  line to the C line at 248 nm were also investigated at four different laser irradiances. This ratio was found to increase linearly with coal moisture content at each irradiance. The H-to-C ratio was also found to increase with irradiance below  $20 \text{ GWcm}^{-2}$ . Above  $20 \text{ GWcm}^{-2}$ , the ratio was found to remain relatively constant as the irradiance was varied. Thus, it was concluded that this ratio could be used as a measure of coal moisture content, provided the irradiance was either constant or above  $20 \text{ GWcm}^{-2}$ . The standard errors of such measurements were found to be less than or equal to 1 % at each of the irradiances used. This is comparable to the results obtained using on-line neutron activation analysis and is only slightly poorer than the results obtained when using on-line microwave instruments [4]. However, since the microwave instruments cannot be used to measure the inorganics and minerals in the coal, LIBS has the advantage of being able to provide a larger range of chemical analyses than these instruments.

In Chapter 7 of the thesis, PCR was applied to LIBS spectral data from fifty Latrobe Valley coal samples in order to develop predictive models for ten of the chemical constituents of the coal. One of the aims of this modelling was to improve the prediction of Na, Mg, Ca, Fe, Al and Si concentrations as well as the moisture content from laser-induced emission spectra. The other aim was to develop a means for predicting Cl and S concentrations as well as the total ash yield of brown coal, properties that were unable to be measured from single peak areas or ratios.

The PCR models were produced using spectral data obtained simultaneously from three 2048 element multichannel detectors and which covered the spectral region from 220 to 830 nm. These models were first optimised by removing outliers from the data. This process improved the correlation between predicted and measured data and, consequently, decreased the RMSEPs of most of the models. The PCR models were then simplified by discarding the independent variables that did not make significant contributions to the models. This process simplified the models without lessening their predictive capabilities. The RMSEPs obtained using the simplified models were 100 (Al), 200 (Mg, Na, Ca, Fe),

300 (Cl), 400 (S), and 600 ppm (Si). The RMSEP of the model for predicting the coal moisture content was 3 %, while that for the model for total ash yield was 0.2 % over the 0.24 to 2.88 % range measured. Both the correlation coefficients and RMSEPs of the simplified models were little different to those of the complete, optimised models.

Predictive models for S, Cl and total ash yield in Latrobe Valley brown coal from laser-induced emission spectra were successfully produced using PCR. PCR modelling was also able to improve the error margins in predictions of Al levels in the coal from the emission spectra. The standard error of prediction obtained from the calibration curve for Al in Chapter 4 was 300 ppm. The 100 ppm prediction error obtained using the PCR model is a significant improvement. However, the prediction errors of the PCR models for Na, Mg, Ca, Fe and Si were comparable to those obtained in Chapter 4. The prediction error of the PCR model for coal moisture content was worse than that obtained using the H-to-C ratio method described in Chapter 6.

The ten PCR models were tested to determine whether the addition of non-linear spectral terms improved their predictive abilities. However, it was found that only the predictions of the Cl model improved when using a non-linear model. Thus, it was concluded that there was little worth in adding the complexity of non-linear terms to the PCR models.

In summary, single peak calibration curves were found to be the optimal method for measuring Na, Mg, Ca, Fe and Si concentrations in Latrobe Valley brown coal from laser-induced emission spectra. The PCR models constructed for these elements in Chapter 7 did not provide any significant improvement to their measurement from LIBS data. Hence, single peak measurements were deemed preferable because of their simplicity. However, the PCR model constructed for Al in the coal was found to improve the results of its analysis. PCR models were also able to be used to successfully measure Cl and S concentrations as well as the total ash yield of the coal, coal properties that were unable to be measured from single peaks or peak ratios from the spectra.

An acoustic signal and temperature normalisation method initially proposed by Chaléard *et al.* [1] was found to produce significant improvement in the LIBS analysis results for Ca, Fe, Si and Mg in different sample matrices. Hence, it may overcome the need for signal calibration in many LIBS analyses.

A method for measuring coal moisture content was also developed. This method involved measuring the intensity ratio of the hydrogen emission line at 486 nm to the carbon emission line at 248 nm. The results of the PCR model developed to predict the moisture content in the Latrobe Valley coal were inferior to those of the hydrogen to carbon ratio. Measuring the coal moisture will be useful for correcting for its effects on the intensity of emission from the inorganic and mineral elements in the coal spectra, as well as predicting the thermal efficiency of power generation fired by a particular coal.

While it was shown in this investigation that LIBS could be used to analyse ten of the variables describing the coal, its usefulness would be further improved if this number was increased. In particular, measurements of the carbon, organic hydrogen, nitrogen and oxygen in the coal would be valuable. Nitrogen oxides, which are major pollutants emitted during coal-fired power generation, are directly related to the amount of nitrogen in the coal. Carbon, organic hydrogen and oxygen levels vary with coal rank and lithotype. Carbon and organic hydrogen are also related to the thermal efficiency of power generation, while the amount of oxygen is related to the ignition reactivity and combustibility of the coal [2]. Thus, analyses of all these organic constituents are important. Currently the oxygen in Latrobe Valley brown coal is usually measured by difference, rather than directly. The successful application of LIBS to the direct analysis of oxygen in coal would make LIBS instruments highly valued in the coal industry.

It is likely that the carbon content of Latrobe Valley brown coals could be measured directly from its emission peaks using LIBS. It is also probable that these results would require corrections for the moisture contents of the coals. The measurement of the organic hydrogen in the coal is likely to require sample drying prior to analysis because the high water content of the coal results in the H emission produced mostly coming from the hydrogen in the water. Measurement of the oxygen and nitrogen in the coal will most probably need to be performed in air-free environments. This is likely to be an obstacle to their measurement on-line or *in situ*.

The CRC for Clean Power from Lignite has already begun applying the findings of this research to chemical analyses in the brown coal industry. Trials of prototype portable instruments have begun at the Loy Yang and Hazelwood power stations in the Latrobe Valley. These instruments, which have been described by Body and Chadwick [38,39],

have been used to analyse the inorganic and mineral content of the coal. The CRC is currently looking to increase the number of coal constituents able to be analysed using this portable LIBS instrument. It is also looking to develop LIBS instruments for *in situ* analyses of the coal. Thus, the future for LIBS in this and other applications appears to be bright.

**Standard Analysis Results**

This appendix contains the standard analysis results of the samples used in this work. These results were obtained using the standard methods described in Chapter 2 of this thesis.

**A.1 Brown Coal Analyses**

Table A.1. Standard Chemical Analyses (obtained using AAS and ICP) of Latrobe Valley Brown Coal Samples.

| Sample – CRC/            | 8-4-18/1  | 8-4-18/2  | 8-4-26/13 | 8-4-26/14 | 8-4-26/15 |
|--------------------------|-----------|-----------|-----------|-----------|-----------|
| c(Si)/ppm                | 130       | 100       | 400       | 20        | 50        |
| c(Al)/ppm                | 100       | 100       | 350       | 140       | 140       |
| c(Fe)/ppm                | 2180      | 2150      | 2420      | 280       | 3160      |
| c(Mg)/ppm                | 770       | 740       | 3110      | 420       | 1080      |
| c(Na)/ppm                | 240       | 240       | 4000      | 1320      | 230       |
| c(Ca)/ppm                | 710       | 710       | 940       | 140       | 720       |
| c(Cl)/ppm                | 400       | 240       | 2070      | 1320      | 410       |
| c(S)/ppm                 | 870       | 910       | 4840      | 1270      | 990       |
| Total ash yield/<br>wt % | 0.77      | 0.74      | 2.42      | 0.43      | 0.99      |
| Moisture/wt %            | 66.4      | 66.4      | 50.6      | 52.8      | 54.8      |
| Sample – CRC/            | 8-4-26/17 | 8-4-26/23 | 8-4-26/26 | 8-4-26/30 | 8-4-26/38 |
| c(Si)/ppm                | 20        | 100       | 50        | 20        | 3770      |
| c(Al)/ppm                | 120       | 390       | 50        | 40        | 160       |
| c(Fe)/ppm                | 2420      | 250       | 1540      | 1990      | 1400      |
| c(Mg)/ppm                | 700       | 390       | 720       | 950       | 1080      |
| c(Na)/ppm                | 250       | 300       | 340       | 290       | 2800      |
| c(Ca)/ppm                | 700       | 250       | 630       | 580       | 270       |
| c(Cl)/ppm                | 490       | 250       | 240       | 250       | 2590      |
| c(S)/ppm                 | 860       | 1430      | 1150      | 950       | 1560      |
| Total ash yield/<br>wt % | 0.78      | 0.39      | 0.63      | 0.70      | 1.99      |
| Moisture/wt %            | 59.0      | 50.8      | 51.9      | 58.6      | 46.1      |

| Sample - CRC/            | 8-4-26/39 | 8-4-26/40 | 8-4-26/42 | 8-4-26/43 | 8-4-26/44 |
|--------------------------|-----------|-----------|-----------|-----------|-----------|
| c(Si)/ppm                | 110       | 1620      | 72        | 60        | 263       |
| c(Al)/ppm                | 0         | 0         | 0         | 280       | 160       |
| c(Fe)/ppm                | 540       | 510       | 600       | 340       | 530       |
| c(Mg)/ppm                | 810       | 760       | 720       | 400       | 420       |
| c(Na)/ppm                | 2600      | 2120      | 2640      | 910       | 790       |
| c(Ca)/ppm                | 220       | 200       | 180       | 230       | 260       |
| c(Cl)/ppm                | 3140      | 2320      | 3360      | 960       | 890       |
| c(S)/ppm                 | 1410      | 1260      | 1560      | 1870      | 2310      |
| Total ash yield/<br>wt % | 0.87      | 1.16      | 1.02      | 0.51      | 0.58      |
| Moisture/wt %            | 45.8      | 49.5      | 40        | 43.4      | 47.4      |
| Sample - CRC/            | 8-4-26/45 | 8-4-26/47 | 8-4-26/48 | 8-4-26/49 | 8-4-26/52 |
| c(Si)/ppm                | 140       | 60        | 3530      | 200       | 190       |
| c(Al)/ppm                | 90        | 190       | 630       | 50        | 1930      |
| c(Fe)/ppm                | 410       | 120       | 1260      | 4490      | 450       |
| c(Mg)/ppm                | 230       | 2990      | 2630      | 2470      | 390       |
| c(Na)/ppm                | 410       | 1490      | 780       | 1260      | 1030      |
| c(Ca)/ppm                | 140       | 2800      | 2270      | 3030      | 130       |
| c(Cl)/ppm                | 320       | 750       | 540       | 560       | 1350      |
| c(S)/ppm                 | 2990      | 2240      | 2450      | 5960      | 3270      |
| Total ash yield/<br>wt % | 0.41      | 1.62      | 2.21      | 2.88      | 0.96      |
| Moisture/wt %            | 54.0      | 37.8      | 40.2      | 49.5      | 35.8      |

| <b>Sample – CRC/</b>             | <b>8-4-30/39</b> | <b>8-4-30/40</b> | <b>8-4-30/42</b> | <b>8-4-30/43</b> | <b>8-4-30/53</b> |
|----------------------------------|------------------|------------------|------------------|------------------|------------------|
| <b>c(Si)/ppm</b>                 | 150              | 20               | 130              | 2100             | 1020             |
| <b>c(Al)/ppm</b>                 | 260              | 50               | 90               | 3860             | 710              |
| <b>c(Fe)/ppm</b>                 | 810              | 840              | 600              | 1660             | 980              |
| <b>c(Mg)/ppm</b>                 | 1050             | 1310             | 1140             | 1490             | 1340             |
| <b>c(Na)/ppm</b>                 | 360              | 370              | 810              | 500              | 1100             |
| <b>c(Ca)/ppm</b>                 | 2510             | 2800             | 2010             | 4300             | 1180             |
| <b>c(Cl)/ppm</b>                 | 200              | 280              | 270              | 170              | 390              |
| <b>c(S)/ppm</b>                  | 930              | 1070             | 920              | 2480             | 1970             |
| <b>Total ash yield/<br/>wt %</b> | 0.97             | 0.93             | 0.88             | 2.77             | 1.40             |
| <b>Moisture/wt %</b>             | 59.5             | 53.3             | 45.6             | 44.8             | 60.7             |
| <b>Sample – CRC/</b>             | <b>8-4-30/54</b> | <b>8-4-30/55</b> | <b>8-4-30/56</b> | <b>8-4-30/57</b> | <b>8-4-30/70</b> |
| <b>c(Si)/ppm</b>                 | 870              | 760              | 600              | 240              | 40               |
| <b>c(Al)/ppm</b>                 | 560              | 480              | 360              | 160              | 40               |
| <b>c(Fe)/ppm</b>                 | 750              | 640              | 480              | 160              | 540              |
| <b>c(Mg)/ppm</b>                 | 990              | 800              | 640              | 200              | 1270             |
| <b>c(Na)/ppm</b>                 | 870              | 760              | 640              | 360              | 500              |
| <b>c(Ca)/ppm</b>                 | 830              | 640              | 480              | 120              | 2270             |
| <b>c(Cl)/ppm</b>                 | 440              | 440              | 320              | 200              | 230              |
| <b>c(S)/ppm</b>                  | 1750             | 1680             | 1480             | 1120             | 850              |
| <b>Total ash yield/<br/>wt %</b> | 1.05             | 0.88             | 0.70             | 0.30             | 0.83             |
| <b>Moisture/wt %</b>             | 60.3             | 60.0             | 60.0             | 60.0             | 61.5             |

## A.2 Analyses of Other Samples

Table A.2. Standard Chemical Analyses (obtained using AAS and ICP) of Samples Used in Chapter 5.

| Sample                     | Cement a  | Cement b | Birdwood clay | Moculta clay | Limestone  | Gypsum |
|----------------------------|-----------|----------|---------------|--------------|------------|--------|
| c(Mn)/wt %                 | 0.01      | 0.02     | 0.01          | -            | -          | -      |
| c(Ca)/wt %                 | 36.60     | 45.30    | 0.30          | 0.20         | 32.60      | 16.30  |
| c(Na)/wt %                 | 0.60      | 0.20     | 0.10          | 0.10         | 0.10       | 0.01   |
| c(Mg)/wt %                 | 1.10      | 0.90     | 0.20          | 0.10         | 0.60       | 2.38   |
| c(K)/wt %                  | 0.50      | 0.40     | 0.50          | 0.40         | 0.20       | 0.25   |
| c(Ti)/wt %                 | 0.40      | 0.20     | 0.80          | 0.70         | 0.10       | 0.05   |
| c(Fe)/wt %                 | 2.50      | 2.40     | 2.20          | 3.50         | 0.70       | 0.35   |
| c(Al)/wt %                 | 5.20      | 2.70     | 13.80         | 9.10         | 0.80       | 0.82   |
| c(Si)/wt %                 | 13.30     | 9.80     | 22.60         | 30.90        | 4.90       | 2.70   |
| c(S)/wt %                  | -         | -        | 0.08          | -            | -          | 10.42  |
| C(Cl)/wt %                 | -         | -        | -             | -            | -          | 0.02   |
| Sample                     | Ironstone | Fly ash  | Copper alloy  | XRF pellet   | Black coal |        |
| c(Mn)/wt %                 | 0.02      | 0.02     | 0.11          | 0.0132       | -          |        |
| c(Ca)/wt %                 | 0.24      | 3.52     | -             | 0.8155       | 0.49       |        |
| c(Na)/wt %                 | 0.16      | 1.84     | -             | 0.1091       | 0.24       |        |
| c(Mg)/wt %                 | 0.32      | 1.28     | -             | 0.3872       | 0.14       |        |
| c(K)/wt %                  | 0.40      | 0.64     | -             | 0.0291       | 0.03       |        |
| c(Ti)/wt %                 | 0.32      | 1.12     | -             | 0.0486       | 0.01       |        |
| c(Fe)/wt %                 | 43.60     | 1.92     | 3.73          | 0.7463       | 0.34       |        |
| c(Al)/wt %                 | 2.96      | 11.84    | 10.05         | 1.056        | 0.32       |        |
| c(Si)/wt %                 | 4.64      | 20.72    | 0.037         | 2.236        | 0.70       |        |
| c(S)/wt %                  | -         | 0.13     | 0.001         | 0.0004       | No result  |        |
| c(P)/wt %                  | -         | -        | <0.01         | 0.0031       | No result  |        |
| c(Cu)/wt %                 | -         | -        | 81.0          | -            | -          |        |
| c(Sn)/wt %                 | -         | -        | 0.019         | -            | -          |        |
| c(Pb)/wt %                 | -         | -        | 0.0069        | -            | -          |        |
| c(As)/wt %                 | -         | -        | 0.002         | -            | -          |        |
| c(Ni)/wt %                 | -         | -        | 4.81          | -            | -          |        |
| c(Zn)/wt %                 | -         | -        | 0.17          | -            | -          |        |
| c(C)/wt %                  | -         | -        | 0.005         | -            | -          |        |
| c(LiBO <sub>2</sub> )/wt % | -         | -        | -             | 90           | -          |        |
| Total ash/wt %             | -         | -        | -             | -            | 3.9        |        |
| Moisture/wt %              | -         | -        | -             | -            | 17.4       |        |

*Error Analysis*

The experimental measurements and calculations given in this thesis have been reported with estimates of their uncertainties. The methods used to estimate these errors are described in this appendix.

*B.1 Errors in the Results in Chapter 3*

Peak areas, ratios of neutral-to-ion peak areas, and signal-to-background ratios were plotted as functions of laser irradiance and time delay in Chapter 3. The errors in the peak areas were calculated from the standard deviation of the three measurements made under identical experimental conditions. The error bars in the peak area plots represent two standard deviations.

The errors in the neutral-to-ion and signal-to-background ratios were estimated using the method of propagation of errors [159]. The error for each measurement used in the ratios was estimated to be two of the standard deviations calculated from the triplicate analyses. Where the ratio was of the form:

$$Z = A/B \tag{B.1}$$

the uncertainty in  $Z$  was calculated as follows:

$$\left(\frac{\Delta Z}{Z}\right)^2 = \left(\frac{\Delta A}{A}\right)^2 + \left(\frac{\Delta B}{B}\right)^2 \tag{B.2}$$

The errors calculated using this method are given in the plots in Chapter 3.

The ionisation temperature of the laser-induced plasma was also calculated in Chapter 3. This calculation incorporated measurements of the electron density, the intensity of the Ca (II) emission line at 393.37 nm, and the intensity of the Ca (I) emission line at 422.67 nm. The peak intensities were measured directly from the emission spectra and thus, their

errors were estimated to be two standard deviations of the triplicate measurements. The electron density of the plasma was calculated using the FWHM of the Stark broadened  $H_{\beta}$  line. The uncertainty of the FWHM of the emission line was estimated to be two standard deviations of the triplicate measurements. This error was then used to estimate the uncertainty in the electron density calculation. The FWHM of the  $H_{\beta}$  line ( $\Delta\lambda_s$ ) was related to the electron density ( $N_e$ ) as such:

$$N_e = C(N_e, T) \Delta\lambda_s^{3/2} \quad (\text{B.3})$$

where  $C(N_e, T)$  is a coefficient that is a weak function of  $N_e$ . Hence, using the method of propagation of errors, the uncertainty of the electron density can be calculated as follows:

$$\frac{\Delta N_e}{N_e} = \frac{3}{2} \frac{\Delta(\Delta\lambda_s)}{\Delta\lambda_s} \quad (\text{B.4})$$

Since the plasma temperature is present in two terms in the Saha equation, the error in its calculation was determined numerically using the errors estimated for the electron density and peak intensities.

## ***B.2 Errors in the Results in Chapter 4***

Calibration curves were constructed for each of the six main elements in Latrobe Valley brown coal in Chapter 4 of this thesis. Squared Pearson product moment coefficients ( $R^2$ ) and standard prediction errors (s) were calculated for each of these curves. The proportion of variance in the y-values of a data set, in this case the peak areas, attributable to variance in the x-values, in this case the standard analysis results, is indicated by the  $R^2$  value. The  $R^2$  value is calculated as follows:

$$R^2 = \left( \frac{n(\sum xy) - (\sum x)(\sum y)}{\sqrt{[n\sum x^2 - (\sum x)^2][n\sum y^2 - (\sum y)^2]}} \right)^2 \quad (\text{B.5})$$

The standard error of prediction estimates the amount of error in a value predicted using the regression line (calibration curve). If, in this case, the y-values are the results from the standard analyses and the x-values are the measured peak areas, s is calculated as follows [stats book]:

$$s = \sqrt{\left[ \frac{1}{n(n-2)} \left[ n \sum y^2 - (\sum y)^2 - \frac{[n \sum xy - (\sum x)(\sum y)]^2}{n \sum x^2 - (\sum x)^2} \right] \right]} \quad (\text{B.6})$$

The  $R^2$  and s values obtained for each of the six calibration curves are detailed in Chapter 4.

### ***B.3 Errors in the Results in Chapters 5 and 6***

The errors in the results detailed in Chapters 5 and 6 of this thesis were estimated using the methods described in sections B.1 and B.2. In Chapter 5, the error bars representing the uncertainty in acoustic signal, mass loss and emission intensity measurements correspond to two standard deviations calculated from the triplicate analyses. As in Chapter 4, the s values obtained for the calibration curves were calculated using equation B.6.

The error bars shown for the peak area data in Chapter 6 again represent two standard deviations. The errors in the H-to-C ratio were calculated using equation B.2, which utilises the method of propagation of errors. The errors in electron density calculations are again estimated using equation B.4.

### ***B.4 Errors in the Results in Chapter 7***

Root mean square errors of prediction (RMSEPs) were calculated for the PCR models developed in Chapter 7. The RMSEP is the average uncertainty expected on future predictions, providing the new samples are similar to the ones used for calibration. The RMSEPs are calculated using validation sets, which are sets of samples that have not been used for calibration and have similar properties to the calibration set. The RMSEP is calculated as follows [stats book]:

$$\text{RMSEP} = \frac{1}{y\text{Weight}} \sqrt{\text{ResYValVar}}$$

where *yWeight* (where applicable) is the weighting used on the data set, and *ResYValVar* is the residual Y validation variance. The residual Y validation variance is a measure of the error made when the fitted Y-value is computed as a function of the X-values.

The RMSEPs calculated for the PCR models developed for the ten variables describing coal are detailed in Chapter 7.

## List of References

---

1. C. Chaléard, P. Mauchien., N. André, J. Uebbing, J. L. Lacour, and C. Geertsen, J. Anal. At. Spectrom. **12**, 183 (1997).
2. R. A. Durie (Editor), *The Science of Victorian Brown Coal: Structure, Properties and Consequences for Utilisation*. (Butterworth-Heinemann, Oxford, 1991).
3. P. J. Jackson, Proceedings of the Seventh Annual Conference of the CRC for Clean Power from Lignite. 1 (2000).
4. N. G. Cutmore, C. S. Lim, B. D. Sowerby, V. Yip, A. L. Ottrey, J. Coal Qual. **12**, 85 (1993).
5. N. G. Cutmore and B. D. Sowerby, Proceedings of the Fifth Japan/Australia Joint Technical Meeting on Coal. (1995).
6. C. J. Clarkson, Aust. J. Mining. **89** (1995).
7. T. Sauer, Braunk. **52**, 302 (2000).
8. P. Storer and K. Smith, Braunk. **52**, 267 (2000).
9. Y. I. Lee, Y.J. Yoo, and J. Sneddon, Spectroscopy. **13**, 14 (1998).
10. V. Majidi and M. R. Joseph, Crit. Rev. Anal. Chem. **23**, 143 (1992).
11. L. J. Radziemski, Microchem. J. **50**, 218 (1994).
12. D. A. Rusak, B. C. Castle, B.W. Smith, and J.D. Winefordner, Crit. Rev. Anal. Chem. **27**, 257 (1997).
13. K. Song, Y. I. Lee, and J. Sneddon, Appl. Spectrosc. Rev. **32**, 183 (1997).
14. P. Venkateswarlu, V. Subba Rao, and M. C. George, *Laser Diagnostics of Mineral Matter and Combustion Processes in Coal*. 7 (1989).
15. D. J. Brockway, and R. M. Borsaru, Proceedings of the International Conference on Coal Science. 593 (1985).
16. A. B. Edwards, Aus. I.M.M. Proceedings, **140**, 205 (1945).
17. J. Holden, S. Hodges, and C. Black, Proceedings of The Science and Technology of Low-Rank Coal. (1998).
18. G. Couch, *Understanding slagging and fouling in pf combustion*. (IEA Coal Research, London, 1994).
19. B. Anderson, R. C. Ledger, and A. L. Ottrey, *Study of Long-Term Fouling Behaviour of Low Rank Coals, Volume 1: Overview*. (SECV, Melbourne, 1987).
20. Standards Australia, Australian Standard, **2434.9** (1991).
21. Standards Australia, Australian Standard, **1038.14.1** (1995).

22. Standards Australia, Australian Standard, 2434.1 (1999).
23. Standards Australia, Australian Standard, 2434.6.1 (1986).
24. Standards Australia, Australian Standard, 1038.3 (2000).
25. Standards Australia, Australian Standard, 2434.2 (1983).
26. K. M. Bone, H. A. Schaap, and T. C. Hughes, *Analysis of brown coal and ash by neutron activation analysis*. (SECV, Melbourne, 1981).
27. L. T. Kiss, *Anal. Chem.* **38**, 1731 (1966).
28. P. Dimitrikakis, D. Rankin, and H. Schaap, *Determination of minor and trace elements in brown coal ash by x-ray emission methods*. (SECV, Melbourne, 1976).
29. P. Arian, A. Zararsiz, and N. Efe, *Appl. Spectrosc. Rev.* **31**, 167 (1996).
30. S. Fiscor, *COLAA*. **104**, 39 (1999).
31. O. N. Krokhin, in *Laser Handbook*, F. T. Arrechi and E. O. Schulz-Dubois, Eds. (North Holland Publishing Co., Amsterdam, 1972), pp.1371-1407.
32. F. Brech and L. Cross, *Appl. Spectrosc.* **16**, 59 (1962).
33. H. Zhang, J. P. Singh, F. Yueh, and R. L. Cook, *Appl. Spectrosc.* **49**, 1617 (1995).
34. J. P. Singh, H. Zhang, F. Yueh, and R. L. Cook, *Proceedings of the 28<sup>th</sup> Intersociety Energy Conversion Engineering Conference*. (1993).
35. D. K. Ottesen, J. C. F. Wang, and L. J. Radziemski, *Appl. Spectrosc.* **43**, 967 (1989).
36. D. K. Ottesen, L. L. Baxter, L. J. Radziemski, and J. F. Burrows, *Laser Spark Emission Spectroscopy for In-Situ, Real-Time Monitoring of Pulverized Coal Particle Composition*. (Sandia National Laboratories, Livermore, 1990).
37. K. Y. Yamamoto, D. A. Cremers, M. J. Ferris, and L. E. Foster, *Appl. Spectrosc.* **50**, 222 (1996).
38. D. G. Body and B. L. Chadwick, *Rev. Sci. Instrum.*, accepted for publication.
39. D. G. Body and B. L. Chadwick, *Spectrochim. Acta Part B*, submitted for publication.
40. D. A. Cremers, M. J. Ferris, and M. Davies, *Proceedings of Advanced Technologies for Environmental Monitoring and Remediation* 190 (1996).
41. B. C. Castle, A. K. Knight, K. Visser, B. W. Smith, and J. D. Winefordner, *J. Anal. At. Spectrom.* **13**, 589 (1998).
42. J. B. Ko, W. Sdorra, and K. Niemax, *Fresenius Z. Anal. Chem.* **335**, 648 (1989).
43. J. Uebbing, J. Brust, W. Sdorra, F. Leis, and K. Niemax, *Appl. Spectrosc.* **45**, 1419 (1991).
44. R. Wisbrun, R. Niessner, and H. Scroder, *Anal. Methods Instrum.* **1**, 17 (1993).
45. H. E. Bauer, F. Leis, and K. Niemax, *Spectrochim. Acta Part B*. **53**, 1815 (1998).

46. C. Aragón, J. A. Aguilera, and F. Peñalba, *Appl. Spectrosc.* **53**, 1259 (1999).
47. D. A. Cremers, *Appl. Spectrosc.* **41**, 572 (1987).
48. J. A. Bolger, *Appl. Spectrosc.* **54**, 181 (2000).
49. U. Panne, C. Haisch, M. Clara, and R. Niessner, *Spectrochim. Acta Part B.* **53**, 1957 (1998).
50. G. Chen and E. S. Yeung, *Anal. Chem.* **60**, 2258 (1988).
51. S. A. Darke, and J. F. Tyson, *J. Anal. At. Spectrom.* **8**, 145 (1993).
52. C. Geertsen, A. Briand, F. Chartier, J. Lacour, P. Mauchien, S. Sjostrom, and J. Mermet, *J. Anal. At. Spectrom.* **9**, 17 (1994).
53. K. Dittrich and R. Wennrich, *Prog. Anal. At. Spectrosc.* **7**, 139 (1984).
54. J. W. Hager, *Anal. Chem.* **61**, 1243 (1989).
55. C. W. Huie and E. S. Yeung, *Anal. Chem.* **58**, 1989 (1986).
56. W. Demtröder, *Laser Spectroscopy*. (Springer-Verlag, Berlin, 1981).
57. M. Kuzuya, H. Matsumoto, H. Takechi, and O. Mikami, *Appl. Spectrosc.* **47**, 1659 (1993).
58. L. M. Cabalín and J. J. Laserna, *Spectrochim. Acta Part B.* **53**, 723 (1998).
59. T. V. Kononenko, S.V. Garnov, S. M. Klimentov, V. I. Konov, E. N. Loubnin, F. Dausinger, A. Raiber, and C. Taut, *Appl. Surf. Sci.* **109/110**, 48 (1997).
60. L. Moenke-Blankenburg, *Laser Microanalysis*. (Wiley Interscience, New York, 1989).
61. A. V. Pakhomov, A. J. Roybal, and M. S. Duran, *Appl. Spectrosc.* **53**, 979 (1999).
62. A. Semerok, C. Chaléard, V. Detalle, J.-L. Lacour, P. Mauchien, P. Meynadier, C. Nouvellon, B. Sallé, P. Palianov, M. Perdrix, and G. Petite, *Appl. Surf. Sci.* **138/139**, 311 (1999).
63. J. Ihlemann, A. Scholl, H. Schmidt, and B. Wolff-Rottke, *Appl. Phys. A* **60**, 411 (1995).
64. V. Margetic, A. Pakulev, A. Stockhaus, M. Bolshov, K. Niemax, and R. Hergenröder, *Spectrochim. Acta Part B* **55**, 1771 (2000).
65. D. G. Jones, *Anal. Chem.* **57**, 1057A (1985).
66. C. Haisch, U. Panne, and R. Niessner, *Spectrochim. Acta Part B* **53**, 1657 (1998).
67. J. V. Sweedler, R. B. Bilhorn, P. M. Epperson, G. R. Sims, and M. Bonner Denton, *Anal. Chem.* **60**, 282A (1988).
68. Andor Technology, <http://www.andor-tech.com> (2001).
69. G. A. Theriault and S. H. Lieberman, *Proceedings SPIE-Int. Soc. Opt. Eng.* **2835**, 83 (1996).

70. G. A. Theriault, S. Bodensteiner, and S. H. Lieberman, *Field Anal. Chem. Technol.* **2**, 117 (1998).
71. Y. W. Kim, in *Laser-Induced Plasmas and Applications*, L. J. Radziemski and D. A. Cremers, Eds. (Marcel Dekker Inc., New York, 1989).
72. B. C. Castle, K. Talabardon, B. W. Smith, and J. D. Winefordner, *Appl. Spectrosc.* **52**, 649 (1998).
73. V. Bulatov, R. Krasniker, and I. Schechter, *Anal. Chem.* **72**, 2987 (2000).
74. F. Leis, W. Sdorra, J. B. Ko, and K. Niemax, *Microchim. Acta* **II**, 185 (1989).
75. P. Shah, R. L. Armstrong, and L. J. Radziemski, *J. Appl. Phys.* **65**, 2946 (1989).
76. H. R. Griem, *Plasma Spectroscopy* (McGraw-Hill, New York, 1964).
77. E. Stoffels, P. Van De Weijer, and J. Van Der Mullen, *Spectrochim. Acta Part B* **46**, 1459 (1991).
78. R. Wisbrun, I. Schechter, R. Niessner, H. Schröder, and K. L. Kompa, *Anal. Chem.* **66**, 2964 (1994).
79. M. Sabsabi and P. Cielo, *Appl. Spectrosc.* **49**, 499 (1995).
80. L. C. Jensen, S. C. Langford, J. T. Dickinson, and R. S. Addleman, *Spectrochim. Acta Part B* **50**, 1501 (1995).
81. J. M. Vadillo, M. Milán, and J. J. Laserna, *Fresenius J. Anal. Chem.* **355**, 10 (1996).
82. R. A. Multari, L. E. Foster, D. A. Cremers, and M. J. Ferris, *Appl. Spectrosc.* **50**, 1483 (1996).
83. B. C. Castle, K. Visser, B. W. Smith, and J. D. Winefordner, *Appl. Spectrosc.* **51**, 1017 (1997).
84. C. Aragón and J. A. Aguilera, *Appl. Spectrosc.* **51**, 1632 (1997).
85. V. Bulatov, R. Krasniker, and I. Schechter, *Anal. Chem.* **70**, 5302 (1998).
86. M. P. Nelson and M. L. Myrick, *Appl. Spectrosc.* **53**, 751 (1999).
87. H. C. Liu, X. L. Mao, J. H. Yoo, and R. E. Russo, *Spectrochim. Acta Part B* **54**, 1607 (1999).
88. W. Setia Budi, H. Suyanto, H. Kurniawan, M. O. Tjia, and K. Kagawa, *Appl. Spectrosc.* **53**, 719 (1999).
89. W. Setia Budi, W. T. Baskoro, M. Pardede, H. Kurniawan, M. O. Tjia, and K. Kagawa, *Appl. Spectrosc.* **53**, 1347 (1999).
90. A. González, M. Ortiz, and J. Campos, *Appl. Spectrosc.* **49**, 1632 (1995).
91. A. S. Eppler, D. A. Cremers, D. D. Hickmott, M. J. Ferris, and A. C. Koskelo, *Appl. Spectrosc.* **50**, 1175 (1996).

| Sample – CRC/            | 8-4-26/53 | 8-4-26/54 | 8-4-26/55 | 8-4-26/56 | 8-4-26/57 |
|--------------------------|-----------|-----------|-----------|-----------|-----------|
| c(Si)/ppm                | 210       | 60        | 30        | 30        | 180       |
| c(Al)/ppm                | 420       | 500       | 510       | 100       | 180       |
| c(Fe)/ppm                | 530       | 320       | 2300      | 2980      | 2580      |
| c(Mg)/ppm                | 420       | 1390      | 1170      | 860       | 790       |
| c(Na)/ppm                | 850       | 3840      | 310       | 300       | 310       |
| c(Ca)/ppm                | 270       | 380       | 710       | 860       | 700       |
| c(Cl)/ppm                | 950       | 3340      | 510       | 610       | 260       |
| c(S)/ppm                 | 1700      | 2460      | 1530      | 1060      | 960       |
| Total ash yield/<br>wt % | 0.58      | 1.32      | 0.92      | 0.96      | 0.88      |
| Moisture/wt %            | 47.0      | 37.0      | 49.0      | 49.5      | 56.2      |
| Sample – CRC/            | 8-4-26/58 | 8-4-26/59 | 8-4-26/60 | 8-4-26/61 | 8-4-26/62 |
| c(Si)/ppm                | 170       | 40        | 310       | 40        | 50        |
| c(Al)/ppm                | 40        | 40        | 90        | 130       | 50        |
| c(Fe)/ppm                | 460       | 2250      | 350       | 820       | 780       |
| c(Mg)/ppm                | 380       | 620       | 400       | 1090      | 1330      |
| c(Na)/ppm                | 420       | 150       | 260       | 300       | 320       |
| c(Ca)/ppm                | 460       | 580       | 440       | 2820      | 2650      |
| c(Cl)/ppm                | 500       | 220       | 220       | 220       | 180       |
| c(S)/ppm                 | 1170      | 840       | 1190      | 1220      | 1050      |
| Total ash yield/<br>wt % | 0.42      | 0.68      | 0.43      | 1.00      | 0.96      |
| Moisture/wt %            | 58.1      | 63.5      | 55.9      | 56.6      | 54.3      |

| Sample - CRC/            | 8-4-26/63 | 8-4-26/64 | 8-4-26/65 | 8-4-26/66 | 8-4-26/67 |
|--------------------------|-----------|-----------|-----------|-----------|-----------|
| c(Si)/ppm                | 1290      | 1280      | 2900      | 2610      | 2890      |
| c(Al)/ppm                | 590       | 620       | 1220      | 270       | 390       |
| c(Fe)/ppm                | 160       | 190       | 340       | 390       | 390       |
| c(Mg)/ppm                | 200       | 190       | 240       | 470       | 430       |
| c(Na)/ppm                | 270       | 270       | 270       | 310       | 310       |
| c(Ca)/ppm                | 200       | 150       | 160       | 700       | 590       |
| c(Cl)/ppm                | 270       | 270       | 270       | 580       | 270       |
| c(S)/ppm                 | 1210      | 1240      | 1410      | 1490      | 1880      |
| Total ash yield/<br>wt % | 0.63      | 0.62      | 1.10      | 1.13      | 1.21      |
| Moisture/wt %            | 61.0      | 61.3      | 60.8      | 61.1      | 60.9      |
| Sample - CRC/            | 8-4-26/68 | 8-4-26/69 | 8-4-26/70 | 8-4-30/36 | 8-4-30/37 |
| c(Si)/ppm                | 20        | 50        | 50        | 30        | 240       |
| c(Al)/ppm                | 180       | 50        | 190       | 210       | 110       |
| c(Fe)/ppm                | 2170      | 1310      | 270       | 870       | 1130      |
| c(Mg)/ppm                | 640       | 1410      | 310       | 830       | 890       |
| c(Na)/ppm                | 210       | 390       | 230       | 230       | 240       |
| c(Ca)/ppm                | 640       | 3750      | 310       | 400       | 410       |
| c(Cl)/ppm                | 210       | 190       | 390       | 370       | 440       |
| c(S)/ppm                 | 750       | 1020      | 1160      | 1270      | 1090      |
| Total ash yield/<br>wt % | 0.63      | 1.22      | 0.24      | 0.57      | 0.61      |
| Moisture/wt %            | 64.5      | 51.3      | 61.2      | 66.7      | 65.9      |

92. L. M. Cabalín, D. Romero, J. M. Baena, and J. J. Laserna, *Surf. Interface Anal.* **27**, 805 (1999).
93. M. Eyett and D. Bäuerle, *Appl. Phys. Lett.* **51**, 2054 (1987).
94. Z. W. Hwang, Y. Y. Teng, K. P. Li, and J. Sneddon, *Appl. Spectrosc.* **45**, 435 (1991).
95. J. M. Vadillo, C. C. García, S. Palanco, and J. J. Laserna, *J. Anal. At. Spectrom.* **13**, 793 (1998).
96. J. M. Vadillo, J. M. Fernández Romero, C. Rodríguez, and J. J. Laserna, *Surf. Interface Anal.* **27**, 1009 (1999).
97. X. Chen and J. Mazumder, *Appl. Phys. Lett.* **57**, 2178 (1990).
98. L. St-Onge, M. Sabsabi, and P. Cielo, *Spectrochim. Acta Part B* **53**, 407 (1998).
99. I. B. Gornushkin, J. M. Anzano, L. A. King, B. W. Smith, N. Omenetto, and J. D. Winefordner, *Spectrochim. Acta Part B* **54**, 491 (1999).
100. K. Song, H. Cha, J. Lee, and Y. I. Lee, *Microchem. J.* **63**, 53 (1999).
101. I. B. Gornushkin, L. A. King, B. W. Smith, N. Omenetto, and J. D. Winefordner, *Spectrochim. Acta Part B*, **54**, 1207 (1999).
102. A. K. Knight, N. L. Scherbarth, D. A. Cremers, and M. J. Ferris, *Appl. Spectrosc.* **54**, 331 (2000).
103. D. A. Cremers, J. E. Barefield II, and A. C. Koskelo, *Appl. Spectrosc.* **49**, 857 (1995).
104. C. M. Davies, H. H. Telle, D. J. Montgomery, and R. E. Corbett, *Spectrochim. Acta Part B* **50**, 1059 (1995).
105. W. E. Ernst, D. F. Farson, and D. J. Sames, *Appl. Spectrosc.* **50**, 306 (1996).
106. B. J. Marquardt, S. R. Goode, and S. M. Angel, *Anal. Chem.* **68**, 977 (1996).
107. B. J. Marquardt, D. N. Stratis, D. A. Cremers, and S. M. Angel, *Appl. Spectrosc.* **52**, 1148 (1998).
108. P. Fichet, P. Mauchien, and C. Moulin, *Appl. Spectrosc.* **53**, 1111 (1999).
109. G. A. Theriault, S. H. Lieberman, and D. S. Knowles, *Proceeding of 4<sup>th</sup> International Symposium, Field Screening Methods for Hazardous Wastes and Toxic Chemicals* 863 (1995).
110. G. A. Theriault and S. H. Lieberman, *Proceedings of European Symposium on Optics for Environmental and Public Safety* (1995).
111. B. Miles and J. Cortes, *Field Anal. Chem. Technol.* **2**, 75 (1998).
112. N. A. Peppers, E. J. Scribner, L. E. Alterton, R. C. Honey, E. S. Beatrice, I. Harding-Barlow, R. C. Rosan, and D. Glick, *Anal. Chem.* **40**, 1178 (1968).

113. K. L. Morton, J. D. Nohe, and B. S. Madsen, *Appl. Spectrosc.* **27**, 109 (1973).
114. H. Pang, D. R. Wiedrin, R. S. Houk, and E. S. Yeung, *Anal. Chem.* **63**, 390 (1991).
115. V. Kanicky, V. Otruba, and J. M. Mermet, *Appl. Spectrosc.* **52**, 638 (1998).
116. A. Ciucci, M. Corsi, V. Palleschi, S. Rastelli, A. Salvetti, and E. Tognoni, *Appl. Spectrosc.* **53**, 960 (1999).
117. R. Wisbrun, I. Schechter, R. Niessner, and H. Schroder, *Proceedings of International Conference on Monitoring of Toxic Chemicals and Biomarkers 2* (1993).
118. S. C. Langford and J. T. Dickinson, *Proc. SPIE-Int. Soc. Opt. Eng.* **2835**, 62 (1996).
119. D. A. Rusak, M. Clara, E. E. Austin, K. Visser, R. Niessner, B. W. Smith, and J. D. Winefordner, *Appl. Spectrosc.* **51**, 1628 (1997).
120. U. Panne, M. Clara, C. Haisch, and R. Niessner, *Spectrochim. Acta Part B* **53**, 1969 (1998).
121. R. Sattmann, I. Mönch, H. Krause, R. Noll, S. Couris, A. Hatziapostolou, A. Mavromanolakis, C. Fotakis, E. Larrauri, and R. Miguel, *Appl. Spectrosc.* **52**, 3 (1998).
122. I. B. Gornushkin, B. W. Smith, H. Nasajpour, and J. D. Winefordner, *Anal. Chem.* **71**, 5157 (1999).
123. J. M. Anzano, I. B. Gornushkin, B. W. Smith, and J. D. Winefordner, *Polym. Eng. Sci.* **40**, 2423 (2000).
124. J. A. Aguilera, C. Aragón, and F. Peñalba, *Appl. Surf. Sci.* **127-129**, 309 (1998).
125. D. R. Alexander, D. E. Poulain, M. U. Ahmad, R. D. Kubik, and E. R. Cespedes, *Proceedings of International Geoscience and Remote Sensing Symposium 767* (1994).
126. D. Anglos, S. Couris, and C. Fotakis, *Appl. Spectrosc.* **51**, 1025 (1997).
127. I. Gobernado-Mitre, A. C. Prieto, V. Zafirooulos, Y. Spetsidou, and C. Fotakis, *Appl. Spectrosc.* **51**, 1125 (1997).
128. S. Klein, T. Stratoudaki, V. Zafirooulos, J. Hildenhagen, K. Dickmann, and Th. Lehmkuhl, *Appl. Phys. A* **69**, 441 (1999).
129. K. T. Lu, D. Baba, and D. Ding, *Am. Environ. Lab.* **10**, 22 (1998).
130. M. Martin, M. Castillejo, R. Torres, and D. Silva, *Laser Chem.* **18**, 155 (1999).
131. C. Nouvellon, C. Chaléard, J. L. Lacour, and P. Mauchien, *Appl. Surf. Sci.* **138/139**, 306 (1999).
132. M. A. Player, J. Watson, and J. M. O. De Freitas, *Proc. SPIE-Int. Soc. Opt. Eng.* **4076**, 260 (2000).
133. D. N. Stratis, K. L. Eland, and S. M. Angel, *Appl. Spectrosc.* **54**, 1270 (2000).
134. L. Xu, V. Bulatov, V. V. Gridin, and I. Schechter, *Anal. Chem.* **69**, 2103 (1997).

135. F. Y. Yueh, J. P. Singh, C. F. Su, R. Vasudev, and J. C. Marra, Proceedings of Environmental Issues and Waste Management Technologies in the Ceramic and Nuclear Industries III (1998).
136. D. A. Cremers, L. J. Radziemski, and T. R. Loree, Appl. Spectrosc. **38**, 721 (1984).
137. R. E. Neuhauser, B. Ferstl, C. Haisch, U. Panne, and R. Niessner, Rev. Sci. Instrum. **70**, 3519 (1999).
138. J. R. Wachter and D. A. Cremers, Appl. Spectrosc. **41**, 1042 (1987).
139. J. P. Singh, H. Zhang, F. Y. Yueh, and K. P. Carney, Appl. Spectrosc. **50**, 764 (1996).
140. H. Zhang, F. Y. Yueh, and J. P. Singh, Appl. Opt., **38**, 1459 (1999).
141. D. A. Cremers, and L. J. Radziemski, Anal. Chem. **55**, 1252 (1983).
142. H. Lancelin, L. Dudragne, P. Adam, and J. Amouroux, High Temp. Mater. Processes **4**, 109 (2000).
143. S. Yalçın, D. R. Crosley, G. P. Smith, and G. W. Faris, Appl. Phys. B. **68**, 121 (1999).
144. L. J. Radziemski, T. R. Loree, D. A. Cremers, and N. M. Hoffman, Anal. Chem. **55**, 1246 (1983).
145. I. Ahmad and B. J. Goddard, J. Fiz. Mal. **14**, 43 (1993).
146. S. Böldeker, S. Günter, A. Könies, L. Hitzschke, and H.-J. Kunze, Phys. Rev. E **47**, 2785 (1993).
147. National Institute of Standards and Technology, Atomic Spectra Database Version 2.0 (1999).
148. A. N. Zaidel', V. K. Prokof'ev, and S. M. Raiskii, *Tables of Spectrum Lines*. (Pergamon Press, Oxford, 1961).
149. R. A. Johnson and G. K. Bhattacharyya, *Statistics: principles and methods*. 2<sup>nd</sup> ed. (John Wiley and Sons, Inc., New York, 1992).
150. W. Mendenhall, D. D. Wackerly, and R. L. Scheaffer, *Mathematical Statistics with Applications*. 4<sup>th</sup> ed. (Duxbury Press, Belmont, 1990).
151. R. Mavrodineanu and H. Boiteux, *Flame Spectroscopy*. (John Wiley and Sons, Inc., New York, 1965).
152. G. Bekefi, C. Deutsch, and B. Yaakobi, in *Principles of Laser Plasmas*, G. Bekefi, Ed. (John Wiley and Sons, Inc., New York, 1976), pp. 549-628.
153. D. Hibbert, Proceedings of The Science and Technology of Low-Rank Coal. (1998).

154. R. F. Gunst and R. L. Mason, *Regression Analysis and its Application*. (Marcel Dekker, Inc., New York, 1980).
155. R. J. Harris, *A Primer of Multivariate Statistics*. 2<sup>nd</sup> ed. (Academic Press, Inc., Orlando, 1985).
156. I. E. Frank and J. H. Friedman, *Technomet.* **35**, 109 (1993).
157. CAMO ASA, *Unscrambler*, v. 7.5 (1999).
158. R. S. Higgins, L. T. Kiss, D. J. Allardice, A. M. George, and T. N. W. King, *Properties of brown coals from the Latobe Valley – A basis for the evaluation of quality*. (SECV, Melbourne, 1980).
159. G. L. Squires, *Practical Physics*. (Cambridge University Press, Cambridge, 1985).